Doctorate Dissertation

博士論文

Monazite as a tracer of crustal evolution

（モナザイトからたどる地殻進化）

A Dissertation Submitted for Degree of Doctor of Science
December 2018

平成30年12月博士（理学）申請

Department of Earth and Planetary Science,
Graduate School of Science, The University of Tokyo

東京大学大学院理学系研究科地球惑星科学専攻

Keita Itano

板野　敬太

Abstract

Orogeny has played an important role in the evolution of continental crust. Orogeny is divided into two types (Dewey and Bird, 1970; Matsuda and Uyeda, 1971): Pacific and collisional types. Pacific type orogeny, associated with the subduction of oceanic plate, is vital for the formation of juvenile continental crust. In contrast, collision type orogeny, causing buoyant continental collision, is significant for the reworking of continental crust. Constraints on the nature and timing of orogeny are essential for a better understanding of crustal evolution over the Earth's history.

Monazite, a light rare earth element (REE) phosphate, has a potential to be a powerful tracer for crustal processes. Monazite has been used as a geochronometer, geochemical tracer, and Nd isotopic tracer. The wide occurrence of monazite enables its various applications to the petrogenesis of granitic and metamorphic rocks. Monazite is also suited as a detrital high-resolution archive of orogenic events. The objective of this study is to advance our understanding of monazite geochemistry in order to use monazite as a tracer of crustal evolution.

It has been demonstrated that detrital monazite potentially provides more detailed insights in various scale orogenic events as compared to detrital zircon (Hietpas et al., 2010). Unfortunately, the various origins of monazite bring the difficulty in an interpretation of detrital monazite age peak. This difficulty can be overcome by linking geochemical fingerprints of monazite and its source rock types. Trace element composition is the key to understand the linkage due to its high dependence on co-existing minerals via element partitioning. However, there are two obstacles in monazite trace element geochemistry: (i) analytical problem in REE determination by laser ablation-inductively coupled plasma mass spectrometry (LA-ICP-MS) and (ii) shortage of trace element data especially for igneous monazite. To overcome these obstacles, I attempted to develop a method of accurate REE analysis. Furthermore, trace element systematics of igneous monazite has been studied by the comprehensive analyses of monazites from various granitic rocks. The synthesis of reliable datasets of monazite chemical compositions demonstrates the utility of monazite REE-Th-U systematics as an indicator of source rock type. The improved analytical method and geochemical provenance indicator were applied to detrital monazites from major African rivers to obtain the constraints on the timing and nature of Pan-African orogenic events.

Accurate REE determination of monazite by LA-ICP-MS can be inhibited by oxide interferences. Yet, the oxide production mechanism has been poorly understood. Here I determined the oxide production rates (MO^+/M^+ ratios) of 15 REEs, Th, and U using synthetic and natural phosphates. I

found two contrasting oxide production behaviors against the Ar sample gas flow rate, depending on the MO^+ dissociation energy ($D_0(MO^+)$): the MO^+/M^+ ratios of elements with $D_0(MO^+) \geq 7$ eV increased with the gas flow rates from 0.85 to 1.00 L min^{-1}, whereas those with $D_0(MO^+) < 7$ eV were nearly constant. Moreover, while there is a generally positive relationship between $\log(MO^+/M^+)$ and $D_0(MO^+)$ among all elements, only the former showed a linear correlation whose slope increased with the gas flow rate. These results indicate that oxide production is a combined result of the following two processes: (i) the equilibrium reaction of $MO^+ \leftrightarrow M^+ + O$ within the plasma and (ii) the bonding of M^+ and O through collisions followed by radiative transition in the interface region. Oxide production through the first process was significant relative to the second process only when the elements had $D_0(MO^+) \geq 7$ eV and the gas flow rate was high enough to decrease the plasma temperature to ~8000 K. We further demonstrate the significance of middle-REE oxide interference on heavy-REEs during the analyses of monazites from pegmatites and garnet-bearing metamorphic rocks, which should be corrected using the determined oxide production rates.

Trace element systematics of igneous monazite has not been well understood so far. I conducted trace element and Nd isotope analyses of monazite in granitic rocks from the Busetsu pluton of the Japan arc to investigate the change of monazite geochemical signatures with granitic magma evolution. Furthermore, by integrating of monazite Nd-isotope and plagioclase Sr-isotope microanalyses, I revisited the magma sources, which were inferred from conventional whole-rock chemistry. The studied monazite grains show variations in the degree of negative Eu anomaly, Ce/Gd, and Th/U ratios. These variations correlate with each other, which can be accounted for by the fractionation of plagioclase and monazite considering the strong partitioning of Eu to plagioclase and of light-REE and Th to monazite, respectively. In the context of Rayleigh fractionation model, the degrees of plagioclase and monazite fractionation were quantitatively evaluated and found to be compatible with the geologic and petrologic observations. The isotopic data revealed significant variations in monazite $^{143}Nd/^{144}Nd$ ratio and plagioclase $^{87}Sr/^{86}Sr$ ratios, which are obviously larger than those of whole-rock samples. This finding reflects that the multiple sources were involved in the generation of the granitic magma. It is demonstrated that an integration of geochemical and isotope microanalyses of monazite enables tracking open system magmatic processes.

To link monazite composition with igneous petrogenesis and differentiation, we carried out comprehensive LA-ICP-MS measurements of REE-Th-U abundances in monazites from magnetite-series and ilmenite-series granitic rocks across the Japan arc. The data revealed systematic

differences in monazite composition between magnetite-series and ilmenite-series samples, and between pegmatites and granites. In ilmenite-series granitic rocks, monazites from pegmatites showed larger negative Eu anomalies, lower light-REE/middle-REE ratios, and higher middle-REE/heavy-REE ratios than those from granites. These geochemical variations were attributed to significant fractional crystallization of feldspars, monazite, xenotime, and garnet during differentiation in relatively reduced peraluminous granitic magmas. In contrast, there was no remarkable difference in the REE fractionation pattern between magnetite-series pegmatites and granites. Furthermore, the magnitudes of the negative Eu anomalies in the magnetite-series monazites were smaller than those observed in the ilmenite-series samples. These features were interpreted to reflect the suppression of monazite, xenotime, and garnet fractionation and limited Eu incorporation into fractionating feldspars in relatively oxidized and non-peraluminous magmas. A comparison of the present data with previously reported data indicates that igneous monazites from granitic rocks are distinct from metamorphic monazites in REE composition, especially due to their larger negative Eu anomalies. Metamorphic monazites are further grouped into garnet-rich metamorphic with high middle-REE/heavy-REE and garnet-poor metamorphic origin with the low ratio. This finding highlights the potential utility of monazite REE-Th-U systematics as a provenance indicator for detrital monazites.

The geochemical indicator for source rock type was applied to detrital monazite from large rivers in Africa. We carried out U–Pb dating and geochemical analyses of approximately 500 detrital monazites from the Nile, Niger, Congo, Zambezi and Orange Rivers. The U–Pb dating defined age peaks at ~600 Ma for the Nile, ~580 Ma for the Niger, ~630, ~610 and ~550 Ma for the Congo, ~500 Ma for the Zambezi and 1200–1000 Ma for the Orange. All but the Orange age peaks correspond to the period of the Pan-African Orogeny. In the Niger, Congo and Zambezi, the Pan-African age peaks are 20–40 Myr younger than those defined by the detrital zircons from the same rivers. Based on the geochemical provenance indicator, the transition between igneous, garnet-rich, and garnet-poor metamorphic events were described in the age spectra of detrital monazite. The interpreted age peaks, together with the discrepancy between the detrital monazite and zircon ages, suggest that the Pan-African monazite age peaks essentially reflect the timing of syn- to post-collisional metamorphic events in the source terranes, whereas the detrital zircons ages provide a more representative record of magmatic events. The results imply that the Pan-African Orogeny was promoted by pre- to syn-collisional felsic magmatism during the early stages and, 20–40 Myr later, it was dominated by syn- and/or post-collisional metamorphism.

Acknowledgement

I would first like to express my deep gratitude to my supervisor, Dr. Tsuyoshi Iizuka. He has consistently encouraged me over the years, as well as showing an ideal attitude as a researcher. He always gave me an interesting and surprising suggestion from the data which I found boring by myself. It was most exciting time that I discuss with him. If I had not met him, I would not have chosen this career.

At various stages of this work, I got a lot of help from Dr. Jun-Ichi Kimura and Dr. Qing Chang at Japan Agency for Marine-Earth Science and Technology and Dr. Tetsuichi Takagi and Dr. Mihoko Hoshino at national Institute of Advanced Industrial Science and Technology. They kindly provided the analytical samples and opportunities to use the analytical machines at the institutes. It was refreshing and fun for me to work in different places from usual office. I also appreciate that Prof. Yasushi Watanabe and Dr. Takuya Echigo kindly share carbonatite samples.

I am grateful to Prof. K. Ozawa, Prof. T. Mikouchi, Dr. K. Ueki, Dr. M. Sato and other seminar members for the insightful comments and suggestions at the weekly seminar. I also thank Hideto Yoshida, Koji Ichimura, and Akihito Kobayashi at the University of Tokyo and Dr. Mukai at AIST for helping analysis. I have been through a lot with the Iizuka laboratory members, Ms. Y. Hibiya, J. Nagao, Y. Homma, K. Ito, H. Enomoto, C. Harada., T. Yamaguchi, and K. Suzuki

Prof. Y. Sano, Prof. Y. Isozaki, Prof. S. Nakai, and Prof. S. Wallis reviewed this thesis and gave me helpful and constructive comments, which improved this thesis.

Last and definitely not least, I thank my parents for their support all along the way.

Table of Contents

1. General Introduction

1.1 Crustal evolution and Orogeny

The Earth is unique among the terrestrial planets in a bimodal topography due to the existence of continental and oceanic crust (Taylor and McLennan, 1996). The oceanic crust is a ~7 km layer and dominantly made up of basaltic rocks, whereas the continental crust is a ~40 km layer and has an andesite composition on average (Christensen and Mooney, 1995; Rudnick and Fountain, 1995). The continental crust is subdivided into upper, middle, and lower layers on the basis of seismological observations (Holbrook et al., 1992; Christensen and Mooney, 1995; Rudnick and Fountain, 1995). The upper part has a granitic composition (SiO_2 66.2% on average), leading to its preservation and long-term stability (Rudnick and Gao, 2003; Hawkesworth et al., 2010; Dhuime et al., 2011). Granitic melts are not in equilibrium with mineral assemblages of any mantle rocks, indicating that granitic crust cannot be directly derived from mantle melting (Rudnick, 1995). Hence, the generation of continental crust requires crust differentiation such as re-melting of mantle-derived materials and/or crystal fractionation (Anderson 1987, Rudnick, 1995; Taylor and McLennan, 1995). Although how continental crust has been formed is still in debate (e.g., Taira et al., 1998; Jagoutz and Schmidt, 2012; Arndt, 2013), the continental crusts with chemically and structurally mature characteristics indicate its generation and evolution through plate tectonics over the Earth's history (Korenaga, 2013; Hawkesworth et al. 2017, Iizuka et al., 2017).

Plate tectonics has driven the interaction of continental crust with not only mantle but also hydrosphere, atmosphere, and biosphere over the Earth's history. It is widely accepted that the continental crust plays an important role in carbon cycle via silicate weathering, which controls the long-term climate change (e.g., Tajika and Matsui, 1992). The secular change in elemental flux from eroded continental crust largely affects the chemical composition of sea water (Large et al., 2018), and it might be a trigger of the evolution of life around the Precambrian-Cambrian boundary (Shimura et al., 2014). Hence, how the continental crust has evolved is one of the most important topics in Earth science.

Orogeny is the results of plate convergence and essential for the evolution of continental crust. Dewey and Bird (1970) originally distinguished the Cordilleran-type orogeny and collision-type orogeny in terms of the geometric relation of thrusts and the development of a paired metamorphic belt (Miyashiro, 1961), and subsequently these types were refined as the Pacific and collision types to emphasize the generality (Matsuda and Uyeda, 1971). The Pacific type, associated with the subduction of oceanic plate, is a continuous process; whereas the collision type, caused by buoyant continental collision, has episodically occurred during the supercontinent cycle (Nance and Murphy, 2013). These two type orogenic events play contrasting roles in the evolution of continental crust. In convergent margins where the Pacific-type orogeny is active, the production of voluminous granitic rocks is thought to have been caused by the differentiation of basaltic and andesitic magma generated by a flux melting of wedge

mantle (Jagoutz, 2010; Annen et al., 2006; Jagoutz et al., 2011; Nandedkar et al., 2014). In contrast, continent-continent collisions have produced granitic magmas through remelting of pre-existing rocks including meta-sedimentary rocks (Collins, 2002; Clemens, 2003; Chappell et al., 2000; Miller et al., 2003). Although the lower layer of continental crust is widely believed as basaltic material, Hacker et al. (2011) proposed that the decompression melting of subducted continental crust resulted in the formation of lower crust consisting of felsic rocks rather than mafic rocks. The Pacific type orogeny is significant for the formation of juvenile continental crust (Santosh et al., 2010), whereas the collision type orogeny is important for the reworking of continental crust (Cawood et al., 2009).

A high-resolution archive of orogenic events has been constructed over several decades through detailed geological, structural, petrological, seismological, and paleomagnetic studies. One approach to sample the continental crust is using detrital minerals derived by weathering and erosion of various exposed rocks. The application of in-situ dating techniques of zircons to detrital samples showed the correspondence between zircon age peaks and the timing of supercontinent assembly accompanying global Pacific- and collision-type orogeneses (Condie et al., 2005; Campbell and Allen, 2008; Rino et al., 2008; Belousova et al., 2010; Iizuka et al., 2010a). Although it is controversial whether the zircon age peaks reflect the major timing of crustal production (Arndt and Davaille, 2013; Condie et al., 2017) or the preservation bias during supercontinent assembly (Hawkesworth et al., 2009; Spencer et al., 2015, 2017), detrital

zircon study has provided insights regarding the timing of orogenic events. The zircon age data basically reflect the timing of voluminous felsic magmatism including both of juvenile magma input (Pacific-type orogeny) and reworking (collision-type orogeny). The Hf and O isotope analyses of zircon enable an estimate of relative contributions of reworking to juvenile magma input (e.g., Valley et al., 1994; Griffin et al., 2000). However, the approach using detrital zircon has limitations in deconvolution between the two-type orogenic events during supercontinent assembly and precise constraints on the timing of small-scale orogenic events.

Monazite [(La, Nd, Ce, Th) PO_4] has the potential to provide more robust constraints on the timing and nature of orogenic events. Due to its wide occurrence, monazite geochemistry, geochronology, and isotope chemistry have been used in the pursuit of understanding various processes in crustal evolution, including magmatic and metamorphic processes and diagenesis (Overstreet, 1967; Parrish, 1990). Recently, it has been shown that detrital monazites derived from igneous and metamorphic rocks record orogenic events more accurately than detrital zircons do (Hietpas et al., 2010, 2011). There are, however, still tasks to maximize the potential of monazite. The prospects and current limitations of monazite as a tool in crustal evolution studies are reviewed in the next section.

1.2 Monazite

1.2.1 Occurrence of monazite

Igneous monazite commonly occurs in low-Ca peraluminous granitoids (e.g., Xie et al., 2006; Kelts et al., 2008; Chattopadhyay et al., 2015) and less frequently in peralkaline igneous rocks (Bea, 1996; Hoshino et al., 2012). Igneous monazite is also found as a primary accessory phase in granitic pegmatites that are highly enriched in rare earth element (REE) (Hoshino et al., 2012; Chen et al., 2017). While monazite geochronology might be complementary to zircon one in many cases, Th–U–Pb dating of monazite is essential for the petrogenesis of rocks where zircon is absent or unstable, such as carbonatites and other highly alkaline systems (Roberts et al., 2010). Monazite plays a critical role in REE behaviors in granitic magma as a host phase of light-REE (LREE). The 80~55 wt% of whole-rock LREE contents reside within monazite in peraluminous granites (Bea, 1996).

Metamorphic monazite is frequently found in pelitic and psamitic low- to high-grade metamorphic rocks (e.g., Rasmussen et al., 2001, 2005; Rubatto et al., 2001, 2006; Buick et al., 2010; Holder et al., 2015), though less commonly reported from intermediate metamorphic rocks (Bingen and van Breemen, 1998). Monazite can grow during not only high- but also low-grade metamorphic events, which is unique among accessory minerals suitable for U–Pb dating. Theses metamorphic monazites are characterized by complicated chemical zoning (Williams et al., 2007). The change in monazite trace element composition has been interpreted to reflect the change in crystallization/growth condition such as co-existing mineral assemblages. Thus, monazite geochemistry might allow us to link the multiple monazite-forming events

with specific points within P-T-t path (Mottram et al., 2014; Štípská et al., 2015).

Hydrothermal monazite typically shows differences in texture and chemical composition from other origins. Its texture is characterized by a cluster of minute grains or highly irregular morphology (e.g., Wing et al., 2003; Grew et al., 2008). Many studies reported that recrystallization *via* dissolution-reprecipitation processes fully or partially reset the Th–U–Pb isotopic system even when temperature is enough low to regard the effect of Pb diffusion as negligible, leading to the potential for dating hydrothermal activity (Ayers et al., 2006; Kelly et al., 2012). Hydrothermal alteration of monazite has been mainly investigated based on experimental studies (Seydoux-Guillaume et al. 2002; Harlov and Hetherington, 2010, 2011; Hetherington et al., 2010; Budzyń et al., 2011, 2017), revealing high dependence of monazite stability on the fluid composition.

1.2.2 Monazite as a geochronometer

The value of monazite as a geochronometer comes from its crystal structure that accommodates Th^{4+} and U^{4+} (Ni et al. 1995; Huminicki and Hawthorne 2002; Clavier et al. 2011). Importantly, monazite contains little common Pb and the diffusion of the isotope system in monazite is slow enough to retain the original isotopic information (Williams et al., 2007). The diffusion experiment reported by Cherniak et al. (2004) demonstrated that the Pb closure temperature of a 10-μm-monazite grain would be >900 ºC, given a cooling rate of 10 ºC/Ma. Similar estimates of Pb closure temperatures have

been reported by many previous studies using natural samples (Rubatto et al., 2001; Bosch et al., 2002; McFarlane and Harrison, 2006). Besides, it is widely reported that metamictization caused by radiation damage is limited for monazite; whereas Pb-loss enhanced by metamictization often occurs for zircon (Black et al., 1984; Meldrum et al., 1998; Seydoux-Guillaume et al., 2007; Nasdala et al., 2010).

Different *in-situ* monazite Th–U–Pb dating methods have different advantages. Radiometric dating is basically conducted by mass spectrometry to obtain isotopic ratios. Monazite, however, can be dated by EPMA thanks to enough high concentrations of Th, U, and Pb. The ages are calculated from the collected Th–U–total Pb data by assuming no common Pb and no Pb-loss or by constructing a chemical isochron (CHIME method) (Suzuki and Adachi, 1998, 1991; Jercinovic and Williams, 2005; Suzuki and Kato, 2008; Montel et al., 1996; Cocherie et al., 1998; Pyle et al., 2005;). The EPMA is advantageous in terms of the high spatial resolution of ~1 μm and the capability of major element mapping. In contrast, the SIMS and LA-ICP-MS techniques provide isotopic information with higher sensitivity although the spatial resolutions are lower than the resolutions possible with EPMA. The concordance of the U–Th–Pb system is essential for robust interpretation of the obtained ages. U–Th–Pb dating using SIMS was pioneered by DeWolf et al. (1993) and has been developed and applied by many workers (Ireland and Gibson, 1998; Stern and Berman, 2001; Vry et al., 1996; Zhu et al., 1997; Rasmussen et al., 2001; Sano et al., 2006; Jantos et al., 2012; Kusiak et al., 2014). Regarding LA-ICP-MS, solid-state 213 nm Nd:YAG or 193 nm ArF excimer

and quadrupole-ICP-MS (Q-ICP-MS) and sector filed-ICP-MS (SF-ICP-MS) are widely deployed (Machado and Gauthier, 1996; Kosler et al., 2001; Foster et al., 2002; Horstwood et al., 2003). LA-ICP-MS is capable of a rapid measurement (e.g., <1 min per a measurement) and, therefore, collecting large statistically meaningful datasets for detrital monazite study.

1.2.3 Monazite as a geochemical tracer

The REE composition of monazite has been used as a geochemical tracer for crustal processes (e.g., Suzuki et al., 1992; Spear and Pyle 2002). Monazite has abundant LREE contents in the order of weight percentage and various heavy-REE (HREE) contents ranging from several thousands to <1 ppm. The variability of monazite REE composition could be linked to its genesis, or crystallization condition, because the REE composition is controlled by co-existing mineral assemblages, whole-rock composition, melt composition, temperature, pressure, and fluid activity (e.g., Williams et al., 2007; Hetherington et al., 2017). The high contents of REEs allow us to carry out spot analysis with high spatial resolution by electron probe microanalyzer (EPMA), laser ablation-inductively coupled plasma-mass spectrometry (LA-ICP-MS), and secondary ion mass spectrometry (SIMS). The trace element behavior in monazite has been investigated mainly for metamorphic monazite, and the geochemical variation described by microanalysis is connected to the change in a stable mineral assemblage of metamorphic rocks (e.g., Mottram et al., 2014; Holder et al., 2015). On the other hand, reports of trace element geochemistry on igneous monazite are limited.

1.2.4 Monazite as an isotope tracer

The Sm–Nd isotope system of monazite is also used as a powerful tracer for crustal processes. The $^{143}Nd/^{144}Nd$ and $^{147}Sm/^{144}Nd$ ratios of monazite can be obtained by the LA-MC-ICP-MS technique with a spatial resolution of 20–30 μm due to high concentrations of Nd and Sm (~10^4 to 10^5 ppm) (Mcfarlane and Mcculloch, 2007; Yang et al., 2008; Iizuka et al., 2011a). Fisher et al. (2017) demonstrated that the Nd isotope variations within single monazite grains in a granite reflect the open-system magmatic processes (Fisher et al., 2017). The Nd isotope analysis has been also applied to monazites in metasedimentary rocks and detrital samples to track the timing of crustal evolutionary events (Iizuka et al., 2011b; Liu et al., 2017). As compared to the Lu–Hf isotope analysis of zircon, the Sm–Nd isotope analysis of monazite is advantageous in minor inheritance of older core and smaller analytical volumes required.

1.2.5 Obstacles for monazite as a tracer of crustal evolution

The typical occurrence of igneous monazites in peraluminous granites, of which voluminous production is associated with the collision-type orogeny, in addition to metamorphic origins is in contrast to common occurrence of zircon in metaluminous to peraluminous granite. This difference in occurrence between monazite and zircon can be a clue to capture the transition from Pacific-type to collision-type orogenic events. However, the various origins of monazite bring the difficulty in interpretations of monazite age spectra. This difficulty can be overcome by linking geochemical

fingerprints of monazite and its source rock types. Trace element composition of monazite is the key to understand the linkage due to its high dependence on co-existing minerals via element partitioning. However, there are two obstacles: (i) analytical problems of REE determination and (ii) limited data of monazite trace element compositions.

Microanalysis techniques are essential for determining reliable geochemical composition of minute monazite grains or individual sub-domains within single grains. Traditionally, the REE systematics has been investigated using the EPMA technique because of its utility for elemental mapping (e.g., Franz et al., 1996; Broska et al., 2005). For instance, the Th- and Y-zoning of monazite grains have been linked to multiple growth in prograde/retrograde metamorphism (e.g., Pyle and Spear 2003; Kohn et al. 2005). However, the EPMA technique has a difficulty in determining accurate HREE and Eu contents in monazite because of their low abundances and serious interferences in the complicated REE L-line series (Suzuki et al., 1990; Holder et al., 2015). As a result, the systematics of trace element in monazite, especially HREE, is still unknown.

Recent advances in LA-ICP-MS have enabled the quantification of trace HREE with high spatial resolution (<20μm). Spectral interferences, however, can be problematic during the REE analysis of monazite by LA-ICP-MS as well. The contrasting concentrations for weight percent-order LREE and ppm-order HREE in monazite result in high signal intensities of LREE-oxides comparable to those of HREEs even when oxide production rates are decreased to less than 1%. Unfortunately, the productions of

REE oxides are inevitable due to the presence of oxygen derived from samples. This impact on the quantification of REE concentrations needs to be assessed and corrected for an accurate measurement.

Monazites in pelitic and psamitic metamorphic rocks have been relatively well studied, and the effects of co-existing minerals, such as feldspars, garnet and zircon on the trace element composition of monazite were inferred (Rubatto et al., 2006; Buick et al., 2010; Iizuka et al., 2010b; Mottram et al., 2014; Štípská et al., 2015). In contrast, the available trace element data of monazites in granitic rocks, carbonatites, and thermal fluid deposits are significantly scarce. Accurate trace element data of various monazite, especially igneous monazite, are required for better understanding of monazite trace element systematics. Comparing the trace element compositions of monazites from various rock types unravels their geochemical characteristics, which leads to its application as a provenance indicator.

1.3 Overview of this thesis

1.3.1 Motivation and Objective

The evolution of continental crust is closely related to orogeny in convergent margins. The questions to be addressed are when orogenic events have occurred through the Earth's history and what is the nature of orogenic events (the nature of orogeny: crustal growth vs. reworking). The objective of this work is to advance our understanding of monazite geochemistry in order to use monazite as a tracer of crustal evolution.

Particular emphasis is placed on a trace element microanalysis of monazite using the LA-ICP-MS technique. Better understanding of the trace element systematics is essential for tracing complex magmatic and metamorphic processes during monazite crystallization/growth. The approach using detrital monazite has a potential to be a breakthrough for more accurate constraints on the timing of orogenic events and tracking the transition from the Pacific-type to collision-type orogeny during supercontinent assembly.

There are some obstacles to be overcome for this objective, which includes an analytical problem, deficit in monazite trace element data, and ambiguity in the relation between monazite origin and its trace element characteristics, as discussed in the previous section. First, more accurate REE analysis by LA-ICP-MS was developed using synthetic REE phosphates. Second, the trace elements systematics of igneous monazite was revealed by the geochemical study of monazite in granitic rocks. The synthesis of reliable datasets of monazite trace element composition clarified the linkage between the geochemical fingerprints and source rock types. Finally, the improved REE analysis method and the developed geochemical indicator of source rock type were applied to detrital monazites to obtain constraints on the timing and nature of orogenic events.

1.3.2 Outline

The following body of this thesis is divided up into five chapters. Each of the

subsequent chapters has been individually published or prepared for submission. Each chapter contains its own introduction, results, discussion, and conclusion. In the final chapter, I summarize these works and provide future perspectives on the utility of monazite.

For reference, Chapter 2 is about the improvement of REE analysis, which was published as "Unraveling the mechanism and impact of oxide production in LA-ICP-MS by comprehensive analysis of REE-Th-U phosphates" in *Journal of Analytical Atomic Spectrometry*, **32**, 2003–2010, 2017. In chapter 3, the REE systematics of igneous monazite is mainly discussed and the contents of this chapter is in preparation for submission. Chapter 4 is based on the published paper entitled "REE-Th-U and Nd isotope systematics of monazites in magnetite-and ilmenite-series granitic rocks of the Japan arc: Implications for its use as a tracer of magma evolution and detrital provenance" in *Chemical Geology*, **484**, 69–80, 2018, in addition to new data obtained in this work. In this chapter, the geochemical indicator of source rock type is proposed based on the comparison of compositions between monazites of various origins. Chapter 5 has been revised from the paper entitled "U–Pb chronology and geochemistry of detrital monazites from major African rivers: Constraints on the timing and nature of the Pan-African Orogeny" in *Precambrian Research*, **282**, 139–156, 2016. Geological interpretation of detrital monazite age peaks is given based on the geochemical compositions for the first time and the comparison between the detrital monazite and zircon provides the insights on orogenic events around the Gondwana

supercontinent assembly.

2. Unraveling the mechanism and impact of oxide production in LA-ICP-MS by comprehensive analysis of REE-Th-U phosphates

2.1 Introduction

Laser ablation inductively coupled plasma mass spectrometry (LA-ICP-MS) has been widely used for trace element and isotopic determinations of geological and biological samples because it offers a means of *in-situ* analysis of solid samples with high spatial resolution and high analytical throughput (Russo et al., 2002, 2013). However, isobaric and polyatomic spectral interferences remain a major challenge in accurate LA-ICP-MS analysis (Hattendorf et al., 2016). One of the most problematic interference is from oxide ions of elements that are abundantly included in the samples because the introduction of oxygen from the sample matrix and entrained air in the plasma is inevitable during ICP-MS analysis. For instance, although rare earth elements (REE) in rock and mineral samples can provide clues to their origins (Condie and Hunter, 1976; Rapp et al., 1991; Plank and Langmuir, 1998; Belousova et al., 2002; Itano et al., 2016), oxide ions of light- and middle-REE (LREE and MREE) interfere with M-REE and heavy-REE (HREE) ions, and these interferences can cause inaccuracies for REE analyses of samples that are depleted in HREE relative to LREE.

Oxide production during ICP-MS measurements has been traditionally studied by analyzing solution samples under wet plasma conditions (Douglas and French, 1986; Vaughan and Horlick, 1990; Niu and Houk, 1996; Longerich et al., 1987; Poussel et al.,

1994; Romero et al., 1997; Aries et al., 2000). The results showed that the oxide production rate (MO^+/M^+ ratio) strongly depends on plasma and interface conditions, such as the radio frequency (RF) power applied to the plasma, sample gas flow rate, sampling depth and geometry of the sampling and skimmer cones (Douglas and French, 1986; Longerich et al., 1987; Vaughan and Horlick, 1990; Poussel et al., 1994; Niu and Houk, 1996; Romero et al., 1997; Aries et al., 2000). Specifically, a higher plasma power or a lower sample gas flow rate results in a lower MO^+/M^+ ratio. These observations suggest that oxide production occurs within the plasma and/or interface regions (Gray, 1986; Gray and Williams, 1987; Vaughan and Horlick, 1990; Niu and Houk, 1996; Lichte et al., 1987; Longerich et al., 1987; Poussel et al., 1994; Payne et al., 2013). Moreover, a positive correlation has been demonstrated between the log (MO^+/M^+) and the MO^+ dissociation energy ($D_0(MO^+)$). This relationship may reflect the thermal equilibrium between M^+ and MO^+ species. However, equilibrium temperatures, estimated by fitting to a Boltzmann distribution, range from ~5000 to ~21000 K (Douglas and French, 1986; Vaughan and Horlick, 1990; Houk and Praphairaksit, 2001; Longerich et al., 1987; Kubota et al., 1989; Shibata et al., 1993; Evans et al., 2002), many of which are apparently higher than the plasma temperature of ~8000K. This led some authors to argue that significant oxide production within the plasma is unlikely (Douglas and French, 1986; Vaughan and Horlick, 1990; Longerich et al., 1987). More recently, oxide production under dry plasma conditions was studied using the desolvating nebulizer technique (Newman et al., 2009; Newman, 2012;

Kimura et al., 2013). The results revealed that oxide production is dependent on the cone geometry and, for some elements such as Nd and Ce, it is associated with mass-independent isotope fractionation. Because the isotope fractionation can be well explained by the nuclear field shift effect, it has been proposed that the oxide production occurs in the interface region through collisional reactions under an excited state of the outermost electron orbital spin that enhance a nuclear volume shift and result in bonding/dissociation between metal and oxygen ions under a metastable state (Newman et al., 2009).

There are a few comprehensive researches on oxide production during LA-ICP-MS analysis (Kent and Ungerer, 2005; Witte and Houk, 2012; Gilbert et al., 2017). Kent and Unger (2005) investigated oxide production of Ba and LREE (La, Ce, Pr, and Nd) during LA-ICP-MS analyses under variable samples gas flow rates and found a dependence of the MO^+/M^+ ratio on the gas flow rate and D_0(MO), generally consistent with the results of solution-ICP-MS measurements. Unlike solution-ICP-MS, however, the relative ratios of MO^+/M^+ between each of L-REE showed a non-monotonic change with the sample gas flow rate (Kent and Ungerer, 2005). Witte and Houk (2012) found that the addition of N_2 and He to Ar sample gas flow reduces MO^+/M^+ ratios of some REE (Y, Ce, Tb, and Tm), Cs, and Ta as a result of temperature increase at the optimum sampling position within the plasma. More recently, Gilbert et al. (2017) showed that MO^+/M^+ ratios of some elements such as Th depend on the matrix of the sample being ablated (e.g., glass, metal, silicate, and phosphate), indicating the requirement of a

matrix-match reference material for a robust correction of interferences by the oxide ions.

To gain a better understanding of oxide production in LA-ICP-MS and to assess the impact of oxide interferences, we analyzed synthetic and natural REE phosphates as well as a synthetic silicate glass using the LA-ICP-MS technique. The synthetic REE phosphates enabled us, for the first time, to directly determine the MO^+/M^+ ratios of all REE during LA-ICP-MS analysis. Since the REE are f-block elements and have similar chemical properties but highly variable $D_0(MO^+)$, our results allow a rigorous evaluation of the dependence of the MO^+/M^+ on $D_0(MO^+)$, which, in turn, provides new insights into the mechanism of oxide production in ICP-MS. Furthermore, the results highlight the importance of oxide interference correction for the accurate determination of REE concentrations in natural monazite, a phosphate mineral that has been widely used for U–Pb dating and REE geochemistry (Rubatto et al., 2006; Mottram et al., 2014; Holder et al., 2015; Stipska et al., 2015).

2.2 Experimental

For determination of REE oxide production rates ($REEO^+/REE^+$) during LA-ICP-MS analysis, we analyzed 15 synthetic phosphates of single REE (Y, La, Ce, Pr, Nd, Sm, Eu, Gd, Tb, Dy, Ho, Er, Tm, Yb, and Lu) that were originally prepared as standards for electron probe microanalysis (EPMA) following the method of Cherniak et al. (2004) (courtesy of K. Ichimura). To evaluate the oxide production rates of U and Th and the

effect of the sample matrix on oxide production, we used the synthetic silicate glass NIST SRM 610 standard (Pearce et al., 1997) and a natural monazite 16-F-6 from the Pilbara Craton, Western Australia, which is used as an in-house standard for U–Pb dating and Sm–Nd isotopic analysis (Black et al., 2004; Simonetti et al., 2006; Iizuka et al., 2011a). In addition, the significance of REE oxide interferences were assessed by analyzing igneous monazites in a granite and pegmatite from Japan (Busetsu and Shichironai granitic bodies, respectively) (Hoshino et al., 2012) and a metamorphic monazite in a meta-conglomerate from Mt. Narryer in the Yilgarn Craton of Western Australia (Iizuka et al., 2010b).

All analyses were performed on a Thermo Fisher Scientific iCAP Qc ICP-MS coupled with a CETAC LSX-213 G2+ Nd:YAG LA system at the Department of Earth and Planetary Science, The University of Tokyo. Operational conditions of the instruments are listed in Table 2-1. The iCAP Qc is equipped with a collision/reaction cell where oxide ions can be attenuated through the collision/reaction with an additional gas. We did not utilize the collision/reaction cell technique, however, because the aim of this study is to better understand the mechanism of oxide production in ICP-MS. The LA system is equipped with the active two-volume HelEx™ Cell, in which He gas was used to flush the ablated aerosol particles (Eggins et al., 1998). Before sample analysis, the sample cell was thoroughly purged with He gas so that the remaining atmospheric oxygen in the cell had less effect on the measured MO^+/M^+ ratios. When the purge was insufficient, the MO^+/M^+ ratios decreased markedly with time during each analytical

session (Kent and Ungerer, 2005). The Ar sample gas flow rate was varied from 0.75 to 1.00 L min^{-1} in a 0.05 L min^{-1} steps to investigate its effect on the oxide production, while other operating conditions thought to control the MO^+/M^+ ratio, such as sampling depth, plasma power, and cone geometry (Douglas and French, 1986; Longerich et al., 1987; Vaughan and Horlick, 1990; Poussel et al., 1994; Niu and Houk, 1996; Romero et al., 1997; Aries et al., 2000) were not changed. Measured MO^+/M^+ ratios were corrected for mass bias using an exponential law. The mass bias factor was obtained for each analytical condition by normalizing the measured $^{160}Gd/^{155}Gd$ ratio to the synthetic Gd phosphate of 1.477 (Berglund and Engi, 2011). Note that the choice of linear or power law for the mass bias correction would not alter the arguments below.

To evaluate the significance of the REE oxide interference correction during LA-ICP-MS analyses of natural monazites, the gas flow rate was set at 0.77 L min^{-1} to reduce the MO^+/M^+ ratio to the same level as in previous studies (Janots et al., 2008; d'Abzac et al., 2010). For the determination of REE concentrations, NIST SRM 610 standard glass was used as an external standard. Furthermore, independently determined Ce concentrations were used as an internal standard. The Ce concentrations were measured by EPMA using a JEOL JXA-8530F at the Department of Earth and Planetary Science, The University of Tokyo.

Table 2-1: Instrumental operational parameters of the LA-ICP-MS

Nd:YAG Laser	CETAC LSX-213 G2+ (CETAC, USA) equipped with the active two-volume HelEx™ Cell
Laser source	213 nm
Pulse width	5 ns
Beam diameter	20 µm
Repetition rate	4 Hz
Laser fluence	20.54 J cm^{-2}
Laser He carrier gas	0.95 L min^{-1}
ICP-MS	iCAP Qc (Thermo Fisher Scientific)
RF-power	1550 W
Sampling depth	5.1 mm
Cool gas (Ar)	14 L min^{-1}
Auxiliary gas (Ar)	0.78 L min^{-1}
Sample gas (Ar)	0.75–1.00 L min^{-1}
Measured isotopes	^{89}Y, ^{105}Pd, $^{139, 138}La$, $^{140, 136, 138, 142}Ce$, ^{141}Pr, $^{143, 142, 146}Nd$, $^{147, 149, 152, 154}Sm$, $^{151, 153}Eu$, $^{157, 154, 155, 156, 158, 160}Gd$, ^{159}Tb, $^{163, 160, 161, 162}Dy$, ^{165}Ho, $^{167, 168, 170}Er$, ^{169}Tm, $^{173, 171, 172, 174, 176}Yb$, $^{175, 176}Lu$, ^{179}Hf, ^{195}Pt, ^{232}Th, ^{238}U, $^{232}Th^{16}O$, $^{238}U^{16}O$

2.3 Results and Discussion

2.3.1 Oxide production rates

The mass-bias-corrected $REEO^+/REE^+$ ratios of the synthetic REE phosphates, 16-F-6 standard monazite, and NIST SRM 610 glass are presented in Appendix Table 2-1. The ThO^+/Th^+ and UO^+/U^+ ratios of the 16-F-6 monazite and NIST SRM 610 glass are listed in Table 2-2, showing that the two different matrix samples yielded indistinguishable MO^+/M^+ ratios within analytical uncertainty at all studied sample gas flow rates except for 0.85 L min^{-1}, where the monazite yielded a ~20% lower ThO^+/Th^+ ratio. The MO^+/M^+ ratios are plotted against sample gas flow rate in Fig. 2-1, together with signal intensities of M^+ and MO^+. Signal intensities of M^+ decreased with the increase of the sample gas flow rate for all analyte elements (Fig. 2-1). By contrast, the response of MO^+ signals and MO^+/M^+ ratios to the change in sample gas flow rate varied and can be divided into two groups: (1) MO^+/M^+ ratios of Sm, Eu, Dy, Ho, Tm, Er, Yb, and Lu were relatively constant over the range of studied sample gas flow rates, whereas (2) those of Y, La, Ce, Pr, Nd, Gd, Tb, Th and U were reasonably constant between the sample gas flow rates of 0.75 and 0.85 L min^{-1} but exponentially increased from 0.85 to 1.00 L min^{-1}. Notably, the first group has low $D_0(MO^+)$ (≤6 eV, hereinafter referred to as weak-oxide formers), whereas the second group has higher $D_0(MO^+)$ (≥7 eV, referred to as strong-oxide formers) (Ackermann, 1976; Haynes, 2013). In addition, detailed examination of the data shows that the YbO^+/Yb^+ and EuO^+/Eu^+ ratios decreased slightly with an increase in the sample gas flow rate (Figs. 2-1 and 2-2).

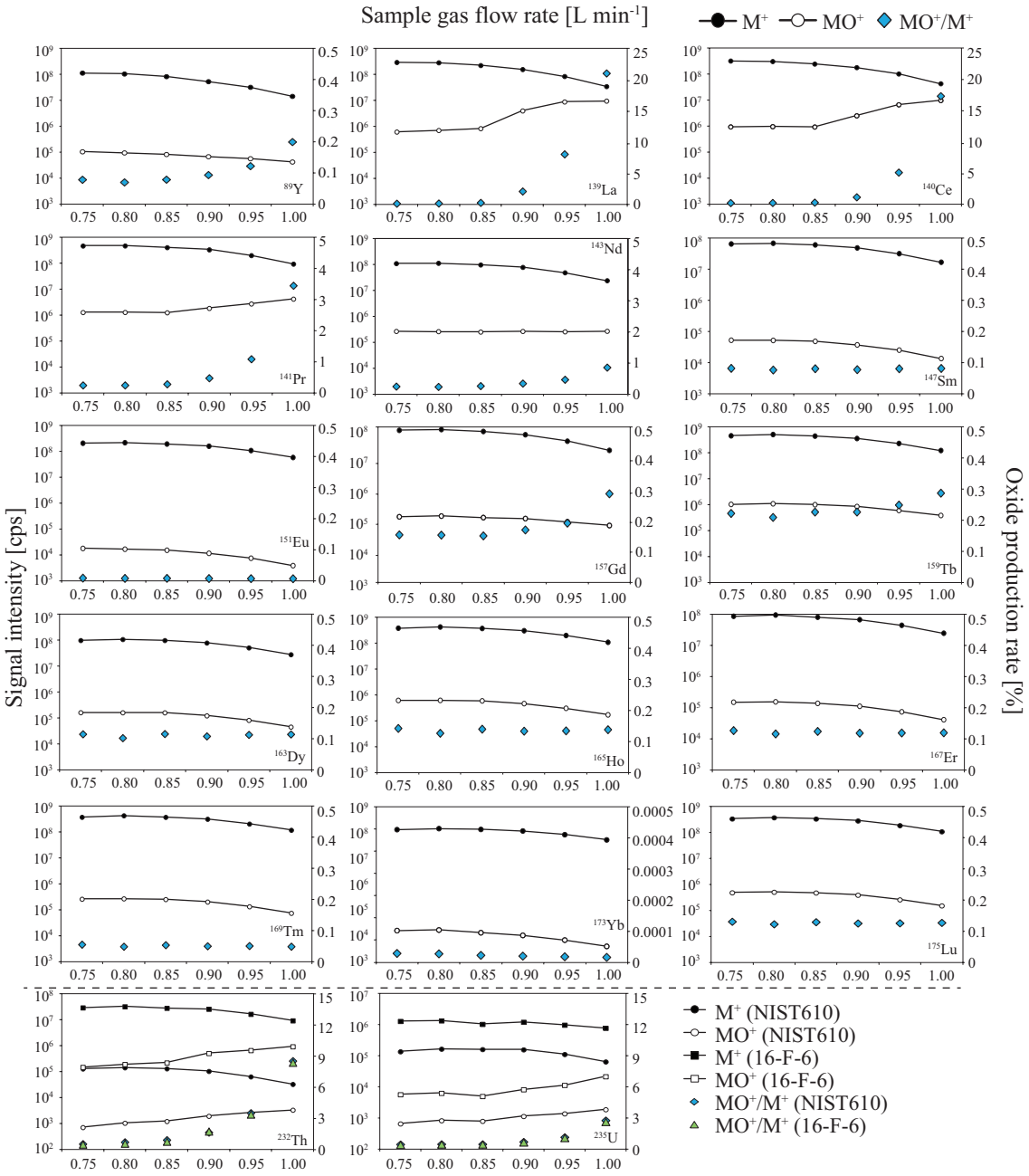

Fig. 2-1. Signal intensities of analyte elements and their oxides and the oxide production rates as a function of sample gas flow rates ranging from 0.75 to 1.00 L min^{-1}. The data were obtained from synthetic REE phosphates for REE and from the NIST SRM 610 and the 16-F-6 monazite for Th and U.

The log (MO^+/M^+) values are plotted as a function of $D_0(MO^+)$ in Fig. 2-2a. The log (MO^+/M^+) values are also plotted against $D_0(MO)$ in the Appendix Fig. S2-1, following several previous studies (Aries et al., 2000; Kent and Ungerer, 2005; Ackermann, 1976). There is a generally positive relationship between the log (MO^+/M^+) and $D_0(MO^+)$ as well as $D_0(MO)$, consistent with the previous studies (Douglas and French, 1986; Longerich et al., 1987; Aries et al., 2000; Litche et al., 1987; Kent and Ungerer, 2005). In detail, however, our data reveal that the positive relationship systematically changes with the ranges of the $D_0(MO^+)$ and sample gas flow rate (Fig. 2-2a). At gas flow rates of 0.75 to 0.85 L min^{-1}, the log (MO^+/M^+) increases markedly with $D_0(MO^+)$ until ~5 eV, but only moderately increases after this point. At higher gas flow rates (0.90 to 1.00 L min^{-1}), while a similar trend is observed among the weak-oxide formers, the log (MO^+/M^+) of the strong-oxide formers increases significantly and is linearly correlated with $D_0(MO^+)$. The rate of increase in the oxide production rates is larger at higher sample gas flow rates. Moreover, at high sample gas flow rates, the linear correlations of log (MO^+/M^+) against $D_0(MO^+)$ (correlation coefficient of 0.96–0.99) are stronger than those of log (MO^+/M^+) against $D_0(MO)$ (correlation coefficient of 0.81–0.87) (Figs. 2-2a and Appendix Fig. 2-1).

Table 2-2. Oxide production rates of Th and U for the NIST SRM 610 standard and the 16-F-6 monazite

	NIST SRM 610		Monazite 16-F-6	
Sample gas flow rate [L min^{-1}]	ThO^+/Th^+ [%]	UO^+/U^+ [%]	ThO^+/Th^+ [%]	UO^+/U^+ [%]
0.75	0.50 ± 0.08	0.44 ± 0.07	0.47 ± 0.04	0.41 ± 0.04
0.80	0.64 ± 0.15	0.44 ± 0.07	0.53 ± 0.03	0.43 ± 0.07
0.85	0.83 ± 0.10	0.44 ± 0.09	0.69 ± 0.03	0.43 ± 0.03
0.90	1.6 ± 0.3	0.63 ± 0.08	1.7 ± 0.1	0.59 ± 0.01
0.95	3.5 ± 0.4	1.1 ± 0.2	3.4 ± 0.1	1.0 ± 0.1
1.00	8.6 ± 1.4	2.5 ± 0.3	8.5 ± 0.8	2.4 ± 0.2

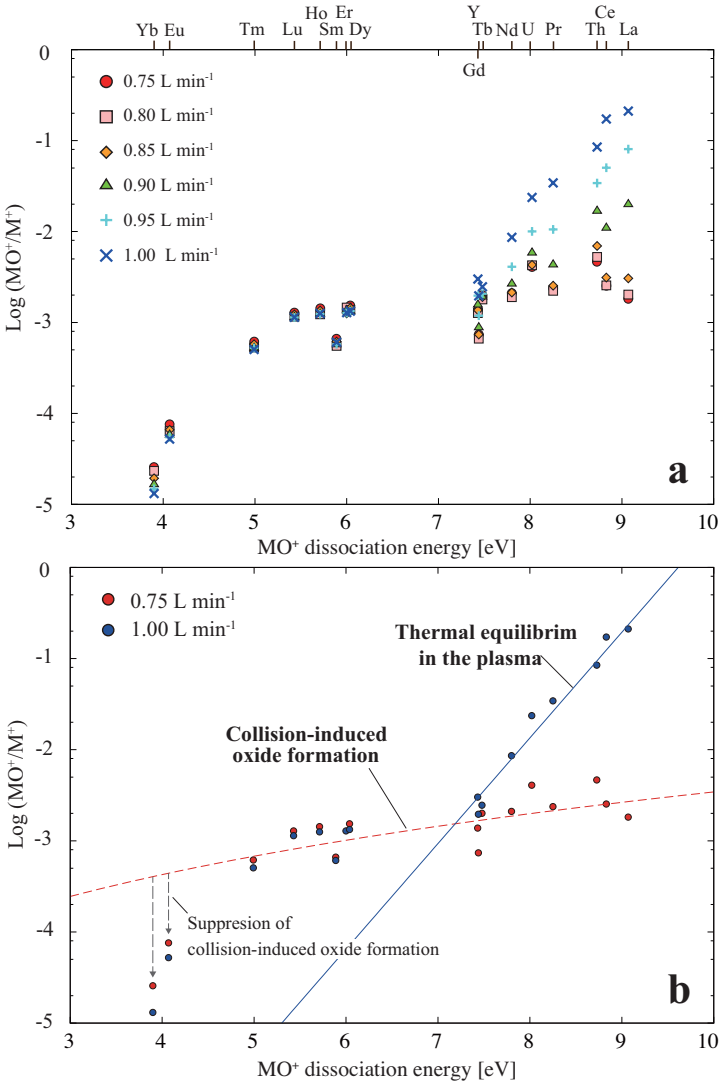

Fig. 2-2: (a) Plot of log (MO^+/M^+) of phosphates versus MO^+ dissociation energy for REE, Th and U with various sample gas flow rates. (b) Schematic diagram showing the effects of oxide production and dissociation processes on the MO^+/M^+ ratio. The solid line represents the best fit with the strong-oxide former data at the gas flow rate of 1.00 L min^{-1}, which is considered to reflect the equilibrium reaction of $MO^+ \leftrightarrow M^+ + O$ within the plasma at 4300 K. The dashed curve represernts the relationship between the MO^+/M^+ ratio and MO^+ dissociation energy obtained from Eq. 2 with $c\tau = 2 \times 10^{-6}$, likely reflecting collision-induced oxide formation. The vertical arrows indicate the suppression of collision-induced oxide formation for Yb and Eu especially at a higher gas flow rate.

2.3.2 Mechanism of oxide production

The distinct behaviors of the MO^+/M^+ ratio between the strong- and weak-oxide formers strongly suggest that the main oxide formation process is different between these two groups, especially at high sample gas flow rates. The strong-oxide formers exhibit a linear correlation between the log (MO^+/M^+) and $D_0(MO^+)$ for each sample gas flow rate ranging from 0.90 to 1.00 L min^{-1}, in which the slope increases with the sample gas flow rate. As a higher sample gas flow rate results in a lower plasma temperature (Lindner and Bogaerts, 2011; Raut et al., 2003), the dependence of the slope of the linear correlation on the sample gas flow rate can be interpreted as reflecting the thermal equilibrium between MO^+ and $M^+ + O$ within the plasma. By fitting the strong-oxide former data to a Boltzmann distribution expressed as (Douglas and French, 1986; Longerich et al., 1987):

$$\frac{MO^+}{M^+} \propto e^{-D_0/kT} \quad (1)$$

where k is Boltzmann's constant and T is the temperature, we derived equilibrium temperatures of ~7900, ~5000, and ~4300 K at sample gas flow rates of 0.90, 0.95, and 1.00 L min^{-1}, respectively (Fig. 2-2b). These equilibrium temperatures are within the range of the plasma temperatures typically sampled in ICP-MS (Houk and Praphairaksit, 2001; Raut et al., 2003; Lindner and Bogaerts, 2011; Bogaerts and Aghaei, 2017), supporting the inference of the oxide production under equilibrium within the plasma.

By contrast, at sample gas flow rates of ≤0.85 L min^{-1}, the strong-oxide former data can be fitted by a line with a slope corresponding to a temperature of >20000 K, significantly higher than the maximum plasma temperature. This unreasonably high temperature, together with the independence of their MO^+/M^+ ratio on the sample gas flow rate change, indicates that a process other than the thermal equilibrium is responsible for oxide production at the low gas flow rates. Note that fitting the data for both strong- and weak-oxide formers at a gas flow rate of ≥0.90 L min^{-1} also results in an apparent high temperature, which might lead some to argue that oxide production within the plasma is insignificant (Douglas and French, 1986; Longerich et al., 1987; Vaughan and Horlick, 1990).

Oxide production through collisions in the interface region has been suggested based on variable MO^+/M^+ ratios depending on the geometry of the sampling and skimmer cones (Douglas and French, 1986; Longerich et al., 1987; Vaughan and Horlick, 1990; Poussel et al., 1994; Shibata et al., 1993). For a stable MO^+ to be formed thorough collisions, the excess energy liberated by oxide bonding needs to be removed by either a collision to the third body or by radiative decay of MO^+ from an excited state to the ground state (Niu and Houk, 1996; Newman et al., 2009). Given that three-body collision is trivial in the low-pressure interface region (Douglas and French, 1986), the latter mechanism is more likely responsible for the oxide production. Indeed, oxide formation involving the collision of M^+ and O followed by radiative transition can account well for the isotope-dependent MO^+/M^+ ratio and concomitant

mass-independent isotope fractionation observed for Nd and Ce (Newman et al., 2009). In this case, the MO^+/M^+ ratio can be expressed as Newman et al., 2009:

$$\ln\left(\frac{MO^+}{M^+}\right) = \ln\left(1 - e^{-c\nu^3\tau}\right) + c\nu^3\tau \qquad (2)$$

where c is a proportional constant reflecting the transition probability, ν is the transition frequency that is proportional to the sum of $D_0(MO^+)$ and the potential energy of the metastable O (1.97 eV), and τ is the life time of the collision. Remarkably, the relationship between log (MO^+/M^+) and $D_0(MO^+)$ calculated from this equation with $c\tau = 2 \times 10^{-6}$ fits the data for both the strong-oxide formers at the gas flow rates of ≤0.85 L min^{-1} and for the weak-oxide formers, except Yb and Eu (Fig. 2-2b). Although the calculation of log (MO^+/M^+) depends highly on the values chosen for c and τ, the shape of the relation curve is insensitive to the choice. Thus, the observed moderate increase of log (MO^+/M^+) with the $D_0(MO^+)$ from 5 to 9 eV is well explained by oxide formation through collisions of M^+ and O followed by radiative energy loss to stabilize the MO^+ ions in the interface region.

The data for Yb and Eu, that have the lowest $D_0(MO^+)$ among the studied elements, deviate from the expected trend for the oxide production in the interface region, even though their MO^+/M^+ ratios are still higher than the values expected for the equilibrium reactions of $MO^+ \leftrightarrow M^+ + O$ within the plasma (Fig. 2-2b). Moreover, the measured YbO^+/Yb^+ and EuO^+/Eu^+ ratios decreased with increased Ar sample gas flow rate.

These observations suggest that Ar suppressed the oxide formation in the interface region only for elements having $D_0(MO^+) \leq 4$ eV. Such energy-threshold behavior may imply that the suppression results from the dissociation of weakly-bound oxides through collisions with Ar species in the interface region.

Overall, the relationship of the MO^+/M^+ ratio with the $D_0(MO^+)$ and the sample gas flow rate can be attributed to a combination of the following two oxide formation processes (Fig. 2-2b): (i) the equilibrium reactions of $MO^+ \leftrightarrow M^+ + O$ within the plasma and (ii) bonding of M^+ and O by collisions and subsequent radiative transition in the interface region. The first process was significant only for oxide production of the elements with $D_0(MO^+) \geq 7$ eV, under low-temperature plasma conditions (≤8000 K). Otherwise, the second process dominated the oxide production. Furthermore, the oxide formation *via* the second process was suppressed for elements having $D_0(MO^+) \leq 4$ eV especially at a higher sample gas flow rate, possibly due to collision-induced dissociation in the interface region. The relative significance of the two oxide production processes may change with the cone geometry and oxygen availability that is controlled mainly by the methods of sample introduction. However, the finding that the MO^+/M^+ ratio reflects a combined result of the two processes should persist regardless of various analytical conditions and be taken into account when applying a correction for oxide interferences.

2.3.3 Matrix effect

Our data for the 16-F-6 monazite and NIST SRM 610 glass (Table 2-2) indicate restricted effect of sample matrix on UO^+/U^+ and ThO^+/Th^+ ratios. This differs from the results of Gilbert et al. showing that ThO^+/Th^+ ratio of monazite can be down to half of that of NIST SRM 610 glass, while UO^+/U^+ ratio was more consistent between the two samples. In detail, the matrix effect was more significant under laser ablation conditions where larger aerosols were generated *i.e.* longer laser wavelength, lower laser fluence, and more opaque samples (Hanselman et al., 1994; Kuhn and Günter, 2004). Because ionization energies of oxides of strong-oxide formers, including Th and U, are generally lower than their D_0(MO) and $D_0(MO^+)$, atomization and ionization of the oxides within the plasma should essentially proceed *via* reactions of (i) $MO \leftrightarrow MO^+ + e^-$ and (ii) $MO^+ \leftrightarrow M^+ + O$. The introduction of large aerosols into the plasma would prevent efficient ionization and atomization of the oxides, leading to the matrix dependency of MO^+/M^+ for strong-oxide formers. The restricted matrix effect in this study would be attributed to a higher laser fluence (20 J cm^{-2}) compared to the previous study (3.5–11 J cm^{-2}) (Gilbert et al., 2017), which resulted in the generation of fine aerosols and allowed the reactions of $MO^+ \leftrightarrow M^+ + O$ to reach equilibrium within the plasma. This inference is consistent with the good linear correlation between the log (MO^+/M^+) and $D_0(MO^+)$ among the strong-oxide formers (Fig. 2-2a).

2.3.4 Impact of oxide interference

The results of the REE analyses of the igneous and metamorphic monazite from the Japan island arc and Yilgarn Craton are presented in Appendix Table 2-2 and the chondrite-normalized REE patterns are shown in Fig. 2-3. The monitored ThO^+/Th^+ and UO^+/U^+ were ~0.6% and ~0.5%, respectively and nearly constant during each analytical session. These oxide production rates are comparable to those during LA-ICP-MS REE analyses in previous studies (Berglund and Wieser, 2011; Janots et al., 2008). The measured $^{139}La/^{173}(Yb + GdO)$ and $^{139}La/^{175}(Lu + TbO)$ ratios range from ~2100 to ~26000 and from ~4300 to ~46000, respectively.

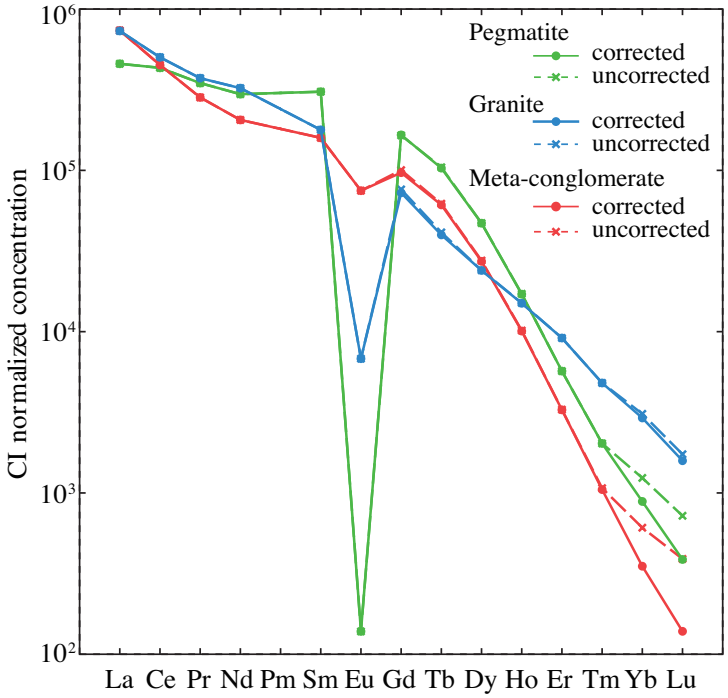

Fig. 2-3: Chondrite-normalized REE plots for monazites in pegmatite, granite, and meta-conglomerate. The solid and broken lines represent the results with and without the oxide interference correction, respectively.

The $REEO^+/REE^+$ ratio during the analyses can be estimated from the measurements of the synthetic REE phosphates within the same analytical session, because the ThO^+/Th^+ and UO^+/U^+ ratios monitored for the analyzed natural monazites indicate insignificant changes of the MO^+/M^+ ratio during the analytical sessions. Moreover, because of the possible matrix dependency for oxide production rates by LA-ICP-MS (Gilbert et al., 2017), the synthetic phosphates, rather than synthetic glass or silicate, provide more robust estimation of the oxide production rate. Applying the $REEO^+/REE^+$ ratios measured for the synthetic phosphates, we have calculated the signal intensities of MO^+ of LREE and MREE that interfere with those of MREE and HREE ions (Fig. 2-4) and compared the REE concentrations obtained with and without the interference correction (Fig. 2-3 and Appendix Table S2-2). The results demonstrate that oxide interferences are most critical for the two heaviest REE, Yb and Lu (Fig. 2-4). The estimated $^{173}GdO/^{173}(Yb + GdO)$ and $^{175}TbO/^{175}(Lu + TbO)$ range from 6% to 42% and from 9% to 64%, respectively. The highest $^{173}GdO/^{173}(Yb + GdO)$ and $^{175}TbO/^{175}(Lu + TbO)$ ratios were obtained for the monazite from the meta-conglomerate that shows a REE pattern characterized by significant HREE depletion (Fig. 2-3). The depletion of HREE is attributed to their strong partitioning into co-existing garnet (Hauri et al., 1994; Johnson, 1998). Importantly, monazite commonly occurs with garnet in high-grade metamorphic rocks, particularly in peraluminous metasedimentary rocks (Rubatto et al., 2006; Mottram et al., 2014; Holder et al., 2015; Stipska et al., 2015). The REE pattern of the monazite from the pegmatite also exhibits

significant H-REE depletion, together with a highly negative Eu anomaly (Fig. 2-3). The REE characteristics likely result from significant fractional crystallization of feldspars and zircon/xenotime that strongly partition Eu and HREE, respectively. Note that although Eu ions are interfered by Ba oxide ions, the oxide interferences should be negligible because of the low dissociation energy of BaO^+ (~4.57 eV) (Fig. 2-2). Specifically, BaO^+/BaO^+ is estimated from Eq.2 to be at most 0.03%, which results in $^{151}BaO/^{151}(Eu + BaO)$ of <3% for the pegmatite monazite even if the monazite contains 1wt% Ba. These results demonstrate that the oxide interference correction is required for accurate LA-ICP-MS determination of HREE in monazites from high-grade metamorphic rocks and pegmatites, unless the analytical setting is optimized to reduce ThO^+/Th^+ and UO^+/U^+ ratios to < 0.1%. Thus, we propose that the oxide interference correction should be made for accurate HREE determination of monazite using synthetic MREE phosphates.

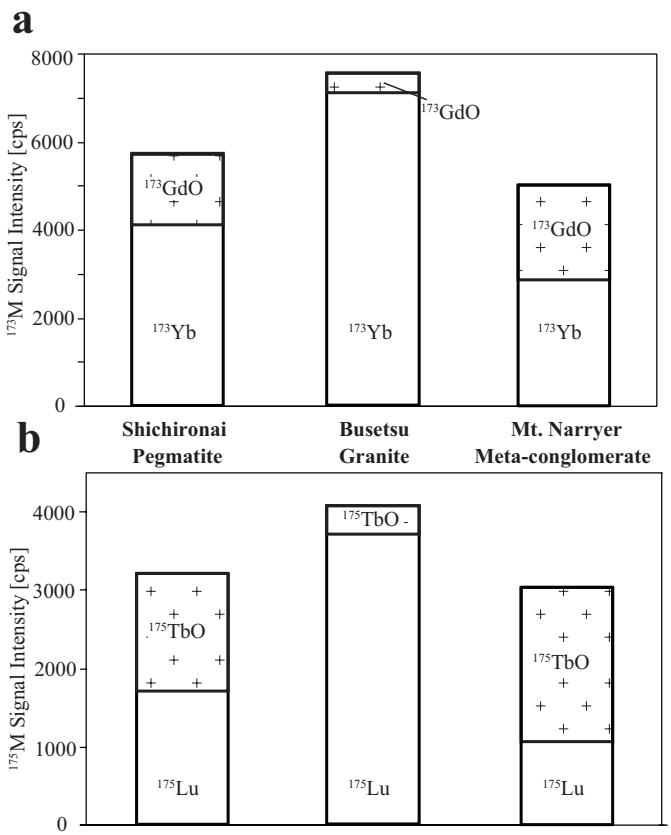

Fig. 2-4: Comparison of signal intensities between (a) ^{173}Yb and ^{173}GdO, and between (b) ^{175}Lu and ^{175}TbO for natural monazites in pegmatite, granite, and meta-conglomerate.

2.4 Conclusion

Our comprehensive analysis of REE-Th-U phosphates revealed systematic changes of the MO^+/M^+ ratio with $D_0(MO^+)$ and sample gas flow rate, which in turn unraveled the two oxide formation processes in ICP-MS: (i) the equilibrium reaction of $MO^+ \leftrightarrow M^+ +$ O within the plasma and (ii) bonding of M^+ and O through collisions and following radiative decay in the interface region. The oxide production *via* the equilibrium reaction in the plasma was significant only when the elements had a $D_0(MO^+)$ higher than 7 eV and the plasma temperature was lower than ~8000 K. Otherwise, the collisional oxide production in the interface region was dominant. In addition, the collisional oxide production was suppressed for the elements with $D_0(MO^+)$ lower than 4 eV especially at a higher Ar sample gas flow. This study further highlighted the impacts of MREE oxide interferences on accurate HREE determination of monazites from pegmatites and garnet-bearing metamorphic rocks, which can be corrected by using synthetic MREE phosphates.

3. Granitic magma evolution deciphered by trace element and Nd isotope microanalysis of monazite

3.1 Introduction

Granitic magma plays an important role in differentiation of continental crust. It is widely accepted that the generation of felsic melts, which is not in equilibrium with the ultramafic mantle mineral assemblage, requires partial melting of crustal rocks as well as differentiation through fractional crystallization (e.g., Clemens, 1990; Patino-Douce and Beard, 1995; Johannes and Holtz, 1996; Montel and Vielzeuf, 1997; Clemens and Watkins, 2001). Experimental study can provide direct constraints on the partial melting in closed systems, which has revealed that the composition of granitic melt is dominantly controlled by the composition of source rock (e.g., Gao et al., 2016). In contrast, the evolution of granitic magma in natural systems involves open-system processes: hybridization of magmas derived from multiple sources, fractional crystallization, and assimilation of country rocks at emplacement levels. Indeed, granitic plutons commonly display geochemical and radiogenic isotopic zonings (Bateman et al., 1979; Barbey et al., 2001; Antunes et al., 2008). Consequently, it is fundamental for understanding granitic magma evolution to identify multiple sources and track subsequent processes to its solidification such as differentiation and assimilation.

Monazite is a well-suited tracer for granitic magma evolution. The Nd isotope composition of monazite can be determined by laser ablation-multiple

collector-inductively coupled plasma mass spectrometry (LA-MC-ICP-MS) (McFarlane and McCulloch, 2007; Gregory et al., 2009; Wu et al., 2010; Iizuka et al., 2011b). Fisher et al. (2017) demonstrated that the inputs of magma from isotopically variable sources are recorded in the heterogeneity of Nd isotope composition within single monazite grains. Moreover, monazite has a potential to track the differentiation of granitic magma through the change of light-, middle-, and heavy-REE (LREE, MREE, HREE) concentrations with the differentiation (Fisher et al., 2017). Most of studies on igneous monazite, however, were conducted by the EPMA technique which has a difficulty in precise and accurate determination of trace element concentration including Eu and HREE (e.g., Suzuki et al., 1990, 1992; Harlov et al., 2008). As a result, trace element systematics of monazite has not been quantitatively explored so far.

The Rb–Sr isotope system is complementary to the Sm–Nd isotope system and a strong tool for the petrogenesis of granitic rocks (e.g., Kagami, 1973). The Sr isotope microanalysis of plagioclase has been widely performed to investigate the heterogeneity in isotope compositions at the mineral or sub-mineral scales (Davidson et al., 1990, 2007, 2008; Gagnevin et al., 2005; Charlier et al., 2006). While the extraction of small sample using mechanical devices such as Micromill™ manufactured by New Wave are suitable to obtain high precision isotopic data, the *in situ* laser ablation technique is capable of enough precise analysis to detect the change in $^{87}Sr/^{86}Sr$ ratios (Christensen et al., 1995; Davidson et al., 2001; Ramos et al., 2004; Tatsumi et al., 2008). Plagioclase also plays an important role in Eu behavior during magma differentiation because

plagioclase as well as K-feldspar is the largest Eu reservoir, accounting for > 80 wt% of total Eu in granitic rocks (Bea, 1996).

In this study, the trace element systematics of monazite in granitic rocks from a single pluton was investigated to assess the utility of monazite as a tracer for granitic magma evolution. Furthermore, I evaluated the utility of the combined monazite Nd and plagioclase Sr isotope analyses to constrain magma sources, which were conventionally investigated by whole-rock isotope analysis. The Busetsu granite is suited for this objective because the geochemical and isotopic heterogeneities within the Busetsu granite were suggested based on whole-rock chemistry but what caused the heterogeneity remains ambiguous (Ishihara and Chappell, 2017).

3.2 The Busetsu granite in the Mikawa area, Japan

The Busetsu pluton is located in Mikwa area, Japan (Fig. 3-1) and a part of the Ryoke granitic rocks. The voluminous Ryoke granitic rocks are associated with low-P/high-T metamorphic rocks including metachert, metasandstone and metamudstone, extending for ~800 km along the Inner Zone of SW Japan (Asami et al., 1982; Miyake et al., 1992, 2014, 2016, 2017; Makimoto et al., 2004; Adachi and Wallis, 2008; Miyazaki, 2010). The Busetsu granite is known as the youngest pluton in this area based on the intrusive relationship and K-Ar biotite ages (Ryoke Research Group, 1972; Yamazaki, 2013). It is noteworthy that the intrusion of the Busetsu granite was obviously subsequent to metamorphic peak of ca. 97–89 Ma (Takatsuka et al., 2018).

The Busetsu granite is characterized by S-type granite affinities, whereas other Ryoke granites in this area are classified into I-type granites (Ishihara and Chappell, 2007). Early isotopic studies on the Rb–Sr isotope system reported different isochron ages of ~71.7 and 82.5 Ma, resulting from different and scattered datasets (Shibata and Ishihara, 1979; Nakai et al., 1982). Besides, the $\delta^{18}O$ values of Busetsu granite ranges from 10.5 to 13.5, which are higher than most of granitic rocks in the Japan arc (Ishihara and Matsuhisa, 2002; Ishihara and Chappell, 2007). These geochemical and isotopic signatures of the Busetsu granite indicate the contributions of sedimentary rocks to its petrogenesis (Ishihara and Chappell, 2007). However, the details of what processes caused the isotopic heterogeneity and the melting of sedimentary component are still unknown.

Suzuki et al. (1992) investigated the geochemistry of accessory minerals including monazite. The intra-grain variation in LREE composition between monazites within biotite and interstitial space was interpreted to reflect the onset and cessation of crystallization of other accessory minerals. The CHIME dating of the monazite in the Busetsu granite yielded ages of ~79–75 Ma (Suzuki et al., 1994; Nakai and Suzuki, 2003), which are inconsistent with the results of a recent zircon study on the Busetsu pluton (Takatsuka et al., 2018). Zircons from the Busetsu granites yielded various ages that are divided into four groups of ~100 Ma, 95–84 Ma, ~80 Ma, and 71–69 Ma (Takatsuka et al., 2018). The youngest ages are interpreted as the crystallization age of the granites, whereas the older ages are considered as reflecting ages of inherited zircon.

The monazite CHIME ages do not correspond to neither magmatic nor inherited zircon ages. This age discrepancy remains enigmatic and requires a re-examination of monazite crystallization by LA-ICP-MS U–Pb isotopic dating.

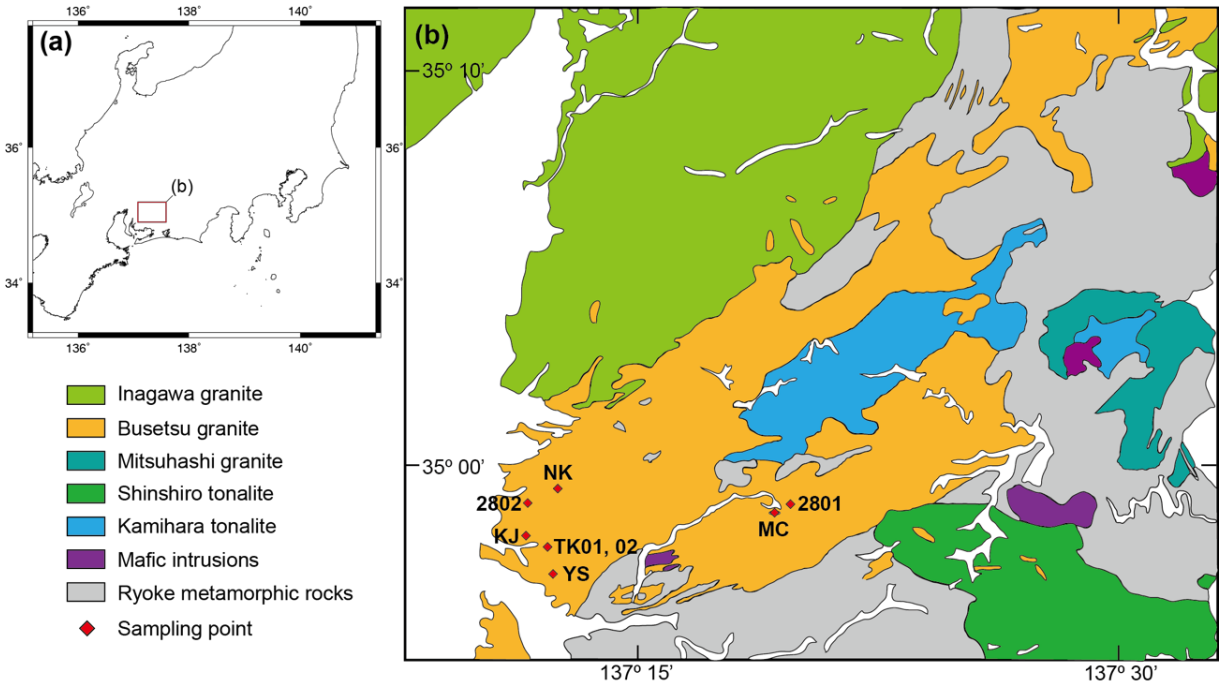

Fig. 3-1. (a) Location of the Busetsu granite pluton in the central area of Japan. (b) Geological map around the Busetsu granite associated with Ryoke metamorphic complex. Sample points of granitic rocks and a metamorphic rock (MC) are presented. The geological map is compiled and modified after Ishihara and Chappell (2017), Miyazaki (2010), and Takatsuka et al. (2018).

3.3 Analytical methods

The whole-rock major element analysis was performed with a PANalytical Axios X-ray fluorescence spectrometer (XRF) using a fused glass bead of silicate rock powder diluted with lithium-tetraborate at the University of Tokyo. After the major element analysis, the trace element compositions were determined for the glass beads using a iCAP Q quadrupole-ICP-MS (ICP-Q-MS) attached to a CETAC LSX-213 G2+ Nd:YAG LA system. Unknown samples were measured in runs of several samples, bracketed by three measurements of a standard NIST SRM 612 glass (Pearce et al., 1997). The ICP source operated with an Ar plasma with a forward RF power of 1550 W. The laser sampling was performed in a raster mode at ~50 μm crater size, a repetition rate of 10 Hz, and 20.54 J m^{-1} fluence. The Mg contents, determined by XRF, were used for internal correction. Analytical uncertainty based on replicate analyses of USGS reference material BCR-2 was at most 20% for trace elements.

For whole-rock isotope analyses, the dissolved samples with a mixture of concentrated HF + HNO_3 in a Savillex® vial were placed in Teflon bombs and heated to 210 ºC for 48 h. After digestion, the solution was evaporated to dryness. The samples were re-digested in HNO_3 and heated in the same way for 12 h and this process was repeated one more time. The sample was then evaporated and dissolved in 6M HCl at 210 ºC using the bomb for 12 h. To separate and purify Sr and Nd from the decomposed whole rock sample solutions, two-step column chromatography was used following the modified recipe of Takahashi et al. (2009) and Hirahara et al. (2012), respectively. A

flow diagram of separation is illustrated in Fig. 3-2. The Sr and Nd isotope analyses were carried out using a Neptune plus multiple collector ICP-MS (MC-ICP-MS). The operating conditions of the instruments are listed in Tables 3-1, 2.

In-situ U–Pb dating, trace element, and Nd isotope analyses for monazite were done on separated monazite grains in addition to grains on thin sections to obtain a better dataset for describing the inter-grain variations. Before analysis, each grain was investigated by back-scattered electron (BSE) imaging to check internal zoning structures and to avoid sampling inclusions during laser ablation. The BSE images were obtained using a JEOL JSM-7000F. The U–Pb ages were measured using the LA-ICP-Q-MS. We measured ^{202}Hg, ^{204}(Pb + Hg), ^{206}Pb, ^{207}Pb, and ^{238}U, of which signal intensities fell within the maximum dynamic range of the counting system. The LA conditions were set at ~20 μm crater size, a repetition rate of 3 Hz, and a fluence of 20.54 J cm^{-1}. The 44069 monazite (Aleinikoff et al., 2006) was used as a primary reference material for Pb/U ratios. The accuracy of our monazite U–Pb dating was evaluated by analyzing the monazite Manangotry standard, for which the U–Pb ages were previously determined by the isotope dilution-thermal ionization mass spectrometry (555 ± 2 Ma, Horstwood et al., 2003). The obtained U–Pb ages for the Manangotry monazite are consistent with the previously reported values within the analytical uncertainty: ^{206}Pb/^{238}U age of 568 ± 18 Ma and ^{207}Pb/^{206}Pb age of 571 ± 23Ma for Manangotry (n=22). Isoplot R (Vermeesch, 2018) was used for visualization of the obtained age data. The concentrations of REEs, Th, and U in the studied monazite

were determined using the same LA-ICP-Q-MS as the U–Pb dating. The LA conditions were set at ~15 μm crater size and a repetition rate of 3 Hz. The Sm contents, measured in advance with a Field Emission-EPMA JEOL JXA 8530F HyperProbe, were used for internal correction. The NIST SRM 612 glass was used as an external standard. Interferences from LREE-oxides on HREE were corrected by determined oxide production rates using the synesthetic REE phosphates during each measurement session (Itano and Iizuka, 2017). The Nd isotopic composition were determined by LA-MC-ICP-MS. The operating parameters for this analysis are summarized in Table 3-3. Faraday amplifier calibration, correction for isobaric interference from ^{144}Sm on ^{144}Nd, and mass bias correction were carried out using a La–Ce–Nd synthetic monazite (Synth-LCN) standard and Nd–Sm–Pr synthetic monazite (Synth-NSP) standard (Iizuka et al., 2011a).

Major element compositions of plagioclase were analyzed by the EPMA. ZAF correction procedures were employed. The operating conditions of the EPMA analysis were: a beam diameter of 2 μm, a probe current of 20 nA, and an accelerating voltage of 15 kV. Natural materials were used as standards for seven elements (Na, K, Ca, Mg, Al, Si, Fe). The trace element and Sr isotope microanalyses of plagioclase were conducted by LA-MC-ICP-MS and LA-ICP-Q-MS. Analytical scheme for plagioclase trace element is almost same as that for monazite. The Ca contents were used as internal standard to determine the concentrations of Li, Mg, Sc, Ti, V, Mn, Zn, Rb, Sr, Y, Ba, La, Ce, Pr, Nd, Sm, Eu, Gd, and Pb. The LA conditions were set at ~30 μm crater size,

repetition rate at 5 Hz, and a fluence of 20.54 J cm^{-1} due to its lower concentration of REEs as compared to monazite. The Sr isotope analysis was performed using a solution-aerosol-dual intake system (Tatsumi et al., 2008; Kimura et al., 2013). Raw data were corrected for by a conventional protocol: blank subtraction, correction for Rb and Kr isobaric interferences, mass bias correction using $^{86}Sr/^{88}Sr$, and normalization to bracketing NIST SRM987 standard values. The operating parameters for this analysis are shown in Table 3-4.

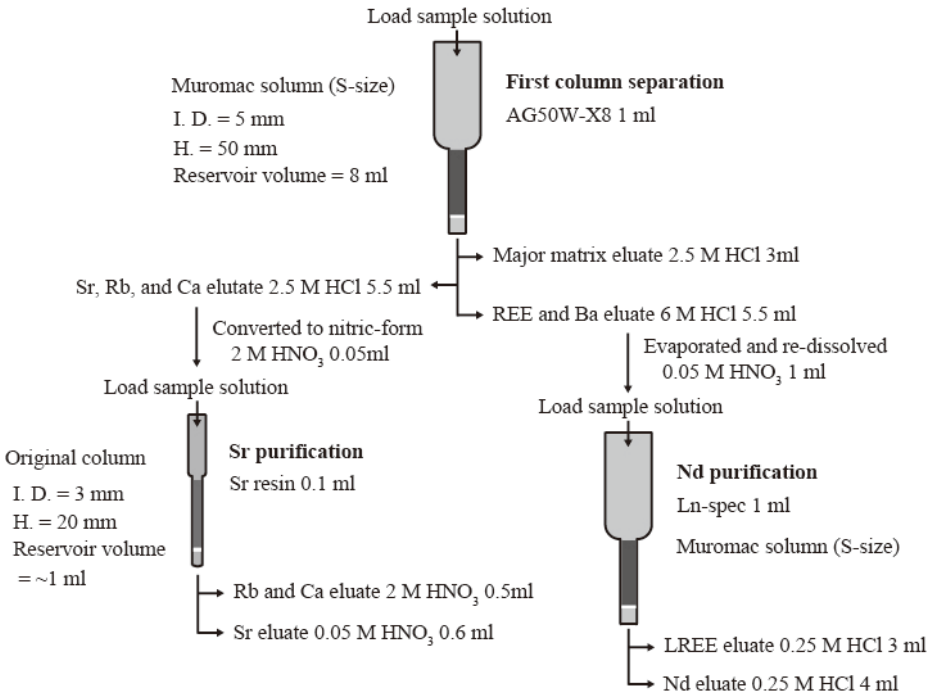

Fig. 3-2. Schematic diagram of Sr-Nd separation. First, major elements are removed using a conventional cation-exchange chromatography. After changing solvents, Sr and Nd are separated using a Sr resin and a Ln resin column, respectively.

Table. 3-1 Operational parameters of the MC-ICP-MS for whole-rock Nd isotope analysis

Sample introduction	ARIDUS (CETAC, USA)						
Sweep gas flow rates (Ar)	6-7 L min						
N_2 Gas flow rates	5 L min^{-1}						
MC-ICP-MS	Neptune plus (Thermo Fisher Scientific)						
RF-power	1200 W						
Interface cones	Ni sample cone	Ni skimmer cone					
Gas flow rates	Ar cooling: 14 L min^{-1}			Ar auxiliary: 1.0 L min^{-1}			
	Ar sample: 0.8–0.9 L min^{-1}						
Mass resolution	Low						
Integration time	8.389 sec						
Analysis mode	static						
Collector arrangement							
Faraday cups	L3	L2	L1	Axial	H1	H2	H3
Analyte isotopes	^{142}(Nd+Ce)	^{143}Nd	^{144}(Sm+Nd)	^{145}Nd	^{146}Nd	^{147}Sm	^{149}Sm

Table. 3-2 Operational parameters of the MC-ICP-MS for whole-rock Sr isotope analysis

Sample introduction	ARIDUS (CETAC, USA)							
Sweep gas flow rates (Ar)	5-5.5 L min							
N_2 Gas flow rates	3–4 L min^{-1}							
MC-ICP-MS	Neptune plus (Thermo Fisher Scientific)							
RF-power	1200 W							
Interface cones	Ni sample cone	Ni skimmer cone						
Gas flow rates	Ar cooling: 14 L min^{-1}			Ar auxiliary: 1.0 L min^{-1}				
	Ar sample: 0.9–1.1 L min^{-1}							
Mass resolution	Low							
Integration time	8.389 sec							
Analysis mode	static							
Collector arrangement								
Faraday cups	L3	L2	L1	Axial	H1	H2	H3	H4
Analyte isotopes	^{82}Kr	^{83}Kr	^{84}(Kr + Sr)	^{85}Rb		^{87}(Rb + Sr)	^{88}Sr	^{89}Y

Table. 3-3 Operational parameters of the LA-MC-ICP-MS for Sm-Nd isotope analysis for monazite

Laser ablation system	CETAC LSX-213 G2+ (CETAC, USA) equipped with the active two-volume HelEx™ Cell						
Laser source	213 nm						
Pulse width	5 ns						
Beam diameter	30 μm						
Repetition rate	4 Hz						
Laser fluence	20.54 J cm^{-2}						
MC-ICP-MS	Neptune plus (Thermo Fisher Scientific)						
RF-power	1200 W						
Interface cones	Ni sample cone			Ni skimmer cone			
Gas flow rates	Ar cooling: 14 L min^{-1}			Ar auxiliary: 1.0 L min^{-1}			
	Ar sample: 1.2–1.3 L min^{-1}		N_2 carrier: ~4 mL min^{-1}		He carrier: 0.95 L min^{-1}		
Mass resolution	Low						
Data acquisition mode	Time resolved analysis						
Integration time	1.02 sec						
Analysis mode	static						
Collector arrangement							
Faraday cups	L3	L2	L1	Axial	H1	H2	H3
Amplifier calibration factor*	0.0021	-0.00097	0.0021		-0.0013	-0.0011	0.0041
Analyte isotopes	^{142}(Nd+Ce)	^{143}Nd	^{144}(Sm+Nd)	^{145}Nd	^{146}Nd	^{147}Sm	^{149}Sm

*The calibration factors were determined by analyzing the synthetic monazite Synth-LCN for Nd isotopes using LA-MC-ICPMS, following Iizuka et al. (2011a).

Table. 3-4 Operational parameters of the dual intake system-MC-ICP-MS for Rb-Sr isotope analysis for plagioclase

Laser ablation system	CETAC LSX-213 G2+ (CETAC, USA) equipped with the active two-volume HelEx™ Cell							
Laser source		Pulse width	5 ns					
Beam diameter	100 μm	Laser fluence	20.54 J cm^{-2}					
Repetition rate	8 Hz							
Dissolvent system	Aridus (CETAC, USA)							
Sweep gas flow rates (Ar)	6-7 L min^{-1}	N_2 Gas flow rates	5 L min^{-1}					
MC-ICP-MS	Neptune plus (Thermo Fisher Scientific)							
RF-power	1200 W							
Interface cones	Ni sample cone			Ni skimmer cone				
Gas flow rates	Ar cooling: 14 L min^{-1}			Ar auxiliary: 1.0 L min^{-1}				
	Ar sample: 1.0–1.1 L min^{-1}			He carrier: 1.2 L min^{-1}				
Mass resolution	Low							
Data acquisition mode	Time resolved analysis							
Integration time	1.02 sec							
Analysis mode	static							
Collector arrangement								
Faraday cups	L3	L2	L1	Axial	H1	H2	H3	H4
Analyte isotopes	^{82}Kr	^{83}Kr	^{84}(Kr + Sr)	^{85}Rb		^{87}(Rb + Sr)	^{88}Sr	^{89}Y

3.4 Sample Descriptions

Seven granitic rock samples were collected at six locations in addition to a sampling of metapsamite in the Mikawa area (Fig. 3-1).

Samples TK01 and TK02 were collected at the same quarry (the Tokai quarry, 34°58'28.69"N, 137°11'55.16"E). In the outcrop, their clear boundaries were observed (Fig. 3-3a, b). Sample TK01 is a biotite granite and sample TK02 is a two-mica granite. Sample TK01 mainly consists of Pl, Qtz, Kfs, and Bt with accessory Ilm, Zrn, Ap, and Xen; whereas sample TK02 is composed of Pl, Qtz, Kfs, Bt, and Ms with accessory Ilm, Grt, Mnz, Zrn, Ap, and Xen (Mineral abbreviations are from Kretz, 1983). Note that monazite could not be identified within sample TK01, whereas the other studied granite samples contain monazite. Based on their mode compositions, sample TK01 and TK02 are classified into granodiorite and monzogranite, respectively (Fig., 3-3g). Metasomatic myrmekitic texture was rarely observed.

Sample NK was collected at the Nakane quarry (34°59'52.76"N, 137°12'17.35"E). Sample NK consists of Pl, Qtz, Kfs, Bt, and Ms with accessory Ilm, Grt, Mnz, Zrn, Ap, Xen, Aln, Py. This sample is classified into monzogranite (Fig., 3-3c, g) and coarsest among the studied samples (>1–2 mm). The co-existence of monazite and allanite indicates the significant change in the composition of granitic magma because relative phase relations of the two minerals depend on bulk CaO contents (Spear, 2010; Budzyń et al., 2017), though the allanite grains are anhedral with minute grain size (~10 μm) and much scarcer than monazite and xenotime.

Sample YS was collected at the Yamasen quarry (34°58'28.69"N, 137°11'55.16"E). Sample YS consists of Pl, Qtz, Kfs, and Bt with accessory ilmenite, Grt, Mnz, Zrn, Ap, Xen, and Aln. This sample is classified into granodiorite (Fig. 3-3d, g).

Sample 2802 was collected at the Nakayama quarry (34°59'36.16"N, 137°11'56.86"E). Sample 2802 comprises Pl, Qtz, Kfs, Bt, and Ms with accessory Ilm, Grt, Mnz, Zrn, Ap, Aln, and Xen. This sample is classified into monzogranite (Fig. 3-3g).

Sample KJ was collected at the Kissho-seki quarry (34°58'37.05"N, 137°11'23.35"E). The major minerals are Pl, Qtz, Kfs, Bt, and Ms, while the accessory phases are Ilm, Grt, Mnz, Zrn, Ap, and Xen. This sample is classified into granodiorite (Fig. 3-3g).

Sample 2801 was collected from a riverbed (34°59'00.18"N, 137°19'20.21"E) and, therefore, is slightly weathered as compared to the other granite samples from the quarries. Sample 2801 consists of Pl, Qtz, Kfs, and Bt with accessory Ilm, Grt, Mnz, Zrn, Ap, and Xen. This sample is classified into granodiorite (Fig. 3-3g).

Sample MC [34°58'58.92"N, 137°18'44.12"E] is a metapsamite, which was collected as an example of country rock (Fig.3-3f). The observed foliation structure is defined by alternating finer and coarser grain bands and preferred orientation of clay minerals.

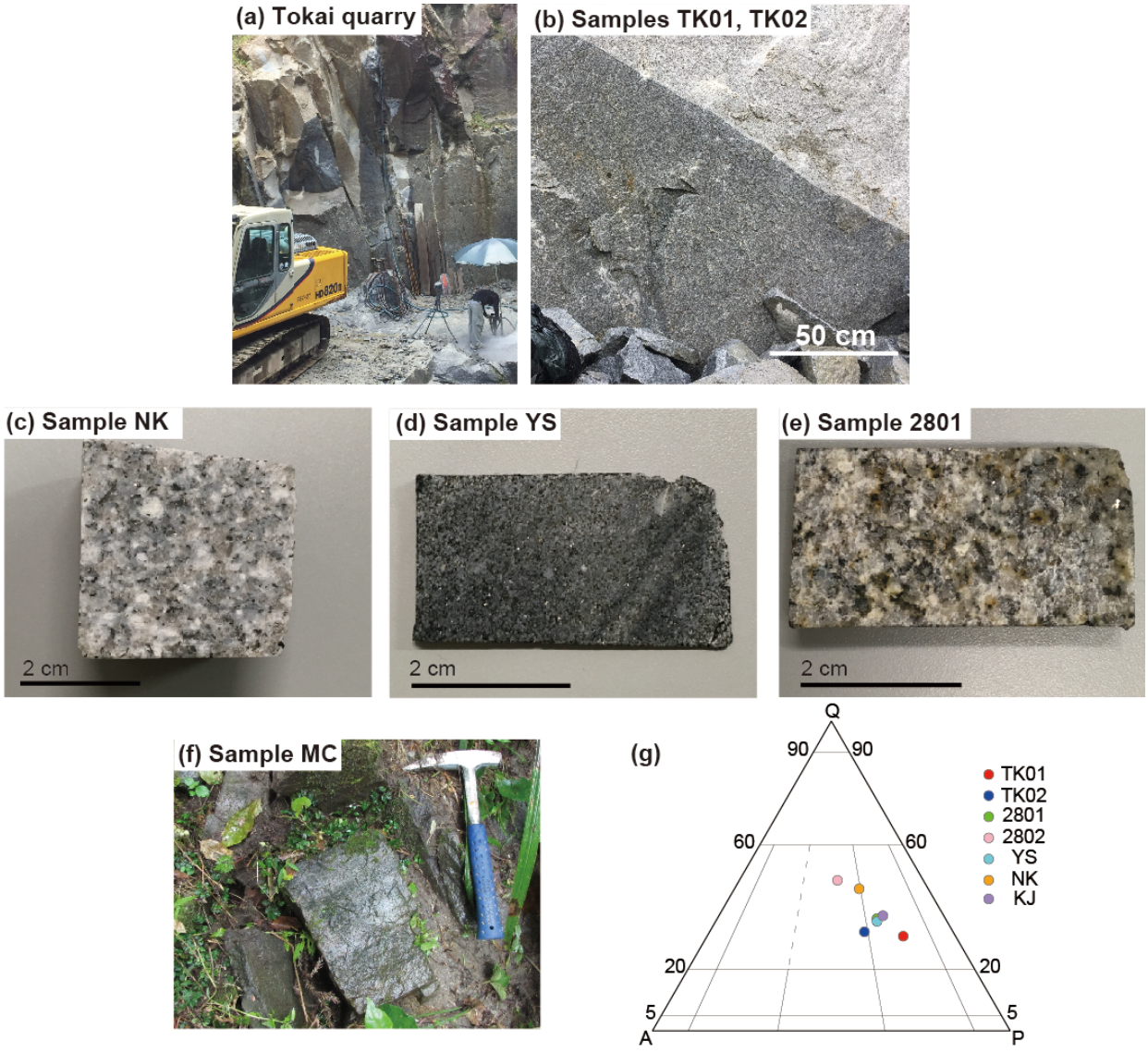

Fig. 3-3. (a) Outcrop in the Tokai quarry, showing a Bt-granite (granodiorite) enclosed by monzogranite (monzogranite). (b) Sharp boundary between monzogranite and granodiorite. (c) Slab photograph of two-mica granite: Sample NK. (d) Slab photograph of Bt-mica granite: Sample YS. (e) Slab photograph of Bt-mica granite: Sample 2801. This sample slightly appears weathered. (f) Field occurrence of sample MC. (g) QAP diagram showing modal abundances of quartz, plagioclase, and K-feldspar in the studied granitic samples. Samples 2802, NK, and TK02 are classified as monzogranites and the others are granodiorites.

3.5 Results

3.5.1 U–Pb age of monazite

The U–Pb ages of 177 monazite grains of monazite from all samples other than TK01 were measured (54 grains for sample 2801; 42 grains for sample 2802; 28 grains for sample NK; 20 grains for sample YS; 18 grains for sample KJ; 15 grains for sample TK02) and summarized in appendix Table 3-1. Most of the data show discordant ages as shown in Fig. 3-4a. Incorporation of even a small amount of non-radiogenic Pb can affect the concordance in the case of young monazite. Assuming an initial $^{206}Pb/^{204}Pb$ of 18.56 and $^{207}Pb/^{204}Pb$ of 15.62 at 68 million years ago based on the two-stage evolution model (Stacey and Kramer, 1975), the highly discordant data are plotted along the line formed by the various μ values ($^{238}U/^{204}Pb$). Therefore, the initial Pb is likely to be a cause of the discordant data. The data yielding concordant U–Pb ages within analytical uncertainty are used for the following discussion. The filtered concordant data yielded 68.4 Ma ± 3.7 Ma (2SD, Fig. 3-4b, c).

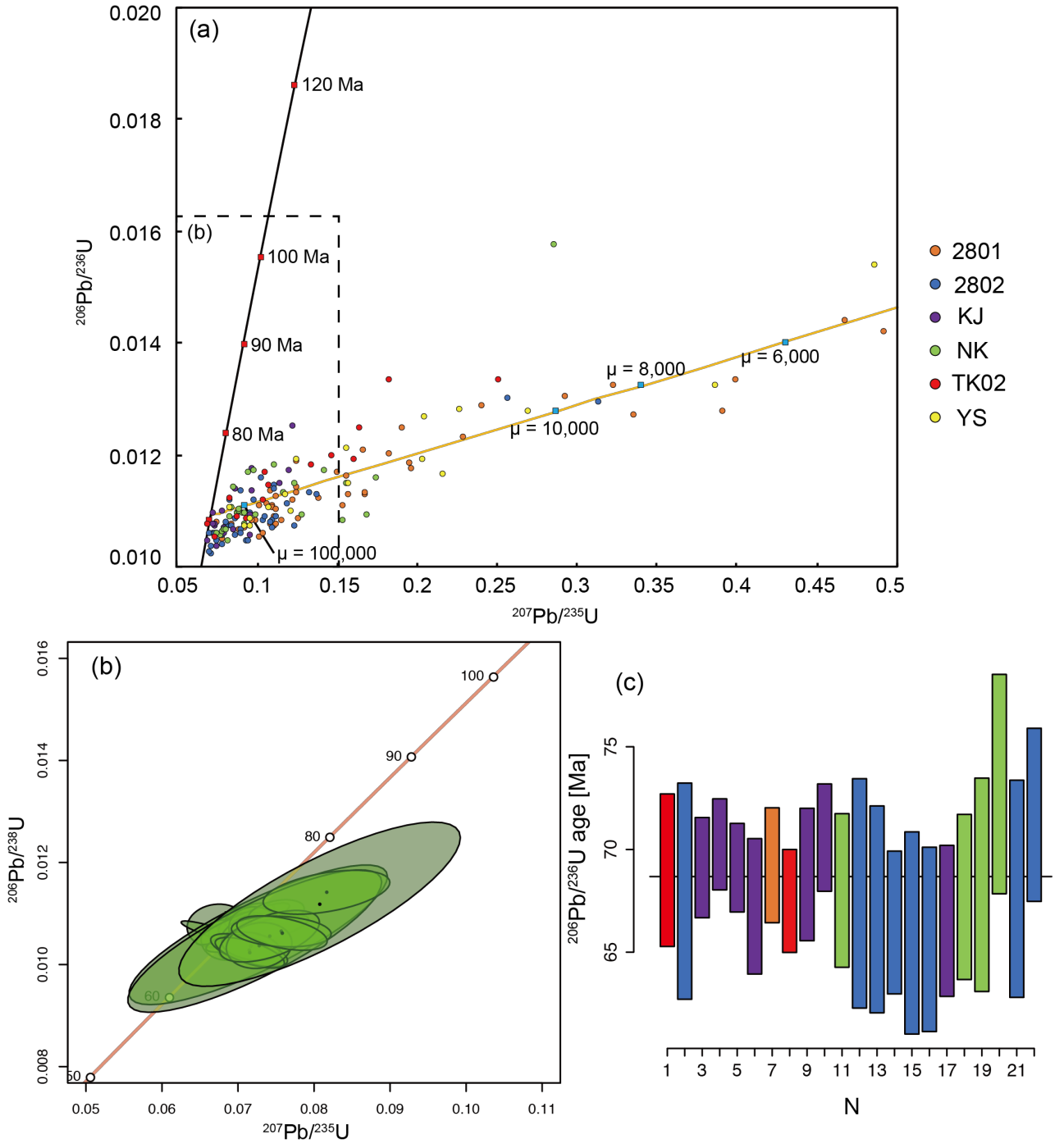

Fig. 3-4. (a) Concordia plot of all U–Pb data for monazite from studied samples. Yellow line represents the mixing between no-common Pb isotope composition yielding 68 Ma and Pb isotope composition of common Pb at 68 Ma, which is calculated using the two-stage evolution model (Stacey and Kramer, 1975). μ is $^{238}U/^{204}Pb$ ratio at the timing of crystallization. (b) Concordia plot for only concordant U–Pb data. Rejected data are not shown. (c) Plot of adopted $^{206}Pb/^{238}U$ ages for the studied monazites. Color represents the samples as with the legend of (a).

3.5.2 Geochemical and Nd isotope compositions of monazite

Monazite grains from the studied samples are basically subhedral and included in biotite or plagioclase (Fig. 3-5). Some grains show homogeneous distribution of Th and other displays oscillatory zoning, suggesting crystallization from melts. The trace element data of 115 monazite grains are listed in Appendix Table 3-2. All monazite grains show typical REE patterns with abundant LREEs relative to HREEs and Eu negative anomalies. However, their slopes and the magnitude of the Eu anomaly are various, which are visualized in Figure 3-6. The variations are quantified by the chondrite-normalized values of $[Eu/Eu^*]_N$, $[Ce/Gd]_N$, and $[Th/U]_N$. These parameters are correlated with each other (Fig. 3-6). The monazite grains from different rock samples yielded the different ranges of these parameters, which cannot be simply explained by the differences in rock types or whole-rock chemical compositions.

The analytical results of monazite Nd isotope compositions are provided in Appendix Table 3-3. The initial Nd isotope compositions of the studied monazites at 68 Ma are shown in Figure 3-7. The $[^{143}Nd/^{144}Nd]_{68Ma}$ ratios range from 0.51193 ± 0.00003 to 0.51228 ± 0.00003. The $[^{143}Nd/^{144}Nd]_{68Ma}$ of analyzed grains are identical within analytical errors for samples 2801, 2802, NK, YS, and KJ. In contrast, a significant isotopic variation was observed for sample TK02, implying the involvement of isotopically different sources during the stage of monazite crystallization. No correlation was observed between the $[^{143}Nd/^{144}Nd]_{68Ma}$ and trace element features such as $[Ce/Gd]_N$.

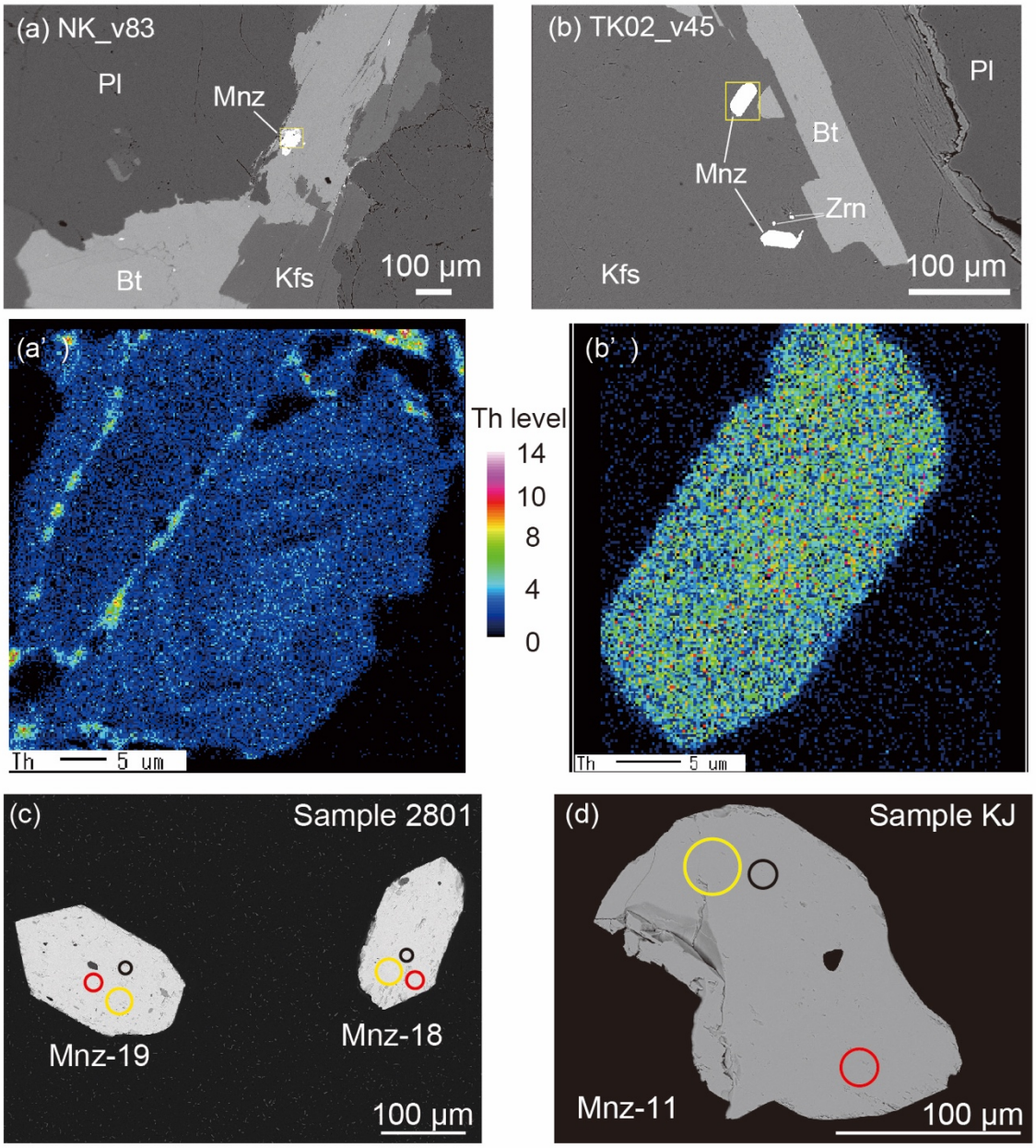

Fig. 3-5. BSE images and elemental mappings of representative monazite grains from Samples NK and TK02. (a) Monazite grain is included by biotite and (a') its Th distribution shows oscillatory zoning. (b) Euhedral monazite grains are next to biotite and included in K-feldspars and (b') these grains show homogenous Th distributions. (c) and (d) are representative BSE image of analyzed grains from samples 2801 and KJ, respectively. Yellow, red, and black circles represent analytical spots for Nd isotope composition, U–Pb age, and trace element composition, respectively.

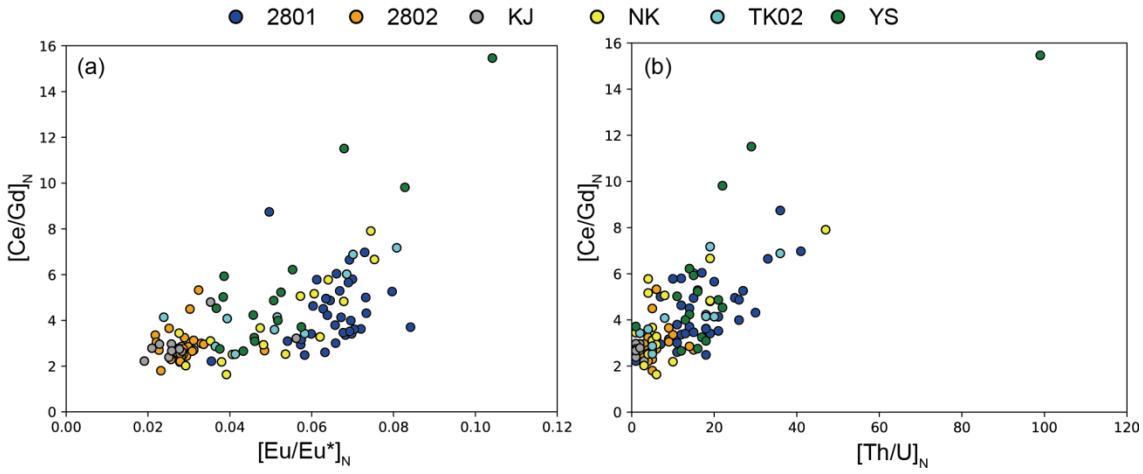

Fig. 3-6. Plots of (a) $[Ce/Gd]_N$ vs. $[Eu/Eu^*]_N$ and (b) $[Ce/Gd]_N$ vs. $[Th/U]_N$ for the measured monazite grains.

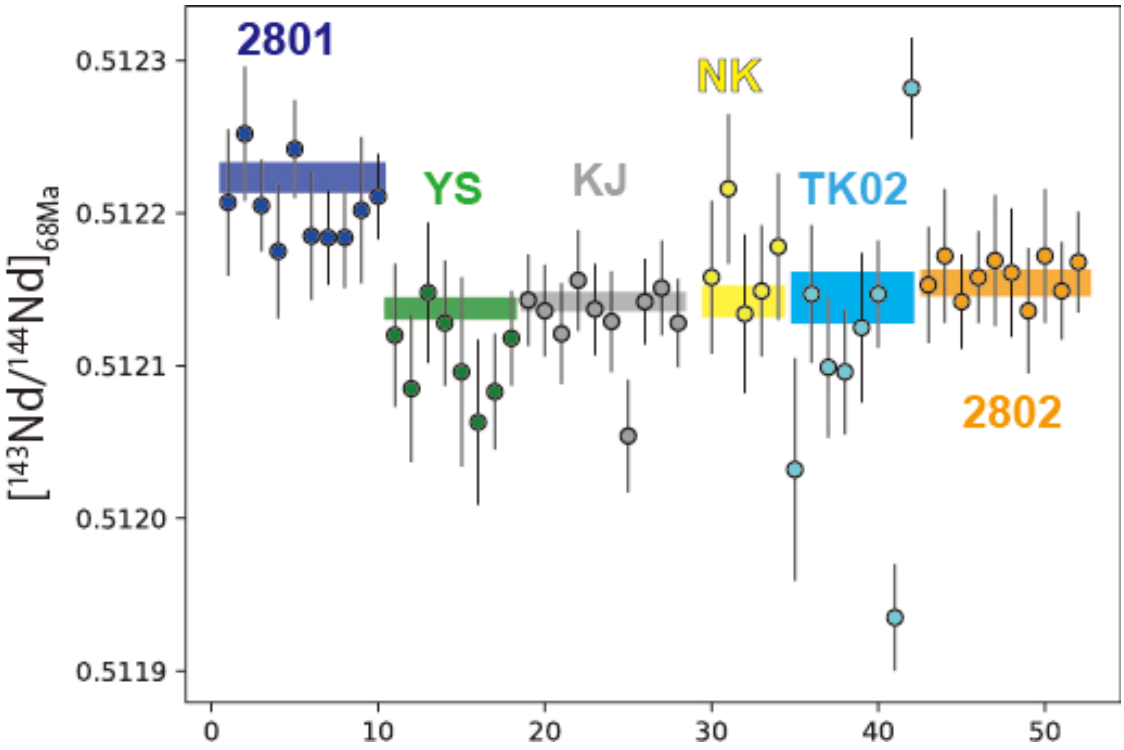

Fig. 3-7. $^{143}Nd/^{144}Nd$ ratios at 68 million years ago of monazites. Bands overlapped plots represent the whole-rock Nd isotope ratios of each granite sample.

3.5.3 Geochemical and Sr isotope compositions of plagioclase

The plagioclase grains for samples NK, YS, TK01, TK02 were analyzed by EPMA, LA-ICP-Q-MS, and LA-MC-ICP-MS. Representative BSE images are presented in Figure 3-8. The analyzed grains have cores and homogeneous rims (Fig. 3-8b, c) or cores, oscillatory-zoned mantles, and rims (Fig. 3-8a, d). In this study, I defined all domains surrounding cores as rim domains. The measured trace element compositions and the averaged anorthite contents (An content: molar Ca / Ca + Na + K) within the measured domains for Sr isotope analysis are summarized in appendix Table 3-4. Figure 3-9 shows the examples of trace element data. The measured Sr contents of plagioclase are positively correlated with REEs, Ti, Mn, and anorthite contents. The correlation coefficient between Sr and Eu contents is ~0.76, which is the strongest correlation between trace elements. The measured $^{87}Sr/^{86}Sr$ ratios are plotted as a function of the An contents (Fig. 3-10). All of the isotope data are given in appendix Table 3-5. The $^{87}Sr/^{86}Sr$ ratios of rim domains are relatively homogenous for each rock sample; in contrast, those of core domains show large variations. The $^{87}Sr/^{86}Sr$ ratios range from 0.7079 ± 0.0002 to 0.7136 ± 0.0002. The $^{87}Sr/^{86}Sr$ ratios of rim domains are deviated from the averaged values, irrespective of whether the rock sample is monzogranite or granodiorite. It is suggested that more than two isotopically different sources were involved for the formation of the Busetsu granites.

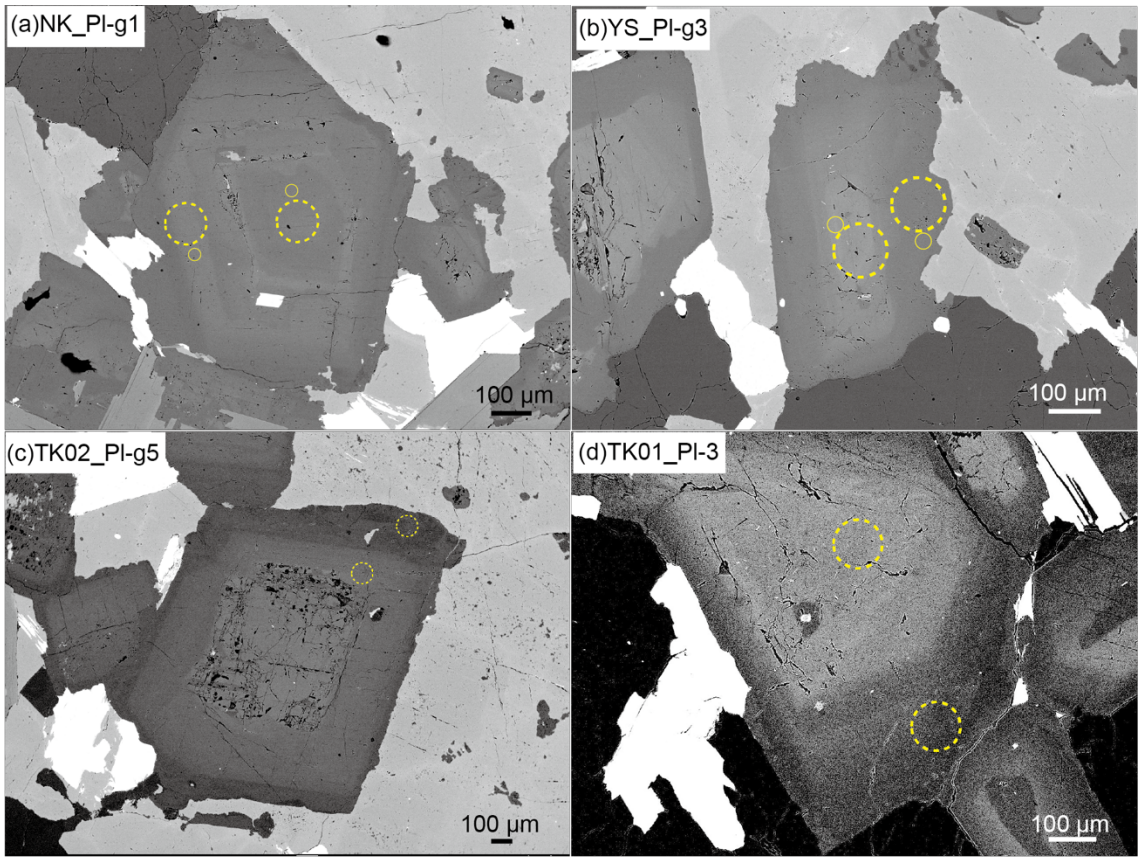

Fig. 3-8. Representative BSE images of plagioclase grains from samples (a)NK, (b) YS, (c) TK02, and (d) TK01. Solid- and dotted-circles represent analytical spots for REE and Sr isotope analyses, respectively.

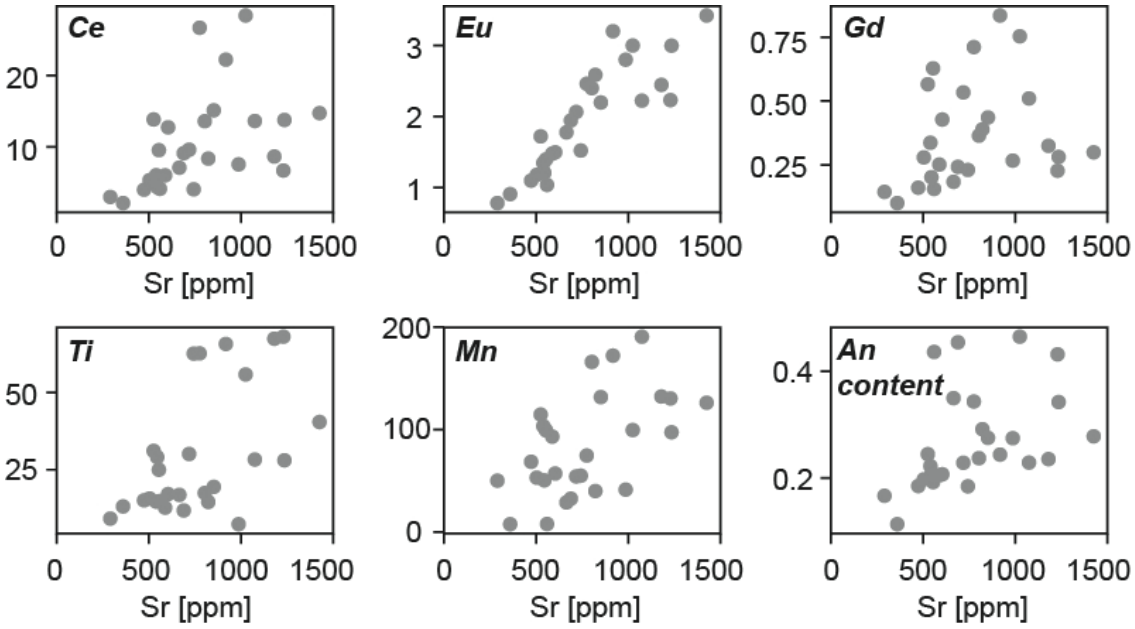

Fig. 3-9. Sr contents vs. Ce, Eu, Gd, Ti, Mn, and An contents of plagioclase grains.

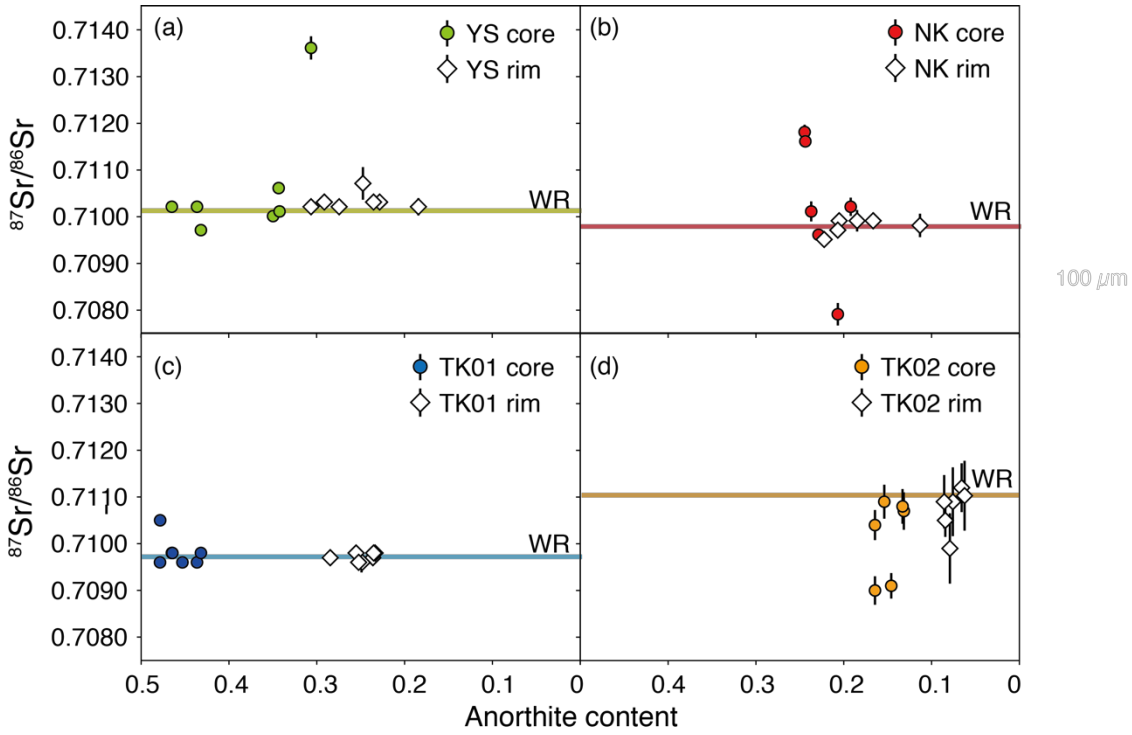

Fig. 3-10. Measured $^{87}Sr/^{86}Sr$ ratios of plagioclases for Samples (a) YS, (b) NK, (c) TK01, and (d) TK02. Solid lines represent the initial Sr isotope ratios of the whole-rock granite samples.

3.5.4 Whole-rock analyses

The correlations between major element contents were observed for the studied samples (Fig. 3-11, Appendix Table 3-6.), which is consistent with the reported data (Ishihara and Chappell, 2007). The SiO_2 content shows negative correlations with MgO, Fe_2O_3, and CaO. In contrast, the contents of SiO_2 and K_2O display a weak positive correlation. For the Al_2O_3, P_2O_5, and Na_2O contents, no obvious correlations with the SiO_2 contents were found. Regarding minor and trace elements, the spider diagram in Figure 3-12a is characterized by positive Pb and negative Ti anomalies. All of the granite samples have negative Eu anomalies (Fig. 3-12b). The REE contents decrease as the SiO_2 contents increase (Fig. 3-12c, d). Trace elements, which tend to concentrate into fewer minerals, are useful in formulating models for magmatic differentiation. When two trace elements are plotted in logarithmic space, the following relation is obtained:

$$Log\left(C^A\right) = \frac{D^A - 1}{D^B - 1} Log\left(C^B\right) + c$$

A, B: arbitrary elements, C^X: the concentration of element, D^X: bulk distribution coefficient, c: constant. The Sr and Ba contents show the strongest correlation and its linear approximation of the plots yielded $(D_{Ba}–1)/(D_{Sr}–1)$ of ~1.03.

The whole-rock Sr-Nd isotopic compositions are presented in Tables 3-5 and -6. The $[^{87}Sr/^{86}Sr]_{68Ma}$ and $[^{143Nd}/^{144}Nd]_{68Ma}$ are also graphically shown in Fig. 13. The isotope compositions of the country rocks are also plotted for a reference. The Sr and Nd

isotopic compositions show a negative correlation (Fig. 3-13), which suggests the isotopically different multiple components were involved for the formation of the Busetsu granite. The $[^{87}Sr/^{86}Sr]_{68Ma}$ values for the studied granitic samples range from 0.70857 ± 0.00003 to 0.71114 ± 0.00005 and the $[^{143}Nd/^{144}Nd]_{68Ma}$ values range from 0.51211 ± 0.00001 to 0.51221 ± 0.00001. Both the Sr and Nd isotope variations of whole rock samples are smaller than those recorded in plagioclase and monazite, respectively (Figs. 3-7, 10).

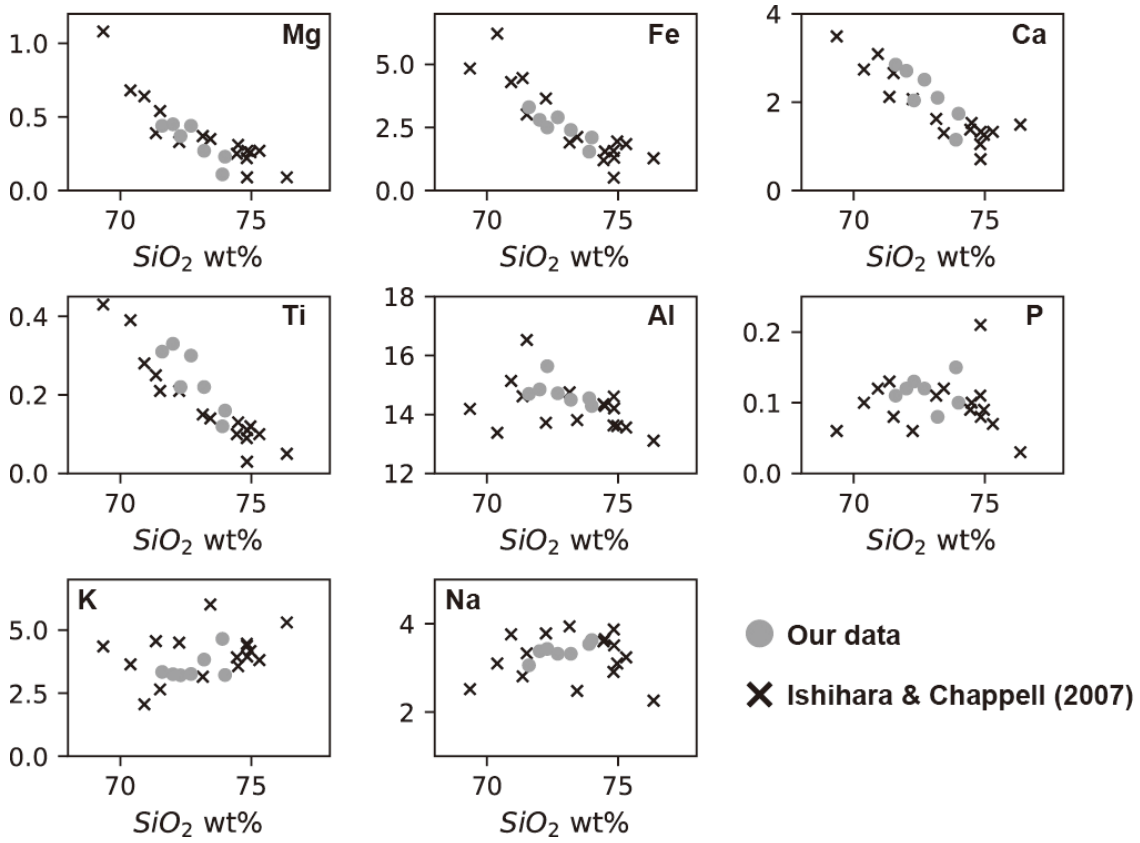

Fig. 3-11. Silica vs. Mg, Fe, Ca, Ti, Al, P, K, and Na of whole-rock granite samples. Circle and cross represent the obtained data in this study and the data of Ishihara and Chappell (2007), respectively. SiO_2 shows negative correlations with Mg, Fe, Ca, and Ti.

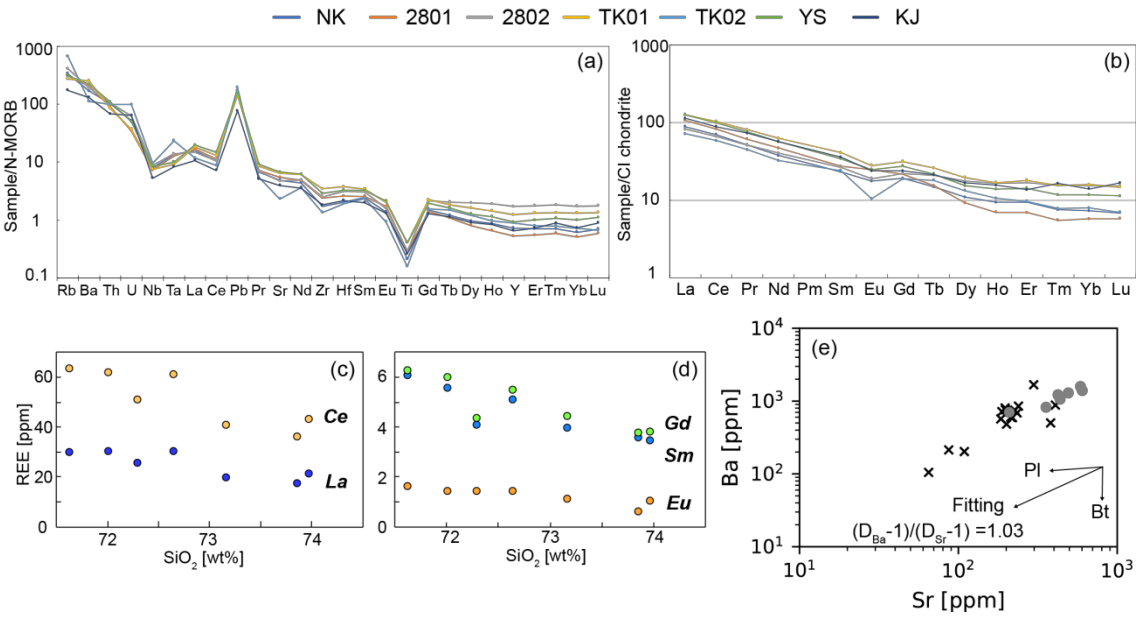

Fig. 3-12. Results of whole-rock trace element analyses of granite samples. (a) N-MORB normalized trace element patters of the studied granites. (b) Chondrite normalized REE patterns of the granite samples. (c) and (d): SiO_2 vs La and Ce and SiO_2 vs. Sm, Eu, and Gd. (e) Plot of Sr and Ba contents. Symbols are the same as in Fig. 3-11.

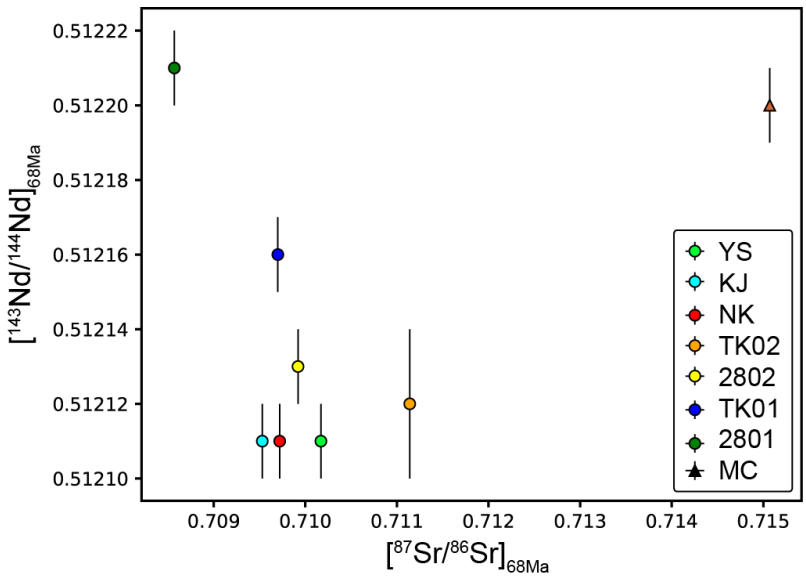

Fig. 3-13. Plots of initial Sr and Nd isotope compositions of bulk granitic and metasedimentary rocks.

Table 3-5. Sr isotopic data of Busetsu granite samples

	$^{84}Sr/^{86}Sr$	2SE	$^{87}Sr/^{86}Sr$	2SE	$^{85}Rb/^{86}Sr$	$^{87}Rb/^{86}Sr$	2SE	$[^{87}Sr/^{86}Sr]_{68\ Ma}$	2σ
NK	0.05639	0.00003	0.71136	0.00001	0.01447	1.7	4.8×10^{-4}	0.70977	0.00001
YS	0.05650	0.00002	0.71111	0.00001	0.00732	0.95	7.1×10^{-4}	0.71019	0.00001
TK01	0.05652	0.00002	0.71062	0.00001	0.00764	0.93	1.1×10^{-4}	0.70973	0.00001
TK02	0.05655	0.00002	0.71552	0.00002	0.05764	4.4	4.6×10^{-4}	0.71126	0.00005
2801	0.05632	0.00006	0.70949	0.00002	0.0004	0.92	2.0×10^{-2}	0.7086	0.00003
2802	0.05640	0.00003	0.71132	0.00003	0.00176	1.4	2.1×10^{-2}	0.70996	0.00003
KJ	0.05647	0.00003	0.71085	0.00002	0.00393	1.3	1.5×10^{-2}	0.70957	0.00002
MC	0.05647	0.00001	0.71630	0.00001	0.00101	1.2	1.0×10^{-2}	0.71511	0.00002

Table 3-6. Sr isotopic data of Busetsu granite samples

	$^{142}Nd/^{144}Nd$	2SE	$^{143}Nd/^{144}Nd$	2SE	$^{145}Nd/^{144}Nd$	2SE	$^{147}Sm/^{144}Nd$	2SE	$^{150}Nd/^{144}Nd$	2SE	$[^{143}Nd/^{144}Nd]_{68\ Ma}$	2σ
NK	1.14305	0.00004	0.51217	0.00001	0.34844	0.00001	0.1259	0.0043	0.241615	0.000012	0.51212	0.00001
YS	1.14299	0.00003	0.51216	0.00001	0.34843	0.00001	0.1223	0.0042	0.241611	0.000011	0.51211	0.00001
TK01	1.14309	0.00004	0.51222	0.00001	0.34841	0.00001	0.1339	0.0041	0.241552	0.000014	0.51216	0.00001
TK02	1.14221	0.00011	0.51219	0.00002	0.34843	0.00002	0.1508	0.0041	0.241614	0.000031	0.51212	0.00002
2801	1.14328	0.00003	0.51226	0.00001	0.34838	0.00001	0.1189	0.0047	0.241517	0.000011	0.51221	0.00001
2802	1.14339	0.00004	0.51219	0.00001	0.34843	0.00001	0.1356	0.0044	0.241599	0.000010	0.51213	0.00001
KJ	1.14272	0.00003	0.51217	0.00001	0.34842	0.00001	0.1272	0.0046	0.241579	0.000011	0.51211	0.00001
MC	1.14318	0.00003	0.51225	0.00001	0.34841	0.00001	0.1203	0.0052	0.241580	0.000011	0.51220	0.00001

3.6 Discussion

3.6.1 Geochronology of the Busetsu granite

The monazite U–Pb age of 68.4 Ma ± 3.7 Ma is distinctly younger than the previously reported monazite CHIME ages of ~79–75 (Suzuki et al., 1994; Nakai and Suzuki, 2003), and consistent with the zircon U-Pb ages of 68–72 Ma (Takatsuka et al., 2018).

The age discrepancy might be due to the existence of multiple components of non-radiogenic Pb such as initial Pb and contaminant Pb, which results in inaccurate U–Pb age estimates in the CHIME dating methods. This problem is critical especially for young samples like the Busetsu granites. Indeed, even a high μ value of 250,000 at the timing of crystallization, corresponding to U/Pb of ~37,000, causes ~10% discordant. If so, the monazite age obtained only from the concordant U-Pb data in this study should be more accurate, because the age estimate is insensitive to the presence of multiple non-radiogenic Pb components. There are two alternative possible explanations for the discrepancy. First, the presence of inherited monazite might account for the older CHIME ages of 79–75 Ma. Note, however, that the monazite CHIME ages do not correspond with the inherited zircon U-Pb ages of ~100 Ma, 95–84 Ma, and ~80 Ma (Takatsuka et al., 2018). In addition, no inherited monazite was observed in BSE images in this study, consistent with the higher solubility of monazite than zircon in crustal magmatic conditions (Yakymuchuk and Brown, 2014). Second, the younger U-Pb ages

of monazite and zircon obtained by LA-ICP-MS may reflect secondary Pb-loss, given that analytical spatial resolution is much poorer in LA-ICP-MS than EPMA, leading to higher potential of analysis of altered domains in the former. I consider this unlikely, however, because the Busetsu granites have undergone little alteration and also because the BSE images show no significant alteration within the analyzed grains. Hence, I conclude that the LA-ICP-MS U-Pb ages are more representative of the crystallization age of the Busetsu pluton than the CHIME U-Pb ages.

Interestingly, the U–Pb age of monazite and zircon are also identical to a biotite K-Ar age of 71.1 ± 3.6 Ma within uncertainty (Yamasaki, 2013). Given that the closure temperatures of the zircon and monazite U–Pb ages are ~800ºC (Lee et al., 1997; Cherniak et al., 2010), whereas that of and K-Ar age is ~350 ºC (Harrison et al., 1985; Grove and Harrison, 1996), a minimum cooling rate in this range is estimated to be ~ 100 ºC/Ma (Fig. 3-14). This estimated rapid cooling rate is consistent with the emplacement of the Busetsu granite magma in a shallow level at ~10 km depth (Takatsuka et al., 2018).

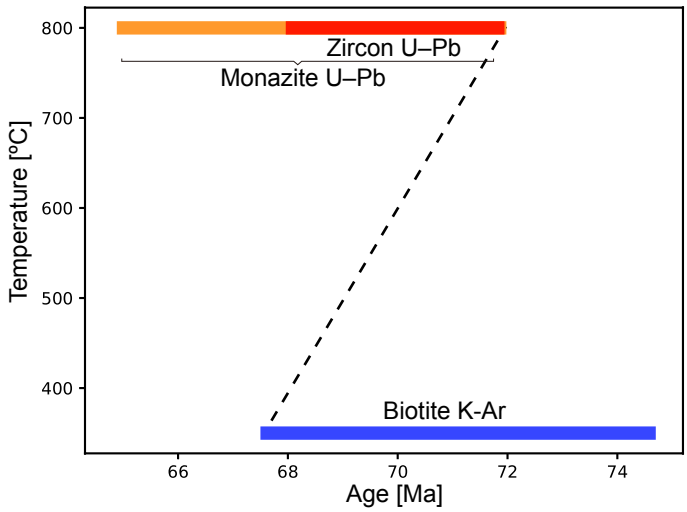

Fig. 3-14. Closure temperatures vs radiometric ages for the Busetsu granite samples. Minimum cooling rate was estimated using the monazite U–Pb age of 68.4 + 3.7 Ma and the youngest biotite K–Ar age of 71.1 – 3.6 Ma. The zircon and biotite age data are from Takatsuka et al. (2018) and Yamasaki (2013), respectively.

Table 3-7. Melt/plagioclase and melt/monazite distribution coefficient for REEs (Bédard et al., 2006; Stepanov et al., 2012)

	D(La)	D(Ce)	D(Pr)	D(Nd)	D(Sm)	D(Eu)			D(Gd)
Plagioclase	0.24	0.15	0.14	0.13	0.085	3.9	7.5	11	0.055
						$Logf_{O2} = -16$	$Logf_{O2} = -17$	$Logf_{O2} = -18$	
Monazite	2.8.E+03	2.5.E+03	2.8.E+03	3.1.E+03	2.5.E+03	1.8.E+03			1.9.E+03

3.6.2 Rare earth element behavior recorded in monazite

The Eu anomaly, LREE/MREE, and Th/U ratios of the studied monazite grains are correlated with each other (Fig. 3-6), likely reflecting the evolution of granitic melt REE compositions during a series of its crystallization. The correlation between negative Eu anomalies and $[Ce/Gd]_N$ of the monazite grains suggests that inter-element fractionation of REEs occurred as the granitic magma evolved. The negative Eu anomaly of monazite has been interpreted to reflect the crystal fractionation of plagioclase (Fisher et al., 2017). However, quantitative evaluation of the effect of plagioclase fractionation has not been made so far.

Here, I examine the impact of plagioclase fractionation on monazite REE composition based on element partitions. The monazite/melt partition coefficients for REEs experimentally determined by Stepanov et al. (2012) were adopted. On the other hand, the plagioclase/melt partition coefficients for REEs are well studied and parameterized by temperature and An molar content (Bédard et al., 2006). The $D^{Pl/melt}$ values for REEs were calculated at 800ºC and An content of 0.4. The used partition coefficients are summarized in Table 3-7.

The core domains of plagioclase are considered as restite from their Sr isotope compositions (details are discussed in the next section), whereas the rim domains of plagioclase would have been crystallized from melts because of textural features such as oscillatory zonings and overgrowth (Fig. 3-8). Monazite is also considered to have been

crystallized from melts, mainly because its U-Pb ages showed the lack of inherited core. As compared with the LREE contents of melts equilibrated with the monazite grains of samples YS and NK, those of melts equilibrated with the plagioclase are low (Fig. 3-15a). This difference suggests that the monazite grains crystallized after the growth of plagioclase rim domains.

The partition of Eu into minerals is subjective to a redox state of magma and the Eu^{2+}/Eu^{3+} ratio in the magma (Philpotts, 1970). Although it is difficult to accurately determine the degree of Eu anomaly in the equilibrium melt from the mineral compositions, the effect of plagioclase fractionation on changes in the Eu anomaly can be estimated. The $D_{Eu}^{Pl/melt}$ can be expressed as a function of $Logf_{O2}$ and temperature based on semi-empirical theory (Bédard et al. 2006). Considering that typical reduced–type granites have f_{O2} below FMQ buffer and also that typical granitic magma temperatures are 700–800 ºC (Frost and Frost, 1997), the partition coefficients of Eu were calculated at a temperature of 800ºC for $Logf_{O2}$ = –16, –17, and –18, respectively (Table 3-5). The melt composition equilibrated with the monazite showing the smallest Eu anomaly (sample NK-8) was assumed as an initial melt composition. The changes in the melt composition, caused by plagioclase fractionation, were calculated based on the Rayleigh fractionation model. Finally, the REE concentrations of monazite equilibrated with the residual melt were obtained. The change in the $[Eu/Eu^*]_N$ of the monazite are expressed as a ratio of the value of monazite crystallized from the fractionated melt to the initial value (Fig. 3-15b). The results indicated that 10–30 % plagioclase

fractionation can cause the decrease in the ratio by 0.75, which is the same as the observed variation for the studied monazite grains (Fig. 3-15b). This amount of removed fraction is consistent with the variation in modal abundance of plagioclase for the studied granite samples (Fig. 3-3g). Therefore, it is quantitatively reasonable that the change in Eu anomaly of monazite reflects the fractional crystallization of plagioclase.

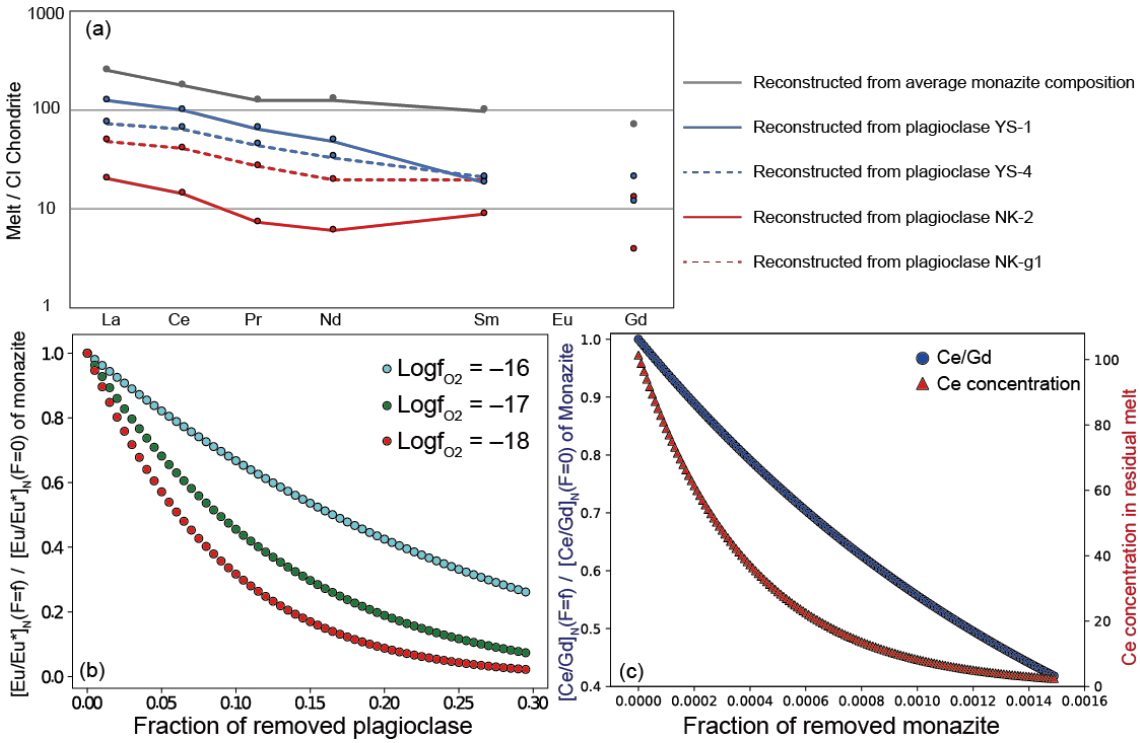

Fig. 3-15. (a) REE patterns of melts equilibrated with plagioclase and monazite. (b) Effect of plagioclase fractionation on REE composition of monazite crystalized from fractionated melt. The change in $[Eu/Eu^*]_N$ is expressed as the ratio to initial value. Three different $D_{Eu}^{Pl/melt}$ were used for $Logf_{O2}$ = –16 (blue), –17(green), and –18(red). (c) Effect of monazite fractionation on REE composition of monazite crystalized from fractionated melt (circle) and Ce contents in residual melt (triangle).

The correlation between the $[Eu/Eu^*]_N$ and $[Ce/Gd]_N$ of monazite suggests that LREEs were more effectively removed from the melt as compared to MREEs during magma differentiation (Fig. 3-6). Regarding the whole-rock trace element compositions, both of the LREE and MREE contents decreased as SiO_2 content increases (Fig. 3-12). The behaviors of lanthanides from La to Gd in peraluminous granites would be governed by monazite and apatite, given that these minerals account for >90% of the elements within the rocks (Bea, 1996). Monazite has higher partition coefficients for LREE than MREE; in contrast, apatite has lower partition coefficients for LREE than MREE (Fig. 3-16). Therefore, it is highly likely that the depletion of LREE relative to MREE in the parent melt resulted from the fractional crystallizations of monazite through its isolation from the melt as inclusions or settling in a magma chamber. When the Ce concentration in the residual melt and the $[Ce/Gd]_N$ of crystallized monazite are calculated using the Rayleigh fractionation model in the same manner as the plagioclase fractionation, a removal of even small fraction (~0.02wt%) created the depletion of LREE in melt and monazite (Fig. 3-15c). When the decrease of $[Ce/Gd]_N$ by 75 % is caused by the Rayleigh fractionation, the decrease of Ce content in melt reaches 100 ppm. This degree of decrease is larger than the observed change in whole-rock Ce concentrations ranging from ~60 to 40 ppm (Fig. 3-12c). Hence, the observed variation in the monazite $[Ce/Gd]_N$ values of ~2–8 would be attributed to its isolation from the parent melt as inclusions rather than settling in a magma chamber. If that is the case, an elemental fraction between Th and U is expected at the same time due to the

significantly different partition coefficients of monazite for Th and U: $D_{Th}/D_U > 7.5$ (Stepanov et al., 2012). Indeed, the observed positive correlation between $[Ce/Gd]_N$ and $[Th/U]_N$ supports the fractional crystallization of monazite (Fig. 3-6b).

The possible effect of xenotime fractionation was also considered using the above model. The distribution coefficients of xenotime for REEs were tentatively calculated using the REE concentrations of xenotime in the Busetsu granite (Suzuki et al., 1992) because the coefficients have not been determined experimentally. According to the modal abundances of monazite and xenotime in granitic rocks (Villaseca et al., 2003), the relative abundance of fractionated monazite and xenotime ($F_{Monazite}/F_{Xenotime}$) were assumed to be 2.5–13. The calculated $[Ce/Gd]_N$ values using the Rayleigh fractionation model were smaller than the original results by ~10–15%, indicating that the xenotime fractionation does not significantly affect the results of calculation. Hence, the $[Ce/Gd]_N$ values of monazite are considered as recording primarily the fractionation of monazite.

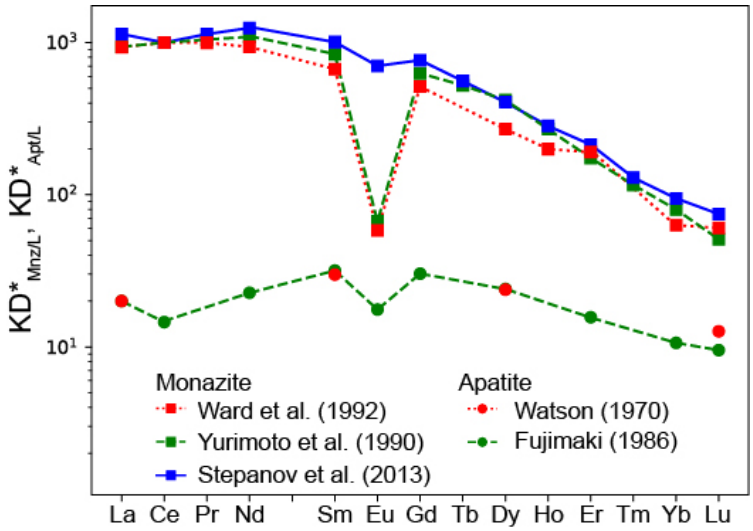

Fig. 3-16. Monazite/melt and Apatite/melt partitioning coefficients of trace elements. The plotted data are from Watson (1970), Fujimaki (1986), Yurimoto et al. (1990), Ward et al. (1992), and Stepanov et al. (2013). $KD^*_{Mnz/L}$ and $KD^*_{Apt/L}$ are monazite/melt partitioning coefficients normalized to D_{Ce} =1000 and apatite/melt partitioning coefficients normalized to D_{La} =20, respectively.

3.6.3 Geochemical evolution of the Busetsu granitic magma: integration of whole-rock and mineral geochemistry

The contents of Fe_2O_3, MgO, CaO, and TiO_2 obviously decrease as the increase of SiO_2 content for whole-rock compositions (Fig. 3-11). Considering that the mineral assemblages include Pl, Qtz, Kfs, and Bt (+ Ms) and that plagioclase and biotite are the major host phases of those major elements, the fractionation of plagioclase and biotite may be responsible for the major element variations in the Busetsu granites. This possibility can be tested using the trace element compositions. The concentrations of Sr and Ba, which are largely controlled by plagioclase and biotite, show a good correlation and the slope of the least squares regression line yielded the $(D_{Ba}–1)/(D_{Sr}–1)$ of ~1.03 (Fig. 3-12e). When the whole-rock partition coefficient is calculated for a major mineral assemblage of 80% plagioclase, 10% biotite, 5% quartz, and 5% K-feldspar, the $(D_{Ba}–1)/(D_{Sr}–1)$ ratio was calculated to be ~1.04, which is in good agreement with the observed value. Therefore, the geochemical variation among the studied granites would be attributed to the fractional crystallization of plagioclase and biotite.

The negative correlation between the whole-rock Sr-Nd isotope compositions in Fig. 3-13 indicates open-system magmatic processes. Although the mineral isotopic data demonstrated that more than two components were involved in the formation of the Busetsu granites, a conventional two component mixing model is tentatively applied here to estimate the relative contributions of mantle-derived and crust-derived rocks. The isotope compositions of the mafic and metamorphic rocks associated with the

Ryoke Belt are plotted in the Sr-Nd isotope diagram (Fig. 3-17). The isotopic data of the Ryoke metamorphic rocks in the Ina area (Yuhara et al., 2000), which is located in the same Chubu district, were used due to the lack of the data in the Mikawa area. The isotopic data of mafic rocks are individually plotted for the Mikawa (Nakajima et al., 2004; Yuhara and Kagami, 2012) and other areas (Izumi et al., 2000). The end components were set on the basis of the maximum range observed in the mineral isotope compositions ($[^{87}Sr/^{86}Sr]_{68Ma}$: 0.71400–0.70814, $[^{143}Nd/^{144}Nd]_{68Ma}$: 0.51993–0.51228). Crust- and mantle-derived components were assumed to have 170 ppm Sr and 32 ppm Nd, and 295 ppm Sr and 13 ppm Nd, respectively based on the averages of the reported data (Yuhara et al., 2000; Nakajima et al., 2004; Yuhara and Kagami, 2012). The outcome of mixing model between the mantle-derived and crust-derived components implies that ~10–60% contribution of the crustal component roughly accounts for the Sr-Nd isotopic variations. The whole-rock geochemistry and isotope chemistry revealed that the reworking of sedimentary rocks in addition to magmatic fractionation of mantle-derived magma was responsible for the formation of the Busetsu granite. Moreover, the isotope compositions of plagioclase and monazite elucidated that the multiple components were involved in the evolution of granitic magma at various timings and levels.

The $^{87}Sr/^{86}Sr$ ratios in core domains of plagioclase show variation, whereas those in rim domains are relatively homogenous for each rock sample (Fig. 3-10). This finding is interpreted by integrating the textural and geochemical information. First, some

$^{87}Sr/^{86}Sr$ ratios of plagioclase core domains are obviously different from the average of $^{87}Sr/^{86}Sr$ ratios in the rim domains and whole-rock values for each sample. By contrast, the rim domains of the plagioclase grains yielded consistent isotope compositions with the whole-rock isotope compositions (Fig. 3-10). The variation in isotope composition of core domains demonstrated the isotopically different multiple sources for the formation of the Busetsu granite. Second, trace element chemistry of plagioclase and monazite suggested the monazite crystallization subsequent to the growth of plagioclase rim domains. This observation indicates that the Sr isotope compositions of the granitic magmas would have been homogenized during an intermediate stage in which the plagioclase rim domains crystallized but accessory phases including monazite have not crystallized. The $[^{143}Nd/^{144}Nd]_{68Ma}$ ratios of monazite grains are generally homogeneous within each rock sample, as with the case of plagioclase rim domains (Fig, 3-7). However, the significant variation of $[^{143}Nd/^{144}Nd]_{68Ma}$ ratios for monzogranite sample TK02 implies assimilations of radiogenic and unradiogenic sources. Indeed, the $[^{143}Nd/^{144}Nd]_{68Ma}$ ratios range from 0.51228 ± 3 to 0.51193 ± 3 is consistent with the Nd isotopic compositions of mafic rocks and metasedimentary rocks in the Ryoke belt, respectively (Fig 3-13; Nakajima et al., 2004; Yuhara and Kagami, 2012). To verify whether the isotopic compositions of magma was changed by assimilation of country rocks at emplacement level, further measurements of $^{87}Sr/^{86}Sr$ ratios of plagioclase-outermost domains are necessary. The obtained mineral isotope

compositions have placed further constraints on the isotopic evolution of the Busetsu granite in addition to conventional whole-rock geochemistry and isotope chemistry.

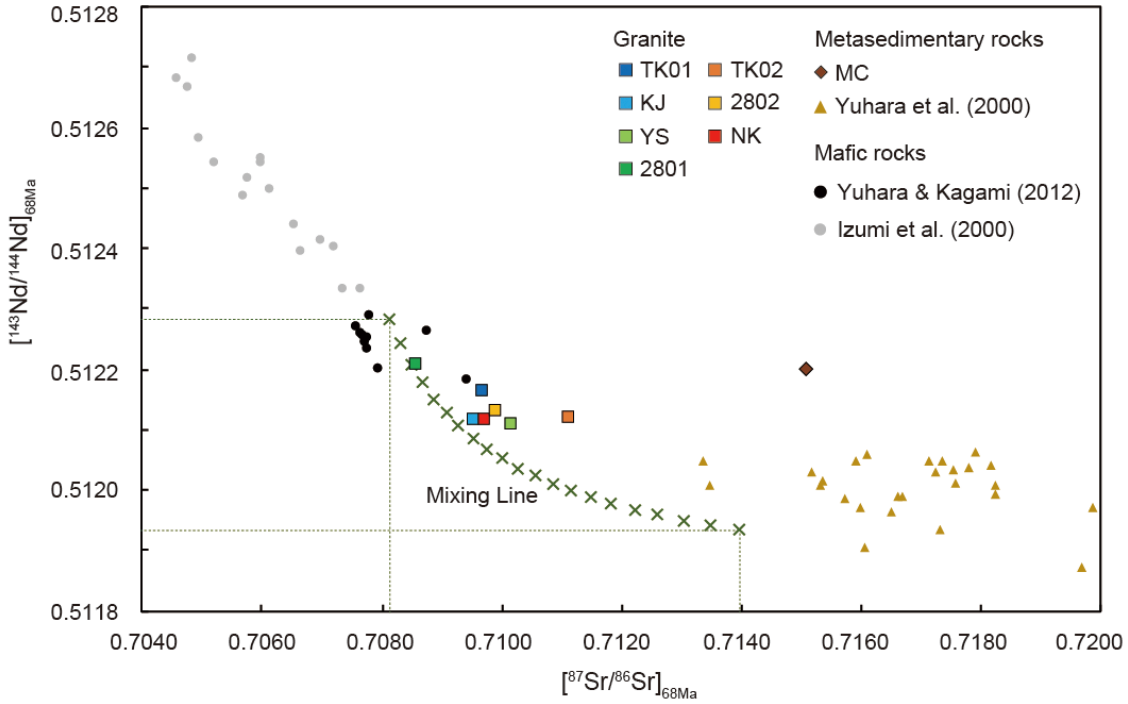

Fig. 3-17. Sr-Nd isotope systematics showing negative correlation associated with mantle-derived and sedimentary components. The mixing line is calculated using two components constrained by monazite and plagioclase isotope compositions: $[^{143}Nd/^{144}Nd]_{68Ma}$ = 0.51227 and $[^{87}Sr/^{86}Sr]_{68Ma}$ = 0.7081; $[^{143}Nd/^{144}Nd]_{68Ma}$ = 0.51185 and $[^{87}Sr/^{86}Sr]_{68Ma}$ = 0.7140. The dotted lines indicate the range of observed variation in Sr and Nd isotope compositions of plagioclase and monazite, respectively. Data source for metasedimentary rocks in the Ryoke Belt: Yuhara et al. (2000); Data sources for mafic rocks in the Mikawa area; Iizumi et al. (2000), Yuhara and Kagami, (2012).

3.7 Conclusion

The U–Pb dating of monazite indicated that the solidification age of the Busetsu is 68.4 ± 3.7 Ma, which is consistent with the recently reported zircon U–Pb age. The systematic variation in the Eu anomaly and LREE deletion relative to MREE of monazite resulted from plagioclase and monazite fractionation. The Sr-Nd isotope compositions revealed the multiple source components for the formation of the Busetsu granite, which could not be constrained only by whole-rock isotope analysis. Moreover, the significant variations in plagioclase Sr and monazite Nd isotopic compositions for a monzogranite sample were taken as evidence of assimilation at emplacement level prior to the solidification. It is demonstrated that an integration of geochemical and isotope microanalyses of monazite and plagioclase enables tracking open system magmatic processes.

4. Trace element systematics of igneous monazite from granitic rocks in the Japan arc: Implication for its use as an indicator of source rock type

4.1 Introduction

Monazite is a common accessory mineral in low-Ca granitic rocks (Bea, 1996; Suzuki et al., 1992, 1990; Kelts et al., 2008; Fisher et al., 2017) and various metamorphic rocks (Overstreet, 1967; Parrish, 1990; Catlos, 2013). Monazite can be precisely dated by the U–Th–Pb system (Rasmussen et al., 2001; Harrison et al., 2002; Williams et al., 2007; Iizuka et al., 2010b), and is well-suited for rare earth element (REE) geochemistry and Nd isotope tracer studies (Evans and Zalasiewicz, 1996; Tomascak et al., 1998; Iizuka et al., 2010b; Stepanov et al., 2012; Fisher et al., 2017). Because monazite, especially from metamorphic rocks, often shows complex chemical zoning (Zhu and O'Nions, 1999; Spear and Pyle, 2002; Kawakami and Suzuki, 2011; Seydoux-Guillaume et al., 2002; Mahan et al., 2006), microanalysis techniques are essential for obtaining reliable data about the compositional variation of monazite grains. The major element composition of monazite has traditionally been determined using an electron probe micro analyzer (EPMA) with a spatial resolution of ~1 μm (Williams et al., 2007). The Th–U–total Pb data collected by the EPMA for monazite have also been used to estimate the timing of its (re)growth by assuming no common Pb and no Pb-loss or by constructing a chemical isochron (Suzuki and Adachi, 1998, 1991; Jercinovic and Williams, 2005; Suzuki and Kato, 2008; Montel et al., 1996; Cocherie et al., 1998; Pyle et al., 2005). In situ monazite U–Th–Pb dating has been also performed with secondary

ion mass spectrometry (SIMS) (Ireland and Gibson, 1998; Stern and Berman, 2001; DeWolf et al., 1993; Vry et al., 1996; Zhu et al., 1997; Rasmussen et al., 2001; Sano et al., 2006; Jantos et al., 2012; Kusiak et al., 2014) and laser ablation-inductively coupled plasma-mass spectrometry (LA-ICP-MS) (Machado and Gauthier, 1996; Kosler et al., 2001; Foster et al., 2002; Horstwood et al., 2003). Although the analytical resolutions achievable with the SIMS and LA-ICP-MS techniques (≥ 5 μm) are lower than the resolutions possible with EPMA, these techniques have lower detection limits and provide Pb isotope data that allow us to evaluate the concordance of the U–Th–Pb system. The LA-ICP-MS technique is also capable of precise analysis of trace element abundances and Sm–Nd isotopic ratios in monazite with a spatial resolution of ≥ 5 μm (Mcfarlane and Mcculloch, 2007; Bea et al., 1994; Poitrasson et al., 2000; Yang et al., 2008; Iizuka et al., 2011a, b).

In the last decade, these in situ analytical techniques have been applied to many metamorphic monazite studies (Rubatto et al., 2006; Buick et al., 2010; Iizuka et al., 2010b; Mottram et al., 2014; Štípská et al., 2015). These studies revealed that the geochemical composition of monazite is largely controlled by co-existing mineral assemblages and it can provide strong constraints on its crystallization conditions. For instance, monazite grains in granulite-facies metasedimentary rocks commonly exhibit significant heavy-REE (HREE) depletion, relative to light-REE (LREE) abundance, and elevated Th/U ratios, reflecting the effects of the co-existence with garnet and zircon on the HREE and Th/U fractionations, respectively (e.g., Rubatto et al., 2006).

Accordingly, the combined use of monazite geochronology and geochemistry is a powerful tool for tracing metamorphic history. In addition, Nd isotope microanalysis of monazites in metasedimentary rocks has indicated that detrital monazites are the primary source of LREE during metamorphic monazite formation (Iizuka et al., 2011b).

Despite its potential as a tracer of magmatic evolution, reports of igneous monazite geochemistry, and particularly trace element geochemistry, are far less common than metamorphic monazite studies. Hoshino et al. (2012) determined the major element compositions of monazites from a wide range of granitic rocks in the Japan arc, which revealed systematic variations in La/Sm ratios between granites and pegmatites and between magnetite-series (oxidized type) and ilmenite-series (reduced type) rocks. They interpreted the systematic LREE variations to indicate differences in the magmatic protolith for magnetite- and ilmenite-series granitic rocks. Recently, Fisher et al. (2017) demonstrated correlated changes in Ce/Gd, Eu/Eu* (i.e., the degree of Eu anomaly), and Nd isotopic ratios in igneous monazites from the Sweetwater Wash pluton in southeastern California, which was interpreted to reflect the fractionation of monazite and plagioclase associated with the assimilation of country rocks.

In this study, to link monazite composition with various igneous petrogenesis and different processes, we conducted comprehensive measurements of REE-Th-U abundances and Sm-Nd isotope ratios in monazites from magnetite- and ilmenite-series granitic rocks in the Japan arc. The data revealed variations in trace elements among monazites from different types of rocks and within a single monazite grain. Based on

the results, we discussed the behavior of REE-Th-U in granitic magmas under different oxidation conditions. Finally, we explored the potential of REE-Th-U geochemistry as an indicator of the provenance of detrital monazites by comparing our results with previously reported data for monazite grains of different origins.

4.2 Geologic outline and samples

The Japan arc sits along the eastern margin of the East Asian continent, having mainly developed through subduction-related orogeny since the Permian, followed by the formation of a back-arc basin ca. 20 Ma (e.g., Maruyama et al., 1997; Taira, 2001; Isozaki et al., 2010). In the southwestern part of the Japan arc, granitic rocks are distributed along the inward side of the Median Tectonic Line and can be divided into the Ryoke, Sanyo, and San-in belts (Fig. 4-1). In the northeastern part of the arc, granitic rocks are exposed mainly in the Abukuma and Kitakami belts. These Japanese granitic rocks have been classified into magnetite-series and ilmenite-series, reflecting distinctive redox states during their formation (Ishihara, 1977). Magnetite-series granites are characterized by a mineral assemblage of magnetite (0.1–2%), ilmenite, hematite, pyrite, titanite, epidote, and high-Mg/Fe biotite. Ilmenite-series granites contain ilmenite (<0.1%), pyrrhotite, graphite, muscovite, and low-Mg/Fe biotite. Both series contain zircon, monazite, and xenotime as accessary phases (Hoshino et al., 2012). The magnetite-series is dominant in the Kitakami and San-in belts, whereas ilmenite-series is dominant in the Abukuma, Ryoke, and Sanyo belts (Ishihara, 1977). The formation of magnetite-series granitic rocks mainly occurred at 120–110 Ma in the

Kitakami belt and 70–55 Ma in the San-in belt, whereas that of ilmenite-series granitic rocks was significant at 110–100 Ma in the Abukuma belt and 95–70 Ma in the Ryoke and Sanyo belts (Seno and Maruyama, 1984; Kinoshita, 1995; Takagi, 2004). The younger (100–55 Ma) Japanese granitic rocks generally have lower initial $^{143}Nd/^{144}Nd$ and higher initial $^{87}Sr/^{86}Sr$ ratios than older rocks (Takagi, 2004). Furthermore, ilmenite-series granitic rocks tend to yield lower $^{34}S/^{32}S$ and higher $^{18}O/^{16}O$ ratios than contemporaneous magnetite-series rocks, suggesting greater contributions from sedimentary components to ilmenite-series granitic magmas (Ishihara and Sasaki, 1989; Takagi, 2004).

In this study, monazite grains from four magnetite-series granitic rocks of the San-in and Kitakami belts and nine ilmenite-series granitic rocks of the Ryoke, Sanyo, and Abukuma belts were investigated. Sample locations are illustrated in Fig. 4-1. The studied rock samples include four granites and nine granitic pegmatites. The sample locations, ages, mineral assemblages, and monazite morphologies of the granitic rocks are summarized in Table 1. Note that the Shirakawa and Nakano magnetite-series and Busetsu ilmenite-series granites were classified as S-type based on the geochemical classification proposed by Chappell and White (1974) (Ishihara, 1971; Hoshino and Ishihara, 2007). On the other hand, the Naegi ilmenite-series granite is I-type (Ishihara and Murakami, 2006). All of these rock samples and monazite grains analyzed in this study were used in the previous EPMA-based major element geochemical study by Hoshino et al. (2012). Geochemical analysis was carried out on monazites mounted in

epoxy resin for all samples except the Naegi and Busetsu ilmenite-series granites, which were studied in thin section.

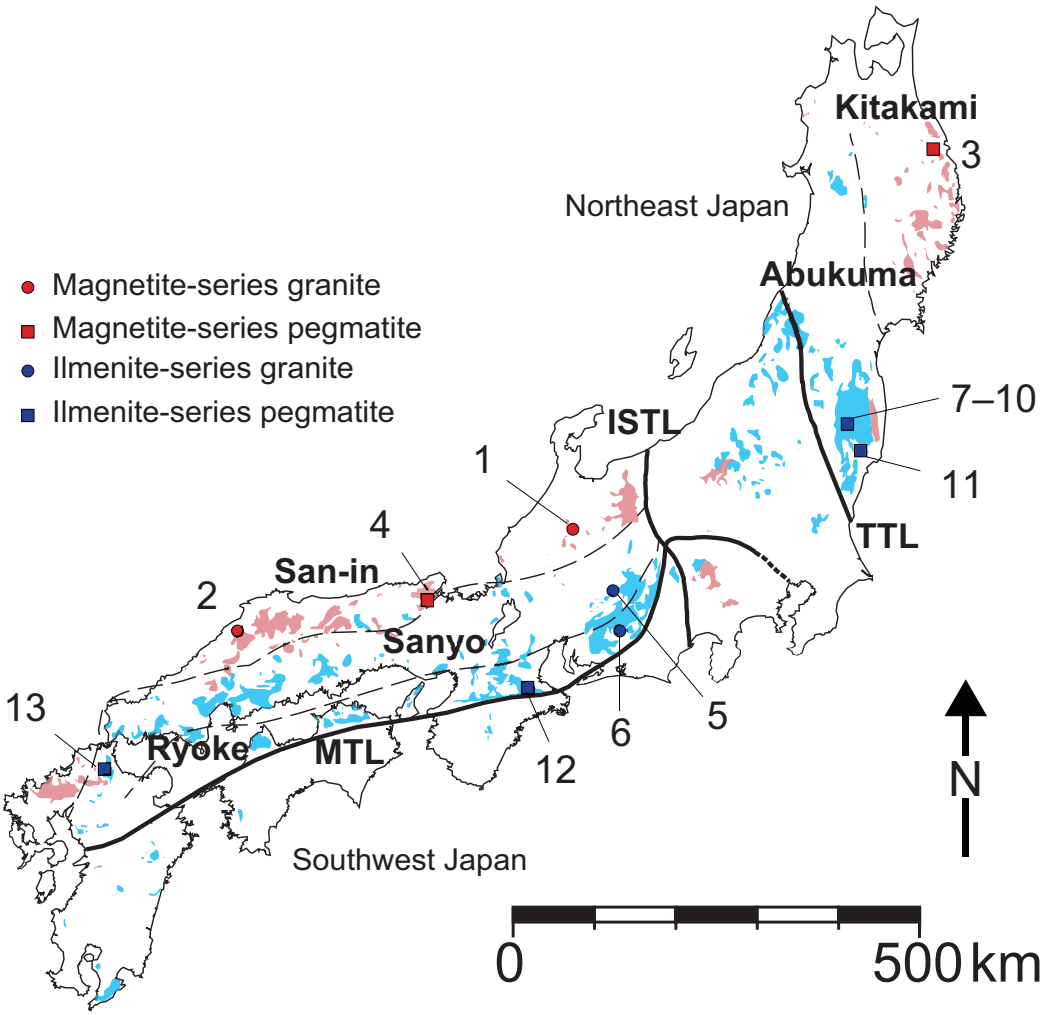

Figure 4-1: Distribution of magnetite (red)- and ilmenite (blue)-series granitic rocks in the Japan arc (modified after Takagi, 2004, Hoshino et al., 2012). Locations of samples are indicated (Table 1). Abbreviations are as follows: TTL, Tanakura tectonic line; ISTL, Itoigawa-Shizuoka tectonic line; MTL, Median tectonic line.

Table 1
Summary of age and mineralogical data for studied granitic smaples.

Sample Nummber	Location	Granite belt	Age of granitic rocks [Ma]	Major mineral assemblage	Accessory mineral assemblage	Monazite morpholofy and grain size	Ref.
Magnettite-series granites							
1	Shirakawa, Gifu	San-in	65.6 ± 1.8	Qtz, Pl, Kfs, Hbl, Bt	allanite, titanite, Nb-Ta minerals, magnetite, zircon	Subhedral-anhedral, 20–100 μm	1–4
2	Nakano, Shimane	San-in	61	Qtz, Pl, Kfs, Hbl, Bt	allanite, titanite, Nb-Ta minerals, allamagnetite, zircon	Subhedral-anhedral, 20–100 μm	1, 3–6
Magnettite-series pegmatites							
3	Kamiotomo, Iwate	Kitakami	135 ± 25	Qtz, Pl, Kfs, Hbl, Bt, Ms	zircon, thorite, xenotime, magnetite	Prismatic crystals, 2–5 mm	1, 7, 8
4	Oro, Kyoto	San-in	61.9 ± 0.9	Qtz, Pl, Kfs, Hbl, Bt, Ms	zircon, xenotime, allanite, magnetite, fergusonite	Platycrystals, 3–8 mm	1, 3, 9
Ilmenite-series granites							
5	Naegi, Gifu	Sanyo	67.2 ± 3.2	Qtz, Pl, Kfs, Bt, Ms	flourite, xenotime, Nb-Ta minerals, thorite, ilmenite, zircon	Subhedral-anhedral, 20–100 μm	1, 10, 11
6	Busetsu, Aichi	Ryoke	82.5 ± 3.9	Qtz, Pl, Kfs, Bt, Ms	apatite, xenotime, almandine, ilmenite, zircon	Subhedral-anhedral, 20–100 μm	1, 2
Ilmenite-series pegmatites							
7	Utsumine, Fukushima	Abukuma	106 ± 16	Qtz, Pl, Kfs, Hbl, Bt, Ms	allanite, zircon, xenotime	Long prismatic crystals, 5–8 mm	3, 4, 12
8	Morita, Fukushima	Abukuma	106 ± 16	Qtz, Pl, Kfs, Hbl, Bt, Ms	thorite	Prismatic crystals, 5–10 mm	12
9	Shichironai, Fukushima	Abukuma	106 ± 16	Qtz, Pl, Kfs, Hbl, Bt, Ms	zircon, xenotime	Lomg prismatic crystals, 5–8 mm	1, 12
10	Shiozawa, Fukushima	Abukuma	106 ± 16	Qtz, Pl, Kfs, Hbl, Bt, Ms	zircon, columbitem xenotime	Prismatic crystals, 2–5 mm	12
11	Shimo-ono, Ibaraki	Abukuma	115	Qtz, Pl, Kfs, Hbl, Bt, Ms	zircon, allanite, ilmenite, magnetite, hematite, fergusonite, xenotime	Lomg prismatic crystals, 10–12 mm	1, 3–5, 13
12	Misugi, Mie	Ryoke	75	Qtz, Pl, Kfs, Hbl, Bt, Ms	zenotime	Lomg prismatic crystals, 5–8 mm	5, 14
13	Masaki, Fukuoka	Sanyo	100 ± 5	Qtz, Pl, Kfs, Hbl, Bt, Ms	zircon, thorite	Lomg prismatic crystals, 5–8 mm	1, 5, 15, 16

Mineral abbreviations are from Kretz (1983); References: data sources are (1) Hoshino et al. (2010), (2) Shibata and Ishihara, (1979), (3) Hoshino et al., (2006), (4) Hoshino et al., (2007), (5) Kagami et al., (1999), (6) Yakushiji et al., (2012), (7) Fujimaki et al., (1992), (8) Takagi (2004), (9) Terakado and Nohda, (1993), (10) Suzuki and Adachi, (1998), (11) Suzuki et al., (1990), (12) Shibata and Tanaka, (1987), (13) Tanaka, (1977), (14) Hayama et al., (1982) (15) Yuhara et al., (2014), and (16) this study

4.3. Analytical method

All monazite grains were investigated by back-scattered electron (BSE) imaging to check their internal zoning structures and the presence of inclusions before geochemical and Sm–Nd isotope analysis. The BSE images were obtained using a JEOL JSM-7000F Field Emission Scanning Electron Microscope at the Department of Earth and Planetary Science, The University of Tokyo. An accelerating voltage of 10 kV, an emission current of 20 nA, and a working distance of 10 mm were used.

Determination of REE-Th-U abundances were carried out using an iCAPQ ICP-MS attached to a Nd:YAG laser ablation (LA) system at the Department of Earth and Planetary Science, The University of Tokyo. The analytical parameters of the LA system and the ICP-MS are shown in Table 4-2. The LA system was equipped with the active two-volume HelExTM Cell (Eggins et al., 2005), in which the effective cell volume is so small (~2.5 cm^3) that aerosol deposition around the ablation pit is minimized. Unknown samples were analyzed in runs of eight samples, bracketed by three measurements of a standard NIST SRM 610 glass (Pearce et al., 1997). The Ce concentrations were used as an internal standard, which were determined by a Field Emission-EPMA JEOL JXA 8530F HyperProbe at The University of Tokyo and at the National Institute of Advanced Industrial Science and Technology (AIST) in Tsukuba, Japan. The operating conditions of the EPMA analysis were: a beam diameter of 5 μm, a probe current of 30 nA, and an accelerating voltage of 25 kV. Other element concentrations were determined using the Ce concentration measured by EPMA and

their abundances relative to Ce determined by LA-ICP-MS. To correlate EPMA data with LA-ICP-MS data, the ~15-μm laser ablation pit was placed in a portion of the sample with a similar internal structure revealed by BSE imaging, and close to the pit created previously during EPMA analysis. Spectral interference from middle-REE (MREE) oxide ions on HREE ions can be problematic for accurate REE determinations in monazites during LA-ICP-MS analysis, but we corrected for them by determining oxide formation rates using synthetic MREE phosphates during each analytical session (Itano and Iizuka, 2017).

The Sm–Nd isotope analysis was performed on a Neptune Plus multi-collector-ICP-MS (MC-ICP-MS), coupled with the Nd:YAG LA system. The operating parameters for this analysis are presented in Table 3. A 30-μm laser beam with a ~20-J/cm^2 laser fluence and 4-Hz repetition rate was used. The laser ablation site was located next to the pit created during REE analysis and within a similar domain, based on BSE imaging. To correct for the different responses of the Faraday amplifiers to signal intensity change, isobaric interference, and mass bias, we followed the protocols used by Iizuka et al. (2011a): after calibrating the amplifier response using the empirically determined inter amplifier calibration factors (Table 4-3), the contribution of ^{144}Sm interference on ^{144}Nd was corrected by measuring ^{149}Sm and the exponential mass bias factors for Sm and Nd were calculated by normalizing the measured ^{147}Sm/^{149}Sm and ^{146}Nd/^{144}Nd to 1.08507 and 0.7219, respectively (O'Nions et al., 1977; Hidaka et al., 1995). To ensure accurate comparison with literature results, the

$^{143}Nd/^{144}Nd$ ratios that had been corrected for the interference and mass bias were further normalized to the thermal ionization mass spectrometry (TIMS) values $^{143}Nd/^{144}Nd = 0.511600$ and $^{145}Nd/^{144}Nd = 0.348415$. This normalization was completed based on the La–Ce–Nd synthetic monazite (Synth-LCN) standard, using the mean value obtained for this standard during each analytical session (Iizuka et al., 2011a). The instrument fractionation of $^{147}Sm/^{144}Nd$ was corrected for using Nd–Sm–Pr synthetic monazite (Synth-NSP) standard. To evaluate the accuracy and precision of the data obtained during the course of this study, we analyzed an in-house monazite standard EDR (from the Western Alps; Paquette and Tiepolo, 2007) in all analytical sessions. These results (0.512254 ±25 with two standard deviations, Appendix Table S4-1) were consistent with the TIMS results (0.512265 ±05, Iizuka et al., 2011a). The accuracy of the ^{144}Sm interference correction was further monitored by checking whether the obtained $^{145}Nd/^{144}Nd$ ratios for sample analyses were consistent with those for analyses of the Sm-free synthetic monazite Synth-LCN.

Table 4-2. Operational parameters of the LA-ICP-MS for REE analysis.

Laser ablation system	CETAC LSX-213 G2+ (CETAC, USA) equipped with the active two-volume HelEx™ Cell
Laser source	213 nm
Pulse width	5 ns
Beam diameter	15 μm
Repetition rate	3 Hz
Laser fluence	20.54 J cm^{-2}
Laser He carrier gas	0.95 L min^{-1}
ICP-MS	iCAP Qc (Thermo Fisher Scientific)
RF-power	1550 W
Sampling depth	5.1 mm
Cool gas (Ar)	14 L min^{-1}
Auxiliary gas (Ar)	0.78 L min^{-1}
Sample gas (Ar)	0.80 L min^{-1}
Measured isotopes	^{89}Y, $^{139, 138}La$, ^{140}Ce, ^{141}Pr, ^{143} Nd, ^{147}Sm, $^{151, 153}Eu$, ^{157}Gd, ^{159}Tb, ^{163} Dy, ^{165}Ho, ^{167}Er, ^{169}Tm, ^{173}Yb, ^{175}Lu, ^{232}Th, ^{238}U, $^{232}Th^{16}O$, $^{238}U^{16}O$

Table 4-3. Operational parameters of the LA-MC-ICP-MS for Sm-Nd isotope analysis.

Laser ablation system	CETAC LSX-213 G2+ (CETAC, USA) equipped with the active two-volume HelEx™ Cell						
Laser source	213 nm						
Pulse width	5 ns						
Beam diameter	30 μm						
Repetition rate	4 Hz						
Laser fluence	20.54 J cm^{-2}						
MC-ICP-MS	Neptune plus (Thermo Fisher Scientific)						
RF-power	1200 W						
Gas flow rates	Ar cooling: 14 L min^{-1}			Ar auxiliary: 1.0 L min^{-1}			
	Ar sample: 1.0–1.1 L min^{-1}						
	N_2 carrier: ~4 mL min^{-1}			He carrier: 0.95 L min^{-1}			
Mass resolution	Low						
Data acquisition mode	Time resolved analysis						
Integration time	1.02 sec						
Analysis mode	static						
Collector arrangement							
Faraday cups	L3	L2	L1	Axial	H1	H2	H3
Amplifier calibration factor*	0.0021	-0.00097	0.0021		-0.0013	-0.0011	0.0041
Analyte isotopes	^{142}(Nd+Ce)	^{143}Nd	^{144}(Sm+Nd)	^{145}Nd	^{146}Nd	^{147}Sm	^{149}Sm

*The calibration factors were determined by analyzing the synthetic monazite Synth-LCN for Nd isotopes using LA-MC-ICPMS, following Iizuka et al. (2011a).

4.4 Results

4.3.1 Monazite from granitic rocks

Monazite grains from our pegmatite samples were generally prismatic, with the long axis ranging from 2 mm to ≥10 mm, whereas those from the granites were subhedral to anhedral with lengths of 20–100 μm (Table 4-1). Representative BSE images of the monazite grains are shown in Fig. 2. The monazite grains from the Oro, Shichironai, Shiozawa, and Masaki pegmatites showed core/rim structure and sector zoning (Figs. 4-2d, i, j, and m). On the other hand, monazite grains from the Kamiotomo, Morita, and Misugi pegmatites exhibited patchy and oscillatory zoning patterns (Figs. 4-2c, h, and l). The monazite grains from the Naegi granite showed complex compositional structures whose spatial scale was smaller than that of the LA-ICP-MS resolution (~15 μm). The brightness contrasts in these BSE images are mainly attributed to the difference in Th contents within the monazite grains (Hoshino et al., 2012; Swain et al., 2005). All analyzed monazite grains from the Shirakawa, Nakano, and Busetsu granites, and the Utsumine and Shimo-ono pegmatites were homogeneous in BSE images. The BSE images further revealed that some of monazite grains from pegmatites contained altered domains that were characterized by exsolution of xenotime and Th-U silicate minerals and by compositional changes along cracks (Figs. 4-2g, h, l, m). Because fluid-mediated alteration processes can significantly modify monazite composition (e.g., Bea, 1996; Budzyń et al., 2017), and because the primary purpose of this study was to link

monazite composition with igneous processes, these altered domains were avoided in our analysis.

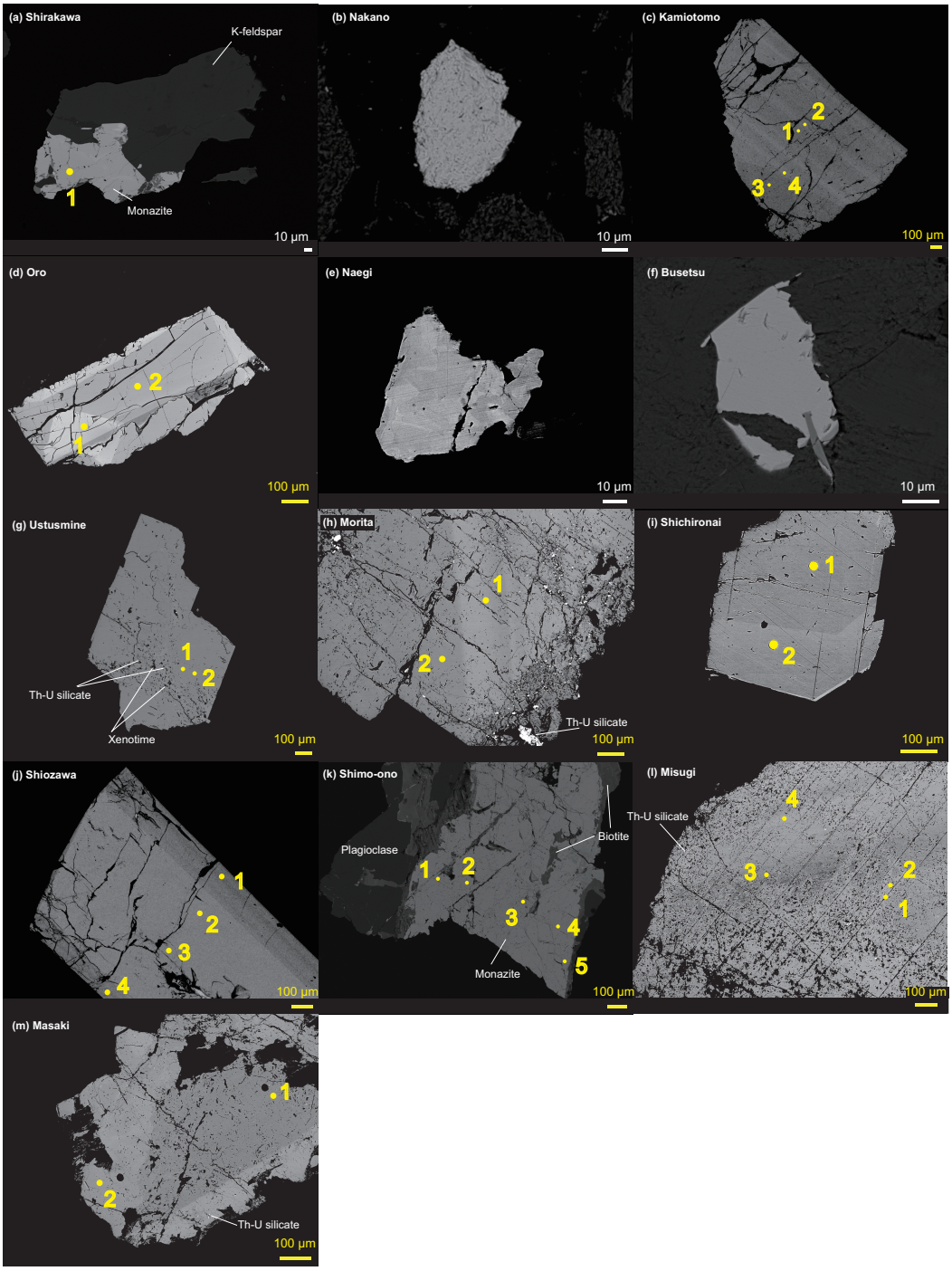

Fig. 4-2. Representative back-scattered electron images of the analyzed monazite samples. Magnetite-series: (a) Shirakawa granite, (b) Nakano granite, (c) Kamiotomo pegmatite, and (d) Oropegmatie. Ilmenite-series: (e) Naegi granite, (f) Busetsu granite, (g) Utsumine pegmatie, (h) Morita pegmatie, (i) Shichironai pegmatite, (j) Shiozawa pegmatite, (k) Shimo-ono pegmatite, (l) Misugi pegmatite, and (m) Masaki pegmatite. Yellow dots represent analyical spots for REE analyses of monazites from the pegmatites (Table S2, ESI).

Thirty-nine REE-Th-U abundance determinations were conducted on twenty-one monazite grains from the 13 granitic rocks. The monazite REE-Th-U data obtained by LA-ICP-MS and EPMA are listed in Appendix Table S4-2, together with the internal structures of the analytical spots. The chondrite-normalized REE patterns of monazites from the ilmenite-series granites and pegmatites and the magnetite-series granites and pegmatites are respectively shown in Fig. 4-3.

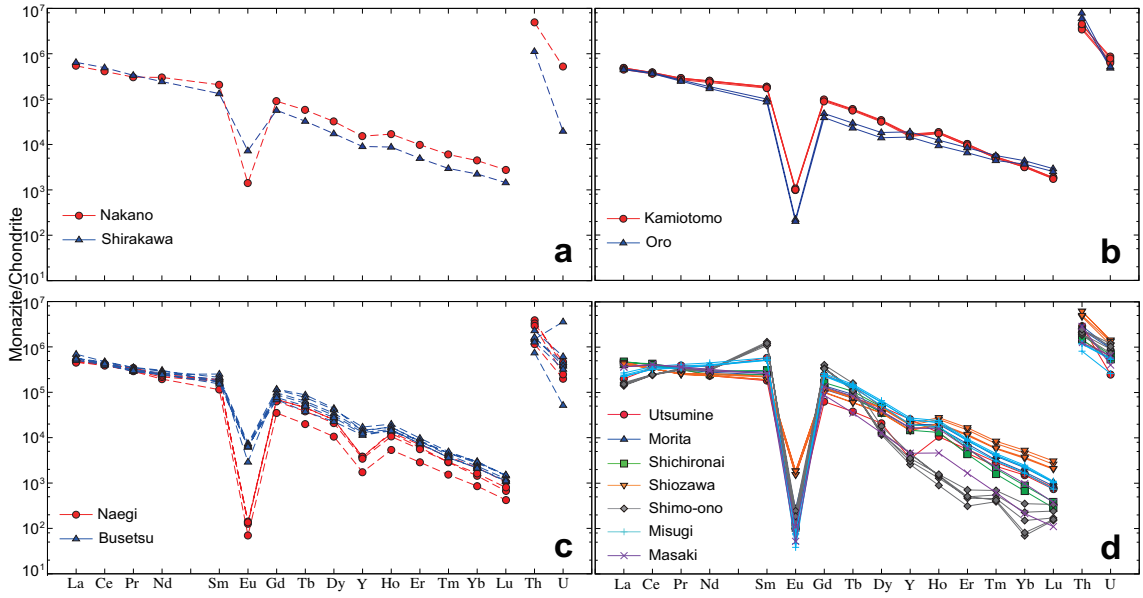

Fig. 4-3. Chondrite-normalized REE and Th-U patterns of monazites from magnetite-series (a) granites and (b) pegmatites and from ilmenite-series (c) granites and (d) pegmatites. Chondrite concentrations are taken from McDonough and Sun, (1995).

The normalized REE abundances generally formed smooth patterns from La to Lu with negative Eu anomalies, except for the Samples Utsumine, Shimo-ono, and Misugi showing the convex patterns with a peak of Sm (4-3d). The chondrite-normalized values

of $[Eu/Eu^*]_N$, $[Ce/Gd]_N$, $[Gd/Lu]_N$, and $[Th/U]_N$ are graphed in Fig. 4-4, allowing a quantitative evaluation of the REE-Th-U systematics. All analyzed monazites exhibited REE patterns with negative Eu anomalies (i.e., $[Eu/Eu^*]_N < 1$) and HREE depletion relative to MREE ($[Gd/Lu]_N > 1$). There were no significant differences in REE composition within all analyzed single grains except for the Masaki monazite grain, in which the core had a less fractionated REE pattern with more prominent negative Eu anomaly and a lower Th/U ratio than the rim (Fig. 4-5). We detected systematic differences between granites and pegmatites and between magnetite- and ilmenite-series samples (Figs. 4-3 and 4-4). Within magnetite- or ilmenite-series, monazites from the pegmatites basically exhibited more significant negative Eu anomalies than those from the granites. Monazites from the ilmenite-series granites and pegmatites tended to have stronger negative Eu anomalies ($[Eu/Eu^*]_N$ ranging from $\sim10^{-2}$ to $\sim10^{-4}$) than their magnetite-series counterparts ($[Eu/Eu^*]_N$ ranging from $\sim10^{-2}$ to $\sim10^{-3}$). The monazites with the most prominent negative Eu negative anomalies, which were from the ilmenite-series pegmatites, exhibited weak LREE enrichment, and sometimes even depletion, relative to MREE (i.e., lower $[Ce/Gd]_N$ as low as 0.6); significant HREE depletion relative to MREE (i.e., high $[Gd/Lu]_N$ of up to ~2400); and less variable Th/U ratios (0.4 to 14). The results of L-MREE analyses are consistent with those obtained using EPMA by Hoshino et al. (2012).

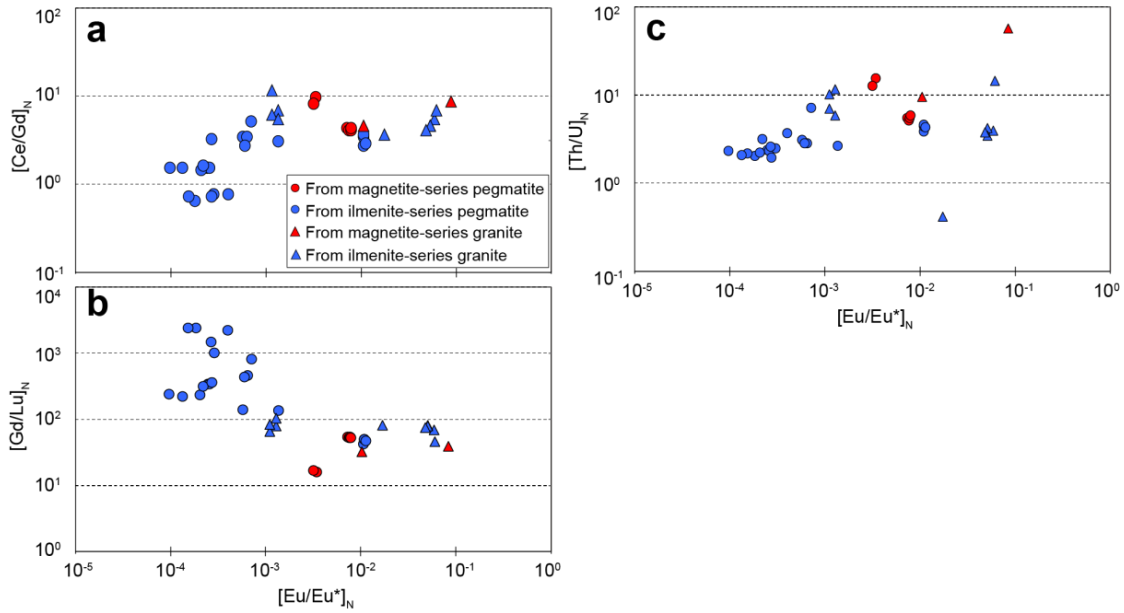

Fig. 4-4. Plots of (a) $[Ce/Gd]_N$, (b) $[Gd/Lu]_N$, and (c) $[Th/U]_N$ vs. $[Eu/Eu^*]_N$ for monazites from magnetite-series granites (red circle) and pegmatites (red triangle) and ilmenite-series granites (blue circle) and pegmatites (blue triangle).

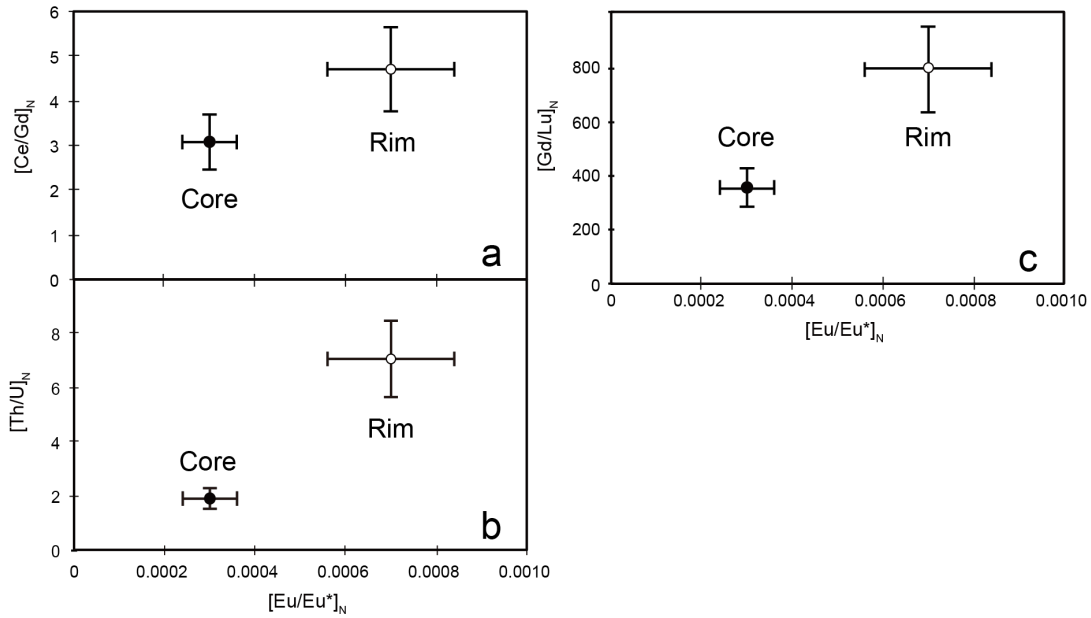

Fig. 4-5. Plots of (a) [Ce/Gd]N, (b) [Th/U]N and (c) [Gd/Lu]N vs. [Eu/Eu*]N for the core and rim of the monazite from the Masaki pegmatite.

Ninety-four Sm–Nd isotope measurements were carried out on nine monazite grains from the two magnetite-series and seven ilmenite-series pegmatites (Appendix Table 4-3). Among these, two measurements of the rim in the Masaki pegmatite monazite yielded $^{145}Nd/^{144}Nd$ ratios that were distinctively higher than those from the synthetic monazite Synth-LCN, indicating the inaccuracy in the ^{147}Sm interference correction. This inaccuracy could be attributed to imperfect correction of the different amplifier responses when Sm and Nd signal intensities changed significantly and independently due to the sample's chemical heterogeneity. Hence, we did not include the data from those two measurements in our discussion. The initial $^{143}Nd/^{144}Nd$ ratios were calculated using the previously reported ages for each sample (Table 4-1) and εNd(t) values are graphically presented in Fig. 6a. The initial $^{143}Nd/^{144}Nd$ ratios ranged from 0.512125 to 0.512525, corresponding to an εNd(t) of –8.3 to 0.6. All monazite grains showed no resolvable intra-grain variation in initial $^{143}Nd/^{144}Nd$, irrespective of their internal structures. There is no systematic difference between the magnetite- and ilmenite-series samples. Samples from the magnetite- and ilmenite-series exhibited the εNd(t) values ranging from –8.3 to 0.1 and from ca. –5.7 to 0.6, respectively. When the monazite εNd(t) values for each pegmatite are plotted against the crystallization age (Fig. 6b), on the other hand, it is evident that the monazites younger than 100 Ma (εNd(t) of –8.9 to –5.6) have lower εNd(t) values than older ones (εNd(t) of –0.7 to 1.0). Such a secular change in Nd isotopic composition has been recognizable in the whole-rock Nd isotopic data from granitic rocks in the Japan arc.

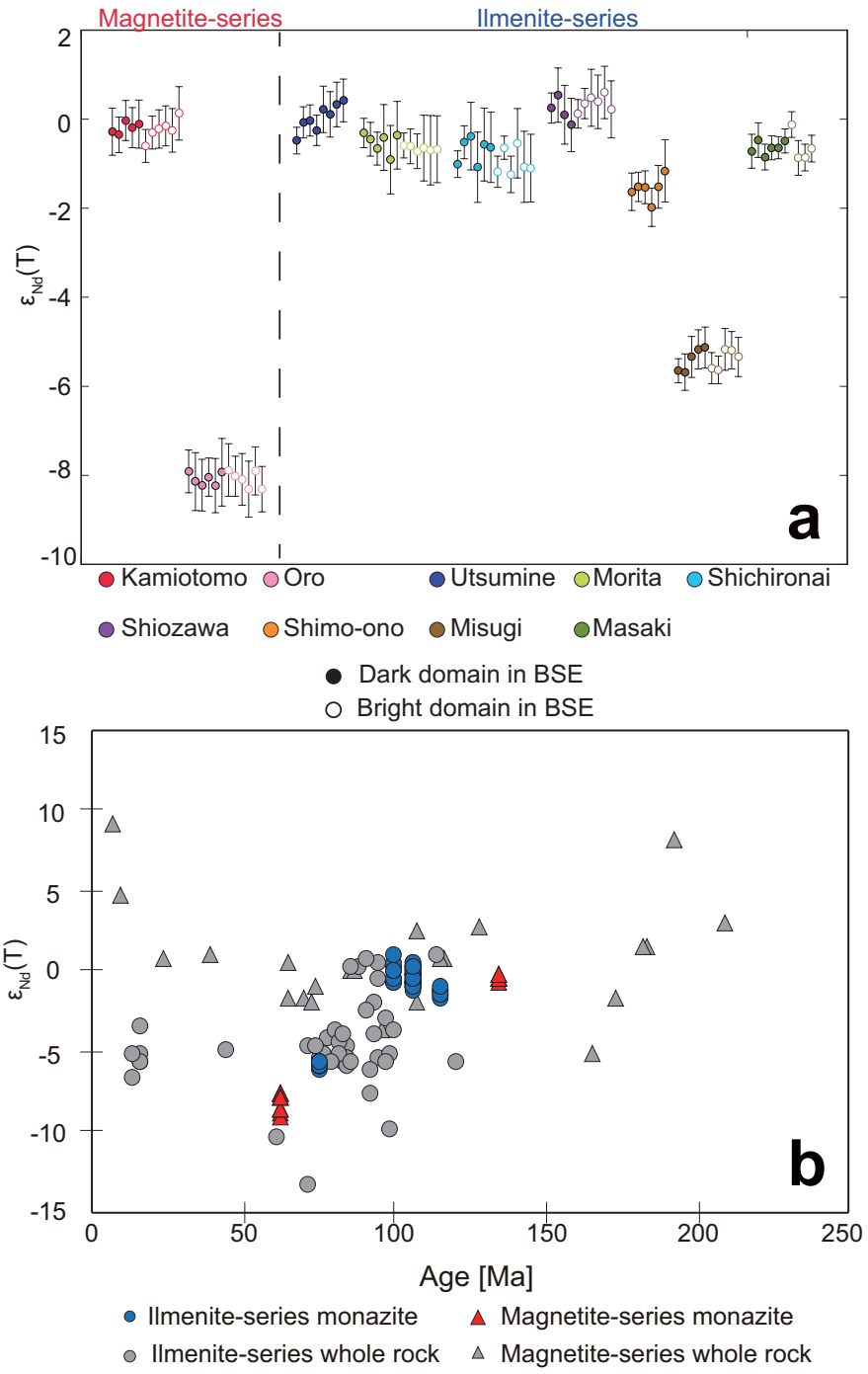

Fig. 4-6. (a) εNd(t) of pegmatite monazites. Filled and open circles represent data for dark and bright domains in back-scattered electron images, respectively. Error bars represent 2σ. (b) Plot of εNd(t) vs. age for the monazites analyzed in this study (red and blue symbols). Whole-rock Nd isotopic data for granitic rocks in the Japan arc (gray symbols; Takagi, 2004) are also shown for comparison. Error bars represent $2\sigma_m$.

4.4 Discussions

4.4.1 Differentiation of granitic magmas recorded by monazite geochemistry

Major and trace element compositions in a monazite reflect the geochemical features of the magma from which it crystallized and its crystallization conditions. Our data reveal notable variations in monazite REE-Th-U abundances between pegmatites and granites, and between ilmenite-series and magnetite-series rocks. Given that granitic pegmatites are crystallized from highly differentiated volatile-rich granitic magmas (e.g., Yurimoto et al., 1990; London, 2005; Linnen et al., 2012), the results allow us to obtain a general picture of monazite REE-Th-U systematics during differentiation in granitic magmas under different redox states.

Monazites from pegmatites showed larger Eu negative anomalies than those from granites for each series (Figs. 4-3 and 4-4). Further, monazites from ilmenite-series rocks exhibited more prominent anomalies than those from the magnetite-series. Europium can exist in both divalent (Eu^{2+}) and trivalent (Eu^{3+}) state in crustal conditions, and Eu^{2+} is more strongly partitioned into feldspars than Eu^{3+} (Fujimaki and Tatsumoto, 1984; Bea et al., 1994; Bea, 1996). Thus, the larger Eu negative anomalies in pegmatitic monazites can be attributed to more significant crystal fractionation of feldspars in their parental magmas, which was discussed in Chapter 3. Moreover, considering that the ratio of Eu^{2+}/Eu^{3+} in magma changes with the redox state of the magma (Philpotts, 1970), the larger Eu negative anomalies in ilmenite-series monazites than magnetite-series monazites are interpreted to reflect more efficient incorporation of

Eu into fractionating feldspars in more reduced magmas. This is consistent with the fact that ilmenite, rather than magnetite, is the common opaque phase in reduced granites. Hence, monazite Eu negative anomalies are considered to be a measure of the degree of feldspar fractionation and the redox state in its parental granitic magma.

The larger Eu negative anomalies in the monazites from ilmenite-series pegmatites are accompanied by smaller Ce/Gd ratios and elevated Gd/Lu ratios (Fig. 4-4a). The variations in Ce/Gd and Gd/Lu ratios that we observed cannot be explained by changing the monazite/melt partition coefficients for MREE and HREE with the temperature and the water content of the melt (Stepanov et al., 2012). Instead, the fractionations between LREE and MREE would be attributed to fractional crystallization of LREE-rich mineral phases (e.g., monazite or allanite) during magma differentiation as discussed in the previous chapter. Similarly, the significant depletion of HREE relative to MREE in parent magma can be caused only by HREE-enriched mineral phases (e.g., titanite, xenotime, and garnet) with higher partition coefficients for HREE as compared to those for MREE (Bea et al., 1994). The lack of large variations in the Ce/Gd and Gd/Lu ratios in monazites from magnetite-series granitic rocks would reflect that such fractional crystallization is more vigorous in ilmenite-series granitic magmas relative to magnetite-series magmas. Fisher et al. (2017) also demonstrated a decrease in Ce/Gd ratios associated with the increase of Eu/Eu* ratios in monazites from a peraluminous pluton in southeastern California, which was interpreted to result from the fractionation of monazite, which is a major host phase for LREE.

Experimental studies have shown that LREE solubility in a granitic melt is negatively correlated with its aluminum saturation index (ASI; $Al_2O_3/[Na_2O+K_2O+CaO]$), although the correlation is insignificant when the ASI is higher than ~1 (Rapp et al., 1987; Montel, 1993; Engi, 2017). Hence, monazites can be more readily saturated in peraluminous granitic melts than metaluminous or peralkaline granitic melts. Ilmenite-series granites are commonly related to sedimentary source rocks containing reducing agents such as organic carbon and, therefore, to peraluminous and S-type granites (Whalen and Chappell, 1988; Ishihara and Sasaki, 1989). By contrast, magnetite-series granites generally correspond to metaluminous or peralkaline I-type granites. Accordingly, the decrease in the Ce/Gd ratio that we observed only in monazites from ilmenite-series pegmatites can be attributed to significant fractionation of earlier-crystallized monazite in more peraluminous granitic magmas. In addition to monazite, crystallization of other LREE-rich minerals such as allanite and titanite, can potentially cause Ce/Gd fractionation, especially in high-Ca granitic magmas. Yet, the tendency of lower Th/U ratios in the monazites from ilmenite-series pegmatites (Fig. 4-4c) suggests that monazite played a more critical role in the host granitic magmas, because fractional crystallization of monazite, rather than allanite and titanite, should decrease the Th/U ratio in the residual melt due to its high partition coefficient of Th relative to U (Bea, 1996; Stepanov et al., 2012). In addition, fractional crystallization of other LREE- and Th-rich minerals, such as thorite-huttonite, could contribute to

produce the observed geochemical trends of ilmenite-series monazite, even though these minerals are generally much less abundant in granitic rocks than monazite (Bea, 1996).

The convex REE pattern with a peak of Sm for the ilmenite-series samples is linked with the fractionation of monazite and extremely differentiated silicic magma (Fig. 4-4d). The REE pattern with a discontinuity between LREE and MREE for highly evolved rocks such as granitic pegmatite has been reported since early 1980s (Goad and Čenrý, 1981; Christiansen et al., 1983; Mittlefeldt and Miller, 1983; Masuda et al., 1987). The large fractionation between LREE and MREE happens during the crystal fractionation of LREE-rich minerals (Mittlefeldt and Miller, 1983; Yurimoto et al., 1990) or loss of CO_2 vapor phase showing strong partition of LREE as comparted to MREE (Wendlandt and Harrison, 1979). Yurimoto et al. (1990) quantitatively demonstrated that Rayleigh fractionation of monazite resulted in the LREE depletion relative to MREE of parent melt, assuming a peraluminous granite as an initial melt composition and that REE fractionation is governed only by monazite. The possible effect of CO_2 vapor phase might have been less significant for the studied samples, because carbonate minerals were not reported as co-existing mineral assemblages (Hoshino et al., 2010). Therefore, the unique REE pattern of pegmatitic monazite was formed by the fractionation of monazite itself.

Similarly, the peraluminosity of granitic magma can greatly affect the HREE behavior, which would be reflected in the REE pattern of crystalized monazites. The peraluminous composition would result in efficient saturation and fractionation of

HREE-rich minerals of xenotime and garnet, as evidenced by their common occurrences in peraluminous granites (Bea, 1996; Casillas et al., 1995; Wark and Miller, 1993). This can account for the depletion of HREE in the monazites from ilmenite-series pegmatites (Fig. 4-4b). In addition to xenotime and garnet, zircon fractionation could contribute to HREE depletion in the residual melt due to its high partition coefficients for HREE relative to MREE. It is considered that the effects of zircon fractionation to be relatively minor in the studied samples, however, because there is little variation in La/Ce ratios in the analyzed monazites, despite the highly contrasting partitioning of these elements into zircon (Hanchar and van Westrenen, 2007). Hence, the fractionation from MREE to HREE in igneous monazites are interpreted to reflect the significance of the fractionation of monazite, xenotime, and garnet in the parental magma, which in turn provides constraints on the degree of differentiation and the source of the parental magma.

4.4.2 Intra-grain compositional variations in the Masaki pegmatite monazite

The monazite grain from the Masaki pegmatite consists of a dark core and a bright rim in the BSE image (Fig. 4-2m), and these domains have different chemical compositions. The rim had a more highly fractionated REE pattern (higher Gd/Lu) with a smaller Eu negative anomaly (higher Eu/Eu*) and a higher Th/U ratio (Fig. 4-5). Despite these geochemical differences, the core and the rim had identical εNd (100 Ma) values within analytical uncertainty (Fig. 4-6). Note that our preliminary U¬–Pb dating showed no resolvable difference (>5 Ma) between the core and the rim, indicating that

the rim formed during a later stage of the pegmatite crystallization or, alternatively, during a hydrothermal alteration shortly after the crystallization. Yet, we consider the latter unlikely because hydrothermal monazites typically have very low Th contents (<~2 wt%) (Bea, 1996; Cabella et al., 2001; Rasmussen and Muhling, 2007; Williams et al., 2007).

The LREE-Th-U change from the core to the rim is essentially the opposite of the compositional evolution of ilmenite-series magma via fractionation of monazite and feldspars (Fig. 4-4). This may reflect that the magma from which the core crystallized underwent more fractionation of monazite and feldspars than the magma that formed the rim. The only exception is that the HREE depletion was more significant in the rim than in the core (Fig. 4-5c), corresponding to a differentiation trend between the ilmenite-series pegmatites and granites (Fig. 4-4b). The HREE trend suggests that the source magma of the rim suffered more fractionation of HREE-rich minerals, such as garnet, than did the core. Given that garnet can crystallize earlier from granitic magmas under high pressure and, to some extent, lower H_2O partial-pressure conditions (Clemens and Wall, 1981; Stern and Wyllie, 1981), the decupling between the LREE-Th-U and HREE trends can be interpreted to reflect that the core crystallized from a magma differentiated at relatively shallow and/or H_2O-rich conditions, where garnet fractionation was suppressed. In addition, the homogeneous Nd isotope composition of the Masaki monazite grain indicates that the source magma of the core and rim had magmatic protoliths with similar crustal residence times. Overall, the

observed intra-grain compositional variations in the Masaki pegmatite monazite can be explained if the core and rim crystallized from distinct magmas that were originally derived from similar crustal rocks, which were subsequently differentiated through fractional crystallization under different conditions.

4.4.3 Geochemical fingerprints of monazites in various rock types for a provenance indicator

The study of detrital monazite has become more important for the investigation of continental crust evolution, as an effective complement to detrital zircon study. Detrital monazite can provide a more thorough record of tectonic events occurred in source terranes due to its crystallization during a wide range of metamorphic conditions and low-Ca granitic magmatism (Kusiak et al., 2006; Hietpas et al., 2010; Itano et al., 2016; Iizuka et al., 2017; Liu et al., 2017). As a result of its wide occurrence, however, interpretation of detrital monazite age spectra remains difficult. In the case of zircons, trace element data have been accumulated for grains of various origins, and their distinctive characteristics have been used as constraints on the provenance of detrital zircons (Hoskin and Ireland, 2000; Rubatto, 2002; Belousova et al., 2002). Given that the trace element composition of monazites reflects their formation environments such as co-existing minerals and the oxidation state, a geochemical indicator of source rock type can potentially be established for monazites.

In Fig. 4-7, a compilation of previously reported REE-Th-U data for monazites of various origins is shown to compare the data in this study. The acquisition of the trace element data for igneous monazite in this study has enabled the quantitative comparison of various origins for the first time.

The data obtained in this study reveal that the Eu negative anomalies of monazites from granitic rocks are generally larger than those of metamorphic and hydrothermal monazites, likely reflecting significant crystal fractionation of feldspars in their parental melts (Fig. 4-7a). Monazites from leucogranitic portions of migmatites also exhibit prominent negative Eu anomalies (Fig. 4-7a). Moreover, the granitic monazites tend to yield lower $[Ce/Gd]_N$ values than metamorphic, hydrothermal, and migmatitic monazites, likely due to the significant fractionation of monazite in their parental melts.

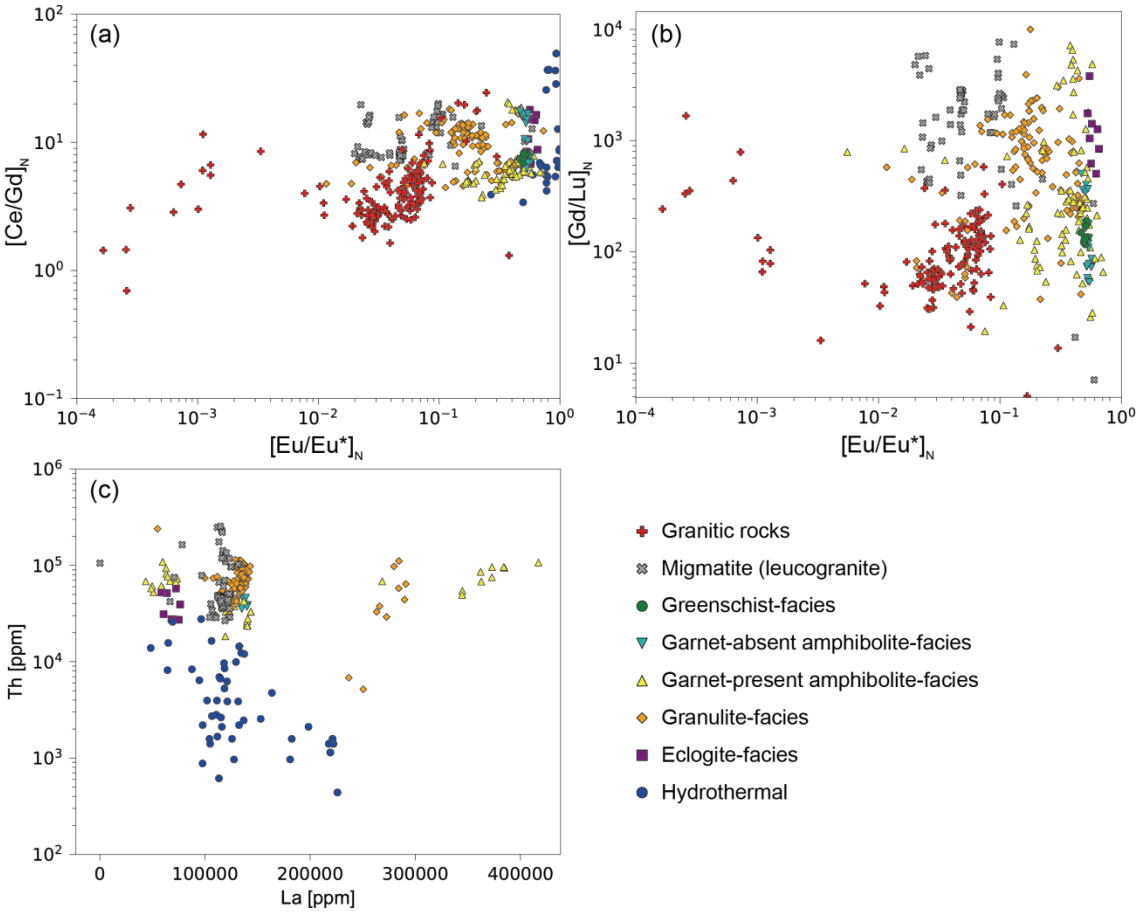

Fig. 4-7. Compilation of REE-Th-U systematics between igneous and metamorphic monazites by plotting (a) $[Ce/Gd]_N$ and (b) $[Gd/Lu]_N$ against $[Eu/Eu^*]_N$and (c) Th concentrations against La concentrations. The data for igneous monazites are from this study and Fisher et al. (2017), whereas those for meteamorphic monazites are from Rubatto et al. (2006), Buick et al. (2010), Iizuka et al. (2010), Mottram et al. (2014), Holder et al. (2015), and Štípská et al. (2015); those for hydrothermal monazites are from Cebella et al. (2001), Poitrasson et al. (2000), Condon et al. (2005), and Rasmussen and Muhling (2007).

The compiled dataset for metamorphic monazites reinforces the view that its geochemical composition is highly dependent on the presence/absence of co-existing garnet. The monazites from low-grade metamorphic rocks display restricted H-REE depletion and negative Eu anomaly (Fig. 4-7b). During low-grade metamorphism, the growth of garnet is limited (e.g., Spandler et al., 2003) and, therefore, this limitation is responsible for the monazites with restricted H-REE depletion. In contrast, the monazite grains from garnet-bearing high-grade metamorphic rocks have more variable and generally higher $[Gd/Lu]_N$ values than those from garnet-absent metamorphic rocks (Fig. 4-7b), as a result of the strong partitioning of HREE into garnet (Rubatto et al., 2006). Most detrital monazites with elevated $[Gd/Lu]_N$ (>400) display large Eu negative anomalies ($[Eu/Eu^*]_N$ <0.3), suggesting their co-existence with not only garnet but also feldspar(s) (Fig. 4-7b). Some HREE-depleted grains with restricted Eu negative anomalies ($[Eu/Eu^*]_N$ of ~0.5) may be derived either from high-temperature metamorphic rocks where feldspars were destabilized during prograde metamorphism (Holder et al., 2015) or from mafic metamorphic rocks which contain feldspars with relatively low abundances.

Hydrothermal monazite shows unique geochemical features: a restricted negative Eu anomaly as compared to other origins (Fig. 4-7a) and a low-Th content (Fig. 4-7c). In terms of texture, hydrothermal monazites are characterized by the presence of many inclusions and anhedral shapes (Rasmussen and Muhling, 2007, 2009; Rasmussen et al., 2007).

Overall, the monazites from different source rock type show different geochemical signatures characterized by $[Eu/Eu]_N$, $[Gd/Lu]_N$, and Th contents (Fig. 4-8). On the basis of the distribution of trace element data, I construct classification criteria for a provenance indicator of detrital monazite on the basis of distribution of the trace element data (Table 4-4). The distribution of $[Eu/Eu^*]_N$ for igneous monazite are different from metamorphic monazites (Fig. 4-8a). Approximately 85% of monazite grains with $[Eu/Eu^*]_N$ of <0.1 are of igneous origin. Furthermore, the monazite grains with $[Gd/Lu]_N$ of >400 are mostly derived from garnet-present metamorphic rocks: the data for garnet-present metamorphic origin account for >90% of the grain with $[Gd/Lu]_N$ of >400 and $[Eu/Eu]_N$ of >0.1 (Fig. 4-8b). It is therefore reasonable to expect that the detrital monazites highly depleted in HREEs ($[Gd/Lu]_N$ of >400) with restricted negative Eu anomalies are originated mainly from garnet-rich metamorphic rocks with typically medium- to high-grades. On the other hand, the grains, showing $[Gd/Lu]_N$ of <400 and $[Eu/Eu]_N$ of <0.1 is likely to be derived from garnet-poor or garnet-rich metamorphic rocks. Indeed, the geochemical features of monazites from garnet-absent metamorphic rocks, such as low-grade metamorphic rocks, are restricted HREE-depletion and Eu anomaly (Fig. 4-8a, b). Hydrothermal monazite is characterized by so low-Th content as compared to other origins (Fig. 4-8c). The grains with low-Th content (<10,000 ppm) can be identified as hydrothermal origins. Thus, the combination of a significant negative Eu anomaly, depletion of HREE relative to MREE, and depletion in Th can be regarded as a strong indicator of source rock types.

Table 4-4. Geochemical criteria for an indicator of source rock type

Igneous	Metamorphic		Hydrothermal
	Garnet-poor to Garnet-rich	Garnet-rich	
$[Eu/Eu^*]_N < 0.1$ $[Gd/Lu]_N < 400$	$[Eu/Eu^*]_N > 0.1$ $[Gd/Lu]_N < 400$	$[Gd/Lu]_N > 400$	Th content $< 10^4$ ppm

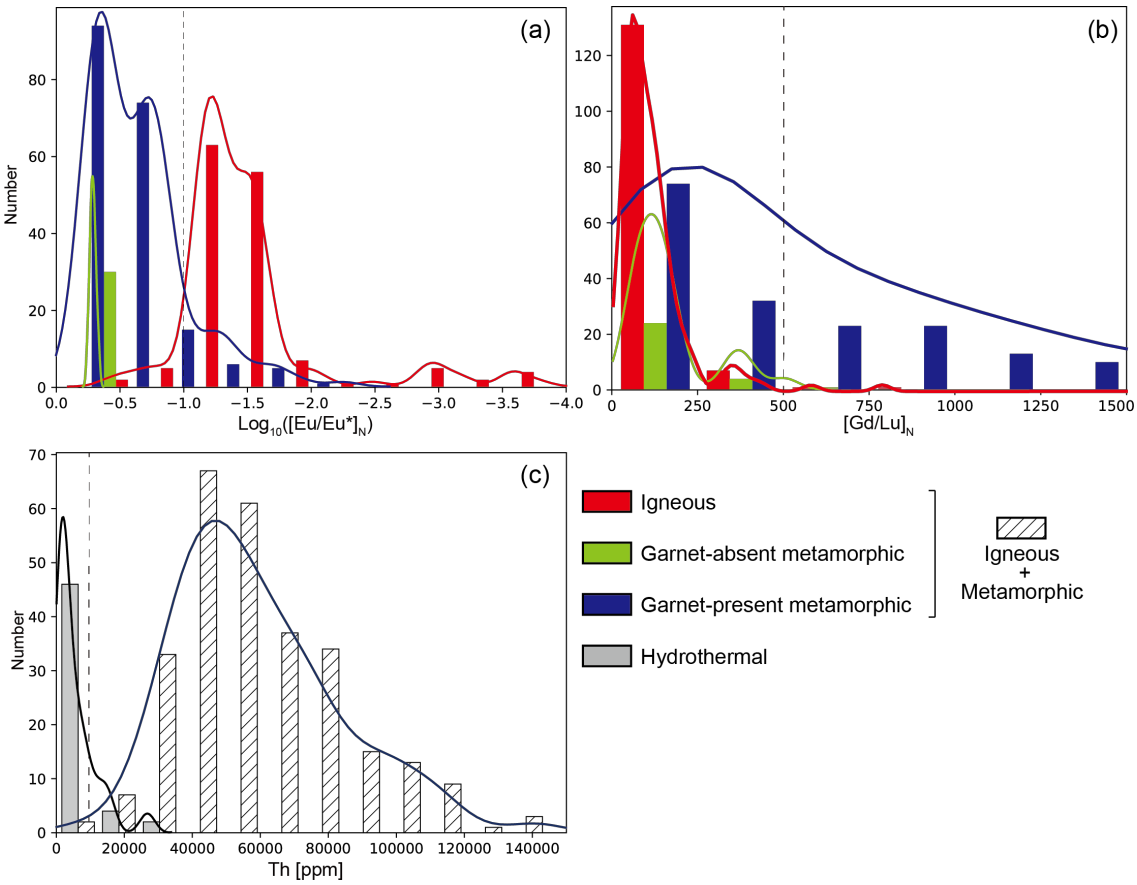

Fig. 4-8. Histograms of geochemical variations in (a) $[Eu/Eu^*]_N$, (b) $[Gd/Lu]_N$, and (c) Th contents for igneous, garnet-absent and garnet-present metamorphic, and hydrothermal monazites. The bold lines represent relative probability density for each genesis.

4.5 Conclusion

The REE-Th-U systematics of monazites reflects different differentiation schemes between magnetite-series and ilmenite-series granitic rocks. In ilmenite-series granitic rocks, monazites from pegmatites show larger negative Eu anomalies, lower LREE/MREE ratios, and higher MREE/HREE ratios than those from granites. These geochemical variations are related to significant fractional crystallization of feldspars, monazite, xenotime, and garnet during differentiation in relatively reduced and peraluminous magmas. In magnetite-series granitic rocks, by contrast, monazites from pegmatites and granites exhibit similarly fractionated REE patterns with variable negative Eu anomalies. The negative Eu anomalies ate smaller compared to those observed in ilmenite-series samples. These features are considered to reflect the suppression of monazite, xenotime, and garnet fractionation and of Eu incorporation into fractionating feldspars in relatively oxidized and non-peraluminous magmas. The monazite from the Masaki ilmenite-series pegmatite shows intra-grain variations in REE–Th–U compositions, but homogeneous Nd isotope composition. The finding may reflect that the core and rim crystallized from magmas that were derived from similar crustal source rocks, but underwent fractional crystallizations under distinctive differentiation conditions. The REE-Th-U compositions of these igneous monazites are variable, but distinct from those of metamorphic and hydrothermal monazites, most notably in their larger negative Eu anomalies. Thus, REE-Th-U systematics shows promise as a provenance indicator for detrital monazites.

5. Application to detrital monazites from major African rives: Constraints on the timing and nature of the Pan-African Orogeny

5.1 Introduction

The African continent comprises five Archean to Paleoproterozoic cratons: the West African Craton, Saharan Metacraton, Congo Craton, Tanzania Craton and Kalahari Craton (Fig. 1). These cratons are surrounded by orogenic belts, formed during the late Neoproterozoic to the earliest Paleozoic time (e.g., Meert, 2003; Kröner and Stern, 2004; Begg et al., 2009). The so-called Pan-African Orogeny is considered to have resulted from collisions of the cratons to form the Gondwana supercontinent and the African continent was located in the central area of the supercontinent (Gray et al., 2008; Meert and Lieberman, 2008). Thus, knowledge of the Pan-African Orogeny is a key to understanding the development of the African continent and Gondwana supercontinent. To better constrain the timing and nature of the Pan-African Orogeny, we have determined U–Pb ages and chemical compositions of ca. 500 detrital grains of monazite, a light rare earth element (LREE) phosphate, from the five largest African rivers: the Nile, Niger, Congo, Zambezi and Orange Rivers.

Detrital minerals in sediments of large rivers have been eroded from exposed crust in extensive drainage basins, which consists of sedimentary, igneous and metamorphic rocks. Since zircon and monazite are mechanically robust and can survive sedimentary recycling (Veizer and Jansen, 1979, 1985; Goldstein et al., 1984; Campbell et al., 2005),

these minerals in river sands would be partially derived from the basements that are currently overlain by a sedimentary cover or have been eroded away and thus inaccessible. Moreover, single grains of zircon and monazite can be precisely dated by U–Pb isotopes due to their high U–Th and low non-radiogenic Pb contents. Thus, detrital zircons and monazites from large rivers offer a unique means of elucidating the timing of major magmatic and/or metamorphic events in a continental scale that might have been overlooked by the researches based on the exposed geology (e.g., Ross et al., 1991; Goldstein et al., 1997; Yokoyama and Zhou, 2002; Rino et al., 2004; Hietpas et al., 2010; Moecher et al., 2011). This is particularly relevant for the African continent where a large area of the basement is covered by Phanerozoic sediments (Fig. 5-1).

Recently, Iizuka et al. (2013) reported U–Pb age and Hf–O isotope data for detrital zircons from the five largest African rivers. The data revealed that granitoid magmatism during the Pan-African Orogeny played a significant role in the formation and reworking of the African continental crust. Yet, because they analyzed detrital zircons of magmatic origin rather than metamorphic origin, the timing of metamorphism related to the Pan-African Orogeny is poorly constrained by the detrital zircon record.

Monazite commonly occurs as an igneous mineral in low-Ca peraluminous felsic rocks (e.g., Overstreet, 1967; Parrish, 1990; Xie et al., 2006; Kelts et al., 2008; Chattopadhyay et al., 2015) and a metamorphic mineral in a wide range of metamorphic rocks (e.g., Overstreet, 1967; Smith and Barreiro, 1990; Buick et al., 2010; Štípská et al., 2015). This is in contrast to zircon which is commonly crystallized from a wide range of

felsic magmas (Chappell and White, 2001; Kelts et al., 2008) and secondarily formed during high-grade metamorphism (Rubatto et al., 2001; Rubatto, 2002; Harley and Nandakumar, 2014). The restricted occurrence of igneous monazite in high-Ca felsic rocks is due to the decomposition of monazite to form allanite (Lee and Bastron, 1967; Watt and Harley, 1993; Kelts et al., 2008). Importantly, the Pb diffusion in monazite crystal is as slow as that in zircon, so the monazite U–Th–Pb system can potentially be preserved thorough high-grade metamorphism (Schaltegger et al., 1999; Rubatto et al., 2001; Cherniak et al., 2004; Schmitz and Bowring, 2004; McFarlane and Harrison, 2006). Thus, monazite is suitable for high-precision dating of peraluminous magmatic and low- to high-grade metamorphic events and detrital monazite is a powerful tool in provenance characterization (Ross et al., 1991; Yokoyama and Zhou, 2002). Indeed, Hietpas et al. (2010, 2011) compared the U–Pb age distributions of detrital monazites and zircons from the French Broad River for which the geology in the drainage basin is well known and demonstrated that the detrital monazites record metamorphic events more accurately than the detrital zircons. In addition, the genesis of monazite can be constrained by geochemical analysis because some elemental abundances in monazite highly depend on the assemblages of co-existing minerals via element partitioning (Hermann and Rubatto, 2003; Rubatto et al., 2006; Mottram et al., 2014; Štípská et al., 2015).

In this contribution, we explore the geological significance of detrital monazite in the five African river systems by combining the U–Pb ages and geochemical data and also

by comparing with previously obtained detrital zircon U–Pb age peaks (Iizuka et al., 2013). Along with the results obtained in the present and previous studies, we discuss new insights into the Pan-African Orogeny and implications for the development of the African continent.

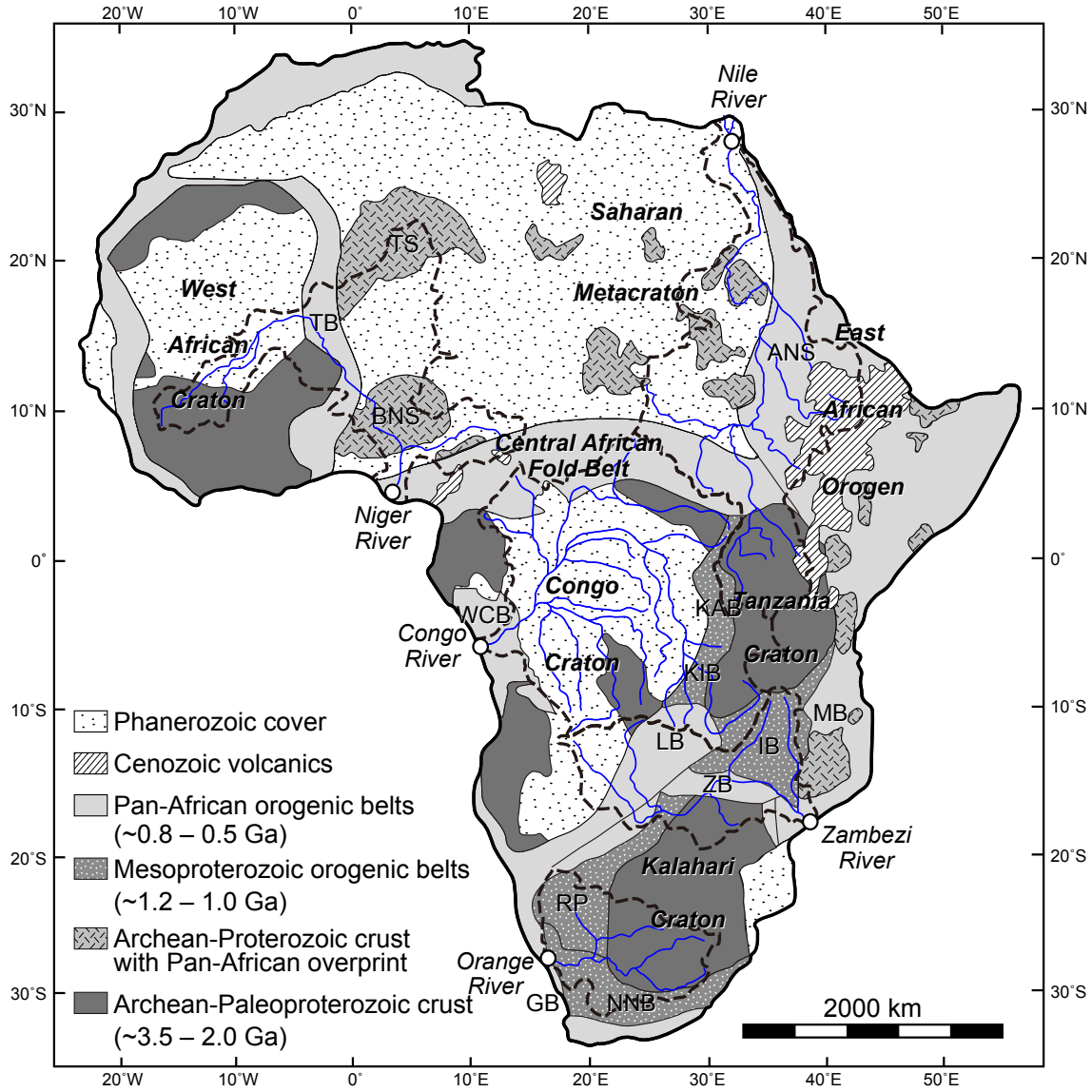

Fig. 5-1. Simplified geological map of Africa (modified after Kampunzu and Popoff, 1991, Tack et al., 2001, Begg et al., 2009 and Iizuka et al., 2013), with sampling locations (dots), major tributaries (blue lines), and drainage basin limits (broken lines) of the Niger, Nile, Congo, Zambezi and Orange Rivers. Abbreviations are as follows: TS, Tuareg Shield; TB, Trans-Saharan Belt; BNS, Benin-Nigeria Shield; ANS, Arabian-Nubian Shield; WCB, West Congo Belt; KAB, Karagwe-Ankole Belt; KIB, Kibaran Belt; Irumide Belt; MB, Mozambique Belt; ZB, Zambezi Belt; LB, Lufilian Belt; RP, Rehobothian Province; NNB, Namaqua-Natal Belt; GB, Gariep Belt.

5.2 Regional geology

The drainage basins of the Nile, Niger, Congo, Zambezi and Orange Rivers collectively occupy 40% surface area of the continental Africa (Fig. 1). The regional geology of the African continent is summarized below, with emphasis on the timing and nature of major orogenic events that occurred in the basement terranes of the drainage basin areas.

The Nile River runs through the north of the Tanzania Craton, the east of the Saharan Metacraton and the north of the East African Orogen. The Tanzania Craton mainly comprises Archean granitoids and greenstone belts (Leggo, 1974; Manya and Maboko, 2003; Manya et al., 2006; De Waele et al., 2008). U–Pb dating of zircons and monazites from the granitoids and metamorphic rocks in the north and east of the Tanzania Craton indicated that the basement rocks underwent multiple metamorphic events at ~2.6 Ga (Johnson et al., 2003), ~640–620 Ma (Sommer et al., 2003; Appel et al., 2005) and ~550 Ma (Cutten et al., 2006). The Saharan Metacraton was highly remobilized during the Pan- African Orogeny but is recognized as a craton by geological, geochronological and isotopic characteristics (Abdelsalam et al., 2002; Liégeois et al., 2013). Because the Saharan Metacraton is widely covered by Phanerozoic sediments, its basement geology especially in the central part is not known in detail. Yet, granitoids, high-grade metamorphic rocks and migmatites are patchily exposed (Abdelsalam et al., 2002; Küster et al., 2008; Shang et al., 2010; Liégeois et al., 2013) and zircon U–Pb dating indicated that the granitoid magmatism and high-grade metamorphism occurred at ca.

600 Ma (Shang et al., 2010). Furthermore, detrital zircon from sandstones from Libya show age peaks at 2750– 2500, 2200–1750, 1060–920 and 720–530 Ma (Meinhold et al., 2011). The Saharan Metacraton faces the East African Orogen that was formed by Neoproterozoic accretionary and collision type orogeny within the Gondwana (e.g., Stern, 1994; Meert, 2003; Johnson et al., 2011; Fritz et al., 2013; Johnson, 2014). The Arabian–Nubian Shield in the northern part of the East Africa Orogen is characterized by Neoproterozoic ophiolites and juvenile arcs that emplaced between 850 and 620 Ma and underwent granulite-facies metamorphism at 650–620 Ma, followed by granitic magmatism related to post-orogenic extension between 610 and 560 Ma (Johnson et al., 2011; Fritz et al., 2013; Johnson, 2014).

The Niger River flows through the west of the Saharan Metacraton and parts of the West African Craton, Trans-Saharan Belt and Central African Fold Belt. In the west area of the Saharan Metacraton, the Tuareg and Benin-Nigeria Shields are exposed. The Tuareg Shield mainly consists of Archean and Paleoproterozoic terranes and Neoproterozoic oceanic terranes, and was intruded by syn-tectonic Pan-African granites between 870 and 580Ma (e.g., Bertrand and Caby, 1978; Bertrand et al., 1986; Black et al., 1994; Paquette et al., 1998; Caby, 2003). The Benin-Nigeria Shield hosts Archean and Paleoproterozoic granitoids that were intruded by 670–580 Ma granites (Dada, 1998; Ferré et al., 2002; Ekwueme and Kröner, 2006). The West African Craton is made up of the northern and southern Archean–Paleoproterozoic domains separated by sedimentary basin. The Niger River basin covers the southern domain comprising an

Archean terrane in the west and Paleoproterozoic (2200–2100Ma) terrane in the east (Boher et al., 1992; Potrel et al., 1996; Lompo, 2010; Parra-Avila et al., 2015). The Trans-Saharan Belt is a collision zone between the West African Craton and Saharan Metacraton and comprises Neoproterozoic (~650–600 Ma) granitoids and high-grade metamorphic rocks (Ferré et al., 2002; Caby, 2003; Liégeois et al., 2003; Agbossoumondé et al., 2007; Goodenough et al., 2014). The initiation of this collision was diachronous (Kröner and Stern, 2004). The central African Fold Belt is a collisional belt between the Saharan Metacraton and Congo Craton and comprises Paleoproterozoic basement gneiss and Neoproterozoic granitoids and gneiss (Toteu et al., 2004; Van Schmus et al., 2008; Bouyo Houketchang et al., 2013, 2015). In the western part of the orogenic belt, where the Niger River runs, granulites and granitoids are exposed (Ferré et al., 2002; Toteu et al., 2004; Bouyo Houketchang et al., 2013, 2015) and these rocks are considered to have been formed by crustal thickening during the collision between the two cartons at ~640–600 Ma (Toteu et al., 2004; Van Schmus et al., 2008; Bouyo Houketchang et al., 2009, 2013, 2015).

The Congo River drains through two cratons (the Congo Craton and southern Tanzania Craton) and four orogenic belts (the southern Central African Fold Belt, Karagwe–Ankole Belt, Kibaran Belt and West African Belt). The Congo Craton is widely covered by Phanerozoic sediments and its basement outcrops only in four shields along the edge of the craton. The basement rocks mainly consist of Paleo- and Neoarchean tonalites-trondhjemites-grano diorites (TTGs) and metamorphic rocks

intruded by Neoarchean and Paleoproterozoic felsic rocks (Walraven and Rumvegeri, 1993; Tchameni et al., 2000, 2001; Shang et al., 2004; Batumike et al., 2009). U–Pb dating of detrital zircons from the central part of the craton (Batumike et al., 2009) revealed a significant Pan- African age peak (850–580 Ma), but little Pan-African granitoids have been found within the craton. The southern part of the Tanzania Craton includes Paleoproterozoic high-grade metamorphic rocks (ca. 2.0 Ga), syn- and post-tectonic granitoids (2.0–1.8 Ga) and metasedimentary rocks (Reddy et al., 2003; Collins et al., 2004; Sommer et al., 2005). The Congo Craton is mantled by the Central African Fold Belt to the north. The southern part of the belt, covered by the Congo River, is characterized by continuous granulite belts with ages of ~640–600 Ma (Pin and Poidevin, 1987; Toteu et al., 2004; Owona et al., 2012; Bouyo Houketchang et al., 2013). The Karagwe–Ankole and Kibaran Belts are located between the Congo and Tanzania Cratons (Tack et al., 2010). The Karagwe–Ankole Belt consists of Archean–Paleoproterozoic basements, whereas the Kibaran Belt consists of Mesoproterozoic basements (Kokonyangi et al., 2004; Tack et al., 2010; Fernandez-Alonso et al., 2012; Koegelenberg et al., 2015). The West Congo Belt is located in the west of the Congo Craton and near the Congo River mouth. The Paleoproterozoic basement of the West Congo Belt is unconformably overlain by Neoproterozoic rocks (Tack et al., 2001). Zircon U–Pb dating indicated the main deformation and metamorphism of the basement rocks occurred at ~570–540 Ma, likely resulting from the collision between the Congo

Craton and São Francisco Craton of Brazil (Tack et al., 2001; Frimmel et al., 2006; Monié et al., 2012).

The Zambezi River runs through orogenic belts among the Tanzania, Congo and Kalahari Cratons: the Irumide, Lufilian, Zambezi and Mozambique Belts. The Irumide Belt consists of 2.7 and 2.0– 1.9 Ga basement rocks and overlying 1.85 Ga supracrustal rocks, which were intruded by various granitoids and underwent peak metamorphism at 1.1–1.0 Ga (Johnson et al., 2005, 2007a; De Waele et al., 2006, 2009). The Lufilian Belt has a complex mass of Paleoproterozoic granitoids and gneisses, which was overlain by Neoproterozoic to Cambrian volcano-sedimentary sequences and intruded by younger granites (Key et al., 2001; John et al., 2004; Johnson et al., 2005). Zircons from the granite intrusions and metamorphic monazites from the gneisses yielded U–Pb ages of ~565– 530 Ma (Hanson et al., 1993) and ~530 Ma (John et al., 2004), respectively. The ~530 Ma magmatism and metamorphism are considered as results of the collision between the Kalahari and Congo Cratons (Hanson et al., 1993; Porada and Berhorst, 2000; John et al., 2004; Johnson et al., 2005; Eglinger et al., 2014). The Zambezi Belt has Mesoproterozoic basements, comprising gneisses and granites that are unconformably overlain by metamorphic and sedimentary rocks. The supracrustal rocks were intruded by granitic rocks at ~820 Ma, possibly related to the continental rifting causing the dispersal of Rodinia (Johnson et al., 2007b). In the Zambezi and Lufilian Belts, eclogites are exposed and yielded Sm–Nd ages of ~600 Ma (John et al., 2003). Besides, metamorphic zircon ages of ca. 530Ma have been reported from these belts

(Goscombe et al., 2000; John et al., 2004). Moreover, metasedimentary and metabasic rocks in the Lufilian belt yielded a garnet-whole rock Lu–Hf isochrones age of ca. 530 Ma (Eglinger et al., 2016). These results suggest the collision between the Congo and Kalahari Cratons at ca. 530 Ma (John et al., 2004). The southern Mozambique Belt continues eastward from the Zambezi Belt. In the Mozambique Belt, the two distinct age groups are recognized. The northeastern domain is characterized by granulite-facies metamorphism and coeval deformation around ~650–610 Ma; by contrast, the southeastern domain is characterized by granulite- to amphibolite-facies metamorphism and granitic magmatism later than ~550 Ma (Bingen et al., 2009; Thomas et al., 2010; Ueda et al., 2012a,b; Fritz et al., 2013). The former is attributed to the collision between the southeast Africa and the fragments of East Gondwana (Meert, 2003; Collins and Pisarevsky, 2005). The latter is considered to represent the timing of crustal thickening and subsequent post-collisional extension possibly due to asthenosphere upwelling following lithospheric delamination (Jacobs et al., 2008a; Viola et al., 2008; Ueda et al., 2012a,b).

The Orange River runs through the Kalahari Craton, Rehobothian Province and Namaqua–Natal Provinces and Gariep Belt. The Kalahari Craton mainly comprises granitoids with intrusion ages between 3.67 and 2.55 Ga (Poujol et al., 2003; Singletary et al., 2003; Schmitz and Bowring, 2004; Jacobs et al., 2008b), which are overlain by Archean Witwatersrand sedimentary rocks (2.95– 2.71Ga), Paleoproterozoic sedimentary rocks of the Transvaal Supergroup (2.55–2.08 Ga) and Karoo sedimentary

rocks (300– 120 Ma) (Catuneanu et al., 2005; Eriksson et al., 2006; Zeh et al., 2016). The northern and western margins of the craton are further covered by Phanerozoic sediments (Jacobs et al., 2008b). The Namaqua–Natal Province contains 1.2–1.0 Ga gneisses and granitic intrusions (Thomas et al., 1994; Robb et al., 1999; Cornell and Pettersson, 2007) and is considered to be accreted to the Kalahari Craton by ~1100–1050Ma during the Rodinia supercontinent amalgamation (Jacobs et al., 2003, 2008b; McCourt et al., 2006). The Rehoboth Province includes late Paleoproterozoic (~1.9–1.7 Ga) gneisses and granites (Van Schijndel et al., 2014) and Mesoproterozoic (~1.2–1.0Ga) meta-sedimentary, volcanic and intrusive rocks (Becker et al., 2005, 2006). The late Paleoproterozoic thermal events are interpreted as resulting from the collision between the Rehoboth Province and Kalahari Craton (Jacobs et al., 2008b). The Rehobothian Province is rimmed by the Gariep Belt which consists mainly of Neoproterozoic sedimentary sequences and oceanic crust. The Gariep Belt further under- went low-grade metamorphism, followed by ~500Ma granite intrusions (Frimmel, 2000). The timing of the metamorphism is determined to be 570–540Ma by hornblende Ar–Ar dating (Frimmel and Frank, 1998; Gray et al., 2008), suggesting the collision between the Kalahari Craton and South America at that time (Frimmel and Frank, 1998; Kröner and Stern, 2004; Gray et al., 2008).

Overall, two main periods are recognizable for Pan-African orogenic events in the African continent (Fig. 5-2): the older one at 640–600 Ma corresponding to the period

of the East African Orogeny and the younger one at 570–530 Ma often referred to as the Kuungan Orogeny (e.g., Meert, 2003; Fritz et al., 2013) (Fig. 5-2).

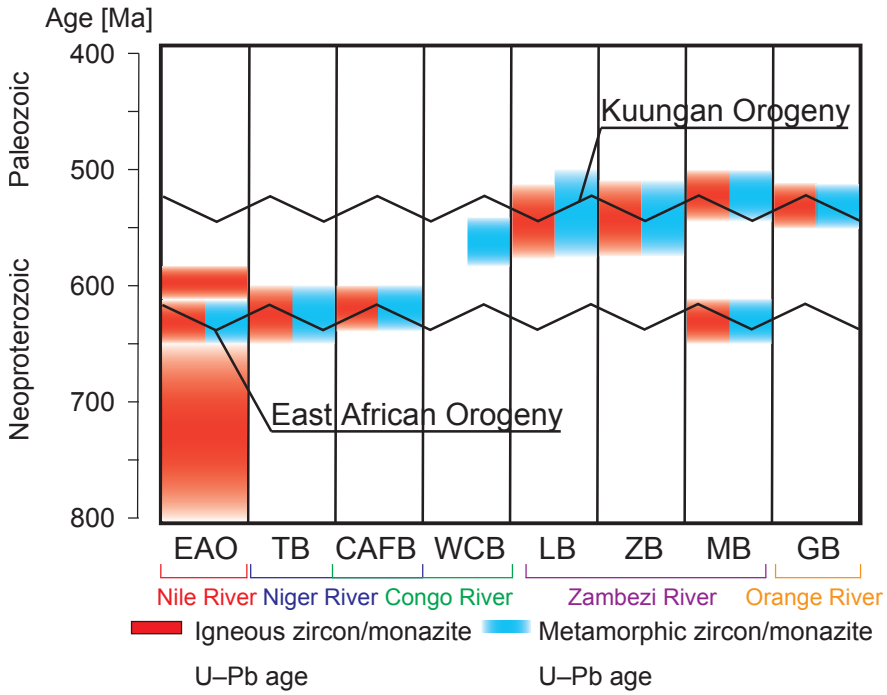

Fig. 5-2. Simplified summary of the major magmatic and metamorphic events/periods in the different orogenic belts related to the Pan-African Orogeny, ranging from 800 Ma to 400 Ma discussed in this paper. Abbreviations and references are as follow: EAO = East African Orogen, Stern (1994); Meert (2003); Stern et al. (2010); Johnson et al. (2011); Fritz et al. (2013); TB = Trans-Saharan Belt, Ferré et al. (2002); Caby et al. (2003); Liégeois et al., 2003; Agbossoumondé et al. (2007); Goodenough et al. (2014); CAFB = Central African Fold Belt, Pin and Poidevin (1987); Toteu et al. (2004); Owona et al. (2012); Bouyo Houketchang et al. (2013); WCB = West Congo Belt, tack et al. (2001); Frimmel et al. (2006); Monié et al. (2012); LB = Lufilian Belt, Hanson et al. (1993); Porada and Berhorst (2000); John et al. (2004); Eglinger et al., 2016; ZB = Zambezi Belt, Goscombe et al. (2000); John et al. (2002); John et al. (2004); Johnson et al. (2005); Grantham et al. (2013); MB = Mozambique Belt, Bingen et al. (2009); Fritz et al. (2013); GB = Gariep Belt, Frimmel and Frank (1998); Frimmel (2000); Gray et al. (2008).

5.3 Samples and analytical methods

The river sand samples were collected at or near the mouths of the Nile (NIL), Niger (NGR1), Congo (CNG2), Zambezi (ZMB2) and Orange (ORG2) Rivers (Fig. 5-1, Table 5-1). These samples were previously used for zircon U–Pb dating and Hf (–O) isotopic studies (Iizuka et al., 2010a, 2013). For this study, monazite grains were newly concentrated from the river sand samples using the conventional magnetic and heavy liquid separation techniques. The analyzed monazite grains were randomly hand-picked from the aliquots of monazite concentrates to reduce sampling bias and mounted in epoxy resin. Before analysis, each grain was investigated by back-scattered electron (BSE) imaging to check internal zoning structures and the presence of inclusions. The BSE images were obtained using a JEOL JSM-7000F at the Department of Earth and Planetary Science, The University of Tokyo. An accelerating voltage of 10 kV, an emission current of 20 nA, and a working distance of 10 mm were used.

Table 5-1. Summary of the samples used in this study

Sample	River	Sample locality
NGR1	Niger	6°08’05’’N, 6°45’19’’E
NIL	Nile	Near Cairo City
CNG2	Congo	40°17’08’’S, 15°27’29’’E
ZMB2	Zambezi	17°48’33’’S, 35°23’39’’E
ORG2	Orange	28°30’25’’S, 16°37’’07’’E

The U–Pb ages were measured with an ELEMENT-XR inductively coupled plasma-mass spectrometer (ICP-MS) attached to a 200 nm femtosecond laser ablation (LA) system at the Department of Solid Earth Geochemistry, Japan Agency for Marine-Earth Science and Technology. We measured ^{202}Hg, ^{204}(Pb + Hg), ^{206}Pb, ^{207}Pb, ^{208}Pb, ^{232}Th and ^{238}U using secondary multiplier with the counting mode. Because signals of ^{232}Th as well as ^{208}Pb during most sample analyses exceeded the maximum dynamic range of the counting mode, however, we report only U–Pb ages in this paper. For laser ablation sampling, a rotation raster ablation protocol (Kimura et al., 2011, 2015) was used to reduce elemental fractionation due to defocusing. In this protocol, a 10 μm laser beam with ~6 J/cm was rotated along a circumference of a circle with a 5 μm radius at a velocity of 2.1 μm s^{-1} and 3 Hz, resulting in a ~20 μm ablation pit. Each analysis consists of 30 s gas blank measurements and following ca. 90 s with laser ablation sampling. These measurements were carried out using a time resolved analytical (TRA) procedure, in which a temporal change in signal intensity is monitored to check a possible age variation within the ablation pit. Unknown samples were analyzed in runs of 6–10 analyses, bracketed by 2 analyses of the reference monazite 44069. The results of the bracketing analyses of the reference monazite 44069 (424.9 ± 0.4 Ma: Aleinikoff et al., 2006) were used to correct for the instrumental mass bias and Pb/U fractionation. Analytical uncertainties of each spot analysis combine the internal precisions (2 SE: two-standard error) and the reproducibility (2 SD: two-standard deviation) of the bracketing standard analyses, added in quadrature. Common Pb was

corrected using the ^{204}Pb method (Williams, 1998) when the ^{204}Pb signal was detectable (higher than 3 SD of back ground measurements); otherwise no common Pb correction has been made. The precision and accuracy of our monazite U–Pb dating were evaluated by analyzing the monazite Manangotry and 16-F-6 standards, whose U–Pb ages were previously determined by the isotope dilution-thermal ionization mass spectrometry (555 ± 2 Ma for Manangotry and 2842.9±0.3Ma for 16-F-6, Horstwood et al., 2003; Simonetti et al., 2006). The mean U–Pb ages obtained for these standards during the course of this study are consistent with the previously reported values: $^{206}Pb/^{238}U$ age of 557 ± 4 Ma and $^{207}Pb/^{206}Pb$ age of 568 ± 24Ma for Manangotry (n=18) and $^{206}Pb/^{238}U$ age of 2823 ± 20 Ma and $^{207}Pb/^{206}Pb$ age of 2849 ± 7 Ma for 16-F-6 (n = 40) (Appendix Table S5-1).

Abundances of Si, P, Ca, Y, La, Ce, Nd, Pr, Sm, Th and U of monazite grains were determined by field emission–electron probe microanalysis (FE-EPMA) using a JEOL JXA-8530F at the Department of Earth and Planetary Science, The University of Tokyo. We used the following standard materials: $MnSiO_4$ (Si, Ka), $CaSiO_3$ (Ca, Ka), $LaPO_4$ (P, Ka; La La) $Y_3Al_5O_{12}$ (Y, La), $CePO_4$ (Ce, La), $PrPO_4$ (Pr, Lß), $NdPO_4$ (Nd, La), $SmPO_4$ (Sm, Lß), ThO_2 (Th, Ma) and UO_2 (U, Mß). The operating conditions were a beam diameter of 5 μm, a probe current of 30 nA, and an accelerating voltage of 25 kV. The FE-EPMA analytical pits were placed within the same zones dated by LA-ICP-MS, closed to the produced laser pits.

Geochemical analyses of monazite grains were further performed using a CETAC LSX-213 G2+ Nd:YAG LA system coupled with an iCAP Q ICP-MS at the Department of Earth and Planetary Science, The University of Tokyo. The following elements were measured: Ca, Sr, Y, La, Ce, Pr, Nd, Sm, Eu, Gd, Tb, Dy, Ho, Er, Tm, Yb, Lu, Th and U. The LA system is equipped with the active two- volume HelExTM Cell (Eggins et al., 2005), in which the effective cell volume is so small (~2.5 cm^3) that aerosol deposition around the ablation pit is minimized. The data were obtained from ~20 lm ablation pits with a laser fluence of 20 J/m2, repetition rate of 3 Hz, cooling gas of 14 L/min and sampling gas of ~0.9 L/min. The laser ablation site was placed on the pit for the FE-EPMA analysis next to the pit for the U–Pb dating. All analyses consist of 20 s baseline measurements and following ca. 40 s measurements with laser ablation sampling, using the TRA procedure. Six to eight analyses of unknown samples were bracketed by four analyses of NIST SRM 610 glass. The Ce concentrations determined by FE-EPMA were used as an internal standard. The other element concentrations were determined using the sensitivity factors relative to Ce obtained from the results of NIST SRM 610 glass analyses (Pearce et al., 1997). Because monazite is highly enriched in LREEs relative to heavy-REEs (HREEs), oxide interferences of L-REEs on H-REEs can be problematic. We corrected for the oxide interferences by monitoring $^{232}Th^{16}O^{+}/^{232}Th^{+}$ (typically ~0.5%) and $^{238}U^{16}O^{+}/^{238}U^{+}$ (typically ~0.4%) and using the correlation between oxide production rate and oxide bond energy (Aries et al., 2000; Kent and Ungerer, 2005).

5.4 Results

The internal structures (e.g., chemical zoning) and U–Pb isotopic data of detrital monazites are provided in Appendix Table S5-2. The internal structures were classified into the following four types (the number in parenthesis indicates the proportion of each type of grains): (1) core/rim structure (10%), (2) patchy structure (30%), (3) mosaic structure (16%) and (4) unzoned (44%) (Fig. 5-3). We defined the mosaic structure as a fine-scale zoning structure relative to analytical spatial resolution of U–Pb dating. Among 523 detrital monazites analyzed for U–Pb isotopes, a grain (CNG2-mnz-70) cannot be dated because of the extremely low U content and this is not included in the discussion below. The U–Pb data for detrital monazites of each river (Used data in Table S5-2) are plotted on Tera-Wasserburg concordia diagram (Fig. 5-4). Some grains yielded highly discordant data, which could be attributed to partial Pb-loss during metamorphism and to mixing analysis of multiple age domains. Because, inaccurate U–Pb ages would result in artificial age peaks, we have used only the data that yield either concordant U–Pb ages within analytical uncertainty or those with <5% discordance for the following discussion. For all studied rivers, approximately 70% of the dated monazite grains satisfy the criteria and the results are shown in the $^{206}Pb/^{238}U$ age histograms (Fig. 5-5).

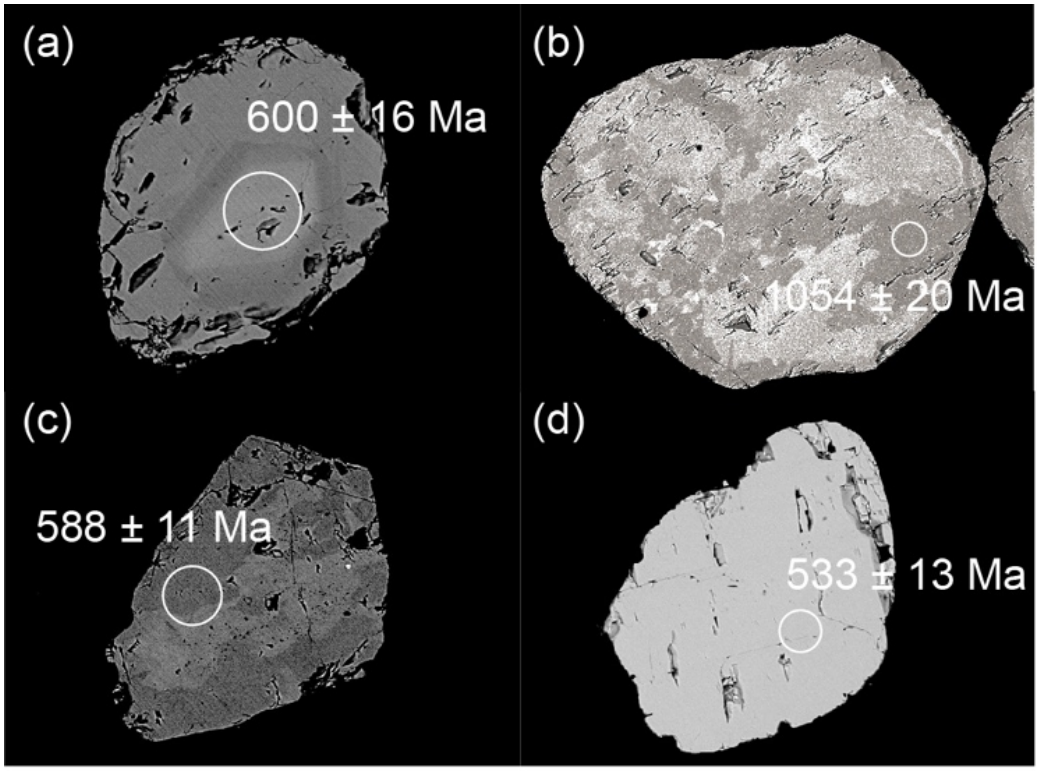

Fig. 5-3. Representative BSE images of detrital monazites from the African studied rivers. (a) NGR1-mnz-4; core-rim structure, (b) ORG2-mnz-105; patchy structure, (c) NGR1-mnz-89; mosaic structure and (d) NGR1-mnz-8; unzoned. White circles represent analytical sites with ~20 μm diameters for U–Pb dating.

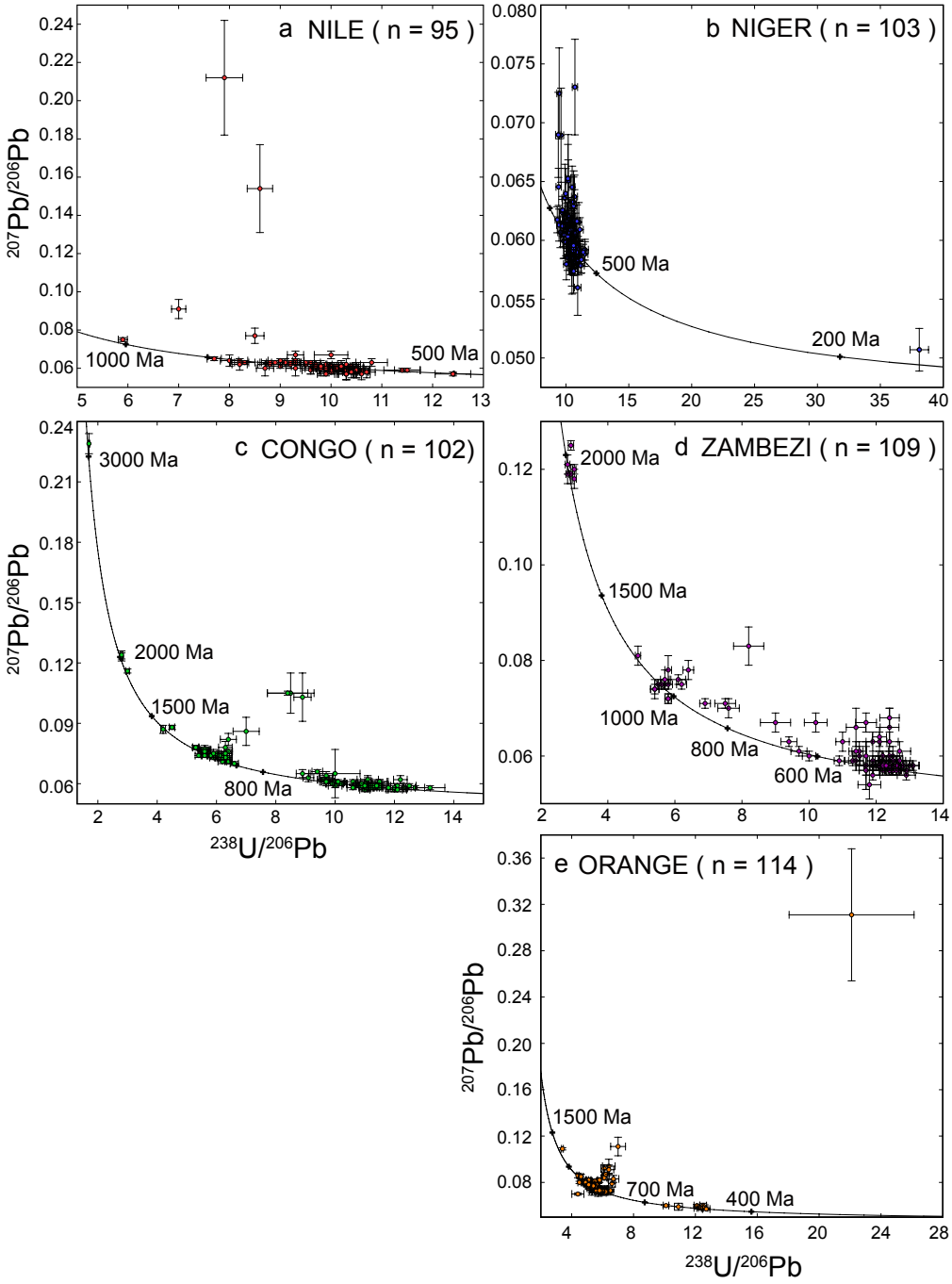

Fig. 5-4. Tera-Wasserburg concordia plots of U–Pb isotopic data for detrital monazites from the (a) Nile River, (b) Niger River, (c) Congo River, (d) Zambezi River and (e) Orange River, respectively. Error bars represent 2σ quoted in Appendix Table S5-2.

For all studied rivers except for the Orange, the detrital monazites are dominated by grains having U–Pb ages between 800 and 400 Ma (Fig. 5-5a–e). However, the monazite populations of the four rivers show distinct Pan-African age peaks (Fig. 5-5f). We see no clear difference in age distribution among grains having different types of internal structure. The detrital monazites from the Nile River (n = 78) have U–Pb ages ranging from 780 to 530 Ma with a peak at ~600 Ma (Fig. 5-5a, f). The U–Pb ages of detrital monazites from the Niger River (n = 73) are mainly between 650 to 530 Ma and exhibited a broad peak around ~580 Ma (Fig. 5-5b, f). The Congo River monazites (n = 71) include the oldest (3015 Ma) grain and define two small age peaks at ~630 and ~610 Ma and a main peak at ~560 Ma (Fig. 5-5c, f). The monazite age population of the Zambezi River (n = 68) spans the range from 1960 to 480 Ma and a prominent peak at ~500 Ma (Fig. 5-5d, f). The U–Pb ages of the

Orange River monazites (n = 88) are characterized by a dominant population between 1200 and 900 Ma, corresponding to the timing of the Grenville Orogeny (Fig. 5-5e).

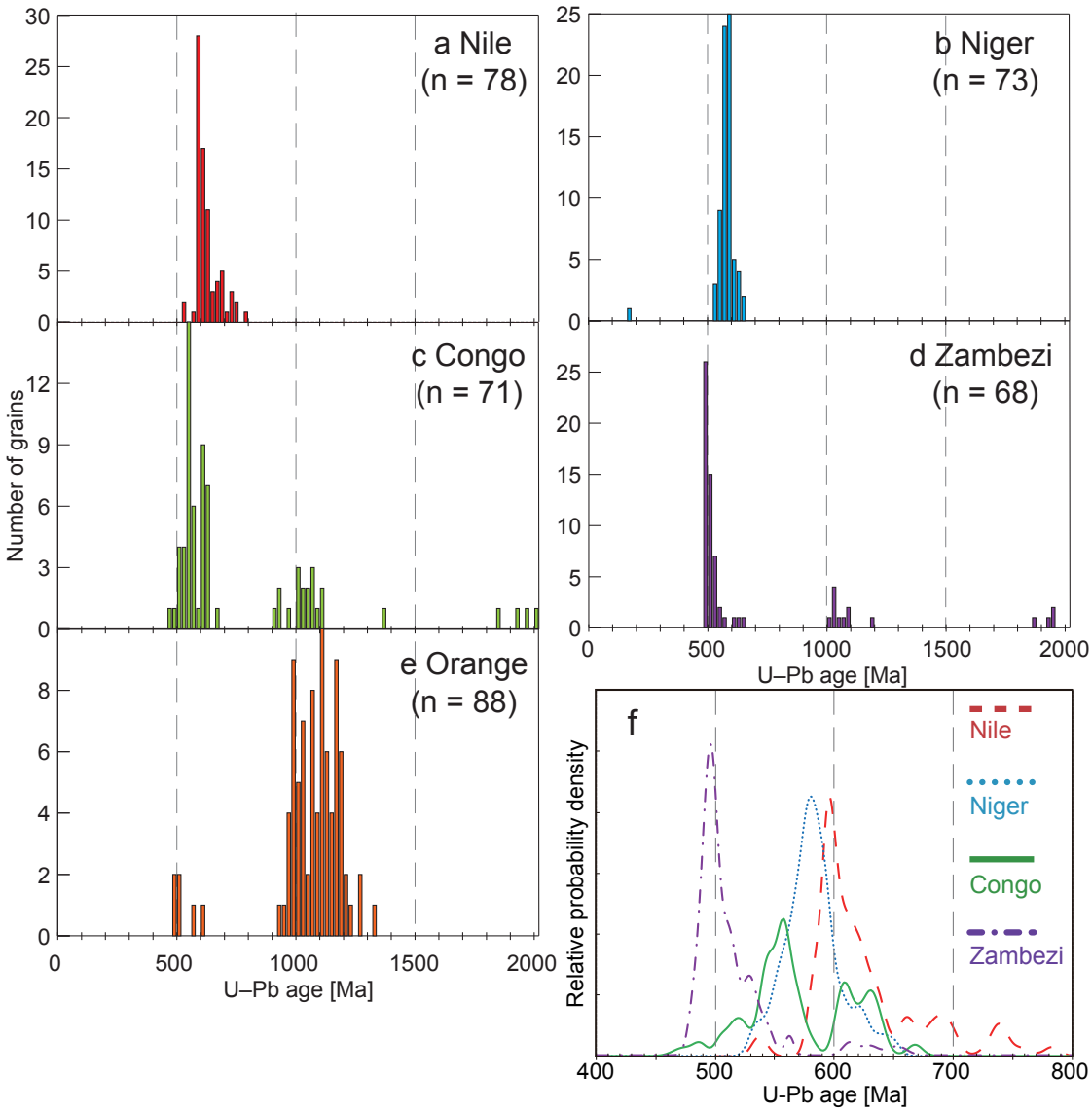

Fig. 5-5. $^{206}Pb/^{238}U$ age histograms of the detrital monazites from the (a) Nile River, (b) Niger River, (c) Congo River, (d) Zambezi River and (e) Orange River, respectively. (f) Probability density graph of the four rivers except for the Orange River during 800–400 Ma. The concordant or <5% discordant data are included.

The elemental abundances determined by FE-EPMA and LA-ICP- MS are listed in Appendix Table S5-3. For the elements analyzed by both FE-EPMA and LA-ICP-MS, we compare the resultant abundances in Appendix Fig. S5-1. While the two data sets generally show good agreement, substantial discrepancies are observed in some grains especially for Ca and U. The discrepancies may be attributed to the different spatial resolution of the two analytical techniques. For the following discussion, we have essentially used the LA-ICP-MS results, because the analytical spatial resolution of LA-ICP-MS U–Pb dating is similar to that of LA-ICP-MS elemental analysis. In Fig. 5-6, however, the FE-EPMA data are shown as a cation plot, normalized to 16 oxygens. The LA-ICP-MS data are graphically presented for each river in Figs. 5-7 and 5-8 as plots of CI-chondrite normalized (McDonough and Sun, 1995) $[Gd/Lu]_N$ vs. $[Eu/Eu^*]_N$ and Th contents, respectively (brackets with subscript N denote CI-chondrite normalized value, $[Eu/Eu^*]_N$ defined by $[Eu]_N/([Sm]_N * [Gd]_N)^{0.5}$). The $[Gd/Lu]_N$ and $[Eu/Eu^*]_N$ reflect the degrees of HREE fractionation and Eu anomaly, respectively. When the $[Gd/Lu]_N$, $[Eu/Eu^*]_N$ and Th contents are displayed together in a 3D plot (each ratio on one axis) (Fig. 5-9), it is evident that the detrital monazites from the five rivers plot preferentially along the x- and y-axes and show a variation in these parameters. The proportion of the grains having $[Gd/Lu]_N$ of >400 varies substantially from river to river as well as among the different age populations (Fig. 5-7). For instance, the proportions are approximately one-third for the 500–480 Ma Zambezi and 640–600 Ma Congo populations, but less than one-tenth for the 600–560 Ma Niger

population. The grains containing <1wt% Th are yielded by the Nile, Congo, Zambezi, and Orange Rivers (Figs. 5-8). The low-Th monazite grains account for ~2% of all grains.

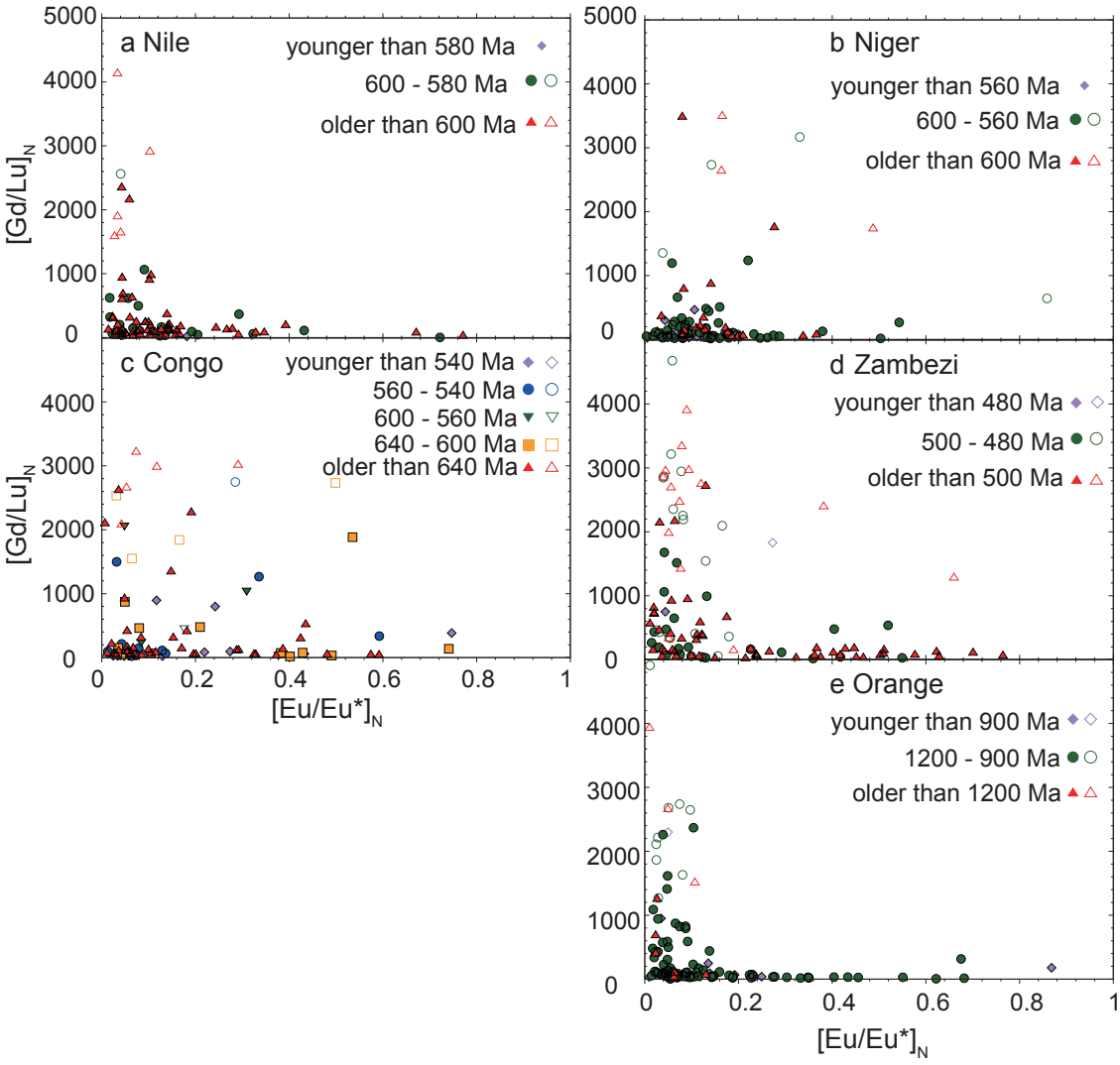

Fig. 5-7. Plots of $[Gd/Lu]_N$ vs. $[Eu/Eu^*]_N$ for detrital monazites from the (a) Nile River, (b) Niger River, (c) Congo River, (d) Zambezi River and (e) Orange River, respectively. The plots are coded according to U–Pb ages. The open symbols represent monazites having Lu contents below the analytical detection limit and therefore, should be regarded as lower limits of the actual values.

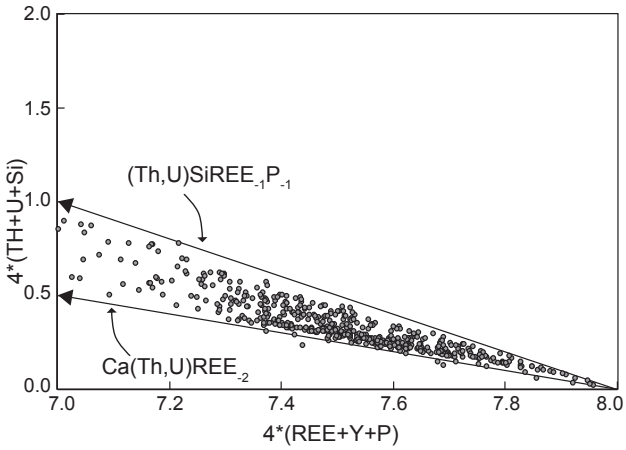

Fig. 5-6. Monazite cation plot, normalized to 16 oxygens. Huttonite exchange [(Th, U)SiREE$_{-1}$P$_{-1}$] and Cheralite exchange [Ca(Th, U)REE$_{-2}$] are represented as vectors.

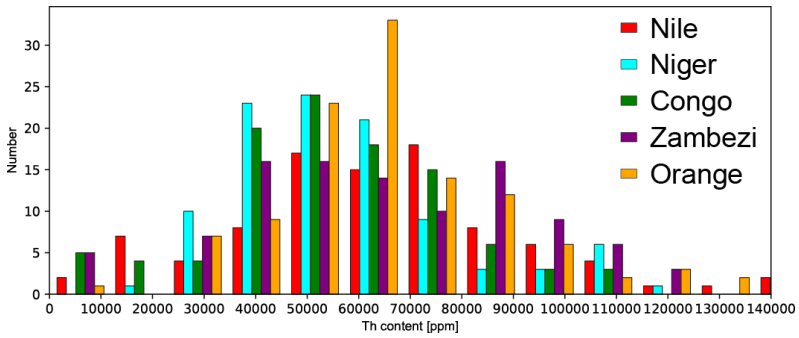

Fig. 5-8. Histogram of Th contents for detrital monazites from the five largest African rivers. Most grains contain more than 1wt% Th.

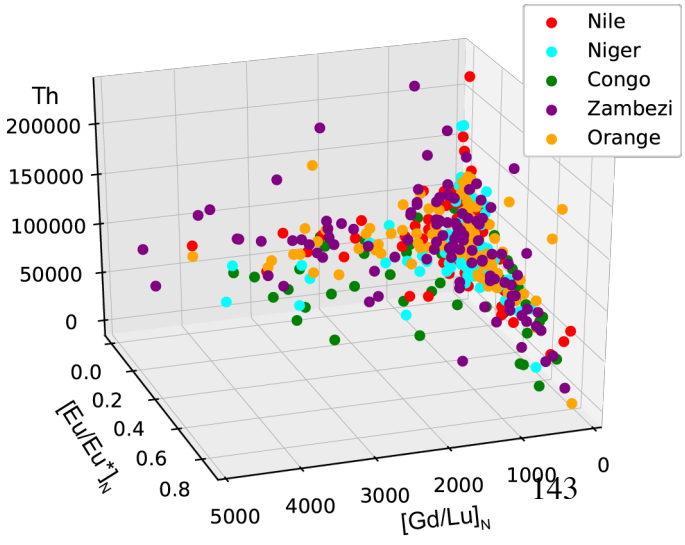

Fig, 5-9. A 3D plots of [Eu/Eu*]$_N$ vs. [Gd/Lu]$_N$ vs. Th content for detrital monazites from the five largest African rivers.

5.5 Discussion

5.5.1 Geochemistry and genesis of the detrital monazites

The significant variation in major element compositions of the detrital monazites from the African rivers (Fig. 6) can be well explained by substitutions of Ca^{2+} + (Th, U)$^{4+}$ = 2REE^{3+} (cheralite substitution) and (Th, U)$^{4+}$ + Si^{4+} = REE^{3+} + P^{5+} (huttonite substitution) (Zhu and O'Nions, 1999, Pyle et al., 2001; Spear and Pyle 2002, Hoshino et al., 2012). Moreover, the detrital monazites plot preferentially along the cheralite substitution line rather than the huttonite substitution line. It has been indicated that the cheralite substitution is predominant in metamorphic monazites (Spear and Pyle 2002), whereas huttonite substitution is more common in magmatic monazite (Broska et al., 2000; Hoshino et al., 2012). The major element geochemistry, therefore, suggests that the detrital monazites were derived from various source rocks and a substantial proportion of them are metamorphic origin.

The significant variations in $[Gd/Lu]_N$ with the increasing negative Eu anomaly ($[Eu/Eu^*]_N$) are the most striking geochemical feature of the detrital monazites from the African rivers (Figs. 5-7). The understanding of the geochemical systematics can help in constraining the genesis of the detrital monazites. Below, I briefly review possible mechanism controlling the variation in geochemical compositions of monazite again, as discussed in the previous chapter.

Europium is unique among REEs in that it can exist as both trivalent and divalent under crustal condition and Eu^{2+} is incorporated into plagioclase and K-feldspars more selectively than other trivalent REEs (Fujimaki and Tatsumoto, 1984; Bea et al. 1994; Bea, 1996). Both plagioclase and K-feldspar are major phases in low-Ca felsic rocks and the former would be residual during the parental magma genesis and also fractionate during the magma differentiation. As result, igneous monazites commonly have pronounced Eu negative anomalies ($[Eu/Eu^*]_N$ of <0.1; shown in Chapter 3). Feldspars are common also in metamorphic rocks and their abundances change with metamorphic grade and chemical composition, leading to variable degrees of Eu negative anomaly in metamorphic monazites. For instance, higher-grade meta-sedimentary rocks contain more abundant K-feldspar due to the continuous breakdown of micas during prograde metamorphism, resulting in more prominent Eu negative anomalies in the monazites (Rubatto et al., 2006).

The observed $[Gd/Lu]_N$ variation spanning three orders of magnitude (Fig. 5-7) is primary due to variable Lu concentrations down to ~1 ppm. The strong depletion in H-REEs including Lu would require the co-existence of minerals having much higher distribution coefficients for HREEs than for LREEs such as garnet and zircon (e.g., Schnetzler and Philpotts, 1970; Fujimaki and Tatsumoto, 1984; Hinton and Upton, 1991; Bea, 1994). In particular, garnet is so abundant in high-grade and sometimes medium-grade metamorphic rocks that the co-existing monazites can exhibit significant

H-REE depletion (Rubatto et al., 2006; Buick et al., 2010; Iizuka et al., 2010b; Mottram et al., 2014; Štípská et la., 2015).

The Th content in monazite are basically governed by cheralite and huttonite substitutions as a solid solution. Although igneous and metamorphic monazites show wide range of Th contents due to the change in co-existing assemblages (e.g., Xie et al., 2006; Kelts et al., 2008; Breiter et al., 2009; Rubatto et al., 2006), it has been reported that hydrothermal monazite is characterized by extremely low Th abundances beyond the range which igneous and metamorphic monazites form (shown in Chapter 3).

Overall, the observed variation in the REE and Th compositions of detrital monazites can be linked to their source rock type. The criteria determined in the previous chapter are used to interpret the genesis of the detrital monazite (Table 5-2). The studied detrital monazites are interpreted to be igneous ($[Eu/Eu^*]_N < 0.1$ and $[Gd/Lu]_N < 400$), garnet-rich metamorphic ($[Gd/Lu]_N > 400$), garnet-poor or garnet-rich metamorphic ($[Eu/Eu^*]_N > 0.1$ and $[Gd/Lu]_N < 400$), and hydrothermal origins (Th content < 1wt%). The interpreted grains as a hydrothermal origin is minor (~2%) in the studied river sands because of the low-Th contents (<1wt%) and scarce inclusions. Therefore, these hydrothermal monazites are not included in the following discussion.

Table 5-2. Geochemical criteria for an indicator of source rock type

Igneous	Metamorphic		Hydrothermal
	Garnet-poor	Garnet-rich	
$[Eu/Eu^*]_N < 0.1$ $[Gd/Lu]_N < 400$	$[Eu/Eu^*]_N > 0.1$ $[Gd/Lu]_N < 400$	$[Gd/Lu]_N > 400$	Th content $< 10^4$ ppm

5.5.2 Comparison with detrital zircon

The U-Pb age populations of detrital monazites and zircons combined for the five African rivers, where concordant or <5% discordant data are included, are compared in Fig. 5-10. Two distinct features are evident. First, the detrital monazite ages are rarely distributed in Archean and Paleoproterozoic times, whereas the detrital zircon ages indicate clear peaks in the period. Second, the peak at ~800 Ma is recognized in the zircon ages but not in the monazite ages.

Although the Pb diffusions in monazite and zircon are comparably slow, monazite can be more readily dissolved during metamorphism and abraded through weathering processes (Townsend et al., 2000; Williams, 2001; Rasmussen and Muhling, 2007, 2009; Harlov and Hetherington, 2010; Erickson et al., 2015). In addition, high-Ca felsic rocks commonly yield zircons but few monazites (Lee and Bastron, 1967; Montel, 1993; Kelts et al., 2008). Therefore, the discrepancy between the detrital monazite and zircon age distributions can be interpreted to reflect either the preferential disappearance of monazite through metamorphic/sedimentary processes or little occurrence of

monazite in high-Ca felsic magmatism. We consider the latter unlikely as a main reason for the lack of >1500 Ma detrital monazites because Hf–O isotopic data for the detrital zircons indicate their crystallization from geochemically evolved, and by extension, low-Ca felsic magmas (Iizuka et al., 2013). Instead, the scarcity of ancient monazites can be explained by dissolution-reprecipitation during the Pan-African as well as Grenville Orogeny and prolonged sedimentary recycling. In contrast, the unique detrital zircon age peak at ~800 Ma would be attributed to significant high-Ca magmatism, considering the juvenile Hf–O isotopic features of the 800–700 Ma detrital zircons (Iizuka et al., 2013) and the preservation of the Mesoproterozoic detrital monazites.

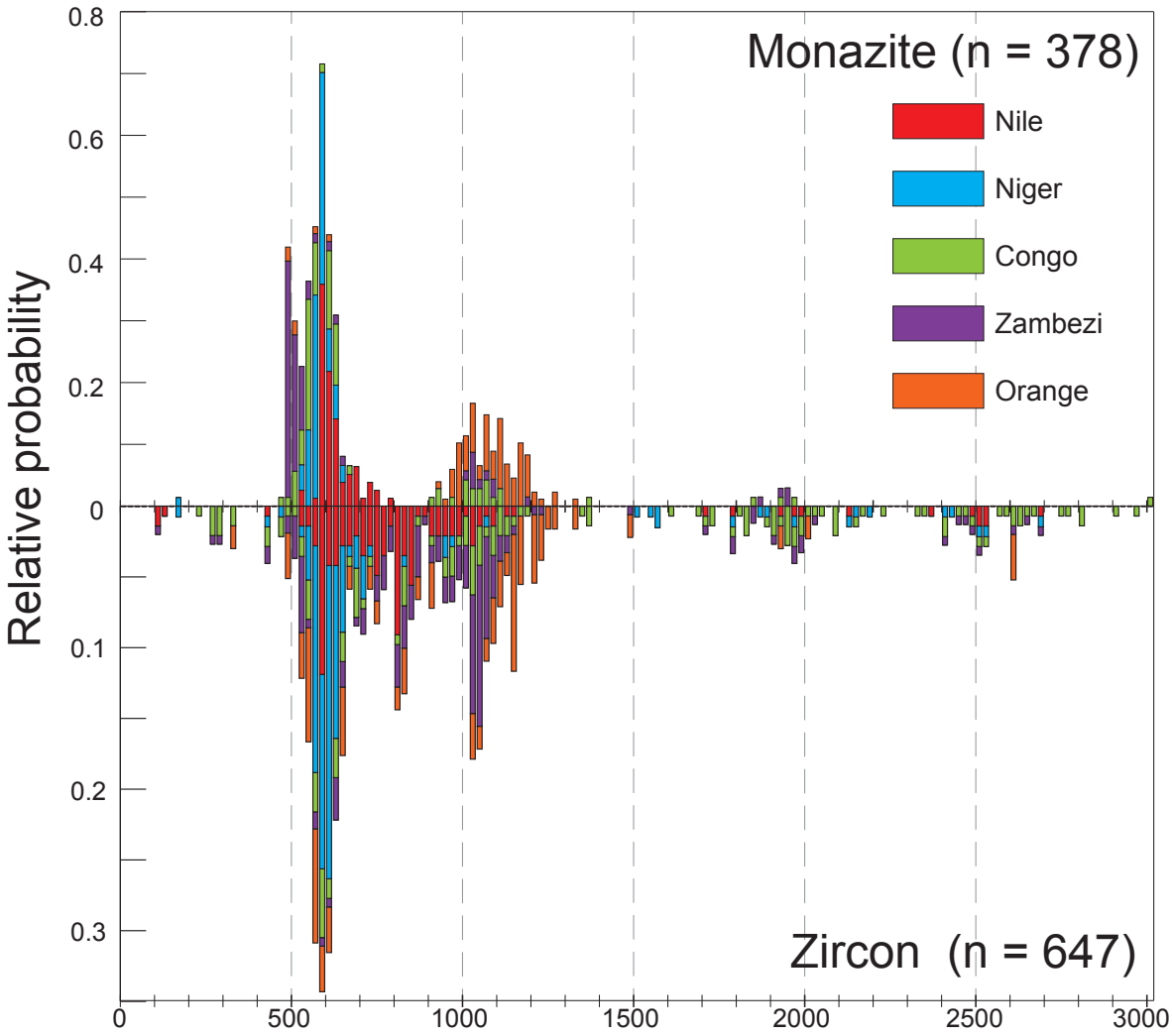

Fig. 5-10. Combined U–Pb age populations of detrital monazites (upper) and zircons (lower) from the five African rivers. The relative frequencies were calculated by accumulating the age proportions rather than the number of detrital grains from the five rivers. The detrital zircon data are from Iizuka et al. (2013).

When examining the Pan-African age distributions of the detrital monazites and zircons (concordant or <5% discordant) for each river (Fig. 5-11), we see that the monazite age peaks of the Niger, Congo and Zambezi Rivers are younger than the detrital zircon age peaks by 20–40 Myr, whereas in the Nile River the monazite and zircon age peaks are indistinguishable. These age gaps are larger than the analytical uncertainties (2SD: ± ~15 Ma and 2SE: ± ~4 Ma). Zircon and monazite U–Pb age gaps of ~20 Myr were previously identified for single metamorphic rocks (e.g., Fitzsimons et al., 1997; Zeh et al., 2003). Yet the detrital zircons analyzed by Iizuka et al. (2013) mostly have oscillatory zoning and Th/U ratios higher than 0.1, which are common characteristics of magmatic zircon (Shore and Fowler, 1996; Hoskin and Ireland, 2000; Rubatto, 2002). Thus, the detrital zircon age peaks should reflect the timing of major felsic magmatic events in the river basins. In contrast, the Pan-African monazite populations of the studied rivers consist of grains interpreted as metamorphic origins as well as igneous origin (Table 5-3 and Fig. 11). High proportions of grains derived from garnet-rich metamorphic rocks are prominent feature of the age population at 640–600Ma for the Congo river and the age population around ~500 Ma for the Zambezi river (Table 5-3). The discordance between the monazite and zircon age peaks is consistent with the large contributions from metamorphic monazites which are independently estimated by the geochemical indicator. Monazite age peaks, therefore, correspond to the timing of major metamorphic events as well as magmatic events. The implication is that during the early stages of the Pan-African Orogeny, felsic

magmatism was important probably due to pre- to syn-collisional subduction of oceanic plate (e.g., Hargrove et al., 2006) and, 20–40 Myr later, syn-collisional and post-collisional metamorphism became dominant. The metamorphism may result from crustal heating caused by asthenosphere upwelling associated with lithospheric delamination (Kay and Kay, 1993; Sacks and Secor, 1990; Massonne, 2005) or radioactive self-heating in a thickened crust (Beaumont et al., 2004; Jamieson et al., 2004). Indeed, numerical models for delamination (Krystopowicz and Currie, 2013) and radioactive self-heating (Jamieson et al., 2004) suggested that regional metamorphism occurs in several tens of million years after a continental collision, which is consistent with the gap between detrital zircon and monazite age peaks.

Table 5-3. Summary of geochemical data for detrital monazites from the five African rivers.

Age [Ma]		Nile River		Niger River		Congo River				Zambezi River		Orange River	
		All	600–580	All	600–560	All	640–620	620–600	560–540	All	500–480	All	900–1200
Igneous		42%	43%	44%	42%	42%	29%	42%	60%	10%	12%	34%	36%
Metamorphic	Garnet-rich	17%	13%	19%	20%	30%	71%	42%	7%	49%	58%	31%	29%
	Garnet-poor	40%	43%	36%	38%	24%	0%	42%	20%	35%	31%	34%	36%
Hydrothermal		1%	0%	0%	0%	4%	0%	0%	13%	6%	0%	1%	0%

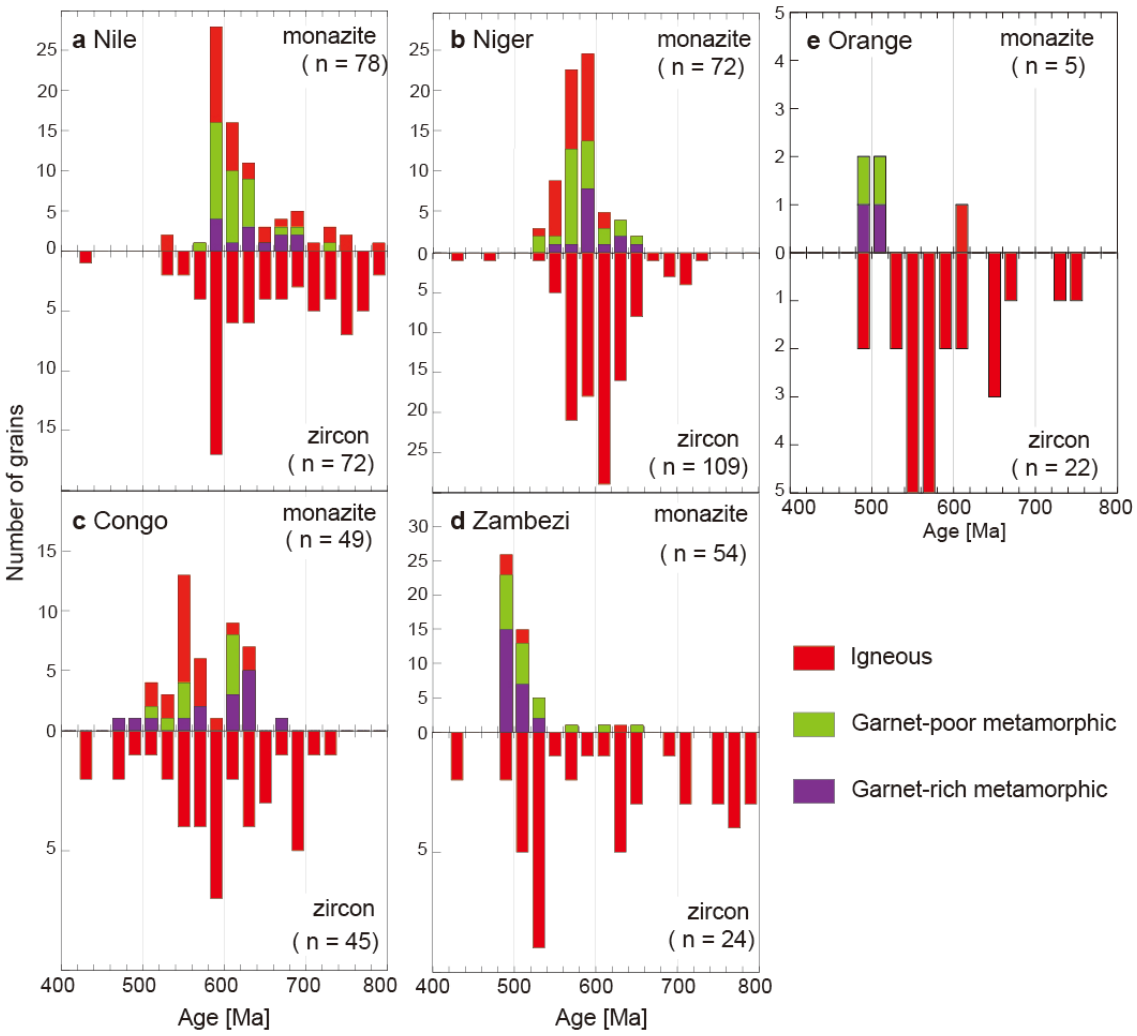

Fig. 5-11. Histograms of U–Pb ages between 800 and 400 Ma of concordant or <5% discordant monazites (upper) and zircons (lower) from the (a) Nile River, (b) Niger River, (c) Congo River, (d) Zambezi River and (e) Orange River, respectively. For the detrital monazites, columns are corded according to potential genesis inferred from the geochemical systematics (Section 5.1 and Table 2). All detrital zircons are interpreted as igneous origin on the basis of the internal structure and Th/U (Iizuka et al., 2013).

5.5.3 Constraints on the timing and nature of the Pan-African Orogeny

The detrital monazites from the Congo, Nile, Niger and Zambezi Rivers are dominated by grains of Pan-African U–Pb ages. Moreover, the Pan-African populations of the four rivers indicate distinctive age peaks (Fig. 5-5), highlighting the asynchrony of major orogenic events in the source terranes of the detrital monazites. Considering that detritus of the large African rivers would have been substantially recycled from older sedimentary rocks, there is a controversy on whether the source terranes properly correspond with the basements of the modern river basins. Nevertheless, because the areas drained by the older riverine systems would be, at least partly, overlapping with the modern river basins, it is reasonable to assume that the basements in the modern drainage basins are important sources of the detrital monazites. Accordingly, we discuss the implications of our results for the timing and nature of orogenic events in the drainage basins.

The oldest Pan-African age peak was obtained from the Congo River (Fig. 5-5f), whose drainage area covers parts of two Neoproterozoic orogenic belts, the Central African Fold Belt and the West Congo Belt (Figs. 5-1 and 5-2). The former belt includes 640–610 Ma granites and granulites with zircon U–Pb ages of ~650–600 Ma (Pin and Poidevin, 1987; Toteu et al., 2001; Owona et al., 2012), overlapping the Congo detrital monazite age peak at ~630 and ~610 Ma. The granulite-facies metamorphism has been interpreted as a result of the collision between the Congo Craton and the Saharan Metacraton (Kröner and Stern, 2004; Bouyo Houketchanget al., 2013). Our

geochemical data indicate that the 640–600 Ma detrital monazites are essentially of metamorphic origin and, in more detail, that the 640–620 Ma grains are derived mainly from garnet-bearing metamorphic rocks, whereas younger ones are sourced from garnet-absent metamorphic rocks (Fig. 5-11c). These results are consistent with the collision between the Congo Craton and Saharan Metacraton occurred between ~640 and 600 Ma and further suggest that the major mode of the metamorphism changed from higher-grade around ~630 Ma to lower-grade around ~610 Ma.

The U–Pb ages of the Congo River monazites indicate another significant peak at 550 Ma (Fig. 5-5f), which is delayed by 40 Myr from the Pan-African detrital zircon age peak (Fig, 5-11c). Similar ages (~570–540 Ma) were yielded by monazite U–Pb dating and clinopyroxene Ar–Ar dating of metamorphic rocks from the West Congo Belt, which have been interpreted as the timing of the collision between the Congo Craton and the São Francisco Craton of Brazil (Tack et al., 2001; Frimmel et al., 2006; Monié et al., 2012). Moreover, zircon U–Pb dating of the orogenic belt indicated zircon crystallization at >580 Ma and a significant zircon Pb-loss event at ~540 Ma (Monié et al., 2012), consistent with the detrital monazite and zircon records. Given that the detrital zircons are essentially of magmatic origin, whereas the ~550 Ma detrital monazites were mainly from granitic rocks (Fig. 5-11c), these detrital records may reflect significant high-Ca felsic magmatism at ~600 Ma due to the subduction of oceanic plates to the assembling the Congo and São Francisco Craton, followed by low-Ca felsic magmatism at ~550 Ma resulting from the collision of these cratons. If

that is the case, the igneous detrital monazite recorded the timing of S-type granite formation associated with continental collision.

The Nile River basin area largely covers the northern part of the East African Orogen, in particular the Arabian-Nubian Shield (Fig. 5-1). Integration of geological, geochronological and geochemical studies revealed that the shield was formed by accretion of juvenile arcs between 850 and 620 Ma, followed by emplacement of low-Ca felsic magmas during post-collisional extension at 610–560 Ma (Meert, 2003; Breitkreuz et al., 2010; Johnson et al., 2011; Fritz et al., 2013; Eliwa et al., 2014). Moreover, the northern part of the East African Orogen underwent peak metamorphic conditions up to granulite-facies at 640–620 Ma (Fritz et al., 2013). The crust formation of the accreted juvenile arcs is recorded by the Nile River zircons of ~840–700 Ma, but not by the monazites, reflecting the limited monazite crystallization during high-Ca felsic magmatism (Figs. 5-5f and 5-11a). Note that the monazite and zircon age peaks of the Nile are coincident, unlike the Niger, Congo and Zambezi. The correspondence of the monazite and zircon age peaks, together with the monazite geochemical features, can be well explained by major low-Ca felsic magmatism associated with metamorphism around 600 Ma in the drainage basins. This interpretation is consistent with the occurrence of low-Ca felsic rocks formed at 610–560 Ma (Johnson et al., 2011; Eliwa et al., 2014).

The Niger River runs through the central and southern parts of the Trans-Saharan Belt (Fig. 5-1). The ~650–600 Ma peraluminous granites and ~600–580 Ma metaluminous

granitoids were reported in the southern area (Ferré et al., 2002; Agbossoumondé et al., 2007; Key et al., 2012; Goodenough et al., 2014). The older granitic magmatism is attributed to the collision of the West African Craton and Saharan Metacraton accompanied by high-temperature metamorphism at ~640 Ma (Ferré et al., 2002; Caby et al., 2003; Liégeois et al., 2013), whereas the younger granitoid magmatism is ascribed to post-collisional extension with the emplacement of mantle-derived magma (Goodenough et al., 2014). In the central area, the continental collisions forming the Trans-Sharan Belt are marked by the voluminous granitic rocks of around 620–580 Ma (Boullier et al., 1986; Liégeois et al., 1987). The detrital monazite ages of the Niger River show a predominant distribution between 640 and 550 Ma with a peak at ~580 Ma (Fig. 5-5f). The age population ranging from 640 to 580 Ma, together with the zircon age population, show generally good agreement with the timing of the continental collisions. However, the age peak of monazite is ~40 Myr younger than that of the detrital zircons. This skewed age distribution towards younger ages was possibly attributed to igneous or metamorphic events relating to the post-collisional extension. Indeed, the thermal history of the Eastern Nigeria terrane in the Trans-Saharan Belt constrained by dating granites and migmatites with multiple isotopic chronometers having different closure temperatures suggests a secular cooling from amphibolite- to granulite-facies condition at ~590 Ma to upper greenschist- to lower amphibolite-facies conditions at ~550 Ma (Ferré et al., 2002), which is consistent with the garnet-poor origins of the monazite grains yielding 600–560 Ma (Fig., 5-11b).

The Zambezi River detrital monazites define a remarkably sharp U–Pb age peak at ~500 Ma (Fig. 5-5f) that is ~30 Myr younger than that of the detrital zircons. The 520–480 Ma monazite population includes grains of igneous and garnet-bearing metamorphic origins with high populations (Fig. 5-11d), indicating that low-Ca felsic magmatism and high-grade metamorphism were significant at that time in the basin area. The river basin covers large parts of the Lufilian and Zambezi Belts and the southernmost part of the Mozambique Belt. These orogenic belts were subjected to thermal events related to the final stage of the Gondwana assembly. The collision between the Congo and Kalahari Cratons resulted in metamorphism and syn-tectonic granitic magmatism in the Lufilian and Zambezi Belts at 550–520 Ma (e.g., John et al., 2004; Johnson et al., 2005; Eglinger et al. 2016), while the collision between the Congo and East Antarctica Cratons caused high-grade metamorphism and migmatization in the Mozambique Belt between 570–530 Ma (Bingen et al., 2009; Fritz et al., 2013). The detrital zircon age peak corresponds to the timing these continental collisions. Moreover, voluminous low-Ca granite emplacement and high-grade metamorphism took place in the southern part of the Mozambique Belt at ca. 500 Ma (Bingen et al., 2009; Thomas et al., 2010; Ueda et al., 2012a, b), coincident with the detrital monazite age peak. Note, however, that the Mozambique Belt is only marginally overlapped by the current Zambezi River basin. Besides, ~500 Ma granites and high-grade metamorphic rocks have been found from the East Antarctica that was adjacent to the Mozambique Belt at that time (e.g., Grantham et al., 2003, 2013). These contemporaneous post-collisional

magmatism and metamorphism are considered to result from asthenosphere upwelling following lithospheric delamination (Jacobs et al., 2008a; Ueda et al., 2012a, b). The detrital monazite peak at ~500 Ma may indicate that post-collisional granitic magmatism and high-grade metamorphism caused by the asthenosphere upwelling were spread into the major source terrane(s) of the Zambezi River sediments, even though a limited number of ~500 Ma granites and metamorphic rocks are currently recognized (Goscombe et al., 2000; Johnson et al., 2006).

5.6 Conclusion

The U–Pb ages and geochemical compositions of the detrital monazites from the Nile, Niger, Congo, Zambezi and Orange Rivers were determined. The U–Pb age data showed peaks at ~600 Ma for the Nile, ~580 Ma for the Niger, ~630, ~610 and ~560 Ma for the Congo and ~500 Ma for the Zambezi and ~1200–900 Ma for the Orange. The Pan-African age peaks of the Niger, Congo and Zambezi are younger by 20–40 Myr than those defined by the detrital zircons from the same rivers, but the detrital monazites and zircons of the Nile show nearly identical Pan-African age peaks. The monazite geochemical data revealed the significant variation in negative Eu anomaly, depletion of HREE, and Th content. The geneses of detrital monazites were estimated based on the geochemical features, which revealed the monazite age spectra consisted of metamorphic monazites essentially reflect the timing of major low- to high-grade metamorphism as well as low-Ca felsic magmatism in the source terranes. The age gaps of 20–40 Myr between the zircon and monazite peaks would reflect the time intervals

between major felsic magmatism in pre-to syn-collisional stages and metamorphism in syn-to post-collisional stages during Pan-African orogenic events. The obtained results highlight the utility of the combined use of detrital monazite and zircon data for investigating the timescales and nature of major orogenic events in the source terranes.

6. Synthesis

This work has focused on a key aspect of monazite as geochemical tracer for various crustal processes and discussed the linkage between the geochemical characteristics of monazite and its crystallization condition.

To elucidate the linkage, accurate determination of monazite trace element composition is essential. Synthetic REE phosphates were analyzed to assess the effect of oxide interference during REE analysis of natural monazite by LA-ICP-MS. The results have demonstrated the necessity of the oxide interference correction even when the plasma condition was optimized to minimize the oxide production rates. The determined oxide production rates using the synthetic REE phosphates allow more accurate quantification of REE concentrations in monazite.

The chapters 3 and 4 set out with the aim of assessing the variation in trace element compositions of igneous monazites from a single granite pluton and various granitic rocks across the Japan arc, respectively. The trace element analysis has shown the systematic variation in Eu anomaly, LREE-depletion, and Th-depletion of monazites in individual granite samples from the single pluton. On the basis of Rayleigh model calculations, it has been quantitatively confirmed that these parameters are controlled by the fractionation of plagioclase and monazite. This work enhances the utility of monazite trace element composition as an indicator of magma differentiation. Furthermore, the comprehensive analyses of monazites in granitic rocks from the Japan

arc have elucidated that Eu anomaly in monazite reflects not only the degree of magma differentiation but also the redox state of magma, the latter of which is controlled by the nature of source rocks.

The accumulation of trace element data of igneous monazite in this study permitted, for the first time, the quantitative comparison of chemical signatures between igneous and metamorphic monazites. The most obvious finding is that the magnitude of Eu anomaly of igneous monazite is much larger than that of metamorphic monazite. Moreover, it has been unraveled, based on the comprehensive compilation, that the chemical compositions of monazite derived from garnet-rich metamorphic rocks are characterized by the significant HREE-depletion. These findings provide a new geochemical indicator for source rock type of detrital monazite. Further accumulation of accurate monazite trace element data by follow-up studies would makes the indicator more robust.

One of the novelties of this work is the integration of U–Pb dating and trace element analysis of detrital monazite for obtaining a high-resolution archive of orogenic events. To verify the geochemical indicator for source rock type, the age spectra of detrital monazite and zircon from the same river sands were compared. The comparison has corroborated the utility of the geochemical indicator. Furthermore, the age gaps of 20–40 Myr between the zircon and monazite peaks have been found. This finding implies that detrital zircon age spectra are the archive of major felsic magmatism in pre- to syn-collisional stages (Pacific-type orogeny); in contrast, detrital monazite age spectra

are the archive of major magmatism and metamorphism in syn- to post-collisional stages (collision-type orogeny). It would be beneficial to apply this approach to the detrital monazites in old sedimentary rocks for elucidating the timing and nature of orogenic events through the Earth's history and possibly gaining new insights into the supercontinent cycle.

References

Abdelsalam, M. G., Liégeois, J. P., & Stern, R. J. (2002). The Saharan Metacraton. Journal of African Earth Sciences, 34, 119–136.

Ackermann, R. J. (1976). The thermodynamics of ionization of gaseous oxides; the first ionization potentials of the lanthanide metals and monoxides. The Journal of Chemical Physics, 65(3), 1027. https://doi.org/10.1063/1.433179

Adachi, Y., & Wallis, S. (2008). Ductile deformation and development of andalusite microstructures in the Hongusan area: Constraints on the metamorphism and tectonics of the Ryoke Belt. Island Arc, 17(1), 41–56. https://doi.org/10.1111/j.1440-1738.2007.00603.x

Agbossoumondé, Y., Ménot, R.-P., Paquette, J. L., Guillot, S., Yéssoufou, S., & Perrache, C. (2007). Petrological and geochronological constraints on the origin of the Palimé–Amlamé granitoids (South Togo, West Africa): A segment of the West African Craton Paleoproterozoic margin reactivated during the Pan-African collision. Gondwana Research, 12(4), 476–488. https://doi.org/10.1016/j.gr.2007.01.004

Aleinikoff, J. N., Schenck, W. S., Plank, M. O., Srogi, L., Fanning, C. M., Kamo, S. L., & Bosbyshell, H. (2006). Deciphering igneous and metamorphic events in high-grade rocks of the Wilmington Complex, Delaware: Morphology, cathodoluminescence and backscattered electron zoning, and SHRIMP U-Pb geochronology of zircon and monazite. Geological Society of America Bulletin, 118(1–2), 39–64. https://doi.org/10.1130/B25659.1

Aleinikoff, J. N., Schenck, W. S., Plank, M. O., Srogi, L., Fanning, C. M., Kamo, S. L., & Bosbyshell, H. (2006). Deciphering igneous and metamorphic events in high-grade rocks of the Wilmington Complex, Delaware: Morphology, cathodoluminescence and backscattered electron zoning, and SHRIMP U-Pb geochronology of zircon and monazite. GSA Bulletin, 118(1–2), 39–64. Retrieved from http://dx.doi.org/10.1130/B25659.1

Annen, C., Blundy, J. D., & Sparks, R. S. J. (2006). The Genesis of Intermediate and Silicic Magmas in Deep Crustal Hot Zones. Journal of Petrology, 47(3), 505–539. Retrieved from http://dx.doi.org/10.1093/petrology/egi084

Antunes, I. M. H. R., Neiva, A. M. R., Silva, M. M. V. G., & Corfu, F. (2008). Geochemistry of S-type granitic rocks from the reversely zoned Castelo Branco pluton (central Portugal). Lithos, 103(3–4), 445–465. https://doi.org/10.1016/J.LITHOS.2007.10.003

Appel, P., Schenk, V., & Schumann, A. (2005). P-T path and metamorphic ages of pelitic schists at Murchison Falls, NW Uganda: Evidence for a Pan-African tectonometamorphic event in the Congo Craton. European Journal of Mineralogy, 17(5), 655–664. https://doi.org/10.1127/0935-1221/2005/0017-0655

Aries, S., Valladon, M., Polvé, M., & Dupré, B. (2000). A routine method for oxide and hydroxide interference corrections in ICP-MS chemical analysis of environmental and geological samples. Geostandards Newsletter, 24(1), 19–31. https://doi.org/10.1111/j.1751-908X.2000.tb00583.x

Arndt, N. T. (2013). The Formation and Evolution of the Continental Crust. Geochemical Perspectives, 2(3), 405. Retrieved from http://dx.doi.org/

Arndt, N., & Davaille, A. (2013). Episodic Earth evolution. Tectonophysics, 609, 661–674. https://doi.org/10.1016/J.TECTO.2013.07.002

Asami, M., Hoshino, M., Miyakawa, K., & Suwa, K. (1982). Metamorphic conditions of staurolite schists of the Ryoke metamorphic belt in the Hazu-Hongusan area, central Japan. Journal of the Geological Society of Japan, 88, 437–450 (in Japanese with English abstract).

Ayers, J. C., Loflin, M., Miller, C. F., Barton, M. D., & Coath, C. D. (2006). In situ oxygen isotope analysis of monazite as a monitor of fluid infiltration during contact metamorphism: Birch Creek Pluton aureole, White Mountains, eastern California. Geology, 34(8), 653. https://doi.org/10.1130/G22185.1

Barbey, P., Nachit, H., & Pons, J. (2001). Magma–host interactions during differentiation and emplacement of a shallow-level, zoned granitic pluton (Tarçouate pluton, Morocco): implications for magma emplacement. Lithos, 58(3–4), 125–143. https://doi.org/10.1016/S0024-4937(01)00053-6

Bartosz, B., Daniel, H., Michael, W., & Michael, J. (2011). Experimental determination of stability

relations between monazite, fluorapatite, allanite, and REE-epidote as a function of pressure, temperature, and fluid composition. American Mineralogist. https://doi.org/10.2138/am.2011.3741

Bateman, P. C., & Chappell, B. W. (1979). Crystallization, fractionation, and solidification of the Tuolumne Intrusive Series, Yosemite National Park, California. GSA Bulletin, 90(5), 465–482. Retrieved from http://dx.doi.org/10.1130/0016-7606(1979)90%3C465:CFASOT%3E2.0.CO

Batumike, J. M., Griffin, W. L., O'Reilly, S. Y., Belousova, E. A., & Pawlitschek, M. (2009). Crustal evolution in the central Congo-Kasai Craton, Luebo, D.R. Congo: Insights from zircon U–Pb ages, Hf-isotope and trace-element data. Precambrian Research, 170(1–2), 107–115. https://doi.org/10.1016/j.precamres.2008.12.001

Bea, F. (1996). Residence of REE, Y, Th and U in Granites and Grustal Protoliths ; Implications for the Chemistry of Crustal Melts. Journal of Petrology, 37(3), 521–552.

Bea, F., Pereira, M. D., Stroh, A., & Gmbtl, P. E. (1994). Mineral/leucosome trace-element partitioning in a peraluminous migmatite (a laser ablation-ICP-MS study). Chemical Geology, 117(94), 291–312. https://doi.org/10.1016/0009-2541(94)90133-3

Becker, T., Garoeb, H., Ledru, P., & Milesi, J. P. (2005). The Mesoproterozoic event within the Rehoboth Basement Inlier of Namibia: Review and new aspects of stratigraphy, geochemistry structure and plate tectonic setting. South African Journal of Geology, 108(4), 465–492. https://doi.org/10.2113/108.4.465

Becker, T., Schreiber, U., Kampunzu, A. B., & Armstrong, R. (2006). Mesoproterozoic rocks of Namibia and their plate tectonic setting. Journal of African Earth Sciences, 46(1–2), 112–140. https://doi.org/10.1016/J.JAFREARSCI.2006.01.015

Bédard, J. H. (2006). Trace element partitioning in plagioclase feldspar. Geochimica et Cosmochimica Acta, 70(14), 3717–3742. https://doi.org/10.1016/J.GCA.2006.05.003

Begg, G. C., Griffin, W. L., Natapov, L. M., O'Reilly, S. Y., Grand, S. P., O'Neill, C. J., … Bowden, P. (2009). The lithospheric architecture of Africa: Seismic tomography, mantle petrology, and tectonic evolution. Geosphere, 5(1), 23–50. https://doi.org/10.1130/GES00179.1

Belousova, E., Griffin, W., O'Reilly, S. Y., & Fisher, N. (2002). Igneous zircon: trace element composition as an indicator of source rock type. Contributions to Mineralogy and Petrology, 143(5), 602–622. https://doi.org/10.1007/s00410-002-0364-7

Belousova, E. A., Kostitsyn, Y. A., Griffin, W. L., Begg, G. C., O'Reilly, S. Y., & Pearson, N. J. (2010). The growth of the continental crust: Constraints from zircon Hf-isotope data. Lithos, 119(3–4), 457–466. https://doi.org/10.1016/J.LITHOS.2010.07.024

Berglund, M., & Wieser, M. E. (2011). Isotopic compositions of the elements 2009 (IUPAC Technical Report)*, 83(2), 397–410. https://doi.org/10.1351/PAC-REP-10-06-02

Bertrand, J. M., Michard, A., Boullier, A. M., & Dautel, D. (1986). Structureand U-Pb geochronology of Central Hoggar (Algeria): a reappraisal of its Pan-African evolution. Tectonics, 5(7), 955–972.

Bertrand, J. M. L., & Caby, M. (1978). Geodynamic Evolution of the Pan-African Orogenic Belt : A new interpretation of the Hoggar Shield (Algerian Sahara). Geologishe Rundschau, 67(2), 357–388.

Beaumont, C., Jamieson, R. A., Nguyen, M. H., & Medvedev, S. (2004). Crustal channel flows: 1. Numerical models with applications to the tectonics of the Himalayan-Tibetan orogen. *Journal of Geophysical Research: Solid Earth*, *109*(B6). https://doi.org/10.1029/2003JB002809

Bingen, B., Jacobs, J., Viola, G., Henderson, I. H. C., Skår, Ø., Boyd, R., … Daudi, E. X. F. (2009). Geochronology of the Precambrian crust in the Mozambique belt in NE Mozambique, and implications for Gondwana assembly. Precambrian Research, 170(3–4), 231–255. https://doi.org/10.1016/j.precamres.2009.01.005

Bingen, B., & van Breemen, O. (1998). U-Pb monazite ages in amphibolite- to granulite-facies orthogneiss reflect hydrous mineral breakdown reactions: Sveconorwegian Province of SW Norway. Contributions to Mineralogy and Petrology, 132(4), 336–353. https://doi.org/10.1007/s004100050428

Black, L. P., Fitzgerald, J. D., & Harley, S. L. (1984). Pb isotopic composition, colour, and microstructure of monazites from a polymetamorphic rock in Antarctica. Contributions to

Mineralogy and Petrology, 85(2), 141–148. https://doi.org/10.1007/BF00371704
Black, L. P., Kamo, S. L., Allen, C. M., Davis, D. W., Aleinikoff, J. N., Valley, J. W., … Foudoulis, C. (2004). Improved 206Pb/238U microprobe geochronology by the monitoring of a trace-element-related matrix effect; SHRIMP, ID–TIMS, ELA–ICP–MS and oxygen isotope documentation for a series of zircon standards. Chemical Geology, 205(1–2), 115–140. https://doi.org/10.1016/j.chemgeo.2004.01.003
Black, R., Latouche, L., Liegeois, J. P., Caby, R., & Bertrand, J. M. (1994). Pan-African displaced terranes in the Tuareg Shield (central Sahara). Geology, 22(7), 641–644. https://doi.org/10.1130/0091-7613(1994)022<0641:PADTIT>2.3.CO;2
Bogaerts, A., & Aghaei, M. (2017). Inductively coupled plasma – mass spectrometry: Insights through computer modeling. J. Anal. At. Spectrom., 32(2), 233–261. https://doi.org/10.1039/C6JA00408C
Boher, M., Abouchami, W., Michard, A., Albarede, F., & Arndt, N. T. (1992). Crustal Growth in West Africa at 2.1 Ga. Journal of Geophisical Research, 97(91), 345–369.
Bosch, D., Hammor, D., Bruguier, O., & Caby, R. (2002). Monazite ‘“ in situ ”’ 207 Pb / 206 Pb geochronology using a small geometry high-resolution ion probe . Application to Archaean and Proterozoic rocks. Chemical Geology, 184, 151–165.
Bosch, D., Hammor, D., Bruguier, O., Caby, R., & Luck, J.-M. (2002). Monazite “in situ” $^{207}Pb/^{206}Pb$ geochronology using a small geometry high-resolution ion probe. Application to Archaean and Proterozoic rocks. Chemical Geology, 184(1–2), 151–165. https://doi.org/10.1016/S0009-2541(01)00361-8
Boullier, A. M., Liégeois, J. P., Black, R., Fabre, J., Sauvage, M., & Bertrand, J. M. (1986). Late Pan-African tectonics marking the transition from subduction-related calc-alkaline magmatism to within-plate alkaline granitoids (Adrar des Iforas, Mali). Tectonophysics, 132, 233–246.
Bouyo Houketchang, M., Toteu, S. F., Deloule, E., Penaye, J., & Van Schmus, W. R. (2009). U–Pb and Sm–Nd dating of high-pressure granulites from Tcholliré and Banyo regions: Evidence for a Pan-African granulite facies metamorphism in north-central Cameroon. Journal of African Earth Sciences, 54(5), 144–154. https://doi.org/10.1016/J.JAFREARSCI.2009.03.013
Bouyo, M. H., Penaye, J., Barbey, P., Toteu, S. F., & Wandji, P. (2013). Petrology of high-pressure granulite facies metapelites and metabasites from Tcholliré and Banyo regions: Geodynamic implication for the Central African Fold Belt (CAFB) of north-central Cameroon. Precambrian Research, 224, 412–433. https://doi.org/10.1016/J.PRECAMRES.2012.09.025
Bouyo, M. H., Zhao, Y., Penaye, J., Zhang, S. H., & Njel, U. O. (2015). Neoproterozoic subduction-related metavolcanic and metasedimentary rocks from the Rey Bouba Greenstone Belt of north-central Cameroon in the Central African Fold Belt: New insights into a continental arc geodynamic setting. Precambrian Research, 261, 40–53. https://doi.org/10.1016/J.PRECAMRES.2015.01.012
Breitkreuz, C., Eliwa, H., Khalaf, I., Gameel, K. El, Bühler, B., Sergeev, S., … Murata, M. (2010). Neoproterozoic SHRIMP U–Pb zircon ages of silica-rich Dokhan Volcanics in the North Eastern Desert, Egypt. Precambrian Research, 182(3), 163–174. https://doi.org/10.1016/j.precamres.2010.06.019
Broska, I., Petrík, I., & Williams, C. T. (2000). Coexisting monazite and allanite in peraluminous granitoids of the Tribeč Mountains, Western Carpathians. American Mineralogist, 85(1), 22–32. Retrieved from http://dx.doi.org/10.2138/am-2000-0104
Broska, I., Williams, C. T., Janák, M., & Nagy, G. (2005). Alteration and breakdown of xenotime-(Y) and monazite-(Ce) in granitic rocks of the Western Carpathians, Slovakia. Lithos, 82(1–2), 71–83. https://doi.org/10.1016/J.LITHOS.2004.12.007
Budzyń, B., Harlov, D. E., Williams, M. L., & Jercinovic, M. J. (2011). Experimental determination of stability relations between monazite, fluorapatite, allanite, and REE-epidote as a function of pressure, temperature, and fluid composition. American Mineralogist, 96(10), 1547–1567. Retrieved from http://dx.doi.org/10.2138/am.2011.3741
Budzyń, B., Harlov, D. E., Kozub-Budzyń, G. A., & Majka, J. (2017). Experimental constraints on the relative stabilities of the two systems monazite-(Ce) – allanite-(Ce) – fluorapatite and xenotime-(Y) – (Y,HREE)-rich epidote – (Y,HREE)-rich fluorapatite, in high Ca and Na-Ca

environments under P-T conditions of 200–1000 . Mineralogy and Petrology, 111(183–217).
Buick, I. S., Clark, C., Rubatto, D., Hermann, J., Pandit, M., & Hand, M. (2010). Constraints on the Proterozoic evolution of the Aravalli-Delhi Orogenic belt (NW India) from monazite geochronology and mineral trace element geochemistry. Lithos, 120(3–4), 511–528. https://doi.org/10.1016/j.lithos.2010.09.011
Cabella, R., Lucchetti, G., & Marescotti, P. (2001). AUTHIGENIC MONAZITE AND XENOTIME FROM PELITIC METACHERTS IN PUMPELLYITE–ACTINOLITE-FACIES CONDITIONS, SESTRI–VOLTAGGIO ZONE, CENTRAL LIGURIA, ITALY. The Canadian Mineralogist, 39(3), 717 LP-727. Retrieved from http://www.canmin.org/content/39/3/717.abstract
Caby, R. (2003). Terrane assembly and geodynamic evolution of central–western Hoggar: a synthesis. Journal of African Earth Sciences, 37(3–4), 133–159. https://doi.org/10.1016/j.jafrearsci.2003.05.003
Campbell, I. H., Reiners, P. W., Allen, C. M., Nicolescu, S., & Upadhyay, R. (2005). He–Pb double dating of detrital zircons from the Ganges and Indus Rivers: Implication for quantifying sediment recycling and provenance studies. Earth and Planetary Science Letters, 237(3–4), 402–432. https://doi.org/10.1016/j.epsl.2005.06.043
Campbell, I. H., & Allen, C. M. (2008). Formation of supercontinents linked to increases in atmospheric oxygen. *Nature Geoscience*, *1*(8), 554–558. https://doi.org/10.1038/ngeo259
Casillas, R., Nagy, G., Panto, G., Braendle, J., & Forizs, I. (1995). Occurrence of Th, U, Y, Zr and REE-bearing accessory minerals in late-Variscan granitic rocks from the Sierra de Guadarrama (Spain). European Journal of Mineralogy, 7(4), 989 LP-1006. Retrieved from http://eurjmin.geoscienceworld.org/content/7/4/989.abstract
Catlos, E. J. (2013). Generalizations about monazite : Implications for geochronologic studies. American Mineralogist, 98, 819–832.
Catuneanu, O., Wopfner, H., Eriksson, P. G., Cairncross, B., Rubidge, B. S., Smith, R. M. H., & Hancox, P. J. (2005). The Karoo basins of south-central Africa. Journal of African Earth Sciences, 43(1–3), 211–253. https://doi.org/10.1016/J.JAFREARSCI.2005.07.007
Cawood, P. A., Kröner, A., Collins, W. J., Kusky, T. M., Mooney, W. D., & Windley, B. F. (2009). Accretionary orogens through Earth history. Geological Society, London, Special Publications, 318(1), 1 LP-36. https://doi.org/10.1144/SP318.1
Chappell, B. W., & White, A. J. R. (2001). Two contrasting granite types : 25 years later. Australian Journal of Earth Sciences, 48, 489–499.
Chappell, B. W., White, A. J. R., Williams, I. S., Wyborn, D., & Wyborn, L. A. I. (2000). Lachlan Fold Belt granites revisited: High ‐ and low ‐ temperature granites and their implications. Australian Journal of Earth Sciences, 47(1), 123–138. https://doi.org/10.1046/j.1440-0952.2000.00766.x
Chappell, B. W., & White, A. J. R. (1974). Two contrasting granite types. Pacific Geology, 8, 173–174.
Charlier, B. L. A., Ginibre, C., Morgan, D., Nowell, G. M., Pearson, D. G., Davidson, J. P., & Ottley, C. J. (2006). Methods for the microsampling and high-precision analysis of strontium and rubidium isotopes at single crystal scale for petrological and geochronological applications. Chemical Geology, 232(3–4), 114–133. https://doi.org/10.1016/J.CHEMGEO.2006.02.015
Chattopadhyay, A., Das, K., Hayasaka, Y., & Sarkar, A. (2015). Syn- and post-tectonic granite plutonism in the Sausar Fold Belt, central India: Age constraints and tectonic implications. Journal of Asian Earth Sciences, 107, 110–121. https://doi.org/10.1016/J.JSEAES.2015.04.006
Chen, W., Honghui, H., Bai, T., & Jiang, S. (2017). Geochemistry of Monazite within Carbonatite Related REE Deposits. Resources, 6(4). https://doi.org/10.3390/resources6040051
Cherniak, D. J. (2010). Diffusion in Accessory Minerals: Zircon, Titanite, Apatite, Monazite and Xenotime. Reviews in Mineralogy and Geochemistry, 72(1), 827–869. https://doi.org/10.2138/rmg.2010.72.18
Cherniak, D. J., Watson, E. B., Grove, M., & Harrison, T. M. (2004). Pb diffusion in monazite: a combined RBS/SIMS study. Geochimica et Cosmochimica Acta, 68(4), 829–840. https://doi.org/10.1016/j.gca.2003.07.012
Christensen, J. N., Halliday, A. N., Lee, D.-C., & Hall, C. M. (1995). In situ Sr isotopic analysis by

laser ablation. Earth and Planetary Science Letters, 136(1–2), 79–85. https://doi.org/10.1016/0012-821X(95)00181-6
Christensen, N. I., & Mooney, W. D. (1995). Seismic velocity structure and composition of the continental crust: A global view. Journal of Geophysical Research: Solid Earth, 100, 9761–9788.
Christiansen, E. H., Burt, D. M., Sheridan, M. F., & Wilson, R. T. (1983). The petrogenesis of topaz rhyolites from the western United States. Contributions to Mineralogy and Petrology, 83(1), 16–30. https://doi.org/10.1007/BF00373075
Clavier, N., Podor, R., & Dacheux, N. (2011). Crystal chemistry of the monazite structure. Journal of the European Ceramic Society, 31(6), 941–976. https://doi.org/10.1016/J.JEURCERAMSOC.2010.12.019
Clemens J. and Watkins, J. (2001). The fluid regime of high-temperature metamorphism during granitoid magma genesis. Contributions to Mineralogy and Petrology, 140(5), 600–606. https://doi.org/10.1007/s004100000205
Clemens, J. D. (1990). The Granulite — Granite Connexion. In P. Vielzeuf D. and Vidal (Ed.), Granulites and Crustal Evolution (pp. 25–36). Dordrecht: Springer Netherlands. https://doi.org/10.1007/978-94-009-2055-2_3
Clemens, J. . (2003). S-type granitic magmas—petrogenetic issues, models and evidence. Earth-Science Reviews, 61(1–2), 1–18. https://doi.org/10.1016/S0012-8252(02)00107-1
Clemens, J. D., & Wall, V. J. (1981). Origin and crystallization of some peraluminous (S-type) granitic magmas. Canadian Mineralogist, 19, 111–131.
Cocherie, A., Legendre, O., Peucat, J. J., & Kouamelan, A. N. (1998). Geochronology of polygenetic monazites constrained by in situ electron microprobe Th-U-total lead determination: implications for lead behaviour in monazite. Geochimica et Cosmochimica Acta, 62(14), 2475–2497. https://doi.org/10.1016/S0016-7037(98)00171-9
Collins, A. S., & Pisarevsky, S. a. (2005). Amalgamating eastern Gondwana: The evolution of the Circum-Indian Orogens. Earth-Science Reviews, 71(3–4), 229–270. https://doi.org/10.1016/j.earscirev.2005.02.004
Collins, W. J. (2002). Hot orogens, tectonic switching, and creation of continental crust. Geology, 30(6), 535–538. Retrieved from http://dx.doi.org/10.1130/0091-7613(2002)030%3C0535:HOTSAC%3E2.0.CO
Condie, K. C., Arndt, N., Davaille, A., & Puetz, S. J. (2017). Zircon age peaks: Production or preservation of continental crust? Geosphere, 13(2), 227–234. Retrieved from http://dx.doi.org/10.1130/GES01361.1
Condie, K. C., Beyer, E., Belousova, E., Griffin, W. L., & O'Reilly, S. Y. (2005). U–Pb isotopic ages and Hf isotopic composition of single zircons: The search for juvenile Precambrian continental crust. Precambrian Research, 139(1–2), 42–100. https://doi.org/10.1016/J.PRECAMRES.2005.04.006
Condie, K. C., & Hunter, D. R. (1976). Trace element geochemistry of Archean granitic rocks from the Barberton region, South Africa. Earth and Planetary Science Letters, 29(2), 389–400. https://doi.org/10.1016/0012-821X(76)90144-8
Condon, D., Zhu, M., Bowring, S., Wang, W., Yang, A., & Jin, Y. (2005). U-Pb ages from the neoproterozoic Doushantuo Formation, China. Science (New York, N.Y.), 308(5718), 95–98. https://doi.org/10.1126/science.1107765
Cornell, D. H., & Pettersson, Å. (2007). Ion probe dating of the Achab Gneiss, a young basement to the Central Bushmanland Ore District? Journal of African Earth Sciences, 47(2), 112–116. https://doi.org/10.1016/J.JAFREARSCI.2006.11.002
Dada, S. S. (1998). Crust-forming ages and proterozoic crustal evoluton in Nigeria: a reappraisal of current interpretations. Precambrian Research, 87(1–2), 65–74. https://doi.org/10.1016/S0301-9268(97)00054-5
Damian Nance, R., & Brendan Murphy, J. (2013). Origins of the supercontinent cycle. Geoscience Frontiers, 4(4), 439–448. https://doi.org/10.1016/J.GSF.2012.12.007
Davidson, J. P., de Silva, S. L., Holden, P., & Halliday, A. N. (1990). Small-scale disequilibrium in a magmatic inclusion and its more silicic host. Journal of Geophysical Research: Solid Earth, 95(B11), 17661–17675. https://doi.org/10.1029/JB095iB11p17661

Davidson, J. P., & Tepley, F. J. (1997). Recharge in Volcanic Systems: Evidence from Isotope Profiles of Phenocrysts. Science, 275(5301), 826. https://doi.org/10.1126/science.275.5301.826
Davidson, J. P., Font, L., Charlier, B. L. A., & Tepley, F. J. (2008). Mineral-scale Sr isotope variation in plutonic rocks – a tool for unravelling the evolution of magma systems. Transactions of the Royal Society of Edinburgh: Earth Sciences, 97(04), 357–367. https://doi.org/10.1017/S0263593300001504
Davidson, J., Tepley, F., Palacz, Z., & Meffan-Main, S. (2001). Magma recharge, contamination and residence times revealed by in situ laser ablation isotopic analysis of feldspar in volcanic rocks. Earth and Planetary Science Letters, 184(2), 427–442. https://doi.org/10.1016/S0012-821X(00)00333-2
De Waele, B., Fitzsimons, I. C. W., Wingate, M. T. D., Tembo, F., Mapani, B., & Belousova, E. A. (2009). The geochronological framework of the Irumide Belt: A prolonged crustal history along the margin of the Bangweulu Craton. American Journal of Science , 309(2), 132–187. https://doi.org/10.2475/02.2009.03
De Waele, B., Johnson, S. P., & Pisarevsky, S. A. (2008). Palaeoproterozoic to Neoproterozoic growth and evolution of the eastern Congo Craton: Its role in the Rodinia puzzle. Precambrian Research, 160(1–2), 127–141. https://doi.org/10.1016/j.precamres.2007.04.020
De Waele, B., Kampunzu, A. B., Mapani, B. S. E., & Tembo, F. (2006). The Mesoproterozoic Irumide belt of Zambia. Journal of African Earth Sciences, 46(1–2), 36–70. https://doi.org/10.1016/J.JAFREARSCI.2006.01.018
Dewey, J. F., & Bird, J. M. (1970). Mountain belts and the new global tectonics. *Journal of Geophysical Research*, *75*(14), 2625–2647. https://doi.org/10.1029/JB075i014p02625
DeWolf, C. P., Belshaw, N., & O'Nions, R. K. (1993). A metamorphic history from micron-scale 207Pb/206Pb chronometry of Archean monazite. Earth and Planetary Science Letters, 120(3–4), 207–220. https://doi.org/10.1016/0012-821X(93)90240-A
Dhuime, B., Hawkesworth, C. J., & Cawood, P. A. (2011). When continents formed. Science, 331(6014), 154–155.
Douglas, D. J., & French, J. B. (1986). An improved interface for inductively coupled plasma-mass spectrometry (ICP-MS). Spectrochimica Acta Part B: Atomic Spectroscopy, 41(3), 197–204. https://doi.org/10.1016/0584-8547(86)80159-8
Eggins, S. M., Kinsley, L. P. J., & Shelley, J. M. G. (1998). Deposition and element fractionation processes during atmospheric pressure laser sampling for analysis by ICP-MS. *Applied Surface Science*, *127*, 278-286.
Eggins, S. M., Grün, R., McCulloch, M. T., Pike, A. W., Chappell, J., Kinsley, L., ... & Taylor, L. (2005). In situ U-series dating by laser-ablation multi-collector ICPMS: new prospects for Quaternary geochronology. *Quaternary Science Reviews*, *24*(23-24), 2523-2538.
Eglinger, A., Tarantola, A., Durand, C., Ferraina, C., Vanderhaeghe, O., André-Mayer, A.-S., … Deloule, E. (2014). Uranium mobilization by fluids associated with Ca–Na metasomatism: A P–T–t record of fluid–rock interactions during Pan-African metamorphism (Western Zambian Copperbelt). Chemical Geology, 386, 218–237. https://doi.org/10.1016/J.CHEMGEO.2014.07.028
Eglinger, A., Vanderhaeghe, O., André-Mayer, A.-S., Goncalves, P., Zeh, A., Durand, C., & Deloule, E. (2016). Tectono-metamorphic evolution of the internal zone of the Pan-African Lufilian orogenic belt (Zambia): Implications for crustal reworking and syn-orogenic uranium mineralizations. Lithos, 240–243, 167–188. https://doi.org/10.1016/J.LITHOS.2015.10.021
Ekwueme, B. N., & Kröner, A. (2006). Single zircon ages of migmatitic gneisses and granulites in the Obudu Plateau: Timing of granulite-facies metamorphism in southeastern Nigeria. Journal of African Earth Sciences, 44(4–5 SPEC. ISS.), 459–469. https://doi.org/10.1016/j.jafrearsci.2005.11.013
Eliwa, H. A., El-Bialy, M. Z., & Murata, M. (2014). Edicaran post-collisional volcanism in the Arabian-Nubian Shield: The high-K calc-alkaline Dokhan Volcanics of Gabal Samr El-Qaa (592±5Ma), North Eastern Desert, Egypt. Precambrian Research, 246, 180–207. https://doi.org/10.1016/j.precamres.2014.03.015
Engi, M. (2017). Petrochronology Based on REE-Minerals: Monazite, Allanite, Xenotime, Apatite.

Reviews in Mineralogy and Geochemistry, 83(1), 365-418. Retrieved from http://rimg.geoscienceworld.org/content/83/1/365.abstract
Erickson, T. M., Pearce, M. a., Taylor, R. J. M., Timms, N. E., Clark, C., Reddy, S. M., & Buick, I. S. (2015). Deformed monazite yields high-temperature tectonic ages. Geology, 43, 383–386. https://doi.org/10.1130/G36533.1
Eriksson, P. G., Altermann, W., & Hartzer, F. J. (2006). The Transvaal Supergroup and its precursors. In M. R. Johnson, C. R. Anhaeusser, & R. J. Thomas (Eds.), The Geology of South Africa (pp. 237–260). Geological Society of South Africa/Council for Geoscience, Johannesburg/Pretoria,.
Evans, E. H., Ebdon, L., & Rowley, L. (2002). Comparative study of the determination of equilibrium dissociation temperature in inductively coupled plasma-mass spectrometry. Spectrochimica Acta Part B: Atomic Spectroscopy, 57(4), 741–754. https://doi.org/10.1016/S0584-8547(02)00003-4
Evans, J., & Zalasiewicz, J. (1996). U–Pb, Pb–Pb and Sm–Nd dating of authigenic monazite: implications for the diagenetic evolution of the Welsh Basin. Earth and Planetary Science Letters, 144(3–4), 421–433. https://doi.org/10.1016/S0012-821X(96)00177-X
Fernandez-Alonso, M., Cutten, H., De Waele, B., Tack, L., Tahon, A., Baudet, D., & Barritt, S. D. (2012). The Mesoproterozoic Karagwe-Ankole Belt (formerly the NE Kibara Belt): The result of prolonged extensional intracratonic basin development punctuated by two short-lived far-field compressional events. Precambrian Research, 216–219, 63–86. https://doi.org/10.1016/J.PRECAMRES.2012.06.007
Ferré, E., Gleizes, G., & Caby, R. (2002). Obliquely convergent tectonics and granite emplacement in the Trans-Saharan belt of Eastern Nigeria: a synthesis. Precambrian Research, 114, 199–219.
Fisher, C. M., Hanchar, J. M., Miller, C. F., Phillips, S., Vervoort, J. D., & Whitehouse, M. J. (2017). Combining Nd isotopes in monazite and Hf isotopes in zircon to understand complex open-system processes in granitic magmas. Geology . https://doi.org/10.1130/G38458.1
Fitzsimons, I. C. W., Kinny, P. D., & Harley, S. L. (1997). Two stages of zircon and monazite growth in anatectic leucogneiss: SHRIMP constraints on the duration and intensity of Pan-African metamorphism in Prydz Bay, East Antarctica. Terra Nova, 9(1), 47–51. https://doi.org/10.1046/j.1365-3121.1997.d01-8.x
Foster, G., Gibson, H. D., Parrish, R., Horstwood, M. S. A., Fraser, J., & Tindle, A. (2002). Textural, chemical and isotopic insights into the nature and behaviour of metamorphic monazite. Chemical Geology, 191(1–3), 183–207. https://doi.org/10.1016/S0009-2541(02)00156-0
Franz, G., Andrehs, G., & Rhede, D. (1996). Crystal chemistry of monazite and xenotime from Saxothuringian-Moldanubian metapelites , NE Bavaria , Germany. European Journal of Mineralogy, 8, 1097–1118.
Frimmel, H. E. (2000). New U-Pb zircon ages for the Kuboos pluton in the Pan-African Gariep belt, South Africa: Cambrian mantle plume or far field collision effect? South African Journal of Geology, 103(3–4), 207–214. Retrieved from http://dx.doi.org/10.2113/1030207
Frimmel, H. E., & Frank, W. (1998). Neoproterozoic tectono-thermal evolution of the Gariep Belt and its basement , Namibia and South Africa. Precambrian Research, 90, 1–28.
Frimmel, H. E., Tack, L., Basei, M. S., Nutman, A. P., & Boven, A. (2006). Provenance and chemostratigraphy of the Neoproterozoic West Congolian Group in the Democratic Republic of Congo. Journal of African Earth Sciences, 46(3), 221–239. https://doi.org/10.1016/J.JAFREARSCI.2006.04.010
Fritz, H., Abdelsalam, M., Ali, K. A., Bingen, B., Collins, A. S., Fowler, A. R., … Viola, G. (2013). Orogen styles in the East African Orogen: A review of the Neoproterozoic to Cambrian tectonic evolution. Journal of African Earth Sciences, 86, 65–106. https://doi.org/10.1016/J.JAFREARSCI.2013.06.004
Fujimaki, H., & Tatsumoto, M. (1984). Partition coefficients of Hf, Zr, and ree between phenocrysts and groundmasses. Journal of Geophisical Research, 89, 662–672.
Fujimaki, H., Wang, C., Aoki, K., & Kato, Y. (1992). Rb-Sr chronological study of the Hashigami plutonic mass, northern Kitakami, northeastern Japan. Journal of Mineralogy, Petrology and Economic Geology, 87, 187–196.
Gagnevin, D., Daly, J. S., Poli, G., & Morgan, D. (2005). Microchemical and Sr Isotopic

Investigation of Zoned K-feldspar Megacrysts: Insights into the Petrogenesis of a Granitic System and Disequilibrium Crystal Growth. Journal of Petrology, 46(8), 1689–1724. Retrieved from http://dx.doi.org/10.1093/petrology/egi031

Gao, P., Zheng, Y., & Zhao, Z. (2016). Experimental melts from crustal rocks: A lithochemical constraint on granite petrogenesis. Lithos, 266–267, 133–157. https://doi.org/10.1016/J.LITHOS.2016.10.005

Gilbert, S., Olin, P., Thompson, J., & Danyushevsky, L. (2017). Matrix dependency for oxide production rates by LA-ICP-MS. Journal of Analytical Atomic Spectrometry, 32, 638–646. https://doi.org/10.1039/C6JA00395H

Glaus, R., Kaegi, R., Krumeich, F., & Günther, D. (2010). Phenomenological studies on structure and elemental composition of nanosecond and femtosecond laser-generated aerosols with implications on laser ablation inductively coupled plasma mass spectrometry. Spectrochimica Acta - Part B Atomic Spectroscopy, 65(9–10), 812–822. https://doi.org/10.1016/j.sab.2010.07.005

Goad, B. E., & Černý, P. (1981). Peraluminous pegmatitic granites and their pegmatite aureoles in the Winnipeg River district, southeastern Manitoba. Canadian Mineralogist, 19, 177–194.

Goldstein, S. L., Arndt, N. T., & Stallard, R. F. (1997). The history of a continent from U-Pb ages of zircons from Orinoco River sand and Sm-Nd isotopes in Orinoco basin river sediments. Chemical Geology, 139(1–4), 271–286. https://doi.org/10.1016/S0009-2541(97)00039-9

Goldstein, S. L., O'Nions, R. K., & Hamilton, P. J. (1984). A Sm-Nd isotopic study of atmospheric dusts and particulates from major river systems. Earth and Planetary Science Letters, 70(2), 221–236. https://doi.org/10.1016/0012-821X(84)90007-4

Goodenough, K. M., Lusty, P. A. J., Roberts, N. M. W., Key, R. M., & Garba, A. (2014). Post-collisional Pan-African granitoids and rare metal pegmatites in western Nigeria: Age, petrogenesis, and the 'pegmatite conundrum.' Lithos, 200–201, 22–34. https://doi.org/10.1016/j.lithos.2014.04.006

Goscombe, B., Armstrong, R., & Barton, J. M. (2000). Geology of the Chewore Inliers, Zimbabwe : constraining the Mesoproterozoic to Palaeozoic evolution of the Zambezi Belt. Journal of African Earth Sciences, 30(3), 589–627.

Grantham, G. H., Maboko, M., & Eglington, B. M. (2003). A review of the evolution of the Mozambique Belt and implications for the amalgamation and dispersal of Rodinia and Gondwana. Geological Society, London, Special Publications, 206(1), 401–425. https://doi.org/10.1144/GSL.SP.2003.206.01.19

Grantham, G. H., Macey, P. H., Horie, K., Kawakami, T., Ishikawa, M., Satish-Kumar, M., … Azevedo, S. (2013). Comparison of the metamorphic history of the Monapo Complex, northern Mozambique and Balchenfjella and Austhameren areas, Sør Rondane, Antarctica: Implications for the Kuunga Orogeny and the amalgamation of N and S. Gondwana. Precambrian Research, 234, 85–135. https://doi.org/10.1016/j.precamres.2012.11.012

Gray, A. L., & Williams, J. G. (1987). Oxide and Doubly Charged Ion Response of a Commercial Inductively Coupled Plasma Mass Spectrometry Instrument. Journal of Analytical Atomic Spectrometry, 2(September), 599–606. https://doi.org/10.1039/ja9870200599

Gray, A. L. (1986). Mass spectrometry with an inductively coupled plasma as an ion source: the influence on ultratrace analysis of background and matrix response. Spectrochimica Acta Part B: Atomic Spectroscopy, 41(1), 151–167. https://doi.org/10.1016/0584-8547(86)80147-1

Gray, D. R., Foster, D. A., Meert, J. G., Goscombe, B. D., Armstrong, R., Trouw, R. A. J., & Passchier, C. W. (2008). A Damara orogen perspective on the assembly of southwestern Gondwana. Geological Society, London, Special Publications, 294(1), 257–278. https://doi.org/10.1144/SP294.14

Gregory, C. J., McFarlane, C. R. M., Hermann, J., & Rubatto, D. (2009). Tracing the evolution of calc-alkaline magmas: In-situ Sm–Nd isotope studies of accessory minerals in the Bergell Igneous Complex, Italy. Chemical Geology, 260(1–2), 73–86. https://doi.org/10.1016/J.CHEMGEO.2008.12.003

Grew, E. S., Yates, M. G., & Wilson, C. J. L. (2008). Aureoles of Pb(II)-enriched feldspar around monazite in paragneiss and anatectic pods of the Napier Complex, Enderby Land, East

Antarctica: the roles of dissolution-reprecipitation and diffusion. Contributions to Mineralogy and Petrology, 155(3), 363–378. https://doi.org/10.1007/s00410-007-0247-z

Griffin, W. L., Pearson, N. J., Belousova, E., Jackson, S. E., van Achterbergh, E., O'Reilly, S. Y., & Shee, S. R. (2000). The Hf isotope composition of cratonic mantle: LAM-MC-ICPMS analysis of zircon megacrysts in kimberlites. *Geochimica et Cosmochimica Acta*, *64*(1), 133–147. https://doi.org/10.1016/S0016-7037(99)00343-9

Grove, M., & Harrison, T. M. (1996). ^{40}Ar* diffusion in Fe-rich biotite. American Mineralogist, 81, 940–951.

Guillong, M., Horn, I., & Gunther, D. (2003). A comparison of 266 nm, 213 nm and 193 nm produced from a single solid state Nd:YAG laser for laser ablation ICP-MS. Journal of Analytical Atomic Spectrometry, 18(10), 1224–1230. https://doi.org/10.1039/B305434A

Guillong, M., & Gunther, D. (2002). Effect of particle size distribution on ICP-induced elemental fractionation in laser ablation-inductively coupled plasma-mass spectrometry. Journal of Analytical Atomic Spectrometry, 17(8), 831–837. https://doi.org/10.1039/b202988j

Hacker, B. R., Kelemen, P. B., & Behn, M. D. (2011). Differentiation of the continental crust by relamination. Earth and Planetary Science Letters, 307(3–4), 501–516. https://doi.org/10.1016/J.EPSL.2011.05.024

Hanchar, J. M., & van Westrenen, W. (2007). Rare Earth Element Behavior in Zircon-Melt Systems. Elements, 3(1), 37 LP-42. Retrieved from http://elements.geoscienceworld.org/content/3/1/37.abstract

Hanselman, D. S., Sesi, N. N., Huang, M., & Hieftje, G. M. (1994). The effect of sample matrix on electron density, electron temperature and gas temperature in the argon inductively coupled plasma examined by Thomson and Rayleigh scattering. Spectrochimica Acta Part B: Atomic Spectroscopy, 49(5), 495–526. https://doi.org/10.1016/0584-8547(94)80042-1

Hanson, R. E., Wardlaw, M. S., Wilson, T. J., Mwale, G., Sciences, G., Diego, S., & Box, P. O. (1993). U-Pb zircon ages from the Hook granite massif and Mwembeshi dislocation : constraints on Pan-African deformation , plutonism , and transcurrent shearing in central Zambia. Precambrian Research, 63, 189–209.

Hargrove, U. S., Stern, R. J., Kimura, J.-I., Manton, W. I., & Johnson, P. R. (2006). How juvenile is the Arabian–Nubian Shield? Evidence from Nd isotopes and pre-Neoproterozoic inherited zircon in the Bi'r Umq suture zone, Saudi Arabia. Earth and Planetary Science Letters, 252(3–4), 308–326. https://doi.org/10.1016/J.EPSL.2006.10.002

Harley, S. L., & Nandakumar, V. (2014). Accessory Mineral Behaviour in Granulite Migmatites: a Case Study from the Kerala Khondalite Belt, India. Journal of Petrology, 55(10), 1965–2002. https://doi.org/10.1093/petrology/egu047

Harlov Daniel E. and Procházka, V. and F. H.-J. and M. D. (2008). Origin of monazite–xenotime–zircon–fluorapatite assemblages in the peraluminous Melechov granite massif, Czech Republic. Mineralogy and Petrology, 94(1), 9–26. https://doi.org/10.1007/s00710-008-0003-8

Harlov, D. E., & Hetherington, C. J. (2010). Partial high-grade alteration of monazite using alkali-bearing fluids: Experiment and nature. American Mineralogist, 95(7), 1105–1108. Retrieved from http://dx.doi.org/10.2138/am.2010.3525

Harrison, T. M., Catlos, E. J., & Montel, J.-M. (2002). U-Th-Pb Dating of Phosphate Minerals. (J. M. Hughes, M. Kohn, & J. Rakovan, Eds.), Reviews in Mineralogy and Geochemistry (Vol. 48). Chantilly, Virginia: Mineralogical Society of America. https://doi.org/10.2138/rmg.2002.48.14

Harrison, T. M., Duncan, I., & McDougall, I. (1985). Diffusion of 40Ar in biotite: Temperature, pressure and compositional effects. Geochimica et Cosmochimica Acta, 49(11), 2461–2468. https://doi.org/10.1016/0016-7037(85)90246-7

Hattendorf, B., Gusmini, B., Dorta, L., Houk, R. S., & Günther, D. (2016). Abundance and Impact of Doubly Charged Polyatomic Argon Interferences in ICPMS Spectra. Analytical Chemistry, 88(14), 7281–7288. https://doi.org/10.1021/acs.analchem.6b01614

Hauri, E. H., Wagner, T. P., & Grove, T. L. (1994). Experimental and natural partitioning of Th, U, Pb and other trace elements between garnet, clinopyroxene and basaltic melts. Chemical Geology, 117(1–4), 149–166. https://doi.org/10.1016/0009-2541(94)90126-0

Hawkesworth, C. J., Cawood, P. A., Dhuime, B., & Kemp, T. I. (2017). Earth's continental

lithosphere through time. Annual Review of Earth and Planetary Sciences, 45, 169–198.
Hawkesworth, C., Cawood, P., Kemp, T., Storey, C., & Dhuime, B. (2009). A Matter of Preservation. Science, 323(5910), 49 LP-50. https://doi.org/10.1126/science.1168549
Hayama, Y., Yamada, T., Ito, M., Kutsukake, T., Masaoka, K., Miyakawa, K., … Tsumura, Y. (1982). Geology of the Ryoke Belt in the eastern Kinki District, Japan-The phase-divisions and the mutual relations of the granitic rocks. J. Geol. Soc. Japan, 88(6), 451–466.
Haynes., W. M. (2013). CRC Handbook of Chemistry and Physics (94th ed.). Boca Raton: CRC Press.
Hetherington, C. J., Backus, E. L., McFarlane, C. R., Fisher, C. M., & Pearson, D. G. (2017). Origins of Textural, Compositional, and Isotopic Complexity in Monazite and Its Petrochronological Analysis. In Desmond E. Moser, Fernando Corfu, James R. Darling, Steven M. Reddy, & Kimberly Tait (Eds.), Microstructural Geochronology: Planetary Records Down to Atom Scale (pp. 63–90). New Jersey: John Wiley & Sons, Inc.
Hetherington, C. J., Harlov, D. E., & Budzyń, B. (2010). Experimental metasomatism of monazite and xenotime: mineral stability, REE mobility and fluid composition. Mineralogy and Petrology, 99(3), 165–184. https://doi.org/10.1007/s00710-010-0110-1
Hidaka, H., Ebihara, M., & Shima, M. (1995). Determination of the isotopic compositions of samarium and gadolinium by thermal ionization mass spectrometry. Analytical Chemistry, 67(8), 1437–1441.
Hietpas, J., Samson, S., Moecher, D., & Schmitt, A. K. (2010). Recovering tectonic events from the sedimentary record: Detrital monazite plays in high fidelity. Geology, 38(2), 167–170. https://doi.org/10.1130/G30265.1
Hietpas, J., Samson, S., & Moecher, D. (2011). A direct comparison of the ages of detrital monazite versus detrital zircon in Appalachian foreland basin sandstones: Searching for the record of Phanerozoic orogenic events. Earth and Planetary Science Letters, 310(3–4), 488–497. https://doi.org/10.1016/j.epsl.2011.08.033
Hinton, R. W., & Upton, B. G. . (1991). The chemistry of zircon: Variations within and between large crystals from syenite and alkali basalt xenoliths. Geochimica et Cosmochimica Acta, 55(11), 3287–3302. https://doi.org/10.1016/0016-7037(91)90489-R
Hirahara, Y., Chang, Q., Miyazaki, T., Takahashi, T., & Kimura, J.-I. (2012). Improved Nd chemical separation technique for $^{143}Nd/^{144}Nd$ analysis in geological samples using packed Ln resin columns. JAMSTEC Report of Research and Development, 15, 27–33. https://doi.org/10.5918/jamstecr.15.27
Holbrook, W. S., Mooney, W. D., & Christensen, N. I. (1992). The seismic velocity structure of the deep continental crust. Continental Lower Crust, 23, 1–43.
Holder, R. M., Hacker, B. R., Kylander-Clark, A. R. C., & Cottle, J. M. (2015). Monazite trace-element and isotopic signatures of (ultra)high-pressure metamorphism: Examples from the Western Gneiss Region, Norway. Chemical Geology, 409, 99–111. https://doi.org/10.1016/j.chemgeo.2015.04.021
Horstwood, M. S. A., Foster, G. L., Parrish, R. R., Noble, S. R., & Nowell, G. M. (2003). Common-Pb corrected in situ U–Pb accessory mineral geochronology by LA-MC-ICP-MS. Journal of Analytical Atomic Spectrometry, 18(8), 837. https://doi.org/10.1039/b304365g
Hoshino, M., & Ishihara, S. (2007). REE-bearing minerals of the late Cretaceous ilmenite-series granites of the inner zone of southwest Japan. Mining Geology, 57, 103–114.
Hoshino, M., Kimata, M., Shimizu, M., Nishida, N., & Fujiwara, T. (2006). Allanite-(Ce) in granitic rocks from Japan: gentetic implications of patterns of REE and Mn enrichment. The Canadian Mineralogist, 44(1), 45–62. https://doi.org/10.2113/gscanmin.44.1.45
Hoshino, M., Kimata, M., Shimizu, M., Nishida, N., Fujiwara, T., Arakawa, Y., … Nakai, S. (2007). Allanite-(Ce) as an indicator of the origin of granitic rocks in Japan: importance of Sr–Nd isotopic and chemical composition. The Canadian Mineralogist, 44(6), 45 LP-62. Retrieved from http://www.canmin.org/content/45/6/1329.abstract
Hoshino, M., Watanabe, Y., & Ishihara, S. (2012). Crystal chemistry of monazite from the granitic rocks of Japan: petrogenetic implications. The Canadian Mineralogist, 50(5), 1331 LP-1346. Retrieved from http://www.canmin.org/content/50/5/1331.abstract

Hoskin, P. W. O., & Ireland, T. R. (2000). Rare earth element chemistry of zircon and its use as a provenance indicator. Geology, 28(7), 627–630. https://doi.org/10.1130/0091-7613(2000)28<627:REECOZ>2.0.CO;2
Houk, R. S., & Praphairaksit, N. (2001). Dissociation of polyatomic ions in the inductively coupled plasma. Spectrochimica Acta Part B: Atomic Spectroscopy, 56, 1069–1096.
Huminicki, D. M. C., & Hawthorne, F. C. (2002). The Crystal Chemistry of the Phosphate Minerals. Reviews in Mineralogy and Geochemistry, 48(1), 123–253. Retrieved from http://dx.doi.org/10.2138/rmg.2002.48.5
Iizuka, T., Campbell, I. H., Allen, C. M., Gill, J. B., Maruyama, S., & Makoka, F. (2013). Evolution of the African continental crust as recorded by U–Pb, Lu–Hf and O isotopes in detrital zircons from modern rivers. Geochimica et Cosmochimica Acta, 107, 96–120. https://doi.org/10.1016/j.gca.2012.12.028
Iizuka, T., Eggins, S. M., McCulloch, M. T., Kinsley, L. P. J., & Mortimer, G. E. (2011). Precise and accurate determination of 147Sm/144Nd and 143Nd/144Nd in monazite using laser ablation-MC-ICPMS. Chemical Geology, 282(1), 45–57. https://doi.org/10.1016/j.chemgeo.2011.01.008
Iizuka, T., Komiya, T., Rino, S., Maruyama, S., & Hirata, T. (2010). Detrital zircon evidence for Hf isotopic evolution of granitoid crust and continental growth. Geochimica et Cosmochimica Acta, 74(8), 2450–2472. https://doi.org/10.1016/j.gca.2010.01.023
Iizuka, T., McCulloch, M. T., Komiya, T., Shibuya, T., Ohta, K., Ozawa, H., … Collerson, K. D. (2010). Monazite geochronology and geochemistry of meta-sediments in the Narryer Gneiss Complex, Western Australia: constraints on the tectonothermal history and provenance. Contributions to Mineralogy and Petrology, 160(6), 803–823. https://doi.org/10.1007/s00410-010-0508-0
Iizuka, T., Nebel, O., & McCulloch, M. T. (2011). Tracing the provenance and recrystallization processes of the Earth's oldest detritus at Mt. Narryer and Jack Hills, Western Australia: An in situ Sm–Nd isotopic study of monazite. Earth and Planetary Science Letters, 308(3–4), 350–358. https://doi.org/10.1016/j.epsl.2011.06.006
Iizuka, T., Yamaguchi, T., Itano, K., Hibiya, Y., & Suzuki, K. (2017). What Hf isotopes in zircon tell us about crust–mantle evolution. *Lithos*, *274*, 304-327.
Iizumi, S., Imaoka, T., & Kagami, H. (2000). Sr–Nd isotope ratios of gabbroic and dioritic rocks in a Cretaceous-Paleogene granite terrain, Southwest Japan. Island Arc, 9(1), 113–127. https://doi.org/10.1046/j.1440-1738.2000.00265.x
Ireland, T. R., & Gibson, G. M. (1998). SHRIMP monazite and zircon geochronology of high-grade metamorphism in New Zealand. Journal of Metamorphic Geology, 16(2), 149–167. https://doi.org/10.1111/j.1525-1314.1998.00112.x
Ishihara, S., & Chappell, B. W. (2007). Chemical compositions of the late Cretaceous Ryoke granitoids of the Chubu District, central Japan–Revisited. Bulletin of the Geological Survey of Japan, 58(9–10), 323–350.
Ishihara, S. (1971). Major molybdenum deposits and related granitic rocks in Japan. Report of the Geological Survey of Japan, 239, 68.
Ishihara, S. (1977). The magnetite-series and ilmenite-series granitic rocks. Mining Geology, 27, 293–305.
Ishihara, S., & Matsuhisa, Y. (2002). Oxygen isotopic constraints on the geneses of the Cretaceous-Paleogene granitoids in the Inner Zone of Southwest Japan. Bull. Geol. Surv. Japan, 53(4), 421–438.
Ishihara, S., & Murakami, H. (2006). Fractionated ilmenite- series granites in southwest Japan: source magma for REE- Sn-W mineralizations. Resource Geology, 56, 235–256.
Ishihara, S., & Sasaki, A. (1989). Sulfur isotopic ratios of the magnetite-series and ilmenite-series granitoids of the Sierra Nevada batholith—A reconnaissance study. Geology, 17(9), 788–791. Retrieved from http://dx.doi.org/10.1130/0091-7613(1989)017%3C0788:SIROTM%3E2.3.CO
Isozaki, Y., Aoki, K., Nakama, T., & Yanai, S. (2010). New insight into a subduction-related orogen: A reappraisal of the geotectonic framework and evolution of the Japanese Islands. Gondwana Research, 18(1), 82–105. https://doi.org/10.1016/j.gr.2010.02.015

Itano, K., & Iizuka, T. (2017). Unraveling the mechanism and impact of oxide production in LA-ICP-MS by comprehensive analysis of REE-Th-U phosphates. Journal of Analytical Atomic Spectrometry, 32(10). https://doi.org/10.1039/c7ja00182g

Itano, K., Iizuka, T., Chang, Q., Kimura, J.-I., & Maruyama, S. (2016). U–Pb chronology and geochemistry of detrital monazites from major African rivers: Constraints on the timing and nature of the Pan-African Orogeny. Precambrian Research, 282(139–156). https://doi.org/10.1016/j.precamres.2016.07.008

Itano, K., Iizuka, T., & Hoshino, M. (2017). REE-Th-U and Nd isotope systematics of monazites in magnetite- and ilmenite-series granitic rocks of the Japan arc: Implications for its use as a tracer of magma evolution and detrital provenance. Chemical Geology. https://doi.org/10.1016/j.chemgeo.2017.11.033

Jacobs, J., Bauer, W., & Fanning, C. M. (2003). New age constraints for Grenville-age metamorphism in western central Dronning Maud Land (East Antarctica), and implications for the palaeogeography of Kalahari in Rodinia. International Journal of Earth Sciences, 92(3), 301–315. https://doi.org/10.1007/s00531-003-0335-x

Jacobs, J., Bingen, B., Thomas, R. J., Bauer, W., Wingate, M., & Feitio, P. (2008). Early Palaeozoic orogenic collapse and voluminous late-tectonic magmatism in Dronning Maud Land and Mozambique : insights into the partially delaminated orogenic root of the East African-Antarctic Orogen? Geodynamic Evolution of East Antarctica: A Key to the East–West Gondwana Connection, 308, 69–90. https://doi.org/10.1144/SP308.3

Jacobs, J., Pisarevsky, S., Thomas, R. J., & Becker, T. (2008). The Kalahari Craton during the assembly and dispersal of Rodinia. Precambrian Research, 160(1–2), 142–158. https://doi.org/10.1016/j.precamres.2007.04.022

Jagoutz, O. E. (2010). Construction of the granitoid crust of an island arc. Part II: a quantitative petrogenetic model. Contributions to Mineralogy and Petrology, 160(3), 359–381. https://doi.org/10.1007/s00410-009-0482-6

Jagoutz, O., Müntener, O., Schmidt, M. W., & Burg, J.-P. (2011). The roles of flux- and decompression melting and their respective fractionation lines for continental crust formation: Evidence from the Kohistan arc. Earth and Planetary Science Letters, 303(1–2), 25–36. https://doi.org/10.1016/J.EPSL.2010.12.017

Jagoutz, O., & Schmidt, M. W. (2012). The formation and bulk composition of modern juvenile continental crust: The Kohistan arc. Chemical Geology, 298–299, 79–96. https://doi.org/10.1016/J.CHEMGEO.2011.10.022

Jamieson, R. A., Beaumont, C., Medvedev, S., & Nguyen, M. H. (2004). Crustal channel flows: 2. Numerical models with implications for metamorphism in the Himalayan-Tibetan orogen. *Journal of Geophysical Research: Solid Earth*, *109*(B6). https://doi.org/10.1029/2003JB002811

Janots, E., Engi, M., Berger, A., Allaz, J., Schwarz, J. O., & Spandler, C. (2008). Prograde metamorphic sequence of REE minerals in pelitic rocks of the Central Alps: Implications for allanite-monazite-xenotime phase relations from 250 to 610??C. Journal of Metamorphic Geology, 26(5), 509–526. https://doi.org/10.1111/j.1525-1314.2008.00774.x

Jantos, E., Berger, A., Gnos, E., Whitehouse, M., Eric, L., & Thomas, P. (2012). Constraints on fluid evolution during metamorphism from U–Th–Pb systematics in Alpine hydrothermal monazite. Chemical Geology, 326–327(61–71).

Jercinovic, M. J., & Williams, M. L. (2005). Analytical perils (and progress) in electron microprobe trace element analysis applied to geochronology: Background acquisition, interferences, and beam irradiation effects. American Mineralogist, 90(4), 526–546. https://doi.org/10.2138/am.2005.1422

Johannes Wilhelm and Holtz, F. (1996). The Granite System Qz-Ab-Or-An. In Petrogenesis and Experimental Petrology of Granitic Rocks (pp. 229–243). Berlin, Heidelberg: Springer Berlin Heidelberg. https://doi.org/10.1007/978-3-642-61049-3_7

John, T., Schenk, V., Haase, K., Scherer, E., & Tembo, F. (2003). Evidence for a Neoproterozoic ocean in south-central Africa from mid-ocean-ridge-type geochemical signatures and pressure-temperature estimates of Zambian eclogites. Geology, 31(3), 243–246. https://doi.org/10.1130/0091-7613(2003)031<0243:EFANOI>2.0.CO;2

John, T., Schenk, V., Mezger, K., & Tembo, F. (2004). Timing and PT Evolution of Whiteschist Metamorphism in the Lufilian Arc–Zambezi Belt Orogen (Zambia): Implications for the Assembly of Gondwana. The Journal of Geology, 112(1), 71–90. https://doi.org/10.1086/379693

Johnson, K. T. M. (1998). Experimental determination of partition coefficients for rare earth and high-field-strength elements between clinopyroxene, garnet, and basaltic melt at high pressures. Contributions to Mineralogy and Petrology, 133(1), 60–68. https://doi.org/10.1007/s004100050437

Johnson, P. R. (2014). An expanding Arabian-Nubian shield geochronologic and isotopic dataset: defining limits and confirming the tectonic setting of a Neoproterozoic Accretionary Orogen. Open Geol. J., (8), 3–33.

Johnson, P. R., Andresen, A., Collins, A. S., Fowler, A. R., Fritz, H., Ghebreab, W., … Stern, R. J. (2011). Late Cryogenian–Ediacaran history of the Arabian–Nubian Shield: A review of depositional, plutonic, structural, and tectonic events in the closing stages of the northern East African Orogen. Journal of African Earth Sciences, 61(3), 167–232. https://doi.org/10.1016/J.JAFREARSCI.2011.07.003

Johnson, S. P., De Waele, B., & Liyungu, K. A. (2006). U-Pb sensitive high-resolution ion microprobe (SHRIMP) zircon geochronology of granitoid rocks in eastern Zambia: Terrane subdivision of the Mesoproterozoic Southern Irumide Belt. Tectonics, 25(6). https://doi.org/10.1029/2006TC001977

Johnson, S. P., De Waele, B., Evans, D., Banda, W., Tembo, F., Milton, J. A., & Tani, K. (2007). Geochronology of the Zambezi Supracrustal Sequence, Southern Zambia: A Record of Neoproterozoic Divergent Processes along the Southern Margin of the Congo Craton. The Journal of Geology, 115(3), 355–374. https://doi.org/10.1086/512757

Johnson, S. P., Rivers, T., & De Waele, B. (2005). A review of the Mesoproterozoic to early Palaeozoic magmatic and tectonothermal history of south-central Africa: implications for Rodinia and Gondwana. Journal of the Geological Society, 162(3), 433–450. https://doi.org/10.1144/0016-764904-028

Kagami, H., Kawano, Y., Ikawa, T., Ishioka, J., Kagashima, S., Yuhara, M., … Tainosho, Y. (1999). Transition of space and time of Cretaceous to Tertiary igneous activity and lower crust of Honshu Arc: examination based on Rb–Sr whole rock isochron ages and Sr and Nd isotopes. Memoirs of the Geological Society of Japan, 53, 1–19.

Kagami, H. (1973). A Rb—Sr Geochronological study of the Ryoke granites in Chubu district, central Japan. The Journal of the Geological Society of Japan, 79(1), 1–10. https://doi.org/10.5575/geosoc.79.1

Kampunzu, a. B., Tembo, F., Matheis, G., Kapenda, D., & Huntsman-Mapila, P. (2000). Geochemistry and Tectonic Setting of Mafic Igneous Units in the Neoproterozoic Katangan Basin, Central Africa: Implications for Rodinia Break-up. Gondwana Research, 3(2), 125–153. https://doi.org/10.1016/S1342-937X(05)70093-9

Katayama, I., Maruyama, S., Parkinson, C. D., Terada, K., & Sano, Y. (2001). Ion micro-probe U–Pb zircon geochronology of peak and retrograde stages of ultrahigh-pressure metamorphic rocks from the Kokchetav massif, northern Kazakhstan. Earth and Planetary Science Letters, 188(1–2), 185–198. https://doi.org/10.1016/S0012-821X(01)00319-3

Kawakami, T., & Suzuki, K. (2011). CHIME monazite dating as a tool to detect polymetamorphism in high-temperature metamorphic terrane: Example from the Aoyama area, Ryoke metamorphic belt, Southwest Japan. Island Arc, 20, 439–453.

Kay, R. W., & Mahlburg Kay, S. (1993). Delamination and delamination magmatism. Tectonophysics, 219(1–3), 177–189. https://doi.org/10.1016/0040-1951(93)90295-U

Kelly, N. M., Harley, S. L., & Möller, A. (2012). Complexity in the behavior and recrystallization of monazite during high-T metamorphism and fluid infiltration. Chemical Geology, 322–323, 192–208. https://doi.org/10.1016/j.chemgeo.2012.07.001

Kelts, A. B., Ren, M., & Anthony, E. Y. (2008). Monazite occurrence, chemistry, and chronology in the granitoid rocks of the Lachlan Fold Belt, Australia: An electron microprobe study. American Mineralogist, 93(2–3), 373–383. https://doi.org/10.2138/am.2008.2600

Kemp, A. I. S., Hawkesworth, C. J., Paterson, B. A., & Kinny, P. D. (2006). Episodic growth of the

Gondwana supercontinent from hafnium and oxygen isotopes in zircon. Nature, 439, 580. Retrieved from https://doi.org/10.1038/nature04505
Kent, A. J. R., & Ungerer, C. A. "Andy." (2005). Production of barium and light rare earth element oxides during LA-ICP-MS microanalysis. Journal of Analytical Atomic Spectrometry, 20, 1256. https://doi.org/10.1039/b505734e
Key, R. M., Liyungu, A. K., Njamu, F. M., Somwe, V., Banda, J., Mosley, P. N., & Armstrong, R. A. (2001). The western arm of the Lufilian Arc in NW Zambia and its potential for copper mineralization. Journal of African Earth Sciences, 33(3–4), 503–528. https://doi.org/10.1016/S0899-5362(01)00098-7
Key, R. M., Johnson, C. C., Horstwood, M. S. A., Lapworth, D. J., Knights, K. V., Kemp, S. J., … Arisekola, T. (2012). Investigating high zircon concentrations in the fine fraction of stream sediments draining the Pan-African Dahomeyan Terrane in Nigeria. Applied Geochemistry, 27(8), 1525–1539. https://doi.org/10.1016/J.APGEOCHEM.2012.04.009
Kimura, J. I., Takahashi, T., & Chang, Q. (2013). A new analytical bias correction for in situ Sr isotope analysis of plagioclase crystals using laser-ablation multiple-collector inductively coupled plasma mass spectrometry. Journal of Analytical Atomic Spectrometry, 28(6), 945–957.
Kimura, J.-I. J.-I., Chang, Q., Itano, K., Iizuka, T., Vaglarov, B. S. B. S., & Tani, K. (2015). An improved U–Pb age dating method for zircon and monazite using 200/266 nm femtosecond laser ablation and enhanced sensitivity multiple-Faraday collector inductively coupled plasma mass spectrometry. J. Anal. At. Spectrom., 30(2), 494–505. https://doi.org/10.1039/C4JA00257A
Kimura, J.-I., Chang, Q., & Hiroshi, K. (2013). Standardless determination of Nd isotope ratios in glasses and minerals using laser-ablation multiple-collector inductively coupled plasma mass spectrometry with a low-oxide molecular yield interface setup, 28, 1522–1529. https://doi.org/10.1039/c3ja50109d
Kimura, J.-I., Chang, Q., & Tani, K. (2011). Optimization of ablation protocol for 200 nm UV femtosecond laser in precise U – Pb age dating coupled to multi-collector ICP mass spectrometry. Geochmical Journal, 45, 283–296.
Kinoshita, O. (1995). Migration of igneous activities related to ridge subduction in Southwest Japan and the East Asian continental margin from the Mesozoic to the Paleogene. Tectonophysics, 245(1–2), 25–35. https://doi.org/10.1016/0040-1951(94)00211-Q
Koegelenberg, C., Kisters, A. F. M., Kramers, J. D., & Frei, D. (2015). U–Pb detrital zircon and 39Ar–40Ar muscovite ages from the eastern parts of the Karagwe-Ankole Belt: Tracking Paleoproterozoic basin formation and Mesoproterozoic crustal amalgamation along the western margin of the Tanzania Craton. Precambrian Research, 269, 147–161. https://doi.org/10.1016/J.PRECAMRES.2015.08.014
Kohn, M. J., Wieland, M. S., Parkinson, C. D., & Upreti, B. N. (2005). Five generations of monazite in Langtang gneisses: implications for chronology of the Himalayan metamorphic core. Journal of Metamorphic Geology, 23(5), 399–406. https://doi.org/10.1111/j.1525-1314.2005.00584.x
Kokonyangi, J., Armstrong, R., Kampunzu, a. B., Yoshida, M., & Okudaira, T. (2004). U-Pb zircon geochronology and petrology of granitoids from Mitwaba (Katanga, Congo): Implications for the evolution of the Mesoproterozoic Kibaran belt. Precambrian Research, 132(1–2), 79–106. https://doi.org/10.1016/j.precamres.2004.02.007
Korenaga, J. (2013). Initiation and evolution of plate tectonics on Earth: theories and observations. Annual Review of Earth and Planetary Sciences, 41(1), 117–151.
Kosler, J., Tubrett, M. N., & Sylvester, P. J. (2001). Application of Laser Ablation ICP-MS to U-Th-Pb Dating of Monazite. Geostandards and Geoanalytical Research, 25(2–3), 375–386. https://doi.org/10.1111/j.1751-908X.2001.tb00612.x
Kretz, R. (1983). Symbols for rock-forming minerals. American Mineralogist, 68, 277–279. Retrieved from http://ci.nii.ac.jp/naid/10023911240/ja/
Kröner, A., & Stern, R. J. (2004). Pan-African Orogeny. In R. Shell, L. R. M. Cocks, & I. R. Plimer (Eds.), Encyclopedia of Geolgoy (Vol. 1, pp. 1–12). Elsevier.
Kubota, M., Fudagawa, N., & Kawase, A. (1989). Monoxide Ion Signals in Inductively Coupled Plasma Mass Spectrometry. Analytical Scinences, 5, 701–706.
Kuhn, H.-R., & Günther, D. (2004). Laser ablation-ICP-MS: particle size dependent elemental

composition studies on filter-collected and online measured aerosols from glass. Journal of Analytical Atomic Spectrometry, 19(9), 1158–1164. https://doi.org/10.1039/B404729J

Kusiak, M. A., Kędzior, A., Paszkowski, M., Suzuki, K., González-Álvarez, I., Wajsprych, B., & Doktor, M. (2006). Provenance implications of Th-U-Pb electron microprobe ages from detrital monazite in the Carboniferous Upper Silesia Coal Basin, Poland. Lithos, 88(1–4), 56–71. https://doi.org/10.1016/j.lithos.2005.08.004

Kusiak, M. A., Williams, I. S., Dunkley, D. J., Konečný, P., Slaby, E., & Martin, H. (2014). Monazite to the rescue: U–Th–Pb dating of the intrusive history of the composite Karkonosze pluton, Bohemian Massif. Chemical Geology, 364, 76–92.

Küster, D., Liégeois, J.-P., Matukov, D., Sergeev, S., & Lucassen, F. (2008). Zircon geochronology and Sr, Nd, Pb isotope geochemistry of granitoids from Bayuda Desert and Sabaloka (Sudan): Evidence for a Bayudian event (920–900Ma) preceding the Pan-African orogenic cycle (860–590Ma) at the eastern boundary of the Saharan Metacrato. Precambrian Research, 164(1–2), 16–39. https://doi.org/10.1016/j.precamres.2008.03.003

Large, R. R., Mukherjee, I., Zhukova, I., Corkrey, R., Stepanov, A., & Danyushevsky, L. V. (2018). Role of upper-most crustal composition in the evolution of the Precambrian ocean–atmosphere system. Earth and Planetary Science Letters, 487, 44–53. https://doi.org/10.1016/J.EPSL.2018.01.019

Lee, D. E., & Bastron, H. (1967). Fractionation of rare-earth elements in allanite and monazite as related to geology of the Mt. Wheeler mine area, Nevada. Geochimica et Cosmochimica Acta, 31, 339–356.

Lee, J. K. W., Williams, I. S., & Ellis, D. J. (1997). Pb, U and Th diffusion in natural zircon. Nature, 390, 159. Retrieved from https://doi.org/10.1038/36554

Leggo, P. J. (1974). A geochronological study of the basement complex of Uganda. Journal of the Geological Society, 130, 263–276. https://doi.org/10.1144/gsjgs.130.3.0263

Lichte, F. E., Meier, A. L., & Crock, J. G. (1987). Determination of the rare-earth elements in geological materials by inductively coupled plasma mass spectrometry. Analytical Chemistry, 59(8), 1150–1157. https://doi.org/10.1021/ac00135a018

Liégeois, J. P., Bertrand, J. M., & Black, R. (1987). The subduction- and collision-related Pan-African composite batholith of the Adrar des Iforas (Mali): A review. Geological Journal, 22(S2), 185–211. https://doi.org/10.1002/gj.3350220615

Liégeois, J. P., Latouche, L., Boughrara, M., Navez, J., & Guiraud, M. (2003). The LATEA metacraton (Central Hoggar, Tuareg shield, Algeria): behaviour of an old passive margin during the Pan-African orogeny. Journal of African Earth Sciences, 37(3–4), 161–190. https://doi.org/10.1016/j.jafrearsci.2003.05.004

Liégeois, J.-P., Abdelsalam, M. G., Ennih, N., & Ouabadi, A. (2013). Metacraton: Nature, genesis and behavior. Gondwana Research, 23(1), 220–237. https://doi.org/10.1016/J.GR.2012.02.016

Lindner, H., & Bogaerts, A. (2011). Multi-element model for the simulation of inductively coupled plasmas: Effects of helium addition to the central gas stream. Spectrochimica Acta Part B: Atomic Spectroscopy, 66(6), 421–431. https://doi.org/10.1016/j.sab.2011.04.007

Linnen, R. L., Van Lichtervelde, M., & Černý, P. (2012). Granitic Pegmatites as Sources of Strategic Metals. Elements, 8(4), 275 LP-280. Retrieved from http://elements.geoscienceworld.org/content/8/4/275.abstract

Liu, X.-C., Wu, Y.-B., Fisher, C. M., Hanchar, J. M., Beranek, L., Gao, S., & Wang, H. (2017). Tracing crustal evolution by U-Th-Pb, Sm-Nd, and Lu-Hf isotopes in detrital monazite and zircon from modern rivers. Geology, 45(2), 103–106. https://doi.org/10.1130/G38720.1

Lompo, M. (2010). Paleoproterozoic structural evolution of the Man-Leo Shield (West Africa). Key structures for vertical to transcurrent tectonics. Journal of African Earth Sciences, 58(1), 19–36. https://doi.org/10.1016/J.JAFREARSCI.2010.01.005

London, D. (2005). Granitic pegmatites: an assessment of current concepts and directions for the future. Lithos, 80(1–4), 281–303. https://doi.org/10.1016/j.lithos.2004.02.009

Longerich, H. P., Fryer, B. J., Strong, D. F., & Kantipuly, C. J. (1987). Effects of operating conditions on the determination of the rare earth elements by inductively coupled plasma-mass spectrometry (ICP-MS). Spectrochimica Acta Part B: Atomic Spectroscopy, 42(1), 75–92.

https://doi.org/10.1016/0584-8547(87)80051-4
Machado, N., & Gauthier, G. (1996). Determination of 207Pb/206Pb ages on zircon and monazite by laser-ablation ICPMS and application to a study of sedimentary provenance and metamorphism in southeastern Brazil. Geochimica et Cosmochimica Acta, 60(24), 5063–5073. https://doi.org/10.1016/S0016-7037(96)00287-6
Mahan, K. H., Gonccalves, P., Williams, M. L., & Jercinovic, M. J. (2006). Dating metamorphic reactions and fluid flow: application to exhumation of high-P granulites in a crustal-scale shear zone, western Canadian Shield. Journal of Metamorphic Geology, 24(3), 193–217. https://doi.org/10.1111/j.1525-1314.2006.00633.x
Makimoto, H., Yamada, N., Mizuno, K., Takada, A., Komazawa, M., & Sudo, S. (2004). Geological map of Japan 1: 200,000, Toyohashi and Irago Misaki. (in Japanese with English Abstract). Geological Survey of Japan.
Manya, S., & Maboko, M. a. H. (2003). Dating basaltic volcanism in the Neoarchaean Sukumaland Greenstone Belt of the Tanzania Craton using the Sm–Nd method: implications for the geological evolution of the Tanzania Craton. Precambrian Research, 121(1–2), 35–45. https://doi.org/10.1016/S0301-9268(02)00195-X
Manya, S., Kobayashi, K., Maboko, M. A. H., & Nakamura, E. (2006). Ion microprobe zircon U–Pb dating of the late Archaean metavolcanics and associated granites of the Musoma-Mara Greenstone Belt, Northeast Tanzania: Implications for the geological evolution of the Tanzania Craton. Journal of African Earth Sciences, 45(3), 355–366. https://doi.org/10.1016/j.jafrearsci.2006.03.004
Maruyama, S., Isozaki, Y., Kimura, G., & Terabayashi, M. (1997). Paleogeographic maps of the Japanese Islands: Plate tectonic synthesis from 750 Ma to the present. The Island Arc, 6(1), 121–142. https://doi.org/10.1111/j.1440-1738.1997.tb00043.x
Maruyama, S., & Seno, T. (1986). Orogeny and relative plate motions: Example of the Japanese Islands. Tectonophysics, 127(3–4), 305–329. https://doi.org/10.1016/0040-1951(86)90067-3
Massonne, H.-J. (2005). Involvement of Crustal Material in Delamination of the Lithosphere after Continent-Continent Collision. International Geology Review, 47(8), 792–804. https://doi.org/10.2747/0020-6814.47.8.792
Masuda, A., Kawakami, O., Dohmoto, Y., & Takenaka, T. (1987). Lanthanide tetrad effects in nature: two mutually opposite types, W and M. GEOCHEMICAL JOURNAL, 21(3), 119–124. https://doi.org/10.2343/geochemj.21.119
Matsuda, T., & Uyeda, S. (1971). On the pacific-type orogeny and its model — extension of the paired belts concept and possible origin of marginal seas. *Tectonophysics*, *11*(1), 5–27. https://doi.org/10.1016/0040-1951(71)90076-X
McCourt, S., Armstrong, R. A., Grantham, G. H., & Thomas, R. J. (2006). Geology and evolution of the Natal belt, South Africa. Journal of African Earth Sciences, 46(1–2), 71–92. https://doi.org/10.1016/J.JAFREARSCI.2006.01.013
McDonough, W. F., & Sun, S. -s. (1995). The composition of the Earth. Chemical Geology, 120(3–4), 223–253. https://doi.org/10.1016/0009-2541(94)00140-4
Mcfarlane, C. R. M., & Mcculloch, M. T. (2007). Coupling of in-situ Sm–Nd systematics and U–Pb dating of monazite and allanite with applications to crustal evolution studies. Chemical Geology, 245(1–2), 45–60. https://doi.org/10.1016/j.chemgeo.2007.07.020
McFarlane, C. R. M., & Mark Harrison, T. (2006). Pb-diffusion in monazite: Constraints from a high-T contact aureole setting. Earth and Planetary Science Letters, 250(1–2), 376–384. https://doi.org/10.1016/J.EPSL.2006.06.050
Meert, J. G. (2003). A synopsis of events related to the assembly of eastern Gondwana. Tectonophysics, 362(1–4), 1–40. https://doi.org/10.1016/S0040-1951(02)00629-7
Meert, J. G., & Lieberman, B. S. (2008). The Neoproterozoic assembly of Gondwana and its relationship to the Ediacaran–Cambrian radiation. Gondwana Research, 14(1–2), 5–21. https://doi.org/10.1016/j.gr.2007.06.007
Meinhold, G., Morton, A. C., & Avigad, D. (2013). New insights into peri-Gondwana paleogeography and the Gondwana super-fan system from detrital zircon U–Pb ages. Gondwana Research, 23(2), 661–665. https://doi.org/10.1016/j.gr.2012.05.003

Meldrum, A., Boatner, L. A., Weber, W. J., & Ewing, R. C. (1998). Radiation damage in zircon and monazite. Geochimica et Cosmochimica Acta, 62(14), 2509–2520. https://doi.org/10.1016/S0016-7037(98)00174-4
Meldrum, A., Boatner, L. A., Weber, W. J., & Ewing, R. C. (1998). Radiation damage in zircon and monazite. Geochimica et Cosmochimica Acta, 62(14), 2509–2520. https://doi.org/10.1016/S0016-7037(98)00174-4
Miller, C. F., McDowell, S. M., & Mapes, R. W. (2003). Hot and cold granites? Implications of zircon saturation temperatures and preservation of inheritance. Geology, 31(6), 529–532. Retrieved from http://dx.doi.org/10.1130/0091-7613(2003)031%3C0529:HACGIO%3E2.0.CO

Mittlefehldt, D. W., & Miller, C. F. (1983). Geochemistry of the Sweetwater Wash Pluton, California: Implications for “anomalous” trace element behavior during differentiation of felsic magmas. Geochimica et Cosmochimica Acta, 47(1), 109–124. https://doi.org/10.1016/0016-7037(83)90095-9

Miyake, A., Hirukawa, T., Sato, M., Taguchi, T., Suzuki, K., & Nakai, Y. (2016). Large thermal aureole around the Inagawa Granodiorite in the southeastern area of Asuke, Aichi Prefecture. Journal of the Geological Society of Japan, 122, 173–191 (in Japanese with English abstract).

Miyake, A., Igarashi, Y., Inaishi, T., & Taguchi, T. (2017). Finding of staurolite-bearing pelitic schists in the Ryoke metamorphic belt of the Dando-san area, Aichi Prefecture and its significance. Journal of the Geological Society of Japan, 123, 59–72 (in Japanese with English abstract).

Miyake, A., Murata, E., & Morishita, O. (1992). Growth stages of andalusite in the Ryoke metamorphic rocks from the Nukata area, Aichi Prefecture. Journal of Mineralogy Petrol- Ogy and Economic Geology, 87, 475–480 (in Japanese with English abstract).

Miyake, A., Yokoe, K., Suzuki, B., & Igarashi, Y. (2014). The thermal structures in the Ryoke metamorphic belt of the Dando-san area, Aichi Prefecture. Journal of Geological Society of Japan, 120, 299–312 (in Japanese with English abstract).

Miyashiro, A., Aki, K., & Şengör, A. M. C. (1982). *Orogeny*. John Wiley & Sons Inc.

Miyazaki, K. (2010). Development of migmatites and the role of viscous segregation in high-T metamorphic complexes: Example from the Ryoke Metamorphic Complex, Mikawa Plateau, Central Japan. Lithos, 116(3–4), 287–299. https://doi.org/10.1016/J.LITHOS.2009.11.012

Moecher, D., Hietpas, J., Samson, S., & Chakraborty, S. (2011). Insights into southern Appalachian tectonics from ages of detrital monazite and zircon in modern alluvium. Geosphere, 7(2), 494–512. https://doi.org/10.1130/GES00615.1

Monié, P., Bosch, D., Bruguier, O., Vauchez, A., Rolland, Y., Nsungani, P., & Buta Neto, A. (2012). The Late Neoproterozoic/Early Palaeozoic evolution of the West Congo Belt of NW Angola: geochronological (U-Pb and Ar-Ar) and petrostructural constraints. Terra Nova, 24(3), 238–247. https://doi.org/10.1111/j.1365-3121.2012.01060.x

Montel Jean-Marc and Vielzeuf, D. (1997). Partial melting of metagreywackes, Part II. Compositions of minerals and melts. Contributions to Mineralogy and Petrology, 128(2), 176–196. https://doi.org/10.1007/s004100050302

Montel, J. M., Foret, S., Veschambre, M., Nicollet, C., & Provost, A. (1996). Electron microprobe dating of monazite. Chemical Geology, 131(1–4), 37–53. https://doi.org/10.1016/0009-2541(96)00024-1

Montel, J.-M. (1993). A model for monazite/melt equilibrium and application to the generation of granitic magmas. Chemical Geology, 110(1–3), 127–146. https://doi.org/10.1016/0009-2541(93)90250-M

Mottram, C. M., Warren, C. J., Regis, D., Roberts, N. M. W., Harris, N. B. W., Argles, T. W., & Parrish, R. R. (2014). Developing an inverted barrovian sequence; insights from monazite petrochronology. Earth and Planetary Science Letters, 403, 418–431. https://doi.org/10.1016/j.epsl.2014.07.006

Nakai, Y. (1982). The Busetsu granite in the Ryoke belt, Central Japan. In Geological Society of Japan The 89th Annual Meeting (p. 404 (in Japanese)).

Nakai, Y., & Suzuki, K. (2003). Post-tectonic two-mica granite in the Okazaki area, central Japan: a field guide for the 2003 Hutton Symposium. In Hutton Symposium, V, Field Guidebook (pp.

115–124). Geological Survey of Japan.
Nakajima, T., Kamiyama, H., Williams, I. S., & Tani, K. (2004). Mafic rocks from the Ryoke Belt, southwest Japan: implications for Cretaceous Ryoke/San-yo granitic magma genesis. Transactions of the Royal Society of Edinburgh: Earth Sciences, 95(1–2), 249–263. https://doi.org/10.1017/S026359330000105X
Nandedkar, R. H., Ulmer, P., & Müntener, O. (2014). Fractional crystallization of primitive, hydrous arc magmas: an experimental study at 0.7 GPa. Contributions to Mineralogy and Petrology, 167(6), 1015. https://doi.org/10.1007/s00410-014-1015-5
Nasdala, L., Hanchar, J. M., Rhede, D., Kennedy, A. K., & Váczi, T. (2010). Retention of uranium in complexly altered zircon: An example from Bancroft, Ontario. Chemical Geology, 269(3–4), 290–300. https://doi.org/10.1016/J.CHEMGEO.2009.10.004
Newman, K., Freedman, P. A., Williams, J., Belshaw, N. S., & Halliday, A. N. (2009). High sensitivity skimmers and non-linear mass dependent fractionation in ICP-MS. Journal of Analytical Atomic Spectrometry, 24(6), 742–751. https://doi.org/10.1039/b819065h
Newman, K. (2012). Effects of the sampling interface in MC-ICP-MS : Relative elemental sensitivities and non-linear mass dependent fractionation of Nd isotopes. Journal of Analytical Atomic Spectrometry, 27, 63–70. https://doi.org/10.1039/c1ja10222b
Ni, Y., Hughes, J. M., & Mariano, A. N. (1995). Crystal chemistry of the monazite and xenotime structures. American Mineralogist, 80, 21–26. https://doi.org/10.2138/am-1995-1-203
Niu, H., & Houk, R. S. (1996). Fundamental aspects of ion extraction in inductively coupled plasma mass spectrometry. Spectrochimica Acta Part B: Atomic Spectroscopy, 51(8), 779–815. https://doi.org/10.1016/0584-8547(96)01506-6
O'Nions, R. K., Hamilton, P. J., & Evensen, N. M. (1977). Variations in143Nd/144Nd and87Sr/86Sr ratios in oceanic basalts. Earth and Planetary Science Letters, 34(1), 13–22. https://doi.org/10.1016/0012-821X(77)90100-5
Overstreet, W. C. (1967). The geologic occurrence of monazite (530th ed.). Washington, DC. U.S. Geol. Surv. Prof. Pap.
Owona, S., Tichomirowa, M., Ratschbacher, L., Ondoa, J. M., Youmen, D., Pfänder, J., … Ekodeck, G. E. (2012). New igneous zircon Pb/Pb and metamorphic Rb/Sr ages in the Yaounde Group (Cameroon, Central Africa): implications for the Central African fold belt evolution close to the Congo Craton. International Journal of Earth Sciences, 101(7), 1689–1703. https://doi.org/10.1007/s00531-012-0751-x
Paquette, J. L., Caby, R., Djouadi, M. T., & Bouchez, J. L. (1998). U-Pb dating of the end of the Pan-African orogeny in the Tuareg shield: The post-collisional syn-shear Tioueine pluton (Western Hoggar, Algeria). Lithos, 45(1–4), 245–253. https://doi.org/10.1016/S0024-4937(98)00034-6
Parra-Avila, L. A., Belousova, E., Fiorentini, M. L., Baratoux, L., Davis, J., Miller, J., & McCuaig, T. C. (2016). Crustal evolution of the Paleoproterozoic Birimian terranes of the Baoulé-Mossi domain, southern West African Craton: U–Pb and Hf-isotope studies of detrital zircons. Precambrian Research, 274, 25–60. https://doi.org/10.1016/J.PRECAMRES.2015.09.005
Parrish, R. R. (1990). U–Pb dating of monazite and its application to geological problems. Canadian Journal of Earth Sciences, 27(11), 1431–1450. https://doi.org/10.1139/e90-152
Patino-Douce, Alberto, E., & Beard, J. S. (1995). Dehydration-melting of Biotite Gneiss and Quartz Amphibolite from 3 to 15 kbar. Journal of Petrology, 36(3), 707–738. Retrieved from http://dx.doi.org/10.1093/petrology/36.3.707
Payne, J. L., Pearson, N. J., Grant, K. J., & Halverson, G. P. (2013). Reassessment of relative oxide formation rates and molecular interferences on in situ lutetium-hafnium analysis with laser ablation MC-ICP-MS. Journal of Analytical Atomic Spectrometry, 28(7), 1068–1079. https://doi.org/10.1039/C3JA50090J
Pearce, N. J. G., Perkins, W. T., Westgate, J. A., Gorton, M. P., Jackson, S. E., Neal, C. R., & Chenery, S. P. (1997). A Compilation of New and Published Major and Trace Element Data for NIST SRM 610 and NIST SRM 612 Glass Ref e rence Materials. Geostandards Newsletter, 21(06), 115–144.
Philpotts, J. A. (1970). Redox estimation from a calculation of Eu^{2+} and Eu^{3+} concentrations in

natural phases. Earth and Planetary Science Letters, 9(3), 257–268. https://doi.org/10.1016/0012-821X(70)90036-1
Pin, C., & Poidevin, J. L. (1987). Series of the northern border of the Congo. Precambrian Research, 36, 303–312.
Plank, T., & Langmuir, C. H. (1998). The chemical composition of subducting sediment and its consequences for the crust and mantle. Chemical Geology, 145(3), 325–394. https://doi.org/10.1016/S0009-2541(97)00150-2
Poitrasson, F., Chenery, S., & Shepherd, T. J. (2000). Electron microprobe and LA-ICP-MS study of monazite hydrothermal alteration: Geochimica et Cosmochimica Acta, 64(19), 3283–3297. https://doi.org/10.1016/S0016-7037(00)00433-6
Porada, H., & Berhorst, V. (2000). Towards a new understanding of the Neoproterozoic-Early Palaeozoic Lufilian and northern Zambezi Belts in Zambia and the Democratic Republic of Congo. Journal of African Earth Sciences, 30(3), 727–771.
Potrel, A., Peucat, J. J., Fanning, C. M., Auvray, B., Burg, J. P., & Caruba, C. (1996). 3.5 Ga old terranes in the West African Craton, Mauritania. Journal of the Geological Society, 153(4), 507–510. https://doi.org/10.1144/gsjgs.153.4.0507
Poujol, M., Robb, L. J., Anhaeusser, C. R., & Gericke, B. (2003). A review of the geochronological constraints on the evolution of the Kaapvaal Craton, South Africa. Precambrian Research, 127(1–3), 181–213. https://doi.org/10.1016/S0301-9268(03)00187-6
Poussel, E., Mermet, J. M., & Deruaz, D. (1994). Dissociation of Analyte Oxide Ions in Inductively-Coupled Plasma-Mass Spectrometry. Journal of Analytical Atomic Spectrometry, 9(2), 61–66.
Pyle, J. M., & Spear, F. S. (2003). Four generations of accessory-phase growth in low-pressure migmatites from SW New Hampshire. American Mineralogist, 88(2–3), 338–351. Retrieved from http://dx.doi.org/10.2138/am-2003-2-311
Pyle, J. M., Spear, F. S., Wark, D. A., Daniel, C. G., & Storm, L. C. (2005). Contributions to precision and accuracy of monazite microprobe ages. American Mineralogist, 90(4), 547–577. https://doi.org/10.2138/am.2005.1340
Ramos, F. C., Wolff, J. A., & Tollstrup, D. L. (2004). Measuring 87Sr/86Sr variations in minerals and groundmass from basalts using LA-MC-ICPMS. Chemical Geology, 211(1–2), 135–158. https://doi.org/10.1016/J.CHEMGEO.2004.06.025
Rapp, R. P., Ryerson, F. J., Miller, C. F., & Hanson, E. S. C. (1987). Robert P. Rapp, 1 F. J. Ryerson, 2 and Calvin F. Miller3. Geophysical Research Letters, 14(3), 307–310.
Rapp, R. P., Watson, E. B., & Miller, C. F. (1991). Partial melting of amphibolite/eclogite and the origin of Archean trondhjemites and tonalites. Precambrian Research, 51(1), 1–25. https://doi.org/10.1016/0301-9268(91)90092-O
Rasmussen, B. (2005). Radiometric dating of sedimentary rocks: the application of diagenetic xenotime geochronology. Earth-Science Reviews, 68(3–4), 197–243. https://doi.org/10.1016/j.earscirev.2004.05.004
Rasmussen, B., Fletcher, I. R., & McNaughton, N. J. (2001). Dating low-grade metamorphic events by SHRIMP U-Pb analysis of monazite in shales. Geology, 29(10), 963. https://doi.org/10.1130/0091-7613(2001)029<0963:DLGMEB>2.0.CO;2
Rasmussen, B., Fletcher, I. R., & Muhling, J. R. (2007). In situ U–Pb dating and element mapping of three generations of monazite: Unravelling cryptic tectonothermal events in low-grade terranes. Geochimica et Cosmochimica Acta, 71(3), 670–690. https://doi.org/10.1016/J.GCA.2006.10.020
Rasmussen, B., & Muhling, J. R. (2007). Monazite begets monazite: evidence for dissolution of detrital monazite and reprecipitation of syntectonic monazite during low-grade regional metamorphism. Contributions to Mineralogy and Petrology, 154(6), 675–689. https://doi.org/10.1007/s00410-007-0216-6
Rasmussen, B., & Muhling, J. R. (2009). Reactions destroying detrital monazite in greenschist-facies sandstones from the Witwatersrand basin, South Africa. Chemical Geology, 264(1–4), 311–327. https://doi.org/10.1016/j.chemgeo.2009.03.017
Raut, N. M., Huang, L.-S., Aggarwal, S. K., & Lin, K.-C. (2003). Determination of lanthanides in rock samples by inductively coupled plasma mass spectrometry using thorium as oxide and

hydroxide correction standard. Spectrochimica Acta Part B: Atomic Spectroscopy, 58(5), 809–822. https://doi.org/10.1016/S0584-8547(03)00016-8
Rino, S., Kon, Y., Sato, W., & Zhao, D. (2008). The Grenvillian and Pan-African orogens: World's largest orogenies through geologic time, and their implications on the origin of superplume. Gondwana Research, 14(1–2), 51–72. https://doi.org/10.1016/J.GR.2008.01.001
Rino, S., Komiya, T., Windley, B. F., Katayama, I., Motoki, A., & Hirata, T. (2004). Major episodic increases of continental crustal growth determined from zircon ages of river sands; implications for mantle overturns in the Early Precambrian. Physics of the Earth and Planetary Interiors, 146(1–2), 369–394. https://doi.org/10.1016/j.pepi.2003.09.024
Robb, L. J., Armstrong, R. A., & Waters, D. J. (1999). The History of Granulite-Facies Metamorphism and Crustal Growth from Single Zircon U–Pb Geochronology: Namaqualand, South Africa. Journal of Petrology, 40(12), 1747–1770. https://doi.org/10.1093/petroj/40.12.1747
Roberts, R. J., Corfu, F., Torsvik, T. H., Hetherington, C. J., & Ashwal, L. D. (2010). Age of alkaline rocks in the Seiland Igneous Province, Northern Norway. Journal of the Geological Society, 167(1), 71–81. Retrieved from http://dx.doi.org/10.1144/0016-76492009-014
Romero, X., Poussel, E., & Mermet, J. M. (1997). Influence of the operating conditions on the efficiency of internal standardization in inductively coupled plasma atomic emission spectrometry. Spectrochimica Acta Part B: Atomic Spectroscopy, 52(4), 487–493. https://doi.org/10.1016/S0584-8547(96)01600-X
Ross, G. M., Parrish, R. R., & Dudás, F. O. (1991). Provenance of the Bonner Formation (Belt Supergroup), Montana: Insights from U-Pb and Sm-Nd analyses of detrital minerals. Geology, 19(4), 340–343. Retrieved from http://dx.doi.org/10.1130/0091-7613(1991)019%3C0340:POTBFB%3E2.3.CO
Rubatto, D. (2002). Zircon trace element geochemistry: partitioning with garnet and the link between U–Pb ages and metamorphism. Chemical Geology, 184(1–2), 123–138. https://doi.org/10.1016/S0009-2541(01)00355-2
Rubatto, D., Hermann, J., & Buick, I. S. (2006). Temperature and Bulk Composition Control on the Growth of Monazite and Zircon During Low-pressure Anatexis (Mount Stafford, Central Australia). Journal of Petrology, 47(10), 1973–1996. https://doi.org/10.1093/petrology/egl033
Rubatto, D., Williams, I. S., & Buick, I. S. (2001). Zircon and monazite response to prograde metamorphism in the Reynolds Range, central Australia. Contributions to Mineralogy and Petrology, 140(4), 458–468. https://doi.org/10.1007/PL00007673
Rudnick, R. L. (1995). Making continental crust. Nature, 378(6557), 571.
Rudnick, R. L., & Fountain, D. M. (1995). Nature and composition of the continental crust: a lower crustal perspective. Reviews of Geophysics, 33(3), 267–309.
Rudnick, R. L., & Gao, S. (2003). Composition of the continental crust. Treatise on Geochemistry, 3, 1–64. Retrieved from http://adsabs.harvard.edu/abs/2003TrGeo...3....1R_Ü
Russo, R. E., Mao, X., Gonzalez, J. J., Zorba, V., & Yoo, J. (2013). Laser ablation in analytical chemistry. Analytical Chemistry, 85(13), 6162–6177. https://doi.org/10.1021/ac4005327
Russo, R. E., Mao, X., Liu, H., Gonzalez, J., & Mao, S. S. (2002). Laser ablation in analytical chemistry—a review. Talanta, 57(3), 425–451. https://doi.org/10.1016/S0039-9140(02)00053-X
Ryoke Research Group. (1972). The mutual relations of the granitic rocks of the Ryoke metamorphic belt in central Japan. Earth Science (Chikyu Kagaku), 26, 205–216 (in Japanese with English abstract).
Sacks, P. E., & Secor, D. T. (1990). Delamination in collisional orogens. Geology, 18(10), 999–1002. https://doi.org/10.1130/0091-7613(1990)018<0999:DICO>2.3.CO;2
Santosh, M., Maruyama, S., Komiya, T., & Yamamoto, S. (2010). Orogens in the evolving Earth: from surface continents to 'lost continents' at the core–mantle boundary. Geological Society, London, Special Publications, 338(1), 77-116. https://doi.org/10.1144/SP338.5
Schaltegger, U., Fanning, C. M., Günther, D., Maurin, J. C., Schulmann, K., & Gebauer, D. (1999). Growth, annealing and recrystallization of zircon and preservation of monazite in high-grade metamorphism: conventional and in-situ U-Pb isotope, cathodoluminescence and microchemical evidence. Contributions to Mineralogy and Petrology, 134(2), 186–201. https://doi.org/10.1007/s004100050478

Schmitz, M. D., & Bowring, S. A. (2004). Lower crustal granulite formation during Mesoproterozoic Namaqua-Natal collisional orogenesis , southern Africa. South African Journal of Geology, 107, 261–284.
Schnetzler, C. C., & Philpotts, J. A. (1970). Partition coefficients of rare-earth elements between igneous matrix material and rock-forming mineral phenocrysts—II. Geochimica et Cosmochimica Acta, 34(3), 331–340. https://doi.org/10.1016/0016-7037(70)90110-9
Seno, T., & Maruyama, S. (1984). Paleogeographic reconstruction and origin of the Philippine Sea. Tectonophysics, 102(1–4), 53–84. https://doi.org/10.1016/0040-1951(84)90008-8
Seydoux-Guillaume, A.-M., Paquette, J.-L., Wiedenbeck, M., Montel, J.-M., & Heinrich, W. (2002). Experimental resetting of the U–Th–Pb systems in monazite. Chemical Geology, 191(1), 165–181. https://doi.org/10.1016/S0009-2541(02)00155-9
Seydoux-Guillaume, A.-M., Wirth, R., & Ingrin, J. (2007). Contrasting response of ThSiO4 and monazite to natural irradiation. European Journal of Mineralogy, 19(1), 7–14. Retrieved from http://dx.doi.org/10.1127/0935-1221/2007/0019-007
Shang, C. K., Satir, M., Morteani, G., & Taubald, H. (2010). Zircon and titanite age evidence for coeval granitization and migmatization of the early Middle and early Late Proterozoic Saharan Metacraton; example from the central North Sudan basement. Journal of African Earth Sciences, 57(5), 492–524. https://doi.org/10.1016/J.JAFREARSCI.2009.12.006
Shang, C. K., Satir, M., Siebel, W., Nsifa, E. N., Taubald, H., Liégeois, J. P., & Tchoua, F. M. (2004). TTG magmatism in the Congo craton; a view from major and trace element geochemistry, Rb–Sr and Sm–Nd systematics: case of the Sangmelima region, Ntem complex, southern Cameroon. Journal of African Earth Sciences, 40(1–2), 61–79. https://doi.org/10.1016/J.JAFREARSCI.2004.07.005
Shibata, K., & Ishihara, S. (1979). Rb-Sr whole-rock and K-Ar mineral ages of granitic rocksin Japan. Geochemical Journal, 13, 113–119.
Shibata, K., & Ishihara, S. (1979). Initial 87Sr/86Sr ratios of plutonic rocks from Japan. Contributions to Mineralogy and Petrology, 70(4), 381–390. https://doi.org/10.1007/BF00371045
Shibata, K., & Tanaka, T. (1987). Age of formation for the Ishikawa composite mass, Abukuma mountains, inferred from Nd and Sr isotopic systematics. Journal of the Japanese Association of Mineralogists Petrologists and Economic Geologists, 82, 433–440.
Shibata, N., Fudagawa, N., & Kubota, M. (1993). Oxide formation in electrothermal vaporization inductively coupled plasma mass spectrometry. Spectrochimica Acta Part B: Atomic Spectroscopy, 48(9), 1127–1137. https://doi.org/10.1016/0584-8547(93)80103-2
Shore, M., & Fowler, A. D. (1996). Oscillatory zoning in minerals: A common phenomenon. Canadian Mineralogist, 34(6), 1111–1126.
Simonetti, A., Heaman, L. M., Chacko, T., & Banerjee, N. R. (2006). In situ petrographic thin section U–Pb dating of zircon, monazite, and titanite using laser ablation–MC–ICP-MS. International Journal of Mass Spectrometry, 253(1–2), 87–97. https://doi.org/10.1016/j.ijms.2006.03.003
Singletary, S. J., Hanson, R. E., Martin, M. W., Crowley, J. L., Bowring, S. A., Key, R. M., … Krol, M. A. (2003). Geochronology of basement rocks in the Kalahari Desert, Botswana, and implications for regional Proterozoic tectonics. Precambrian Research, 121(1–2), 47–71. https://doi.org/10.1016/S0301-9268(02)00201-2
Sommer, H., Kröner, A., Hauzenberger, C., Muhongo, S., & Wingate, M. T. D. (2003). Metamorphic petrology and zircon geochronology of high-grade rocks from the central Mozambique Belt of Tanzania : crustal recycling of Archean and Palaeoproterozoic material during the Pan-African orogeny. Journal of Metamorphic Geology, 21, 915–934. https://doi.org/10.1046/j.1525-1314.2003.00491.x
Spandler, C., Hermann, J., Arculus, R., & Mavrogenes, J. (2003). Redistribution of trace elements during prograde metamorphism from lawsonite blueschist to eclogite facies; implications for deep subduction-zone processes. Contributions to Mineralogy and Petrology, 146(2), 205–222. https://doi.org/10.1007/s00410-003-0495-5
Spear, F. S., & Pyle, J. M. (2002). Apatite, Monazite, and Xenotime in Metamorphic Rocks. Reviews

in Mineralogy and Geochemistry, 48(1), 293-335. Retrieved from http://rimg.geoscienceworld.org/content/48/1/293.abstract
Spear, F. S., & Pyle, J. M. (2010). Theoretical modeling of monazite growth in a low-Ca metapelite. *Chemical Geology*, *273*(1-2), 111-119.
Spencer, C. J., Roberts, N. M. W., & Santosh, M. (2017). Growth, destruction, and preservation of Earth's continental crust. Earth-Science Reviews, 172, 87–106. https://doi.org/10.1016/J.EARSCIREV.2017.07.013
Spencer, C. J., Cawood, P. A., Hawkesworth, C. J., Prave, A. R., Roberts, N. M. W., Horstwood, M. S. A., & Whitehouse, M. J. (2015). Generation and preservation of continental crust in the Grenville Orogeny. Geoscience Frontiers, 6(3), 357–372. https://doi.org/10.1016/J.GSF.2014.12.001
Stepanov, A. S., Hermann, J., Rubatto, D., & Rapp, R. P. (2012). Experimental study of monazite/melt partitioning with implications for the REE, Th and U geochemistry of crustal rocks. Chemical Geology, 300–301, 200–220. https://doi.org/10.1016/j.chemgeo.2012.01.007
Stern, C. R., & Wyllie, P. J. (1981). Phase Relationships of I-type Granite With H2O to 35 Kilobars: The Dinkey Lakes Biotite-Granite From the Sierra Nevasa Batholith. Journal of Geophisical Research, 86, 10412–10422.
Stern, R. A., & Berman, R. G. (2001). Monazite U–Pb and Th–Pb geochronology by ion microprobe, with an application to in situ dating of an Archean metasedimentary rock. Chemical Geology, 172(1–2), 113–130. https://doi.org/10.1016/S0009-2541(00)00239-4
Stern, R. J. (1994). Arc assembly and continental collision in the Neoproterozoic East African Orogen; Implications for the Consolidation of Gondwanaland. Annual Review of Earth and Planetary Sciences, 22, 319–351.
Štípská, P., Hacker, B. R., Racek, M., Holder, R., Kylander-Clark, A. R. C., Schulmann, K., & Hasalová, P. (2015). Monazite Dating of Prograde and Retrograde P-T-d paths in the Barrovian terrane of the Thaya window, Bohemian Massif. Journal of Petrology, 56(5), 1007–1035. https://doi.org/10.1093/petrology/egv026
Suzuki, K., Morishita, T., Kajizuka, I., Nakai, Y., Adachi, M., & Shibata, K. (1994). CHIME ages of monazites from the Ryoke metamorphic rocks and some granitoids in the Mikawa-Tono area, central Japan. Bulletin of the Nagoya University Furukawa Museum, 10, 7–38 (in Japanese with English abstract).
Suzuki, K., & Adachi, M. (1998). Denudation history of the high T/P Ryoke metamorphic belt, southwest Japan: constraints from CHIME monazite ages of gneisses and granitoids. Journal of metamorphic geology, 16(1), 23–37. https://doi.org/10.1111/j.1525-1314.1998.00057.x
Suzuki, K., & Adachi, M. (1991). Precambrian provenance and Silurian metamorphism of the Tsubonosawa paragneiss in the South Kitakami terrane, Northeast Japan, revealed by the Th-U-total Pb chemical isochron ages of monazite, zircon and xenotime. Geochmical Journal, 25, 357–376.
Suzuki, K., Adachi, M., & Yamamoto, K. (1990). Possible effects of grain-boundary REE on the REE distribution in felsic melts derived by partial melting. GEOCHEMICAL JOURNAL, 24(2), 57–74. https://doi.org/10.2343/geochemj.24.57
Suzuki, K., Adachi, M., Yamamoto, K., & Nakai, Y. (1992). Intra-grain distribution of REE and crystallization sequence of accessory minerals in the Cretaceous Busetsu Granite at Okazaki, central Japan. GEOCHEMICAL JOURNAL, 26, 383–394.
Suzuki, K., & Kato, T. (2008). CHIME dating of monazite, xenotime, zircon and polycrase: Protocol, pitfalls and chemical criterion of possibly discordant age data. Gondwana Research, 14(4), 569–586.
Tack, L., Wingate, M. T. ., Liégeois, J.-P., Fernandez-Alonso, M., & Deblond, A. (2001). Early Neoproterozoic magmatism (1000–910 Ma) of the Zadinian and Mayumbian Groups (Bas-Congo): onset of Rodinia rifting at the western edge of the Congo craton. Precambrian Research, 110(1–4), 277–306. https://doi.org/10.1016/S0301-9268(01)00192-9
Tack, L., Wingate, M. T. D., De Waele, B., Meert, J., Belousova, E., Griffin, B., … Fernandez-Alonso, M. (2010). The 1375 Ma "Kibaran event" in Central Africa: Prominent emplacement of bimodal magmatism under extensional regime. Precambrian Research, 180(1–2),

63–84. https://doi.org/10.1016/j.precamres.2010.02.022
Taira, A. (2001). Tectonic evolution of the Japanese island arc system. Annual Review of Earth and Planetary Sciences, 29(1), 109–134.
Taira, A., Saito, S., Aoike, K. A. N., Morita, S., Tokuyama, H., Suyehiro, K., … Klaus, A. (1998). Nature and growth rate of the Northern Izu–Bonin (Ogasawara) arc crust and their implications for continental crust formation. Island Arc, 7(3), 395–407.
Tajika, E., & Matsui, T. (1992). Evolution of terrestrial proto-CO2 atmosphere coupled with thermal history of the earth. Earth and Planetary Science Letters, 113(1–2), 251–266. https://doi.org/10.1016/0012-821X(92)90223-I
Takagi, T. (2004). Origin of magnetite- and ilmenite-series granitic rocks in the Japan Arc. American Journal of Science, 304(2), 169–202. https://doi.org/10.2475/ajs.304.2.169
Takahashi, T., Hirahara, Y., Miyazaki, T., Vaglarov, B. S., Chang, Q., Kimura, J., & Tatsumi, Y. (2009). Precise determination of Sr isotope ratios in igneous rock samples and application to micro-analysis of plagioclase phenocrysts. JAMSTEC Report of Research and Development, 2009, 59–64. https://doi.org/10.5918/jamstecr.2009.59
Takatsuka, K., Kawakami, T., Skrzypek, E., Sakata, S., Obayashi, H., & Hirata, T. (2018). Spatiotemporal evolution of magmatic pulses and regional metamorphism during a Cretaceous flare-up event: Constraints from the Ryoke belt (Mikawa area, central Japan). Lithos, 308–309, 428–445. https://doi.org/10.1016/J.LITHOS.2018.03.018
Tanaka, H. (1977). Petrochemistry of some Mesozoic granitic rocks in the northern Abukuma Mountains. J. Japan. Assoc. Min. Petlr. Econ. Geol., 72, 373–382.
Tatsumi, Y., Takahashi, T., Hirahara, Y., Chang, Q., Miyazaki, T., Kimura, J.-I., … Sakayori, A. (2008). New Insights into Andesite Genesis: the Role of Mantle-derived Calc-alkalic and Crust-derived Tholeiitic Melts in Magma Differentiation beneath Zao Volcano, NE Japan. Journal of Petrology, 49(11), 1971–2008. Retrieved from http://dx.doi.org/10.1093/petrology/egn055
Taylor, S. R., & McLennan, S. M. (1996). The evolution of continental crust. Scientific American, 274(1), 76–81.
Tchameni, R., Mezger, K., Nsifa, N. E., & Pouclet, A. (2000). Neoarchaean crustal evolution in the Congo Craton: evidence from K rich granitoids of the Ntem Complex, southern Cameroon. Journal of African Earth Sciences, 30(1), 133–147.
Terakado, Y., & Nohda, S. (1993). Rb–Sr dating of acidic rocks from the middle part of the Inner Zone of southwest Japan: tectonic implications for the migration of the Cretaceous to Paleogene igneous activity. Chemical Geology, 109(1), 69–87. https://doi.org/10.1016/0009-2541(93)90062-N
Thomas, R. J., Agenbacht, A. L. D., Cornell, D. H., & Moore, J. M. (1994). The Kibaran of southern Africa: Tectonic evolution and metallogeny. Ore Geology Reviews, 9(2), 131–160. https://doi.org/10.1016/0169-1368(94)90025-6
Thomas, R. J., Jacobs, J., Horstwood, M. S. A., Ueda, K., Bingen, B., & Matola, R. (2010). The Mecubúri and Alto Benfica Groups, NE Mozambique: Aids to unravelling ca. 1 and 0.5Ga events in the East African Orogen. Precambrian Research, 178(1–4), 72–90. https://doi.org/10.1016/j.precamres.2010.01.010
Tomascak, P. B., Krogstad, E. J., & Walker, R. J. (1998). Sm-Nd isotope systematics and the derivation of granitic pegmatites in southwestern Maine. The Canadian Mineralogist, 36(2), 327 LP-337. Retrieved from http://www.canmin.org/content/36/2/327.abstract
Toteu, S. F., Penaye, J., & Djomani, Y. P. (2004). Geodynamic evolution of the Pan-African belt in central Africa with special reference to Cameroon. Canadian Journal of Earth Sciences, 41(1), 73–85. https://doi.org/10.1139/e03-079
Townsend, K. . J., Miller, C. . F., D'Andrea, J. . L., Ayers, J. . C., Harrison, T. M., & Coath, C. D. (2000). Low temperature replacement of monazite in the Ireteba granite , Southern Nevada : geochronological implications. Chemical Geology, 172(1–2), 95–112. https://doi.org/10.1016/S0009-2541(00)00238-2
Ueda, K., Jacobs, J., Thomas, R. J., Kosler, J., Jourdan, F., & Matola, R. (2012). Delamination-induced late-tectonic deformation and high-grade metamorphism of the

Proterozoic Nampula Complex, northern Mozambique. Precambrian Research, 196–197, 275–294. https://doi.org/10.1016/j.precamres.2011.05.012
Ueda, K., Jacobs, J., Thomas, R. J., Kosler, J., Horstwood, M. S. A., Wartho, J.-A., … Matola, R. (2012). Postcollisional High-Grade Metamorphism, Orogenic Collapse, and Differential Cooling of the East African Orogen of Northeast Mozambique. The Journal of Geology, 120(5), 507–530. https://doi.org/10.1086/666876
Valley, J. W., Chiarenzelli, J. R., & McLelland, J. M. (1994). Oxygen isotope geochemistry of zircon. *Earth and Planetary Science Letters*, *126*(4), 187–206. https://doi.org/10.1016/0012-821X(94)90106-6
van Schijndel, V., Cornell, D. H., Frei, D., Simonsen, S. L., & Whitehouse, M. J. (2014). Crustal evolution of the Rehoboth Province from Archaean to Mesoproterozoic times: Insights from the Rehoboth Basement Inlier. Precambrian Research, 240, 22–36. https://doi.org/10.1016/J.PRECAMRES.2013.10.014
van Schmus, W. R., Oliveira, E. P., da Silva Filho, a. F., Toteu, S. F., Penaye, J., & Guimaraes, I. P. (2008). Proterozoic links between the Borborema Province, NE Brazil, and the Central African Fold Belt. Geological Society, London, Special Publications, 294(1), 69–99. https://doi.org/10.1144/SP294.5
Vaughan, M. A., & Horlick, G. (1990). Effect of sampler and skimmer orifice size on analyte and analyte oxide signals in inductively coupled plasma-mass spectrometry. Spectrochimica Acta Part B: Atomic Spectroscopy, 45(12), 1289–1299. https://doi.org/10.1016/0584-8547(90)80183-J
Veizer, J., & Jansen, S. L. (1979). Basement and sedimentary recycling and continental evolution. The Journal of Geology, 87(4), 341–370. Retrieved from
Vermeesch, P. (2018). IsoplotR: A free and open toolbox for geochronology. Geoscience Frontiers, 9(5), 1479–1493. https://doi.org/10.1016/J.GSF.2018.04.001
Viola, G., Henderson, I. H. C., Bingen, B., Thomas, R. J., Smethurst, M. A., & de Azavedo, S. (2008). Growth and collapse of a deeply eroded orogen: Insights from structural, geophysical, and geochronological constraints on the Pan-African evolution of NE Mozambique. Tectonics, 27(5). https://doi.org/10.1029/2008TC002284
Vry, J., Compston, W., & Cartwright, I. (1996). SHRIMP II dating of zircons and monazites: reassessing the timing of high-grade metamorphism and fluid flow in the Reynolds Range, northern Arunta Block, Australia. Journal of Metamorphic Geology, 14(3), 335–350. https://doi.org/10.1111/j.1525-1314.1996.00335.x
Walraven, F., & Rumvegeri, B. T. (1993). Implications of whole-rock Pb□Pb and zircon evaporation dates for the early metamorphic history of the Kasaï craton, Southern Zaïre. Journal of African Earth Sciences (and the Middle East), 16(4), 395–404. https://doi.org/10.1016/0899-5362(93)90098-B
Wark, D. A., & Miller, C. F. (1993). Accessory mineral behavior during differentiation of a granite suite : monazite, xenotime and zircon in the Sweetwater Wash pluton, southeasyern California, U.S.A. Chemical Geology, 110(1–3), 49–67. https://doi.org/10.1016/0009-2541(93)90247-G
Watt, G. R., & Harley, S. L. (1993). Accessory phase controls on the geochemistry of crustal melts and restites produced during water-undersaturated partial melting. Contributions to Mineralogy and Petrology, 114(4), 550–566. https://doi.org/10.1007/BF00321759
Wendlandt, R. F., & Harrison, W. J. (1979). Rare earth partitioning between immiscible carbonate and silicate liquids and CO_2 vapor: Results and implications for the formation of light rare earth-enriched rocks. Contributions to Mineralogy and Petrology, 69(4), 409–419. https://doi.org/10.1007/BF00372266
Whalen, J. B., & Chappell, B. W. (1988). Opaque mineralogy and mafic mineral chemistry of I- and S-type granites of the Lachlan fold belt, Southeast Australia. American Mineralogist, 73(3–4), 281 LP-296. Retrieved from http://ammin.geoscienceworld.org/content/73/3-4/281.abstract
Williams, I. S. (1998). U-Th-Pb Geochronology by Ion Microprobe. Reviews in Economical Geology, 7(1991), 1–35.
Williams, I. S. (2001). Response of detrital zircon and monazite, and their U–Pb isotopic systems, to regional metamorphism and host‐rock partial melting, Cooma Complex, southeastern Australia. Australian Journal of Earth Sciences, 48(4), 557–580.

https://doi.org/10.1046/j.1440-0952.2001.00883.x
Williams, M. L., Jercinovic, M. J., & Hetherington, C. J. (2007). Microprobe Monazite Geochronology: Understanding Geologic Processes by Integrating Composition and Chronology. Annual Review of Earth and Planetary Sciences, 35(1), 137–175. https://doi.org/10.1146/annurev.earth.35.031306.140228
Wing, B. A., Ferry, J. M., & Harrison, T. M. (2003). Prograde destruction and formation of monazite and allanite during contact and regional metamorphism of pelites: petrology and geochronology. Contributions to Mineralogy and Petrology, 145(2), 228–250. https://doi.org/10.1007/s00410-003-0446-1
Witte, T. M., & Houk, R. S. (2012). Origins of polyatomic ions in laser ablation-inductively coupled plasma-mass spectrometry: An examination of metal oxide ions and effects of nitrogen and helium in the aerosol gas flow. Spectrochimica Acta Part B: Atomic Spectroscopy, 69, 9–19. https://doi.org/10.1016/j.sab.2012.02.005
Wu, F.-Y., Yang, Y.-H., Marks, M. A. W., Liu, Z.-C., Zhou, Q., Ge, W.-C., … Markl, G. (2010). In situ U–Pb, Sr, Nd and Hf isotopic analysis of eudialyte by LA-(MC)-ICP-MS. Chemical Geology, 273(1–2), 8–34. https://doi.org/10.1016/J.CHEMGEO.2010.02.007
Xie, L., Wang, R. C., Wang, D. Z., & Qiu, J. S. (2006). A survey of accessory mineral assemblages in peralkaline and more aluminous A-type granites of the southeast coastal area of China. Mineralogical Magazine, 70(6), 709–729. https://doi.org/10.1180/0026461067060362
Yakushiji, A., Kamei, A., & Shibata, T. (2012). Igneous activity forming hybrid rocks and leucogranites in the Obara area, San'in zone, Southwest Japan. In Annual Meeting of the Geological Society of Japan The 121st Annual Meeting (2014'Kagoshima) (Vol. 118, pp. 20–38). The Geological Society of Japan. https://doi.org/10.5575/geosoc.2011.0021
Yakymchuk, C., & Brown, M. (2014). Behaviour of zircon and monazite during crustal melting. *Journal of the Geological Society*, *171*(4), 465–479. Retrieved from http://dx.doi.org/10.1144/jgs2013-115
Yamasaki, T. (2013). K–Ar ages of the Ryoke plutonic rocks in the Asuke area, Aichi prefecture, central Japan. Journal of the Geological Society of Japan, 119, 421–431 (in Japanese with English abstract).
Yang, Y., Sun, J., Xie, L., Fan, H., & Wu, F. (2008). In situ Nd isotopic measurement of natural geological materials by LA-MC-ICPMS. Chinese Science Bulletin, 53(7), 1062–1070. https://doi.org/10.1007/s11434-008-0166-z
Yokoyama, K., & Zhou, B. (2002). Preliminary Studyof Ages of Monazites in Sands from the Yangtze River. National Science Museum Monographs, 22, 83–88.
Yuhara, M., & Kagami, H. (2012). Geochronological and Rb-Sr and Sm-Nd isotopic study of mafic rocks in the Ryoke Metamorphic Belt of the Mikawa District, Southwest Japan Arc. Fukuoka Univ. Sci. Rep., 42(1), 37–55 (in Japanese with English Abstract).
Yuhara, M., Kagami, H., & Nagao, K. (2000). Geochronological characterization and petrogenesis of granitoids in the Ryoke belt, Southwest Japan Arc: constraints from K–Ar, Rb–Sr and Sm-Nd systematics. Island Arc, 9(1), 64–80. https://doi.org/10.1046/j.1440-1738.2000.00262.x
Yuhara, M., Mizuta, F., Nishi, E., Kiyoura, K., & Teramoto, K. (2014). The field occurrence and chemical compositions of syn-plutonic mafic rocks in the Masaki Granite, northern Kyusyu (p. 395).
Yurimoto, H., Duke, E. F., Papike, J. J., & Shearer, C. K. (1990). Are discontinuous chondrite-normalized REE patterns in pegmatitic granite systems the results of monazite fractionation? Geochimica et Cosmochimica Acta, 54(7), 2141–2145. https://doi.org/10.1016/0016-7037(90)90277-R
Zeh, A., Williams, I. S., Brätz, H., & Millar, I. L. (2003). Different age response of zircon and monazite during the tectono-metamorphic evolution of a high grade paragneiss from the Ruhla Crystalline Complex, central Germany. Contributions to Mineralogy and Petrology, 145(6), 691–706. https://doi.org/10.1007/s00410-003-0462-1
Zeh, A., Wilson, A. H., & Ovtcharova, M. (2016). Source and age of upper Transvaal Supergroup, South Africa: Age-Hf isotope record of zircons in Magaliesberg quartzite and Dullstroom lava, and implications for Paleoproterozoic (2.5–2.0 Ga) continent reconstruction. Precambrian

Research, 278, 1–21. https://doi.org/10.1016/J.PRECAMRES.2016.03.017
Zhu, X. K., & O'Nions, R. (1999). Zonation of monazite in metamorphic rocks and its implications for high temperature thermochronology: a case study from the Lewisian terrain. Earth and Planetary Science Letters, 171(2), 209–220. https://doi.org/10.1016/S0012-821X(99)00146-6
Zhu, X. K., O'Nions, R. K., Belshaw, N. S., & Gibb, A. J. (1997). Significance of in situ SIMS chronometry of zoned monazite from the Lewisian granulites, northwest Scotland. Chemical Geology, 135(1–2), 35–53. https://doi.org/10.1016/S0009-2541(96)00103-9

Appendix

Appendix Figure 2-1

Electronic Supplementary Information

***ESI* Figure S-1**. Plot of log (MO^+/M^+) of phosphate versus MO dissociation energy for REE, Th, and U with various sample gas flow rates.

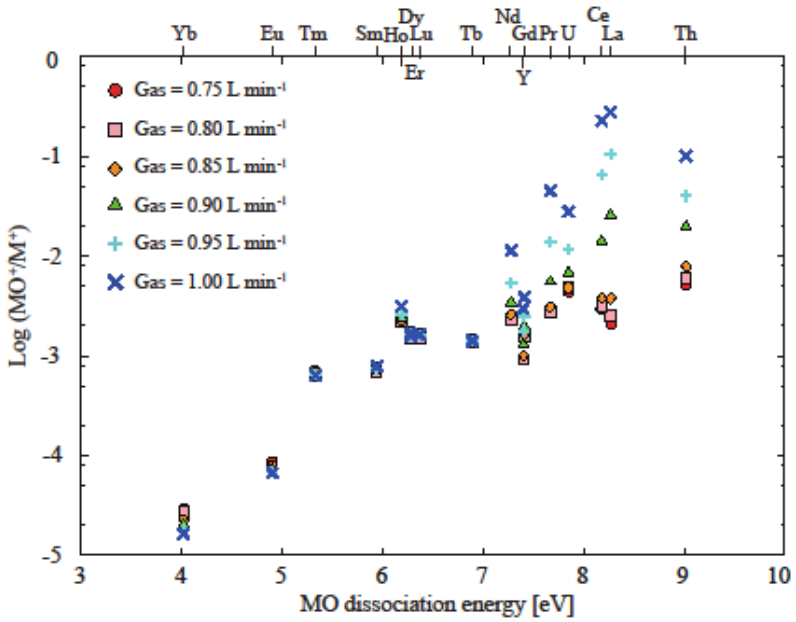

References

(1) Haynes., W. M. *CRC Handbook of Chemistry and Physics*, 94th ed.; CRC Press: Boca Raton, 2013.

(2) Ackermann, R. J. *J. Chem. Phys.* **1976**, *65* (3), 1027.

Appendix Figure 2-2

Electronic Supplementary Information

***ESI* Figure S-2**. Plot of log (MO^+/M^+) of zircon versus MO^+ dissociation energy for REE, Th, and U with various sample gas flow rates.

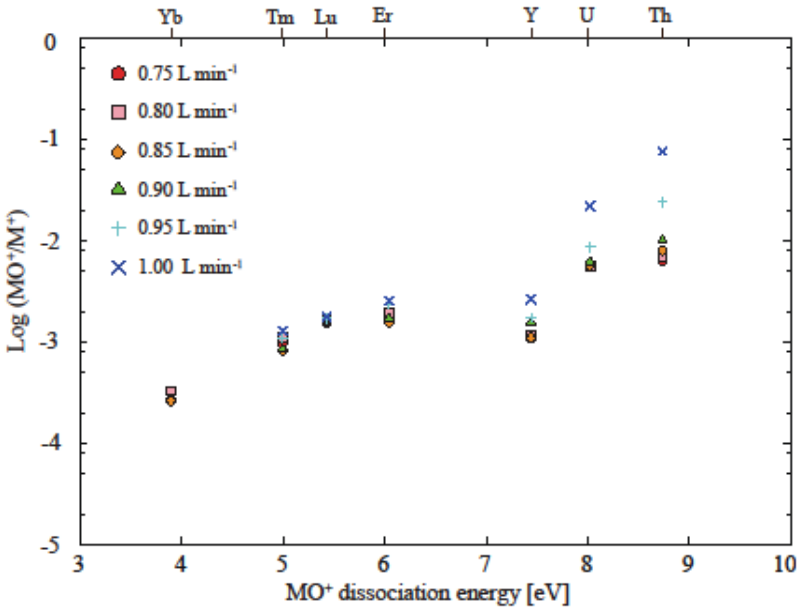

References

(1) Haynes., W. M. *CRC Handbook of Chemistry and Physics*, 94th ed.; CRC Press: Boca Raton, 2013.

(2) Ackermann, R. J. *J. Chem. Phys.* **1976**, *65* (3), 1027.

Appendix Table 2-1. Results of LA-ICP-MS analyses of synthetic REE phosphates

Appendic Table 2-1 Results of solution nebulization-ICP-MS analysis of standard solutions

Signal Intensity - elemental ions

Gas flow rate [L/min]	88Sr	138Ba	139La	140Ce	141Pr	143Nd	149Sm	151Eu	159Tb	232Th	238U
0.95	5.4.E+05	4.7.E+05	7.1.E+05	6.5.E+05	7.6.E+05	8.7.E+04	9.4.E+04	3.3.E+05	6.9.E+05	4.1.E+05	4.0.E+05
0.975	1.7.E+06	1.5.E+06	9.7.E+05	8.8.E+05	1.1.E+06	1.4.E+05	1.6.E+05	5.5.E+05	1.0.E+06	1.4.E+06	1.4.E+06
1	1.2.E+06	1.1.E+06	1.6.E+06	1.5.E+06	1.8.E+06	2.1.E+05	2.4.E+05	8.3.E+05	1.7.E+06	1.1.E+06	1.1.E+06
1.025	1.6.E+06	1.4.E+06	2.0.E+06	1.9.E+06	2.3.E+06	2.8.E+05	3.2.E+05	1.1.E+06	2.3.E+06	1.6.E+06	1.7.E+06
1.05	1.0.E+06	9.6.E+05	2.1.E+06	2.0.E+06	2.7.E+06	3.3.E+05	3.9.E+05	1.4.E+06	2.8.E+06	9.8.E+05	1.1.E+06
1.075	4.1.E+06	3.6.E+06	1.4.E+06	1.5.E+06	2.3.E+06	3.5.E+05	4.4.E+05	1.6.E+06	2.6.E+06	2.7.E+06	3.6.E+06

2SD

Gas flow rate [L/min]	88Sr	138Ba	139La	140Ce	141Pr	143Nd	149Sm	151Eu	159Tb	232Th	238U
0.95	4.2.E+04	5.2.E+04	5.5.E+04	7.2.E+04	1.0.E+05	7.4.E+03	7.9.E+03	2.1.E+04	1.7.E+04	7.2.E+04	6.2.E+04
0.975	1.5.E+05	2.1.E+05	5.5.E+04	1.2.E+05	1.4.E+05	1.5.E+04	1.1.E+04	7.9.E+04	5.8.E+04	2.2.E+05	1.9.E+05
1	9.1.E+04	1.2.E+05	8.9.E+04	1.6.E+05	1.6.E+05	1.8.E+04	1.0.E+04	6.0.E+04	1.6.E+05	8.8.E+04	1.6.E+05
1.025	6.8.E+04	8.0.E+04	2.0.E+05	9.8.E+04	1.8.E+05	2.5.E+04	1.1.E+04	5.6.E+04	9.8.E+04	9.4.E+04	1.5.E+05
1.05	1.0.E+06	9.3.E+05	8.9.E+04	1.1.E+05	7.1.E+04	1.2.E+04	1.1.E+04	6.5.E+04	5.3.E+04	9.1.E+05	1.0.E+06
1.075	7.8.E+04	2.0.E+05	1.3.E+05	2.0.E+05	2.1.E+05	2.0.E+04	4.8.E+03	4.1.E+04	1.0.E+05	2.5.E+05	3.3.E+05

Signal Intensity - oxide ions

Gas flow rate [L/min]	88Sr	138Ba	139La	140Ce	141Pr	143Nd	149Sm	151Eu	159Tb	232Th	238U
0.95	1.5.E+02	2.8.E+02	9.4.E+03	1.2.E+04	1.5.E+04	1.7.E+03	3.8.E+02	1.8.E+02	7.4.E+03	1.5.E+04	1.4.E+04
0.975	3.5.E+02	8.7.E+02	1.3.E+04	1.6.E+04	2.0.E+04	2.4.E+03	6.5.E+02	2.9.E+02	9.8.E+03	4.8.E+04	4.4.E+04
1	2.8.E+02	6.9.E+02	2.4.E+04	2.9.E+04	3.4.E+04	3.8.E+03	9.6.E+02	4.8.E+02	1.8.E+04	4.5.E+04	3.8.E+04
1.025	3.6.E+02	1.0.E+03	5.8.E+04	5.5.E+04	4.9.E+04	5.2.E+03	1.3.E+03	7.1.E+02	2.5.E+04	1.2.E+05	6.6.E+04
1.05	3.0.E+02	9.3.E+02	3.1.E+05	2.5.E+05	1.2.E+05	9.0.E+03	1.7.E+03	8.3.E+02	3.9.E+04	2.6.E+05	1.1.E+05
1.075	2.0.E+03	8.8.E+03	8.7.E+05	7.0.E+05	4.3.E+05	3.1.E+04	2.3.E+03	1.0.E+03	8.3.E+04	1.9.E+06	1.0.E+06

2SD

Gas flow rate [L/min]	88Sr	138Ba	139La	140Ce	141Pr	143Nd	149Sm	151Eu	159Tb	232Th	238U
0.95	7.4.E+01	1.2.E+02	1.2.E+03	1.0.E+03	8.8.E+02	3.6.E+02	1.6.E+02	6.9.E+01	2.9.E+02	1.8.E+03	8.1.E+02
0.975	1.2.E+02	2.2.E+02	1.1.E+03	1.7.E+03	1.5.E+03	3.4.E+02	2.3.E+02	8.4.E+01	1.4.E+03	5.4.E+03	4.6.E+03
1	7.5.E+01	1.7.E+02	1.9.E+03	2.5.E+03	2.8.E+03	5.5.E+02	2.0.E+02	1.0.E+02	1.2.E+03	4.3.E+03	3.0.E+03
1.025	1.3.E+02	2.9.E+02	1.4.E+04	1.6.E+04	2.3.E+03	4.6.E+02	2.0.E+02	2.0.E+02	1.6.E+03	3.0.E+04	9.2.E+03
1.05	3.9.E+02	8.4.E+02	1.1.E+05	7.7.E+04	3.7.E+04	2.0.E+03	2.4.E+02	2.9.E+02	9.1.E+03	2.5.E+05	1.0.E+05
1.075	4.4.E+02	1.0.E+03	1.1.E+05	9.1.E+04	7.5.E+04	4.0.E+03	3.7.E+02	2.2.E+02	1.4.E+04	1.3.E+05	2.0.E+05

Oxide Producrion Rates

Gas flow rate [L/min]	SrO/Sr	BaO/Ba	LaO/La	CeO/Ce	PrO/Pr	NdO/Nd	SmO/Sm	EuO/Eu	TbO/Tb	ThO/Th	UO/U
0.95	0.02%	0.06%	1.32%	1.86%	2.00%	1.97%	0.41%	0.06%	1.06%	3.56%	3.50%
0.975	0.02%	0.06%	1.31%	1.81%	1.85%	1.68%	0.41%	0.05%	0.99%	3.47%	3.24%
1	0.02%	0.06%	1.49%	1.95%	1.93%	1.79%	0.40%	0.06%	1.01%	4.05%	3.43%
1.025	0.02%	0.07%	2.93%	2.93%	2.14%	1.83%	0.42%	0.06%	1.07%	7.19%	3.88%
1.05	0.03%	0.09%	15.23%	12.32%	4.49%	2.70%	0.43%	0.06%	1.38%	25.59%	9.50%
1.075	0.05%	0.25%	60.71%	47.69%	18.61%	8.82%	0.53%	0.07%	3.13%	71.16%	28.25%

2SD

Gas flow rate [L/min]	SrO/Sr	BaO/Ba	LaO/La	CeO/Ce	PrO/Pr	NdO/Nd	SmO/Sm	EuO/Eu	TbO/Tb	ThO/Th	UO/U
0.95	0.010%	0.019%	0.138%	0.174%	0.199%	0.317%	0.117%	0.015%	0.031%	0.534%	0.401%
0.975	0.005%	0.013%	0.092%	0.219%	0.192%	0.605%	0.109%	0.012%	0.109%	0.473%	0.389%
1	0.005%	0.011%	0.104%	0.176%	0.166%	0.212%	0.060%	0.009%	0.081%	0.326%	0.384%
1.025	0.006%	0.015%	0.548%	0.592%	0.131%	0.163%	0.044%	0.013%	0.058%	1.307%	0.454%
1.05	0.111%	0.250%	3.628%	2.707%	0.890%	0.405%	0.044%	0.015%	0.203%	78.843%	29.981%
1.075	0.007%	0.022%	6.708%	6.408%	2.454%	0.881%	0.059%	0.010%	0.371%	5.676%	4.253%

Appendix Table2-2. Concentrations of REE, Th and U of the natural monazites in pegmatite and granite from Japan and meta-conglomerate from the Yilgarn Craton.

Uncorrected values for oxide interferences †**Ce concentrations were measured by Electron microprobe to be used as an internal standard**

Concentration

[ppm]	La	Ce†	Pr	Nd	Sm	Eu	Gd	Tb
Monazite from Pegmatite	1.1.E+05	2.6.E+05	3.2.E+04	1.4.E+05	4.5.E+04	7.8.E+00	3.3.E+04	3.8.E+03
Monazite from Granite	1.7.E+05	3.1.E+05	3.5.E+04	1.5.E+05	2.6.E+04	3.8.E+02	1.5.E+04	1.5.E+03
Monazite from Meta-conglomerate	1.7.E+05	2.8.E+05	2.6.E+04	9.4.E+04	2.4.E+04	4.2.E+03	2.0.E+04	2.2.E+03
[ppm]	Dy	Ho	Er	Tm	Yb	Lu	Th	U
Monazite from Pegmatite	1.2.E+04	9.4.E+02	9.1.E+02	5.0.E+01	2.0.E+02	1.8.E+01	5.4.E+04	4.9.E+03
Monazite from Granite	5.9.E+03	8.2.E+02	1.5.E+03	1.2.E+02	5.0.E+02	4.3.E+01	2.3.E+04	4.1.E+02
Monazite from Meta-conglomerate	6.8.E+03	5.5.E+02	5.3.E+02	2.6.E+01	9.8.E+01	9.6.E+00	7.4.E+04	1.3.E+04

Corrected for oxide interferences using REEO+/REE+ determined for the synthetic phosphates

Concentration

[ppm]	La	Ce	Pr	Nd	Sm	Eu	Gd	Tb
Monazite from Pegmatite	-	-	-	-	-	-	3.3.E+04	3.7.E+03
Monazite from Granite	-	-	-	-	-	-	1.4.E+04	1.4.E+03
Monazite from Meta-conglomerate	-	-	-	-	-	-	1.9.E+04	2.2.E+03
[ppm]	Dy	Ho	Er	Tm	Yb	Lu	Th	U
Monazite from Pegmatite	1.2.E+04	9.3.E+02	9.1.E+02	5.0.E+01	1.4.E+02	9.5.E+00	-	-
Monazite from Granite	5.9.E+03	8.2.E+02	1.5.E+03	1.2.E+02	4.7.E+02	3.9.E+01	-	-
Monazite from Meta-conglomerate	6.7.E+03	5.5.E+02	5.2.E+02	2.6.E+01	5.7.E+01	3.4.E+00	-	-

Considered interferences

from	141PrO/Pr	143NdO/Nd	147SmO/Sm	149SmO/Sm	151EuO/Eu	153EuO/Eu	157GdO/Gd	159TbO/Tb
to	157Gd	159Tb	163Dy	165Ho	167Er	169Tm	173Yb	175Lu

Appendix Table 3-11. Results of U–Pb dating of monazite in the Busetsu granite

sample name	206Pb/238U	2 σ	207Pb/206Pb	2 σ	207Pb/235U	2 σ	206Pb/204Pb	Age 206/238	2 σ	Age 207/206	2 σ	Age 207/235	2 σ	%discordance	204Pb/206Pb
2801_mnz-01	0.011	0.0004	0.108	0.016	0.166	0.021	UDL	72	3	1765	135	156	19	54%	0.01
2801_mnz-02	0.011	0.0004	0.074	0.010	0.126	0.019	UDL	70	3	1041	136	121	17	42%	0.00
2801_mnz-06	0.011	0.0004	0.069	0.010	0.110	0.016	UDL	73	2	898	150	106	14	31%	0.02
2801_mnz-07	0.023	0.0008	0.418	0.025	1.481	0.208	UDL	144	5	3974.4	45	923	85	85%	0.03
2801_mnz-08	0.011	0.0003	0.057	0.007	0.084	0.009	UDL	69	2	491	135	82	9	16%	(0.01)
2801_mnz-09	0.011	0.0004	0.075	0.009	0.118	0.012	UDL	73	3	1068	121	113	11	36%	0.01
2801_mnz-10	0.012	0.0004	0.098	0.015	0.173	0.029	UDL	74	3	1586	143	162	25	54%	(0.03)
2801_mnz-11	0.011	0.0004	0.077	0.009	0.123	0.013	UDL	70	2	1120	117	118	12	41%	0.02
2801_mnz-12	0.011	0.0003	0.069	0.012	0.107	0.017	UDL	71	2	898	179	103	15	31%	(0.02)
2801_mnz-13	0.013	0.0011	0.222	0.027	0.410	0.045	UDL	82	7	2994.5	97.9	349	32	77%	0.01
2801_mnz-14	0.011	0.0003	0.067	0.008	0.106	0.012	UDL	69	2	837	124	102	11	32%	0.01
2801_mnz-15	0.013	0.0003	0.177	0.006	0.319	0.018	UDL	85	2	2624.2	28.4	281	14	70%	0.01
2801_mnz-16	0.013	0.0004	0.135	0.015	0.251	0.027	UDL	83	3	2163.2	96.9	227	22	64%	0.00
2801_mnz-17	0.011	0.0004	0.090	0.011	0.160	0.020	UDL	72	3	1425	117	151	17	52%	(0.01)
2801_mnz-18	0.012	0.0004	0.100	0.014	0.169	0.022	UDL	77	3	1623	130	158	19	51%	0.00
2801_mnz-19	0.011	0.0003	0.061	0.005	0.090	0.008	UDL	68	2	638.3	88.2	87	7	22%	0.01
2801_mnz-20	0.011	0.0002	0.051	0.002	0.071	0.005	UDL	69	2	239.8	45.3	69	5	0%	0.00
2801_mnz-22	0.014	0.0005	0.236	0.014	0.493	0.050	UDL	92	3	3092.5	47.5	407	34	78%	0.01
2801_mnz-23	0.011	0.0003	0.080	0.010	0.118	0.012	UDL	73	2	1196	123	114	10	36%	(0.01)
2801_mnz-24	0.011	0.0003	0.072	0.008	0.105	0.011	UDL	71	2	985	113	101	10	30%	(0.02)
2801_mnz-25	0.011	0.0003	0.065	0.007	0.096	0.010	UDL	70	2	773	113	93	9	25%	(0.00)
2801_mnz-26	0.012	0.0004	0.120	0.012	0.203	0.015	UDL	76	3	1955.4	89.3	188	13	60%	0.01
2801_mnz-28	0.018	0.0005	0.409	0.025	1.041	0.067	UDL	118	3	3941.8	46	725	33	84%	0.03
2801_mnz-29	0.011	0.0003	0.062	0.006	0.092	0.008	UDL	69	2	673	104	90	7	24%	(0.00)
2801_mnz-30	0.014	0.0005	0.251	0.019	0.496	0.036	UDL	91	3	3190.4	60	409	24	78%	0.02
2801_mnz-31	0.011	0.0006	0.107	0.031	0.182	0.052	UDL	73	4	1748	265	170	45	58%	0.00
2801_mnz-32	0.012	0.0004	0.076	0.012	0.131	0.016	UDL	76	3	1094	158	125	15	39%	0.02
2801_mnz-33	0.012	0.0009	0.135	0.028	0.254	0.049	UDL	79	6	2163	181	230	40	66%	0.01
2801_mnz-34	0.015	0.0005	0.269	0.023	0.585	0.057	UDL	94	3	3299.5	67.2	467	36	80%	0.02
2801_mnz-35	0.011	0.0003	0.075	0.008	0.111	0.009	UDL	70	2	1068	107	107	8	35%	0.00
2801_mnz-36	0.011	0.0003	0.072	0.009	0.108	0.010	UDL	71	2	985	127	104	9	32%	(0.00)
2801_mnz-37	0.011	0.0004	0.070	0.009	0.097	0.008	UDL	68	2	927	132	94	8	28%	(0.00)
2801_mnz-39	0.013	0.0005	0.192	0.019	0.378	0.043	UDL	81	3	2758.6	81.3	325	32	75%	0.02
2801_mnz-40	0.011	0.0004	0.074	0.009	0.110	0.011	UDL	71	3	1041	123	106	10	34%	0.01
2801_mnz-41	0.013	0.0005	0.217	0.024	0.462	0.058	UDL	85	3	2957.8	89.3	386	40	78%	(0.00)
2801_mnz-42	0.011	0.0004	0.084	0.011	0.131	0.013	UDL	70	2	1292	127	125	12	45%	0.01
2801_mnz-43	0.011	0.0003	0.075	0.007	0.112	0.008	UDL	69	2	1067.6	93.8	108	8	36%	0.00
2801_mnz-44	0.011	0.0004	0.101	0.016	0.181	0.027	UDL	71	3	1642	147	169	23	58%	0.01
2801_mnz-45	0.013	0.0005	0.163	0.023	0.335	0.044	UDL	84	3	2486	119	293	33	72%	(0.00)
2801_mnz-46	0.012	0.0003	0.121	0.010	0.217	0.018	UDL	75	2	1970.2	73.7	199	15	63%	0.00
2801_mnz-47	0.012	0.0003	0.093	0.009	0.144	0.010	UDL	75	2	1487	91.7	137	8	45%	0.00
2801_mnz-48	0.014	0.0004	0.275	0.043	0.490	0.052	UDL	89	3	3334	122	405	35	79%	0.01
2801_mnz-50	0.011	0.0004	0.076	0.012	0.116	0.016	UDL	69	2	1094	158	112	15	38%	0.01
2801_mnz-51	0.011	0.0003	0.067	0.006	0.111	0.010	UDL	71	2	836.8	93.3	107	9	34%	0.01
2801_mnz-52	0.011	0.0003	0.080	0.007	0.129	0.009	UDL	73	2	1196.1	86.3	123	8	41%	0.01
2801_mnz-53	0.021	0.0011	0.444	0.030	1.478	0.185	40.96401938	133	7	4064.6	50.5	922	76	86%	0.08
2801_mnz-54	0.011	0.0003	0.073	0.008	0.111	0.012	UDL	69	2	1013	111	106	11	35%	(0.02)
2801_mnz-55	0.011	0.0004	0.071	0.009	0.109	0.011	UDL	68	2	956	130	105	10	36%	0.01
2801_mnz-56	0.011	0.0002	0.054	0.005	0.077	0.005	UDL	67	2	370	104	76	5	11%	0.00
2801_mnz-57	0.012	0.0006	0.111	0.019	0.170	0.019	UDL	80	4	1815	155	160	16	50%	(0.00)
2801_mnz-58	0.012	0.0006	0.111	0.029	0.198	0.047	UDL	77	4	1815	237	183	40	58%	(0.01)
2801_mnz-59	0.011	0.0003	0.101	0.015	0.178	0.019	UDL	72	2	1642	138	166	17	57%	0.01
2801_mnz-61	0.011	0.0004	0.079	0.009	0.136	0.014	UDL	72	2	1171	113	129	12	45%	0.00
2801_mnz-62	0.011	0.0003	0.072	0.009	0.112	0.011	UDL	72	2	985	127	107	10	33%	(0.01)
2802_mnz-01	0.011	0.0004	0.063	0.005	0.096	0.007	UDL	70	3	707.3	84.4	93	7	24%	(0.00)
2802_mnz-03	0.011	0.0008	0.085	0.006	0.132	0.026	UDL	73	5	1314.7	68.5	126	23	43%	0.00
2802_mnz-04	0.011	0.0007	0.054	0.003	0.081	0.015	UDL	72	5	370	62.6	79	14	9%	0.00
2802_mnz-05	0.013	0.0006	0.143	0.010	0.262	0.021	UDL	83	4	2263.1	60.4	236	17	65%	0.01
2802_mnz-06	0.010	0.0007	0.055	0.004	0.076	0.015	UDL	67	4	411.2	81.3	74	14	10.4%	0.01
2802_mnz-08	0.011	0.0007	0.054	0.003	0.079	0.015	UDL	68	5	370	62.6	77	14	12%	(0.00)
2802_mnz-09	0.010	0.0007	0.052	0.004	0.072	0.014	UDL	67	4	284.4	88	71	13	5%	(0.00)
2802_mnz-10	0.011	0.0007	0.061	0.005	0.088	0.017	UDL	68	5	638.3	88.2	85	16	20%	0.01
2802_mnz-12	0.011	0.0004	0.070	0.005	0.117	0.012	UDL	73	3	927.4	73.4	113	11	35%	0.00
2802_mnz-13	0.013	0.0005	0.176	0.010	0.298	0.020	UDL	83	3	2614.8	47.4	265	16	69%	0.00
2802_mnz-14	0.011	0.0004	0.064	0.005	0.094	0.008	UDL	72	3	740.7	82.7	91	7	22%	0.01
2802_mnz-15	0.011	0.0007	0.051	0.004	0.073	0.014	UDL	68	5	239.8	90.4	71	13	5%	0.01
2802_mnz-16	0.010	0.0002	0.050	0.003	0.072	0.003	UDL	66	1	193.9	69.8	70	3	5%	0.00
2802_mnz-17	0.011	0.0003	0.056	0.004	0.086	0.005	UDL	69	2	451.4	79.3	84	5	18%	0.00
2802_mnz-18	0.011	0.0003	0.074	0.007	0.112	0.009	UDL	69	2	1040.6	95.5	108	8	36%	(0.00)
2802_mnz-19	0.010	0.0003	0.065	0.006	0.092	0.006	UDL	67	2	773.4	97.1	90	5	25%	0.00
2802_mnz-20	0.010	0.0002	0.051	0.004	0.072	0.004	UDL	66	2	239.8	90.4	70	4	7%	0.00
2802_mnz-24	0.011	0.0003	0.059	0.006	0.089	0.007	UDL	68	2	566	111	87	6	22%	0.00
2802_mnz-26	0.011	0.0003	0.078	0.006	0.120	0.007	UDL	71	2	1146	76.5	115	6	38%	0.01
2802_mnz-28	0.011	0.0003	0.073	0.005	0.112	0.006	UDL	69	2	1013	69.5	108	5	36%	0.00
2802_mnz-29	0.011	0.000	0.050	0.004	0.076	0.005	UDL	68	2	193.9	93	74	5	8%	(0.00)
2802_mnz-31	0.011	0.0003	0.058	0.005	0.094	0.007	UDL	73	2	528.8	94.5	91	6	20%	(0.00)
2802_mnz-32	0.011	0.0002	0.051	0.004	0.076	0.004	UDL	68	2	239.8	90.4	74	4	8%	0.00
2802_mnz-34	0.010	0.0003	0.050	0.004	0.071	0.004	UDL	66	2	193.9	93	70	4	6%	0.00
2802_mnz-35	0.011	0.0002	0.074	0.006	0.114	0.007	UDL	70	1	1040.6	81.9	110	7	37%	0.00
2802_mnz-37	0.011	0.0002	0.058	0.005	0.089	0.006	UDL	70	1	528.8	94.5	86	5	19%	0.00
2802_mnz-38	0.011	0.0003	0.084	0.012	0.124	0.012	UDL	69	2	1292	139	119	11	42%	0.00
2802_mnz-39	0.011	0.0002	0.057	0.003	0.083	0.004	UDL	69	1	490.5	58.1	81	4	15%	0.00
2802_mnz-40	0.011	0.0002	0.055	0.005	0.082	0.005	UDL	69	1	411	102	80	5	14%	0.00
2802_mnz-41	0.011	0.0003	0.069	0.006	0.102	0.007	UDL	69	2	897.8	89.7	99	7	30%	(0.00)
2802_mnz-43	0.010	0.0002	0.066	0.005	0.101	0.008	UDL	67	1	805.4	79.3	97	7	31%	(0.00)
2802_mnz-45	0.011	0.0002	0.054	0.005	0.082	0.005	UDL	69	1	370	104	80	5	13%	0.00
2802_mnz-46	0.011	0.0002	0.062	0.004	0.092	0.005	UDL	68	1	673.1	69	89	5	24%	0.00
2802_mnz-48	0.011	0.0002	0.048	0.004	0.068	0.004	UDL	68	1	98.2	98.6	66	4	-2%	0.00

sample name	206Pb/238U	2 σ	207Pb/206Pb	2 σ	207Pb/235U	2 σ	206Pb/204Pb	Age 206/238	2 σ	Age 207/206	2 σ	Age 207/235	2 σ	%discordance	204Pb/206Pb
2802_mnz-50	0.011	0.0002	0.073	0.004	0.109	0.006	UDL	69	1	1013	55.6	105	5	34%	0.00
2802_mnz-51	0.011	0.0002	0.054	0.004	0.080	0.004	UDL	69	1	370	83.5	79	4	13%	(0.00)
2802_mnz-52	0.011	0.0002	0.053	0.004	0.077	0.005	UDL	68	1	327.8	85.7	75	4	10%	(0.00)
2802_mnz-53	0.011	0.0002	0.070	0.006	0.101	0.008	UDL	70	1	927.4	88	98	7	29%	0.00
2802_mnz-54	0.011	0.0003	0.070	0.007	0.107	0.008	UDL	73	2	927	103	104	7	30%	(0.00)
2802_mnz-55	0.011	0.0003	0.089	0.006	0.145	0.008	UDL	72	2	1403.3	64.6	137	7	48%	0.00
2802_mnz-56	0.012	0.0003	0.065	0.004	0.104	0.006	UDL	74	2	773.4	64.8	101	5	26%	0.00
2802_mnz-57	0.011	0.0002	0.051	0.004	0.077	0.005	UDL	68	2	239.8	90.4	75	5	10%	0.00
KJ_mnz-01	0.010	0.0004	0.052	0.003	0.073	0.004	UDL	67	2	284.4	66	71	3	7%	(0.00)
KJ_mnz-02	0.011	0.0003	0.050	0.002	0.072	0.003	UDL	69	2	193.9	46.5	71	3	3%	0.00
KJ_mnz-04	0.011	0.0003	0.066	0.004	0.091	0.004	UDL	68	2	805.4	63.5	88	3	23%	(0.00)
KJ_mnz-05	0.011	0.0003	0.058	0.003	0.084	0.004	UDL	68	2	528.8	56.7	82	4	17%	0.00
KJ_mnz-06	0.010	0.0003	0.048	0.002	0.068	0.003	UDL	67	2	98.2	49.3	67	3	0%	(0.00)
KJ_mnz-07	0.011	0.0002	0.049	0.002	0.070	0.002	UDL	69	1	146.8	47.9	69	2	0%	0.00
KJ_mnz-08	0.013	0.0003	0.071	0.005	0.119	0.006	UDL	80	2	956.5	72	114	6	30%	0.00
KJ_mnz-09	0.011	0.0002	0.048	0.002	0.072	0.003	UDL	70	1	98.2	49.3	70	3	0%	0.00
KJ_mnz-10	0.012	0.0003	0.060	0.002	0.095	0.004	UDL	75	2	602.6	36.1	92	4	18%	0.00
KJ_mnz-11	0.011	0.0003	0.064	0.008	0.099	0.010	UDL	70	2	741	132	96	9	27%	0.01
KJ_mnz-12	0.011	0.0002	0.055	0.003	0.082	0.004	UDL	73	1	411.2	61	80	3	9%	0.00
KJ_mnz-13	0.011	0.0003	0.062	0.004	0.097	0.005	UDL	73	2	673.1	69	94	5	22%	0.00
KJ_mnz-14	0.011	0.0002	0.052	0.002	0.075	0.003	UDL	71	1	284.4	44	73	3	4%	(0.00)
KJ_mnz-15	0.011	0.0002	0.054	0.003	0.076	0.004	UDL	68	1	370	62.6	74	3	9%	0.00
KJ_mnz-16	0.011	0.0004	0.072	0.005	0.112	0.007	UDL	74	2	985	70.7	108	7	32%	0.00
KJ_mnz-17	0.012	0.0004	0.074	0.011	0.117	0.011	UDL	75	3	1041	150	112	10	33%	0.00
KJ_mnz-18	0.011	0.0003	0.049	0.002	0.070	0.003	UDL	69	2	146.8	47.9	68	3	-1%	(0.00)
KJ_mnz-19	0.011	0.0003	0.054	0.002	0.075	0.003	UDL	69	2	370	41.8	74	3	7%	0.00
NK_mnz-02	0.010	0.0004	0.057	0.004	0.083	0.007	UDL	67	3	490.5	77.4	81	6	17%	0.00
NK_mnz-03	0.011	0.0004	0.058	0.006	0.084	0.008	UDL	70	2	529	113	82	8	15%	(0.00)
NK_mnz-04	0.011	0.0003	0.056	0.005	0.084	0.008	UDL	71	2	451.4	99.2	82	8	13%	(0.00)
NK_mnz-06	0.011	0.0004	0.053	0.003	0.074	0.005	UDL	68	3	327.8	64.3	73	5	7%	0.00
NK_mnz-07	0.011	0.0004	0.085	0.014	0.142	0.022	UDL	70	3	1315	160	135	19	48%	(0.03)
NK_mnz-08	0.011	0.0005	0.112	0.024	0.208	0.043	UDL	70	3	1831	194	192	36	64%	0.01
NK_mnz-09	0.011	0.0004	0.060	0.006	0.089	0.009	UDL	70	2	603	108	86	8	18%	(0.01)
NK_mnz-10	0.011	0.0004	0.055	0.004	0.082	0.007	UDL	73	2	411.2	81.3	80	6	8%	0.00
NK_mnz-11	0.016	0.0019	0.131	0.025	0.261	0.045	UDL	101	12	2111	167	236	36	58%	0.01
NK_mnz-12	0.011	0.0006	0.103	0.020	0.258	0.064	UDL	69	4	1678	179	233	52	71%	(0.02)
NK_mnz-13	0.011	0.0004	0.063	0.006	0.092	0.008	UDL	69	3	707	101	90	8	23%	(0.00)
NK_mnz-14	0.011	0.0005	0.056	0.005	0.084	0.007	UDL	70	3	451.4	99.2	82	7	14%	(0.01)
NK_mnz-16	0.011	0.0003	0.052	0.003	0.073	0.006	UDL	68	2	284.4	66	71	5	4%	(0.00)
NK_mnz-17	0.012	0.0004	0.068	0.007	0.119	0.011	UDL	76	2	868	107	114	10	34%	0.01
NK_mnz-18	0.011	0.0003	0.059	0.005	0.088	0.007	UDL	71	2	566.1	92.3	85	6	17%	(0.01)
NK_mnz-19	0.012	0.0003	0.059	0.006	0.096	0.009	UDL	75	2	566	111	93	8	20%	0.00
NK_mnz-20	0.011	0.0002	0.054	0.004	0.076	0.005	UDL	68	2	370	83.5	74	5	8%	0.00
NK_mnz-21	0.011	0.0005	0.099	0.020	0.182	0.027	UDL	74	3	1605	188	170	23	57%	(0.01)
NK_mnz-22	0.011	0.0002	0.055	0.005	0.081	0.005	UDL	68	1	411	102	79	5	14%	0.00
NK_mnz-23	0.011	0.0002	0.058	0.003	0.086	0.004	UDL	71	2	528.8	56.7	83	4	15%	0.00
NK_mnz-24	0.011	0.0004	0.078	0.013	0.135	0.015	UDL	74	2	1146	166	128	14	43%	0.00
NK_mnz-25	0.012	0.0004	0.061	0.005	0.097	0.006	UDL	75	2	638.3	88.2	94	5	20%	0.00
NK_mnz-28	0.011	0.0002	0.066	0.004	0.096	0.005	UDL	70	2	805.4	63.5	94	4	25%	0.00
NK_mnz-30	0.012	0.0004	0.088	0.006	0.140	0.008	UDL	75	2	1381.6	65.6	133	7	44%	(0.00)
NK_mnz-31	0.011	0.0003	0.075	0.008	0.123	0.012	UDL	73	2	1068	107	118	11	39%	0.01
NK_mnz-33	0.011	0.0003	0.055	0.005	0.078	0.005	UDL	68	2	411	102	76	5	11%	(0.00)
NK_mnz-34	0.012	0.0004	0.109	0.015	0.180	0.019	UDL	74	3	1782	125	168	16	56%	0.01
NK_mnz-36	0.011	0.0002	0.062	0.003	0.089	0.004	UDL	70	2	673.1	51.8	87	4	19%	0.00
TK02_mnz-01	0.013	0.0004	0.095	0.018	0.192	0.029	UDL	80	3	1527	178	178	25	55%	0.03
TK02_mnz-02	0.012	0.0002	0.066	0.006	0.107	0.011	UDL	75	1	805.4	95.2	103	10	28%	0.00
TK02_mnz-03	0.013	0.0007	0.137	0.032	0.297	0.079	UDL	85	5	2189	203	264	62	68%	(0.01)
TK02_mnz-04	0.012	0.0004	0.083	0.009	0.146	0.015	UDL	76	2	1268	106	138	13	45%	(0.01)
TK02_mnz-05	0.011	0.0003	0.047	0.003	0.067	0.003	UDL	69	2	48.2	76.3	66	3	-4%	(0.00)
TK02_mnz-06	0.012	0.0005	0.098	0.017	0.166	0.023	UDL	76	3	1586	162	156	20	51%	0.01
TK02_mnz-09	0.011	0.0004	0.068	0.007	0.110	0.009	UDL	73	3	868	107	106	8	31%	(0.00)
TK02_mnz-10	0.011	0.0003	0.054	0.006	0.083	0.007	UDL	72	2	370	125	81	7	12%	0.00
TK02_mnz-11	0.013	0.0006	0.100	0.019	0.176	0.019	UDL	85	4	1623	177	165	16	49%	0.00
TK02_mnz-12	0.011	0.0004	0.059	0.005	0.087	0.006	UDL	70	3	566.1	92.3	84	6	17%	(0.00)
TK02_mnz-13	0.011	0.0003	0.062	0.009	0.087	0.010	UDL	70	2	673	155	85	9	18%	(0.00)
TK02_mnz-15	0.012	0.0004	0.089	0.013	0.173	0.025	UDL	77	2	1403	140	162	22	53%	(0.01)
TK02_mnz-18	0.011	0.0004	0.051	0.002	0.071	0.003	UDL	67	2	239.8	45.3	69	2	3%	(0.00)
TK02_mnz-19	0.011	0.0005	0.067	0.010	0.103	0.012	UDL	72	3	837	155	100	11	28%	0.01
TK02_mnz-20	0.014	0.0006	0.270	0.022	0.598	0.060	UDL	90	4	3305.3	64	476	38	82%	(0.03)
YS_mnz-02	0.015	0.0011	0.229	0.019	0.460	0.096	UDL	98	7	3044.4	66.5	384	67	75%	0.01
YS_mnz-03	0.011	0.0008	0.065	0.008	0.097	0.021	UDL	69	5	773	130	94	19	27%	(0.01)
YS_mnz-06	0.012	0.0008	0.099	0.011	0.152	0.032	UDL	74	5	1605	104	143	28	49%	0.01
YS_mnz-07	0.011	0.0005	0.064	0.008	0.098	0.011	UDL	70	3	741	132	95	10	26%	0.00
YS_mnz-08	0.017	0.0013	0.322	0.023	0.784	0.160	UDL	107	8	3578.7	55	588	92	82%	0.02
YS_mnz-09	0.012	0.0006	0.134	0.017	0.246	0.036	UDL	75	4	2150	111	224	29	67%	0.01
YS_mnz-10	0.012	0.0005	0.076	0.009	0.125	0.013	UDL	76	3	1094	119	119	11	36%	0.01
YS_mnz-11	0.011	0.0009	0.076	0.011	0.114	0.013	UDL	72	5	1094	145	109	12	34%	(0.01)
YS_mnz-12	0.016	0.0008	0.281	0.025	0.694	0.087	UDL	100	5	3367.8	69.5	535	52	82%	(0.00)
YS_mnz-13	0.011	0.0003	0.063	0.008	0.094	0.009	UDL	69	2	707	135	91	8	25%	0.01
YS_mnz-14	0.013	0.0005	0.128	0.018	0.242	0.027	UDL	82	3	2070	124	220	22	63%	0.05
YS_mnz-15	0.011	0.0004	0.080	0.017	0.111	0.013	UDL	71	3	1196	210	107	12	34%	0.01
YS_mnz-16	0.012	0.0003	0.124	0.006	0.208	0.010	UDL	76	2	2013.8	43	192	8	61%	0.00
YS_mnz-17	0.012	0.0004	0.094	0.010	0.172	0.020	UDL	78	2	1507	101	161	17	52%	0.00
YS_mnz-18	0.017	0.0016	0.351	0.069	0.657	0.124	UDL	110	10	3711	150	513	76	79%	0.04
YS_mnz-19	0.013	0.0004	0.153	0.018	0.298	0.029	UDL	82	3	2379	100	265	23	70%	0.01
YS_mnz-20	0.013	0.0004	0.212	0.019	0.399	0.037	UDL	85	3	2920.2	72.6	341	27	76%	0.01
YS_mnz-22	0.013	0.0005	0.117	0.011	0.209	0.016	UDL	81	3	1910.1	84.4	192	14	58%	0.00
YS_mnz-23	0.011	0.0002	0.055	0.004	0.082	0.004	UDL	71	2	411.2	81.3	80	4	12%	0.00
YS_mnz-25	0.011	0.0002	0.070	0.005	0.101	0.005	UDL	71	2	927.4	73.4	98	4	28%	0.00

Appendix Table 3-2. Results of trace element analysis of monazite in the Busetsu granite

Concentration [ppm]	Y	La	Ce	Pr	Nd	Sm	Eu	Gd	Tb	Dy	Ho	Er	Tm	Yb	Lu	Th	U
2801_mnz-06	11643	121537	253259	25431	111445	16911	290	11279	1165	4597	537	819	52	172	12	23349	407
2801_mnz-10	4943	144351	274901	26502	104072	10768	134	6041	509	1847	213	302	20	59	4	26044	181
2801_mnz-12	5489	142683	270555	25204	101574	10179	178	5857	537	2044	241	342	22	75	5	20326	313
2801_mnz-15	9203	130646	262046	23780	102417	12283	232	8033	818	3484	448	724	51	189	16	24321	500
2801_mnz-17	3952	143695	271275	24702	98119	9995	185	5532	411	1451	172	225	18	68	5	28585	176
2801_mnz-18	6330	128205	249849	26115	106027	13473	242	8163	675	2550	293	429	27	93	7	43647	330
2801_mnz-19	10007	121568	250111	25488	108081	16831	349	11617	1186	4114	373	413	19	45	3	35934	1241
2801_mnz-20	14984	104785	240563	24714	110588	20370	214	15447	1844	7175	862	1189	82	263	18	23418	4295
2801_mnz-23	8601	123708	248941	27838	102126	13922	261	9139	866	3357	397	624	41	142	11	33908	422
2801_mnz-24	8558	128441	256440	25731	109505	14707	271	9314	868	3444	403	587	41	125	10	19831	299
2801_mnz-25	8070	131448	255396	22230	100106	12229	207	8294	840	3317	383	586	38	123	9	16646	334
2801_mnz-26	8552	129955	258378	26411	99723	13281	248	8846	860	3143	383	561	40	113	8	16731	343
2801_mnz-28	10749	108545	244402	26958	106290	20007	345	12637	1074	3722	463	653	47	153	15	28023	391
2801_mnz-29	10518	123450	256440	26599	102586	14100	217	9885	947	3522	471	725	52	163	13	13812	631
2801_mnz-30	8086	110813	241705	26454	103563	17722	294	10612	869	2941	357	506	34	93	8	24257	251
2801_mnz-33	7967	146642	267966	26181	95873	10944	180	7516	758	2849	344	500	37	107	8	11894	453
2801_mnz-34	7444	123296	251728	26633	101326	15937	273	9435	799	2736	330	464	28	72	6	23145	236
2801_mnz-35	6939	133810	262988	26240	99491	13151	253	8354	722	2597	329	484	33	98	8	24186	357
2801_mnz-36	8838	129273	252265	26386	102063	14479	242	9762	931	3334	402	546	35	100	7	18424	366
2801_mnz-38	11109	119237	250140	27197	102895	17394	316	11509	1095	4005	492	694	51	165	16	21394	475
2801_mnz-40	5414	134321	264013	26813	101874	12901	202	7529	567	2013	237	350	31	132	18	18372	436
2801_mnz-42	6247	137792	260265	25770	98197	11806	205	8178	749	2534	332	436	36	112	9	28417	395
2801_mnz-43	3388	150061	271441	26052	91750	9710	159	5964	458	1389	147	198	14	33	3	14921	244
2801_mnz-44	8363	120840	245606	25882	96833	13091	235	8718	819	3052	377	547	38	108	8	17904	419
2801_mnz-45	5907	122418	244727	26548	100177	14350	273	8767	692	2370	278	381	26	63	5	21302	178
2801_mnz-46	7574	130706	258506	25813	99577	14341	312	8898	799	2829	342	479	35	105	8	22805	401
2801_mnz-47	8838	129828	253520	26428	100434	13893	259	9420	860	3213	400	561	40	119	10	18921	327
2801_mnz-48	11683	111359	245657	26548	103923	18515	294	12804	1255	4567	534	724	48	134	10	19794	562
2801_mnz-49	4174	142916	265029	25685	96448	10909	222	6550	469	1638	194	270	19	48	4	17841	168
2801_mnz-50	6401	134048	260274	26232	101840	13479	241	8370	677	2469	291	402	26	70	5	20920	208
2801_mnz-51	7760	127031	257678	27522	102672	14730	277	9897	901	3257	383	520	39	104	8	23794	325
2801_mnz-52	12296	118751	235122	25283	102963	16299	293	11706	1097	4304	556	852	66	212	18	23845	564
2801_mnz-53	6784	135728	264739	26710	98402	11685	217	7590	676	2499	301	443	29	86	7	16900	243
2801_mnz-54	7920	125462	244522	26189	99825	14566	276	9813	821	2979	369	530	39	113	9	30119	362
2801_mnz-55	6801	127986	255527	26873	101789	13151	236	8600	726	2633	299	422	27	72	6	18919	228
2802_mnz-01	14400	113004	235074	25802	111631	19542	118	14055	1520	5766	694	1128	85	342	27	35003	851
2802_mnz-03	15995	118311	246056	26346	113551	19317	171	13101	1530	5743	704	1135	86	323	24	17280	727
2802_mnz-05	13554	104526	220509	26050	114860	20919	133	14650	1563	5673	667	1080	79	313	25	64250	1111
2802_mnz-06	20790	120954	250251	27101	109719	17667	179	15504	1886	8035	1009	1570	134	536	43	26565	1199
2802_mnz-10	16942	108343	226050	24981	112157	21617	162	14343	1653	7420	826	1350	105	401	31	26886	1216
2802_mnz-12	14345	116188	237063	23925	108847	18375	118	13667	1537	5713	684	1116	85	348	28	37514	1088
2802_mnz-13	15269	109727	231297	25676	115180	20237	144	14797	1618	6049	736	1161	89	344	27	37933	1043
2802_mnz-14	16359	119382	249226	28126	108404	16081	140	11755	1370	5642	694	1172	93	359	28	18660	860
2802_mnz-15	11124	119442	250433	23794	110082	17780	157	12848	1309	4669	505	814	68	289	28	31274	605
2802_mnz-16	15875	108895	232202	25104	103795	19766	168	15560	1938	8043	1001	1601	138	524	42	20328	1681
2802_mnz-17	17776	113976	245265	27026	105715	18783	174	12724	1533	6276	771	1171	91	349	26	19041	932
2802_mnz-18	16703	116415	230896	26155	99414	18981	156	13436	1509	6025	724	1120	93	337	27	16263	988
2802_mnz-19	19049	117012	242055	27291	100143	17627	154	13300	1644	6890	876	1360	112	415	33	13438	978
2802_mnz-20	18029	113687	238588	26146	104601	19404	157	14160	1636	6442	823	1166	95	350	27	16842	954
2802_mnz-28	18404	116620	239630	25984	102492	18722	157	14099	1731	7173	915	1445	127	472	38	15014	1035
2802_mnz-29	16678	115938	248236	27052	103941	18127	154	13688	1563	6220	757	1126	92	327	25	13994	852
2802_mnz-32	17196	113959	239442	26300	102723	18395	155	14185	1706	6841	875	1300	108	407	32	17805	1316
2802_mnz-34	15112	115452	240210	25839	101763	18110	164	11276	1362	5270	664	1004	91	369	29	27372	2180
2802_mnz-38	21649	113183	235284	26240	105295	21051	185	14804	1811	7460	954	1486	126	491	39	14929	982
2802_mnz-39	15251	115417	236027	24711	97545	16817	131	11817	1384	5528	710	1068	92	345	27	18365	1081
2802_mnz-40	19466	104367	221684	25531	103752	22836	153	17015	1996	8096	1025	1653	134	528	42	28366	1553
2802_mnz-41	19502	114966	239792	25796	103615	19205	154	14086	1734	7070	903	1429	121	476	38	16710	1005
2802_mnz-43	15262	114326	235207	26283	105098	19809	145	13652	1543	5815	712	1024	77	285	21	13801	606
2802_mnz-48	19789	103949	224980	26967	104738	21974	160	15404	1951	7558	952	1451	116	449	35	23302	1328
2802_mnz-50	17884	113516	228548	27505	101789	20680	184	16916	1874	8412	976	1396	103	420	32	24090	1044
2802_mnz-52	18197	115682	236847	27642	102329	19343	162	15394	1770	6918	907	1437	112	442	34	19400	1197
2802_mnz-55	11797	120994	251668	27069	103040	17118	209	9918	1165	4350	478	804	76	357	29	31361	4161
2802_mnz-56	15754	118623	245913	25702	100940	16756	145	11833	1364	5562	683	1114	91	329	25	14676	750

Concentration [ppm]	Y	La	Ce	Pr	Nd	Sm	Eu	Gd	Tb	Dy	Ho	Er	Tm	Yb	Lu	Th	U
KJ_mnz-01	15892	109526	238836	28026	108733	23267	146	15829	1694	6308	690	1087	98	422	37	23683	3769
KJ_mnz-05	13481	116091	239049	27838	110122	22112	120	15838	1725	6517	753	1217	110	462	40	31839	2892
KJ_mnz-06	16129	118521	246187	27129	104609	20240	150	15022	1660	6500	740	1216	108	466	39	15949	3311
KJ_mnz-08	11926	117438	240706	27924	105518	18972	155	14250	1713	7144	860	1518	143	647	57	17242	4804
KJ_mnz-09	11805	115264	243258	27573	103975	19783	158	14783	1741	7029	826	1416	131	579	50	16735	4186
KJ_mnz-10	12643	117788	247903	27411	103666	20568	149	15264	1890	7698	918	1585	152	694	61	20430	5632
KJ_mnz-11	5262	127312	251113	26898	97219	13634	128	8698	715	2251	217	271	15	35	3	38346	510
KJ_mnz-12	12807	114599	239101	26821	104198	20378	153	15371	1828	7362	918	1535	152	711	63	20106	5175
KJ_mnz-14	18000	112382	232117	27343	108459	21517	333	14600	1618	6275	722	1192	132	626	63	37688	1635
KJ_mnz-19	11686	117643	235464	27488	102843	21672	126	15011	1613	5833	672	1063	95	423	36	22246	3684
NK_mnz-02	11311	125414	240193	26995	98825	11521	199	7780	890	3769	521	889	69	258	22	11849	753
NK_mnz-03	7749	123802	240680	27021	108250	13631	216	8908	874	3054	325	414	25	73	5	27270	903
NK_mnz-06	9712	127665	250749	25582	105824	14672	112	9840	1154	4096	422	617	49	176	13	17140	5319
NK_mnz-09	7243	131283	253936	23828	104241	11639	238	7357	714	2547	300	428	30	99	8	23555	299
NK_mnz-11	10225	114892	231499	23287	101826	15287	154	11162	1264	4464	458	574	37	115	8	19326	979
NK_mnz-12	5546	113721	243808	27160	104861	18633	351	10544	827	2495	244	285	16	52	4	43299	232
NK_mnz-13	6954	131871	263139	24828	103403	11734	200	7368	719	2628	288	427	29	123	13	26239	1660
NK_mnz-14	11178	129447	257189	24409	105821	13554	181	9704	1144	4483	557	885	71	283	24	12640	667
NK_mnz-18	16245	122623	252772	26784	106704	17917	216	14513	1524	6086	728	1047	75	263	20	30576	754
NK_mnz-20	10981	121125	257505	26001	109593	18849	270	13129	1280	4661	475	585	43	134	10	30901	1341
NK_mnz-22	9302	118027	229547	22575	86983	10625	175	8829	950	3782	423	611	44	145	12	12936	879
NK_mnz-23	9889	120337	236719	24514	96688	16998	309	11100	928	3530	420	624	43	121	10	23345	315
NK_mnz-25	11242	125104	255569	26941	103280	15014	282	11255	1235	4336	493	685	46	120	9	22249	822
NK_mnz-30	11766	123936	244069	24976	94047	14471	126	11528	1272	4613	486	666	44	118	8	16503	1308
NK_mnz-31	18423	107283	232996	26420	102895	20706	250	18378	1932	8308	1109	1789	127	441	36	16425	707
NK_mnz-33	13254	125377	249636	26539	100143	14781	181	12358	1370	5150	561	780	51	139	10	17337	979
TK02_mnz-01	7082	130291	260015	24739	108430	14313	261	8255	744	2751	316	453	30	101	8	27941	202
TK02_mnz-03	12689	123592	253981	24335	101712	15756	231	11673	1384	5213	573	750	51	172	12	24652	1493
TK02_mnz-05	18658	118984	245925	26895	106355	17728	221	14595	1700	7230	978	1574	125	470	39	14079	682
TK02_mnz-06	8448	124854	256056	24959	103812	11797	127	7738	889	3466	375	528	41	149	11	13754	466
TK02_mnz-09	6334	114494	252960	26437	107341	17360	111	11355	984	2913	277	311	18	49	4	42943	571
TK02_mnz-11	6471	125388	245968	24922	101537	14149	301	8389	743	2547	286	403	31	142	16	36577	510
TK02_mnz-12	13393	108650	229348	23968	97662	13936	160	11831	1399	5339	616	832	57	182	14	27168	1513
TK02_mnz-13	5895	127989	261859	24520	105775	13240	213	7061	621	2204	260	363	28	100	9	30504	521
TK02_mnz-18	10265	118982	234029	25095	90824	14419	244	10882	1169	4180	464	652	44	142	11	28389	3259
TK02_mnz-19	6786	141236	265029	27240	92967	10995	152	6973	666	2388	295	434	29	92	7	13104	179
YS_mnz-02	11969	119209	243995	27898	112437	16736	254	10860	1174	4504	550	819	56	176	13	28482	501
YS_mnz-03	7174	127690	258421	24406	105069	14390	300	7962	710	2663	322	494	35	116	10	27396	321
YS_mnz-05	10650	121560	248808	27656	110130	14563	150	9221	982	3877	467	689	50	178	14	26483	440
YS_mnz-06	9108	124072	259312	25460	108973	15325	223	9953	959	3633	432	630	46	143	11	21710	339
YS_mnz-07	9823	126320	250996	26386	107761	15267	159	10211	991	3764	468	684	49	164	12	32333	376
YS_mnz-09	3417	126715	254659	25272	108859	15842	249	7138	495	1531	147	204	14	47	4	47083	414
YS_mnz-10	7399	140205	270368	26069	103895	9480	102	6436	696	2731	334	515	36	124	10	14592	354
YS_mnz-11	13271	115255	240726	25272	110573	17253	225	12231	1312	5202	683	1051	77	268	21	29652	539
YS_mnz-13	7144	126843	258962	25204	111914	14229	183	8122	695	2531	324	480	33	102	8	27020	315
YS_mnz-14	10111	114931	244308	26736	101737	17196	217	11461	1060	3869	474	666	43	126	9	15468	229
YS_mnz-15	11389	114897	228395	26369	104729	18283	230	12070	1181	4428	542	786	52	151	11	17235	247
YS_mnz-17	15752	107419	239109	27889	111219	21887	240	16260	1505	5891	728	1100	73	238	18	35490	577
YS_mnz-18	3119	111248	221667	25488	105158	19921	466	8649	476	1352	129	181	20	23	3	59412	148
YS_mnz-19	6975	148416	260094	25514	97271	8822	130	6473	623	2397	304	472	30	87	6	10354	204
YS_mnz-20	11743	126775	252931	26027	98299	14919	188	11332	1091	4158	542	803	55	169	13	17990	383
YS_mnz-25	23282	126204	261050	27958	103812	16170	271	12158	1405	6723	1006	1925	183	804	71	29426	5716

Appendix Table 3-3. Results of Nd isotope analysis of monazite in the Busetsu granite

Results	147Sm/144Nd	2s	143Nd/144Nd	2s	145Nd/144Nd	2s	150Nd/144Nd	2SE	Age (Ma)	**143Nd/144Nd(t)	2s
2801_mnz-06	0.1083	0.0024	0.512255	0.000048	0.348409	0.000028	0.236424	0.000035	68	0.512207	0.000048
2801_mnz-10	0.0778	0.0018	0.512287	0.000044	0.348412	0.000029	0.236390	0.000026	68	0.512252	0.000044
2801_mnz-15	0.0945	0.0023	0.512217	0.000044	0.348423	0.000031	0.236435	0.000036	68	0.512175	0.000044
2801_mnz-18	0.0924	0.0021	0.512226	0.000042	0.348440	0.000024	0.236429	0.000021	68	0.512185	0.000042
2801_mnz-23	0.1016	0.0023	0.512247	0.000048	0.348403	0.000026	0.236421	0.000029	68	0.512202	0.000048
2801_mnz-37	0.0831	0.0016	0.512242	0.000030	0.348421	0.000019	0.236395	0.000024	68	0.512205	0.000030
2801_mnz-42	0.0731	0.0012	0.512275	0.000032	0.348408	0.000017	0.236381	0.000023	68	0.512242	0.000032
2801_mnz-44	0.1013	0.0021	0.512229	0.000031	0.348431	0.000019	0.236375	0.000021	68	0.512184	0.000031
2801_mnz-45	0.1329	0.0022	0.512243	0.000033	0.348414	0.000021	0.236360	0.000029	68	0.512184	0.000033
2801_mnz-50	0.1043	0.0017	0.512258	0.000028	0.348432	0.000022	0.236373	0.000029	68	0.512211	0.000028
YS_mnz-7	0.1073	0.0025	0.512168	0.000047	0.348406	0.000029	0.236422	0.000035	68	0.512120	0.000047
YS_mnz-9	0.0847	0.0043	0.512123	0.000048	0.348411	0.000029	0.236416	0.000035	68	0.512085	0.000048
YS_mnz-10	0.1184	0.0027	0.512201	0.000046	0.348430	0.000027	0.236395	0.000031	68	0.512148	0.000046
YS_mnz-11	0.1135	0.0026	0.512178	0.000041	0.348415	0.000025	0.236387	0.000021	68	0.512128	0.000041
YS_mnz-12	0.0929	0.0023	0.512137	0.000062	0.348427	0.000031	0.236463	0.000056	68	0.512096	0.000062
YS_mnz-14	0.0999	0.0016	0.512108	0.000054	0.348467	0.000027	0.236546	0.000064	68	0.512063	0.000054
YS_mnz-15	0.1019	0.0017	0.512128	0.000038	0.348449	0.000022	0.236454	0.000051	68	0.512083	0.000038
YS_mnz-20	0.1104	0.0019	0.512167	0.000031	0.348419	0.000018	0.236398	0.000031	68	0.512118	0.000031
NK_mnz-02	0.0960	0.0022	0.512201	0.000050	0.348420	0.000028	0.236406	0.000035	68	0.512158	0.000050
NK_mnz-06	0.1105	0.0038	0.512265	0.000049	0.348449	0.000034	0.236572	0.000060	68	0.512216	0.000049
NK_mnz-12	0.1148	0.0034	0.512185	0.000052	0.348449	0.000039	0.236566	0.000084	68	0.512134	0.000052
NK_mnz-13	0.0863	0.0021	0.512187	0.000042	0.348429	0.000025	0.236439	0.000022	68	0.512149	0.000043
NK_mnz-14	0.1218	0.0028	0.512232	0.000048	0.348418	0.000028	0.236406	0.000035	68	0.512178	0.000048
TK02_mnz-03	0.1233	0.0028	0.512087	0.000073	0.348487	0.000047	0.236648	0.000065	68	0.512032	0.000073
TK02_mnz-05	0.1192	0.0027	0.512200	0.000045	0.348430	0.000027	0.236441	0.000029	68	0.512147	0.000045
TK02_mnz-09	0.1200	0.0027	0.512152	0.000046	0.348407	0.000027	0.236407	0.000030	68	0.512099	0.000046
TK02_mnz-11	0.0992	0.0041	0.512140	0.000041	0.348376	0.000026	0.236404	0.000015	68	0.512096	0.000041
TK02_mnz-12	0.1342	0.0031	0.512185	0.000049	0.348419	0.000028	0.236406	0.000031	68	0.512125	0.000049
TK02_mnz-13	0.0956	0.0015	0.512190	0.000035	0.348433	0.000026	0.236473	0.000038	68	0.512147	0.000035
TK02_mnz-18	0.1144	0.0021	0.511986	0.000035	0.348408	0.000018	0.236371	0.000037	68	0.511935	0.000035
TK02_mnz-19	0.1003	0.0016	0.512326	0.000033	0.348425	0.000020	0.236390	0.000021	68	0.512282	0.000033
2802_mnz-03	0.1216	0.0019	0.512208	0.000038	0.348440	0.000018	0.236391	0.000026	68	0.512153	0.000038
2802_mnz-05	0.1420	0.0032	0.512235	0.000044	0.348419	0.000026	0.236417	0.000025	68	0.512172	0.000044
2802_mnz-06	0.1170	0.0018	0.512194	0.000031	0.348426	0.000019	0.236391	0.000027	68	0.512142	0.000031
2802_mnz-10	0.1461	0.0023	0.512223	0.000030	0.348435	0.000018	0.236387	0.000027	68	0.512158	0.000030
2802_mnz-12	0.1244	0.0028	0.512225	0.000043	0.348401	0.000028	0.236412	0.000031	68	0.512169	0.000043
2802_mnz-13	0.1316	0.0030	0.512220	0.000042	0.348423	0.000029	0.236441	0.000027	68	0.512161	0.000042
2802_mnz-14	0.1137	0.0026	0.512187	0.000041	0.348410	0.000024	0.236418	0.000018	68	0.512136	0.000041
2802_mnz-15	0.1248	0.0029	0.512228	0.000044	0.348430	0.000027	0.236407	0.000031	68	0.512172	0.000044
2802_mnz-20	0.1252	0.0020	0.512205	0.000032	0.348425	0.000019	0.236367	0.000026	68	0.512149	0.000032
2802_mnz-52	0.1208	0.0020	0.512222	0.000033	0.348418	0.000018	0.236362	0.000025	68	0.512168	0.000033
KJ-4	0.1243	0.0020	0.512199	0.000030	0.348421	0.000019	0.236374	0.000026	68	0.512143	0.000030
KJ-5	0.1308	0.0021	0.512194	0.000030	0.348421	0.000018	0.236376	0.000017	68	0.512136	0.000030
KJ-6	0.1199	0.0019	0.512174	0.000033	0.348422	0.000019	0.236390	0.000026	68	0.512121	0.000033
KJ-8	0.1173	0.0018	0.512208	0.000033	0.348417	0.000019	0.236347	0.000023	68	0.512156	0.000033
KJ-9	0.1393	0.0022	0.512199	0.000030	0.348425	0.000017	0.236364	0.000022	68	0.512137	0.000030
KJ-10	0.1352	0.0021	0.512189	0.000033	0.348424	0.000018	0.236379	0.000023	68	0.512129	0.000033
KJ-11	0.0974	0.0018	0.512097	0.000037	0.348424	0.000024	0.236388	0.000026	68	0.512054	0.000037
KJ-12	0.1284	0.0020	0.512199	0.000028	0.348403	0.000019	0.236388	0.000019	68	0.512142	0.000028
KJ-14	0.1333	0.0021	0.512210	0.000031	0.348427	0.000018	0.236377	0.000032	68	0.512151	0.000031
KJ-19	0.1337	0.0021	0.512187	0.000029	0.348420	0.000020	0.236388	0.000019	68	0.512128	0.000029

Appendix Table 3-4. Geochemical composition of plagioclase in the Busetsu granite

	Major elements [wt%]									
Sample	Na2O	MgO	Al2O3	SiO2	K2O	CaO	FeO	SrO	Total	An content
YS-1_core	6.2	0.0	26.4	54.6	0.1	9.4	0.0	0.1	96.9	45.4%
YS-1_rim	8.8	0.0	24.0	58.8	0.2	6.2	0.0	0.1	98.0	27.8%
YS-3_core	6.9	0.0	27.6	55.0	0.2	9.7	0.0	0.0	99.5	43.2%
YS-3_rim	8.5	0.0	24.5	59.2	0.2	6.3	0.0	0.0	98.8	29.1%
YS-4_core	6.1	0.1	27.8	54.0	0.3	9.8	0.2	0.0	98.2	46.5%
YS-4_rim	9.6	0.0	23.6	60.6	0.3	5.2	0.0	0.1	99.5	22.8%
YS-5_core	7.7	0.0	25.2	57.1	0.2	7.6	0.0	0.1	98.0	35.0%
YS-5_rim	10.7	0.0	22.4	61.4	0.2	4.3	0.0	0.1	99.1	18.4%
YS-g1_core	6.6	0.0	27.1	55.3	0.2	9.3	0.0	0.0	98.6	43.6%
YS-g1_rim	9.7	0.0	24.0	60.6	0.3	5.5	0.0	0.0	100.1	23.5%
YS-g2_core	8.1	0.0	25.5	57.0	0.2	7.7	0.0	0.1	98.7	34.2%
YS-g2_rim	8.8	0.0	24.0	58.6	0.3	6.2	0.0	0.1	98.1	27.5%
YS-g5_core	8.0	0.0	25.2	56.7	0.2	7.7	0.0	0.1	97.9	34.3%
YS-g5_rim	8.8	0.0	23.1	60.1	0.3	5.3	0.0	0.1	97.8	24.7%
YS-g3_core	7.4	0.0	26.9	54.7	0.1	9.7	0.0	0.1	99.0	41.8%
YS-g3_rim	9.6	0.0	23.1	60.5	0.4	5.1	0.0	0.1	98.8	22.6%
NK-1_core	8.6	0.0	23.1	57.8	0.2	5.9	0.0	0.1	95.9	27.5%
NK-1_rim	10.2	0.0	22.7	60.8	0.3	4.6	0.0	0.1	98.6	19.7%
NK-2_core	9.9	0.0	23.4	59.6	0.3	5.4	0.0	0.1	98.8	22.9%
NK-2_rim	11.9	0.0	21.1	63.2	0.3	2.8	0.0	0.0	99.3	11.3%
NK-4_core	10.3	0.0	24.6	60.7	0.2	5.9	0.0	0.0	101.7	23.7%
NK-4_rim	11.2	0.0	23.6	62.5	0.3	4.7	0.0	0.0	102.3	18.5%
NK-5_core	9.6	0.0	23.6	59.5	0.3	5.7	0.0	0.1	98.8	24.5%
NK-5_rim	9.7	0.0	21.7	61.9	0.4	3.6	0.0	0.0	97.3	16.7%
NK-g1_core	10.5	0.0	22.7	60.8	0.3	4.6	0.0	0.1	99.1	19.2%
NK-g1_rim	9.8	0.0	23.1	60.0	0.3	5.1	0.0	0.0	98.4	22.2%
NK-g2_core	10.2	0.0	24.7	60.3	0.2	6.0	0.0	0.0	101.4	24.4%
NK-g2_rim	10.8	0.0	23.8	61.5	0.3	5.1	0.0	0.0	101.7	20.5%
NK-g3_core	10.1	0.0	23.1	60.2	0.2	5.2	0.0	0.0	98.8	22.1%
NK-g3_rim	10.0	0.0	22.0	61.5	0.3	3.9	0.0	0.1	97.8	17.4%

Appendix Table 3-4. Geochemical composition of plagioclase in the Busetsu granite								
Trace elements [ppm]								
Li	Mg	Ti	Mn	Zn	Rb	Sr	Y	Ba
3	26	12	33	6	1	689	0	104
4	519	40	126	13	3	1425	0	207
6	234	68	130	27	8	1229	0	190
3	21	15	40	12	1	822	0	156
7	874	56	99	51	15	1025	2	194
4	19	30	54	12	1	718	1	68
2	7	17	29	7	1	665	1	113
3	220	63	55	11	3	743	0	48
2	58	15	8	11	2	560	0	40
3	34	68	132	12	0	1180	0	129
1	13	28	97	5	0	1235	1	197
1	14	7	41	7	1	986	0	198
1	18	63	75	11	1	775	1	309
3	45	47	105	15	1	1475	2	408
3	268	31	52	12	4	614	0	98
2	27	19	132	10	0	852	0	236
2	10	16	53	4	0	504	0	62
18	678	28	191	7	1	1074	1	321
3	19	13	8	13	1	360	0	46
2	14	17	166	6	0	803	1	239
3	19	15	69	11	1	473	0	25
3	19	31	115	6	1	525	1	92
2	11	9	50	4	0	290	0	41
3	13	25	99	10	1	554	1	103
1	13	15	103	6	1	539	1	74
2	10	66	172	5	1	917	1	238
3	16	13	93	10	1	588	0	69
4	48	17	57	5	5	604	1	83
4	26	29	50	12	2	545	0	37

La	Ce	Pr	Nd	Sm	Eu	Gd	Pb
6	9	0.8	2.7	0.4	1.9	0.2	22
10	15	1.3	4.3	0.4	3.4	0.3	17
5	7	0.7	2.0	0.3	2.2	0.2	8
6	8	0.7	2.5	0.5	2.6	0.4	22
19	28	2.6	8.2	1.4	3.0	0.8	32
6	10	0.9	2.9	0.5	2.1	0.5	34
4	7	0.6	2.2	0.4	1.8	0.2	24
3	4	0.4	1.5	0.3	1.5	0.2	15
2	4	0.4	1.1	0.2	1.0	0.2	17
6	9	0.8	2.6	0.4	2.4	0.3	8
9	14	1.2	4.3	0.4	3.0	0.3	8
6	8	0.7	2.4	0.3	2.8	0.3	18
17	27	3.1	9.2	1.3	2.5	0.7	18
18	27	2.4	8.0	1.2	4.2	0.9	22
6	10	0.9	2.3	0.3	1.6	0.2	13
10	15	1.2	3.8	0.5	2.2	0.4	27
4	5	0.5	1.6	0.3	1.2	0.3	26
8	14	1.2	4.4	0.6	2.2	0.5	31
2	2	0.1	0.5	0.2	0.9	0.1	21
9	14	1.1	3.7	0.4	2.4	0.4	33
3	4	0.3	0.9	0.2	1.1	0.2	34
8	14	1.3	4.4	0.7	1.7	0.6	27
2	3	0.3	1.0	0.2	0.8	0.1	16
6	10	0.9	2.8	0.7	1.4	0.6	36
4	6	0.5	1.7	0.4	1.3	0.3	30
14	22	2.1	7.1	1.2	3.2	0.8	32
4	6	0.6	1.8	0.3	1.5	0.3	33
8	13	1.2	3.0	0.6	1.5	0.4	31
3	4	0.3	0.8	0.3	1.2	0.2	44

Appendix Table 3-5. Results of Sr isotope analysis of plagioclase in the Busetsu granite

Sample	87Sr/86Sr	2SE	84Sr/86Sr	2SE	85Rb/86Sr
NK_Pl-1_core	0.70989	0.00006	0.05701	0.00021	0.00964
NK_Pl-1_rim	0.70930	0.00009	0.05700	0.00031	0.01099
NK_Pl-2_core	0.70963	0.00005	0.05710	0.00020	0.00589
NK_Pl-2_rim	0.70980	0.00017	0.05733	0.00074	0.02034
NK_Pl-4_core	0.71007	0.00014	0.05679	0.00050	0.01169
NK_Pl-4_rim	0.70990	0.00015	0.05685	0.00046	0.02791
NK_Pl-5_core	0.71177	0.00010	0.05709	0.00030	0.03203
NK_Pl-5_rim	0.70995	0.00012	0.05698	0.00042	0.00919
NK_Pl-g1_core	0.71021	0.00013	0.05657	0.00037	0.01210
NK_Pl-g1_rim	0.70952	0.00010	0.05761	0.00034	0.01622
NK_Pl-g2_core	0.71159	0.00008	0.05715	0.00012	0.02895
NK_Pl-g2_rim	0.70992	0.00011	0.05685	0.00042	0.01573
NK_Pl-g3_core	0.70788	0.00016	0.05646	0.00041	0.39300
NK_Pl-g3_rim	0.70968	0.00011	0.05684	0.00037	0.04678
YS_Pl-1_core	0.71007	0.00006	0.05658	0.00021	0.13917
YS_Pl-1_rim	0.71023	0.00008	0.05609	0.00024	0.00432
YS_Pl-2_core	0.71359	0.00017	0.05586	0.00051	0.03096
YS_Pl-2_rim	0.71016	0.00009	0.05609	0.00051	0.00689
YS_Pl-3_core	0.70965	0.00006	0.05613	0.00019	0.06845
YS_Pl-3_rim	0.71032	0.00008	0.05617	0.00026	0.01932
YS_Pl-4_core	0.71023	0.00008	0.05588	0.00019	0.01668
YS_Pl-4_rim	0.71029	0.00009	0.05607	0.00030	0.00534
YS_Pl-5_core	0.71004	0.00006	0.05629	0.00024	0.19730
YS_Pl-5_rim	0.71016	0.00012	0.05615	0.00057	0.01615
YS_Pl-g1_core	0.71016	0.00005	0.05640	0.00012	0.03182
YS_Pl-g1_rim	0.71034	0.00009	0.05728	0.00028	0.00312
YS_Pl-g2_core	0.71012	0.00007	0.05633	0.00020	0.00346
YS_Pl-g2_rim	0.71020	0.00009	0.05669	0.00034	0.00678
YS_Pl-g5_core	0.71057	0.00007	0.05586	0.00025	0.00565
YS_Pl-g5_rim	0.71073	0.00023	0.05256	0.00145	0.00515
TK01_Pl-1_core	0.70978	0.00007	0.05626	0.00020	0.02099
TK01_Pl-1_rim	0.70965	0.00013	0.05666	0.00019	0.22427
TK01_Pl-10_core	0.70982	0.00007	0.05610	0.00026	0.13448
TK01_Pl-10_rim	0.70974	0.00007	0.05660	0.00026	0.00745
TK01_Pl-3_core	0.71047	0.00007	0.05614	0.00016	0.01736
TK01_Pl-3_rim	0.70978	0.00009	0.05570	0.00038	0.00466
TK01_Pl-4_core	0.70963	0.00009	0.05646	0.00027	0.02732
TK01_Pl-4_rim	0.70958	0.00007	0.05653	0.00031	0.00444
TK01_Pl-5_core	0.70976	0.00007	0.05614	0.00017	0.01092
TK01_Pl-5_rim	0.70976	0.00008	0.05653	0.00029	0.22090
TK01_Pl-7_core	0.70960	0.00008	0.05658	0.00022	0.02590
TK01_Pl-7_rim	0.70977	0.00012	0.05583	0.00035	0.00713
TK01_Pl-8_core	0.70963	0.00006	0.05626	0.00021	0.02995
TK01_Pl-8_rim	0.70959	0.00009	0.05626	0.00021	0.00439
TK01_Pl-g1_core	0.70979	0.00008	0.05614	0.00026	0.01973
TK01_Pl-g1_rim	0.70974	0.00010	0.05621	0.00023	0.00943
TK02_Pl-3_core	0.71032	0.00017	0.05673	0.00103	0.08343
TK02_Pl-3_rim	0.70981	0.00033	0.05988	0.00124	0.04869
TK02_Pl-4_core	0.71041	0.00021	0.05616	0.00117	0.03629
TK02_Pl-4_rim	0.71049	0.00024	0.05408	0.00096	0.04695
TK02_Pl-7_core	0.70914	0.00018	0.05656	0.00066	0.10392
TK02_Pl-7_rim	0.70990	0.00050	0.05666	0.00235	0.08549
TK02_Pl-9_core	0.70903	0.00020	0.05639	0.00067	0.06751
TK02_Pl-9_rim	0.71087	0.00049	0.05487	0.00294	0.14441
TK02_Pl-g1_core	0.71069	0.00027	0.05678	0.00104	0.11028
TK02_Pl-g1_rim	0.71119	0.00035	0.05093	0.00189	0.06126
TK02_Pl-g4_core	0.71095	0.00024	0.05450	0.00111	0.24733
TK02_Pl-g4_rim	0.71092	0.00038	0.05546	0.00179	0.05090
TK02_Pl-g5_core	0.71084	0.00025	0.05434	0.00113	0.08871
TK02_Pl-g5_rim	0.71103	0.00050	0.05450	0.00295	0.33805

Appendix Table 3-6. Results of whole-rock geochemical analyses of the Busetsu granites

Major elements [wt%]

Sample	NK	YS	TK01	TK02	2801	2802	KJ	MC
SiO2	74.0	72.7	71.6	73.9	72.3	73.2	72.01	74.78
TiO2	0.16	0.3	0.31	0.12	0.22	0.22	0.33	0.49
Al2O3	14.29	14.72	14.7	14.55	15.64	14.5	14.85	12.81
Fe2O3	2.1	2.9	3.3	1.54	2.5	2.4	2.8	4.31
MnO	0.04	0.05	0.05	0.07	0.05	0.05	0.05	0.1
MgO	0.23	0.44	0.44	0.11	0.37	0.27	0.45	1.32
CaO	1.74	2.51	2.85	1.15	2.04	2.1	2.71	0.42
Na2O	3.63	3.32	3.06	3.54	3.43	3.32	3.38	1.3
K2O	3.22	3.26	3.34	4.65	3.21	3.83	3.25	3.36
P2O5	0.10	0.12	0.11	0.15	0.13	0.08	0.12	0.07
Total	99.519	100.316	99.775	99.736	99.85	99.906	99.921	98.941
Trace elements [ppm]								
Rb	190	175	152	377	173	230	98	102
Ba	1065	1396	1588	703	1296	1221	824	442
Th	13	13	10	12	11	13	8	10
U	2.4	2.4	1.7	4.7	1.6	3.0	3	3
Nb	19	20	18	22	17	21	12	10
Ta	1.8	1.3	1.2	3.1	1.7	1.8	1	1
La	88	125	125	71	107	82	126	21
Ce	70	99	103	58	82	66	101	49
Pb	47	47	43	58	52	51	23	20
Pr	51	75	81	44	61	51	76	5
Sr	437	603	587	209	492	423	356	81
Nd	37	57	62	32	47	40	60	18
Zr	129	214	257	100	179	185	135	100
Hf	4.1	6.7	7.7	4.0	5.3	6.4	4	3
Sm	23	34	41	24	27	27	37	3
Eu	17	24	28	10	25	19	25	1
Ti	1600	3100	3100	1200	2200	2200	1978	2937
Gd	19	27	31	19	22	22	30	4
Tb	15	22	26	18	15	21	23	1
Dy	11	15	20	13	9	18	15	3
Ho	9	14	17	11	7	16	13	1
Y	14	19	24	16	9	24	18	16
Er	9	14	18	10	7	17	13	2
Tm	7	12	15	8	5	16	11	0.3
Yb	7	12	16	8	6	15	12	2
Lu	7	11	15	7	6	15	11	0.3

Appendix table 4-1. Externally calibrated Sm-Nd isotopic data for EDR4

Results	147Sm/144Nd	2σ	143Nd/144Nd	2σ	145Nd/144Nd	2σ	150Nd/144Nd	2SE
20160511_EDR4-01	0.1102	0.0623	0.512255	0.000021	0.348413	0.000009	0.236462	0.000019
20160511_EDR4-02	0.1105	0.0625	0.512252	0.000015	0.348414	0.000009	0.236476	0.000017
20160511_EDR4-03	0.1105	0.0625	0.512255	0.000013	0.348411	0.000010	0.236493	0.000023
20160511_EDR4-04	0.1103	0.0624	0.512256	0.000015	0.348417	0.000010	0.236461	0.000018
20160511_EDR4-05	0.1108	0.0627	0.512255	0.000014	0.348420	0.000010	0.236486	0.000013
20160511_EDR4-06	0.1103	0.0624	0.512267	0.000015	0.348428	0.000012	0.236475	0.000020
20160512_EDR4-01	0.1014	0.0016	0.512259	0.000012	0.348421	0.000008	0.236425	0.000017
20160512_EDR4-02	0.1013	0.0016	0.512277	0.000020	0.348424	0.000011	0.236404	0.000026
20160512_EDR4-03	0.1010	0.0016	0.512248	0.000016	0.348416	0.000009	0.236431	0.000023
20160512_EDR4-04	0.1015	0.0016	0.512235	0.000015	0.348423	0.000011	0.236433	0.000020
20160512_EDR4-05	0.1017	0.0016	0.512253	0.000013	0.348423	0.000010	0.236416	0.000018
20160512_EDR4-06	0.1014	0.0016	0.512261	0.000020	0.348424	0.000011	0.236404	0.000022
20160512_EDR4-07	0.1016	0.0016	0.512239	0.000021	0.348416	0.000011	0.236392	0.000030
20160512_EDR4-08	0.1010	0.0016	0.512244	0.000019	0.348416	0.000010	0.236387	0.000025
20170418_EDR-01	0.1012	0.0016	0.512229	0.000026	0.348407	0.000017	0.236519	0.000026
20170418_EDR-02	0.1039	0.0016	0.512266	0.000021	0.348416	0.000016	0.236479	0.000027
20170418_EDR-03	0.1030	0.0016	0.512252	0.000028	0.348428	0.000018	0.236478	0.000033
20170418_EDR-04	0.1028	0.0016	0.512253	0.000030	0.348428	0.000016	0.236494	0.000027
20170418_EDR-05	0.1024	0.0016	0.512253	0.000034	0.348411	0.000014	0.236497	0.000024
20170418_EDR-06	0.1016	0.0016	0.512239	0.000028	0.348404	0.000016	0.236489	0.000024
20170418_EDR-07	0.0908	0.0014	0.512250	0.000021	0.348412	0.000019	0.236506	0.000026
20170418_EDR-08	0.0972	0.0015	0.512258	0.000023	0.348405	0.000014	0.236501	0.000033
20170418_EDR-09	0.1009	0.0016	0.512260	0.000025	0.348413	0.000016	0.236490	0.000021
20170418_EDR-10	0.1016	0.0016	0.512237	0.000029	0.348410	0.000017	0.236507	0.000033
20170418_EDR-11	0.1011	0.0016	0.512252	0.000024	0.348408	0.000014	0.236470	0.000024
20170418_EDR-12	0.1002	0.0016	0.512247	0.000020	0.348412	0.000014	0.236484	0.000025
20170704a_EDR-07	0.1009	0.0007	0.512265	0.000019	0.348414	0.000013	0.236381	0.000019
20170704a_EDR-08	0.1009	0.0007	0.512262	0.000020	0.348420	0.000012	0.236377	0.000018
20170704a_EDR-09	0.1000	0.0007	0.512274	0.000021	0.348412	0.000011	0.236404	0.000022
20170704a_EDR-10	0.1011	0.0007	0.512275	0.000029	0.348439	0.000010	0.236271	0.000017
20170704a_EDR-11	0.1008	0.0007	0.512248	0.000020	0.348437	0.000012	0.236312	0.000015
20170704a_EDR-12	0.1009	0.0007	0.512241	0.000024	0.348434	0.000012	0.236284	0.000024
20170704a_EDR-13	0.1005	0.0007	0.512250	0.000022	0.348422	0.000014	0.269686	0.000033
20170704a_EDR-14	0.1000	0.0007	0.512257	0.000020	0.348413	0.000013	0.269663	0.000029
20170704a_EDR-15	0.1009	0.0007	0.512260	0.000022	0.348419	0.000015	0.269664	0.000028
20170704a_EDR-16	0.1014	0.0009	0.512257	0.000026	0.348421	0.000016	0.236347	0.000020
20170704a_EDR-17	0.1001	0.0009	0.512242	0.000023	0.348416	0.000017	0.236351	0.000017
20170704a_EDR-18	0.1011	0.0009	0.512242	0.000025	0.348423	0.000016	0.236348	0.000022
20170704b_EDR-1	0.1018	0.0020	0.512260	0.000017	0.348419	0.000012	0.236295	0.000020
20170704b_EDR-2	0.1020	0.0020	0.512277	0.000016	0.348416	0.000012	0.236306	0.000021
20170704b_EDR-3	0.1013	0.0020	0.512263	0.000017	0.348419	0.000012	0.236316	0.000020
20170704b_EDR-4	0.1019	0.0020	0.512256	0.000024	0.348447	0.000012	0.236246	0.000015
20170704b_EDR-5	0.1016	0.0020	0.512250	0.000027	0.348430	0.000012	0.236264	0.000017
20170704b_EDR-6	0.1009	0.0020	0.512271	0.000026	0.348447	0.000013	0.236255	0.000020
20170704b_EDR-7	0.1026	0.0024	0.512256	0.000019	0.348443	0.000012	0.269639	0.000029
20170704b_EDR-8	0.1026	0.0024	0.512235	0.000020	0.348437	0.000013	0.236290	0.000017
20170704b_EDR-9	0.1026	0.0024	0.512256	0.000021	0.348441	0.000012	0.236289	0.000020
20170704b_EDR-10	0.1013	0.0021	0.512230	0.000031	0.348433	0.000013	0.236309	0.000021
20170704b_EDR-11	0.1014	0.0021	0.512267	0.000027	0.348439	0.000011	0.236303	0.000031
20170704b_EDR-12	0.1015	0.0021	0.512232	0.000028	0.348448	0.000012	0.236305	0.000021
20170704c_EDR-1	0.1019	0.0020	0.512265	0.000036	0.348440	0.000021	0.270293	0.000033
20170704c_EDR-2	0.1020	0.0020	0.512286	0.000035	0.348436	0.000022	0.270226	0.000036
20170704c_EDR-3	0.1018	0.0020	0.512274	0.000035	0.348437	0.000021	0.270120	0.000025
20170704c_EDR-4	0.1007	0.0020	0.512256	0.000035	0.348419	0.000012	0.269323	0.000022
20170704c_EDR-5	0.1013	0.0020	0.512252	0.000034	0.348404	0.000013	0.269354	0.000022
20170704c_EDR-6	0.1009	0.0020	0.512266	0.000034	0.348421	0.000014	0.269319	0.000022
20170704c_EDR-7	0.1014	0.0020	0.512252	0.000035	0.348437	0.000012	0.269049	0.000029
20170704c_EDR-8	0.1011	0.0020	0.512252	0.000037	0.348442	0.000011	0.268986	0.000023
20170704c_EDR-9	0.1011	0.0020	0.512229	0.000035	0.348447	0.000013	0.269021	0.000030
Mean	0.1021		**0.512254**		0.348424		0.243706	
2SD	0.0065		**0.000025**		0.000024		0.027733	
2SE	0.0009		0.000003		0.000003		0.003611	
%2SE	0.8%		0.001%		0.001%		1.482%	
Sm/Nd and Nd isotopic ratios were calibrated based on the results of Synth-NSP and Synth-LCN, respectively.								

Appendix Table 4-2. Results of trace element analysis of monazite in granitic rocks in the Japan arc [ppm] * Ce concentrations were determined by electron microprobe analysis

Sample #	Rock-type	Measurment spot	Contrast in BSE	Y	La	Ce*	Pr	Nd	Sm	Eu	Gd	Tb	Dy	Ho	Er	Tm	Yb	Lu	Th	U
1	From magnetite-series granite	Shirakawa-1		23965	128569	250912	28363	137350	30721	79	17940	2077	7950	926	1584	149	713	67.9	142780	3856
2	From magnetite-series granite	Nakano-1		14247	153104	303291	31206	111625	19647	410	11332	1179	4273	480	794	73	361	36	32757	146
3	From magnetite-series pegmatite	Kamiotomo-1	Darker	24854	115806	235105	26744	114750	27830	55	18725	2099	8083	959	1521	123	509	44	108486	5144
3	From magnetite-series pegmatite	Kamiotomo-2	Brighter	25414	110152	228464	26056	112479	26660	56	18774	2119	8223	998	1626	130	534	46	125295	6392
3	From magnetite-series pegmatite	Kamiotomo-3	Darker	26340	114744	237366	26901	115113	27969	60	19557	2171	8487	1024	1630	132	539	46	99865	4696
3	From magnetite-series pegmatite	Kamiotomo-4	Brighter	23505	106004	220859	24814	105858	25837	56	17718	1995	7724	945	1526	124	505	43	130260	5839
4	From magnetite-series pegmatite	Oro-1	Brighter	22814	105953	222760	22984	78064	12807	11	7787	833	3457	513	1050	109	592	62	230037	3842
4	From magnetite-series pegmatite	Oro-2	Darker	29693	109791	233194	24453	85804	14817	13	9588	1066	4493	678	1357	140	704	72	173818	3588
5	From ilmenite-series granite	Naegi_mnz-1		5436	106625	256935	30641	107186	26953	8	12499	1371	5142	579	890	72	262	20	83982	1853
5	From ilmenite-series granite	Naegi_mnz-2		5993	116096	257337	31786	113564	28334	7	13835	1648	6106	712	1122	94	351	26	94681	3459
5	From ilmenite-series granite	Naegi_mnz-3		5922	111272	235677	27806	99693	25735	8	13820	1662	6079	678	981	71	231	16	33474	1469
5	From ilmenite-series granite	Naegi_mnz-4		2737	121765	248261	26872	89262	16960	4.0	6966	721	2591	292	460	38	138	10	110992	2764
6	From ilmenite-series granite	Busetsu-1		19130	128777	260883	27971	112439	22730	356	15239	1802	6807	779	1199	89	344	28	37447	2406
6	From ilmenite-series granite	Busetsu-2		20380	120131	244773	26761	110588	25230	350	17562	2069	7611	829	1176	91	344	27	47380	2838
6	From ilmenite-series granite	Busetsu-3		22807	131041	270835	29518	121514	28092	388	19445	2295	8487	936	1343	102	381	30	45537	3382
6	From ilmenite-series granite	Busetsu-4		26916	133151	283927	32243	132238	31668	419	22736	2767	10151	1087	1559	122	469	37	66642	4546
6	From ilmenite-series granite	Busetsu-5		17746	164089	291277	32734	139798	24967	362	13674	1359	5577	775	1382	112	444	37	21570	384
6	From ilmenite-series granite	Busetsu-6		22149	134571	258073	27459	114357	37301	164	23309	3162	10924	934	1316	113	484	35	42941	26551
7	From ilmenite-series pegmatite	Utusmine-1		40627	48441	220546	36790	172639	86375	5	48743	4970	12012	706	718	59	244	18	41102	4521
7	From ilmenite-series pegmatite	Utusmine-2		40413	47489	215608	36517	168067	86275	6	48755	4960	11938	707	731	58	243	18	40757	4597
8	From ilmenite-series pegmatite	Morita-1	Brighter	25746	92912	234017	29340	128843	36159	6	23466	2692	9322	914	1181	80	285	21	84096	7076
8	From ilmenite-series pegmatite	Morita-2	Darker	30768	94213	242484	31274	136950	42269	16	27929	3280	11313	1088	1407	97	354	26	69864	6902
9	From ilmenite-series pegmatite	Shichironai-1	Darker	23173	114057	249711	29292	115609	36289	7	25608	2854	8908	719	702	39	108	7	42968	3976
9	From ilmenite-series pegmatite	Shichironai-2	Brighter	30518	108567	264913	32265	135626	45483	8	33006	3823	11902	957	934	51	143	10	53749	4912
10	From ilmenite-series pegmatite	Shiozawa-1	Darker (rim)	32223	101505	203755	23966	121185	33543	104	25038	2825	11631	1530	2662	209	853	76	145042	9769
10	From ilmenite-series pegmatite	Shiozawa-2	Brighter (core)	23418	109243	207104	23352	106286	28506	87	20322	2193	8773	1130	1902	147	600	52	178991	10591
10	From ilmenite-series pegmatite	Shiozawa-3	Brighter (core)	22589	109710	208390	23273	108703	28302	86	19818	2143	8634	1092	1797	142	567	50	179410	10155
10	From ilmenite-series pegmatite	Shiozawa-4	Darker (rim)	29520	100223	205477	24054	112688	32616	105	24146	2693	11136	1397	2391	184	740	64	136049	8300
11	From ilmenite-series pegmatite	Shimo-ono-1		5572	36222	151310	30065	144074	179826	11	66415	3957	3029	86	114	17	57	8	70982	7659
11	From ilmenite-series pegmatite	Shimo-ono-2		7100	39287	153457	30254	144260	160362	14	67704	4049	3319	81	82	10	13	4	59966	4239
11	From ilmenite-series pegmatite	Shimo-ono-3		6953	36679	153457	31348	150262	193687	8	80681	5776	4449	79	75	11	24	4	69646	8850
11	From ilmenite-series pegmatite	Shimo-ono-4		4793	33433	148179	29174	139348	176313	10	69161	4225	3171	71	80	14	37	6	53863	5432
11	From ilmenite-series pegmatite	Shimo-ono-5		4061	34343	149380	29936	146394	177453	6	69826	4144	2856	49	50	10	11	4	56445	6703
12	From ilmenite-series pegmatite	Misugi-1	Brighter	39415	53460	199035	32425	179336	75557	3	45878	4997	14880	1199	1426	102	376	26	34499	4283
12	From ilmenite-series pegmatite	Misugi-2	Brighter	39083	54291	199035	33329	181697	76688	4	46897	5151	14953	1185	1366	102	363	25	33977	4001
12	From ilmenite-series pegmatite	Misugi-3	Darker	30819	57401	213612	35324	187803	77916	4	45613	4637	12762	964	1051	77	269	18	23652	1939
12	From ilmenite-series pegmatite	Misugi-4	Brighter	43132	64029	229221	38560	205540	86389	2	51879	5483	16259	1310	1514	111	402	27	35395	4002
13	From ilmenite-series pegmatite	Masaki-1	Darker (core)	26319	86683	253485	33126	136961	39094	3	26751	2987	9664	860	934	55	157	9	36077	4841
13	From ilmenite-series pegmatite	Masaki-2	Brighter (rim)	7181	87038	252445	34269	148676	38537	6	17415	1270	3141	254	267	15	35	3	82830	2993

Appendix table 4-3. Sm-Nd isotopic data of monazite form granitic rocks in Japan

Sample #	Rock-type	Measurment spot	Contrast in BSE	147Sm/144Nd	2σ	143Nd/144Nd	2σ	145Nd/144Nd	2σ	150Nd/144Nd	2SE	Age (Ma)	**143Nd/144Nd(t)	2s
3	From magnetite-series pegmatite	Kamiotomo_d-1	Darker	0.1488	0.0023	0.51257	0.00002	0.34842	0.00001	0.23643	0.00002	135	0.51244	0.00002
		Kamiotomo_d-2	Darker	0.1493	0.0023	0.51257	0.00003	0.34842	0.00001	0.23642	0.00002	135	0.51244	0.00003
		Kamiotomo_d-3	Darker	0.1483	0.0023	0.51257	0.00002	0.34841	0.00001	0.23640	0.00002	135	0.51244	0.00002
		Kamiotomo_d-4	Darker	0.1476	0.0010	0.51259	0.00002	0.34842	0.00001	0.23637	0.00001	135	0.51246	0.00002
		Kamiotomo_d-5	Darker	0.1476	0.0010	0.51258	0.00002	0.34843	0.00001	0.23637	0.00001	135	0.51245	0.00002
		Kamiotomo_d-6	Darker	0.1477	0.0010	0.51258	0.00003	0.34843	0.00001	0.23632	0.00002	135	0.51245	0.00003
		Kamiotomo_b-1	Brighter	0.1482	0.0023	0.51256	0.00002	0.34843	0.00001	0.23643	0.00003	135	0.51243	0.00002
		Kamiotomo_b-2	Brighter	0.1474	0.0023	0.51257	0.00002	0.34841	0.00001	0.23642	0.00003	135	0.51244	0.00002
		Kamiotomo_b-3	Brighter	0.1477	0.0023	0.51258	0.00002	0.34842	0.00001	0.23641	0.00003	135	0.51245	0.00002
		Kamiotomo_b-4	Brighter	0.1480	0.0010	0.51258	0.00002	0.34844	0.00001	0.23634	0.00002	135	0.51245	0.00002
		Kamiotomo_b-5	Brighter	0.1479	0.0010	0.51257	0.00003	0.34843	0.00001	0.23634	0.00002	135	0.51244	0.00003
		Kamiotomo_b-6	Brighter	0.1473	0.0010	0.51259	0.00003	0.34842	0.00001	0.23632	0.00002	135	0.51246	0.00003
4	From magnetite-series pegmatite	Oro_d-1	Darker	0.1030	0.0012	0.51219	0.00002	0.34841	0.00002	0.23641	0.00004	61.9	0.51215	0.00002
		Oro_d-2	Darker	0.1033	0.0012	0.51218	0.00003	0.34842	0.00002	0.23646	0.00003	61.9	0.51213	0.00003
		Oro_d-3	Darker	0.1034	0.0012	0.51217	0.00003	0.34841	0.00002	0.23644	0.00003	61.9	0.51213	0.00003
		Oro_d-4	Darker	0.1048	0.0008	0.51218	0.00002	0.34842	0.00002	0.23626	0.00002	61.9	0.51214	0.00002
		Oro_d-5	Darker	0.1048	0.0008	0.51217	0.00003	0.34843	0.00002	0.23626	0.00003	61.9	0.51213	0.00003
		Oro_d-6	Darker	0.1053	0.0008	0.51219	0.00004	0.34843	0.00002	0.23626	0.00003	61.9	0.51214	0.00004
		Oro_b-1	Brighter	0.1025	0.0015	0.51219	0.00003	0.34839	0.00002	0.23644	0.00004	61.9	0.51215	0.00003
		Oro_b-2	Brighter	0.0989	0.0013	0.51218	0.00002	0.34841	0.00001	0.23641	0.00004	61.9	0.51214	0.00002
		Oro_b-3	Brighter	0.1014	0.0010	0.51218	0.00003	0.34843	0.00002	0.23626	0.00003	61.9	0.51214	0.00003
		Oro_b-4	Brighter	0.1022	0.0010	0.51217	0.00003	0.34842	0.00002	0.23627	0.00002	61.9	0.51212	0.00003
		Oro_b-5	Brighter	0.1018	0.0013	0.51219	0.00003	0.34840	0.00001	0.23640	0.00004	61.9	0.51215	0.00003
		Oro_b-6	Brighter	0.1003	0.0010	0.51217	0.00003	0.34843	0.00002	0.23627	0.00002	61.9	0.51212	0.00003
7	From ilmenite-series pegmatite	Utsumine-1		0.3166	0.0050	0.51269	0.00002	0.34842	0.00001	0.23641	0.00002	106	0.51247	0.00002
		Utsumine-2		0.3165	0.0050	0.51271	0.00002	0.34842	0.00001	0.23639	0.00002	106	0.51249	0.00002
		Utsumine-3		0.3165	0.0050	0.51271	0.00002	0.34842	0.00001	0.23639	0.00002	106	0.51249	0.00002
		Utsumine-4		0.3160	0.0050	0.51270	0.00002	0.34842	0.00001	0.23640	0.00001	106	0.51248	0.00002
		Utsumine-5		0.3148	0.0022	0.51272	0.00003	0.34843	0.00001	0.23632	0.00001	106	0.51251	0.00003
		Utsumine-6		0.3153	0.0022	0.51272	0.00003	0.34843	0.00001	0.23630	0.00001	106	0.51250	0.00003
		Utsumine-7		0.3147	0.0022	0.51273	0.00003	0.34844	0.00001	0.23629	0.00001	106	0.51251	0.00003
		Utsumine-8		0.3150	0.0022	0.51273	0.00002	0.34844	0.00001	0.23629	0.00001	106	0.51252	0.00002
8	From ilmenite-series pegmatite	Morita_d-1	Darker	0.1833	0.0029	0.51261	0.00002	0.34842	0.00001	0.23638	0.00002	106	0.51248	0.00002
		Morita_d-2	Darker	0.1725	0.0027	0.51259	0.00002	0.34842	0.00001	0.23638	0.00002	106	0.51247	0.00002
		Morita_d-3	Darker	0.1811	0.0028	0.51259	0.00002	0.34842	0.00001	0.23642	0.00002	106	0.51246	0.00002
		Morita_d-4	Darker	0.1879	0.0037	0.51260	0.00004	0.34838	0.00002	0.23631	0.00001	106	0.51247	0.00004
		Morita_d-5	Darker	0.1838	0.0036	0.51258	0.00004	0.34840	0.00002	0.23631	0.00001	106	0.51245	0.00004
		Morita_d-6	Darker	0.1886	0.0037	0.51261	0.00004	0.34840	0.00002	0.23631	0.00001	106	0.51248	0.00004
		Morita_b-1	Brighter	0.1661	0.0026	0.51258	0.00001	0.34842	0.00001	0.23641	0.00002	106	0.51246	0.00001
		Morita_b-2	Brighter	0.1695	0.0027	0.51258	0.00002	0.34841	0.00001	0.23643	0.00002	106	0.51246	0.00002
		Morita_b-3	Brighter	0.1659	0.0026	0.51257	0.00002	0.34842	0.00001	0.23642	0.00002	106	0.51246	0.00002
		Morita_b-4	Brighter	0.1877	0.0037	0.51259	0.00004	0.34840	0.00002	0.23628	0.00001	106	0.51246	0.00004
		Morita_b-5	Brighter	0.1879	0.0037	0.51259	0.00004	0.34840	0.00002	0.23625	0.00002	106	0.51246	0.00004
		Morita_b-6	Brighter	0.1875	0.0037	0.51259	0.00004	0.34840	0.00002	0.23627	0.00002	106	0.51246	0.00004
9	From ilmenite-series pegmatite	Shichironai_b-1	Brighter	0.2070	0.0024	0.51258	0.00002	0.34842	0.00001	0.23648	0.00002	106	0.51243	0.00002
		Shichironai_b-2	Brighter	0.2084	0.0024	0.51261	0.00001	0.34841	0.00001	0.23647	0.00002	106	0.51246	0.00001
		Shichironai_b-3	Brighter	0.2065	0.0024	0.51257	0.00002	0.34842	0.00001	0.23647	0.00002	106	0.51243	0.00002
		Shichironai_b-4	Brighter	0.2074	0.0040	0.51261	0.00004	0.34843	0.00002	0.23623	0.00002	106	0.51247	0.00004
		Shichironai_b-5	Brighter	0.2076	0.0040	0.51258	0.00004	0.34845	0.00002	0.23625	0.00002	106	0.51244	0.00004
		Shichironai_b-6	Brighter	0.2075	0.0040	0.51258	0.00004	0.34846	0.00002	0.23625	0.00002	106	0.51244	0.00004
		Shichironai_d-1	Darker	0.1924	0.0022	0.51258	0.00002	0.34841	0.00001	0.23646	0.00002	106	0.51244	0.00002
		Shichironai_d-2	Darker	0.1933	0.0022	0.51260	0.00002	0.34841	0.00001	0.23646	0.00002	106	0.51247	0.00002
		Shichironai_d-3	Darker	0.1932	0.0038	0.51261	0.00004	0.34843	0.00002	0.23625	0.00001	106	0.51247	0.00004
		Shichironai_d-4	Darker	0.1929	0.0038	0.51257	0.00004	0.34844	0.00002	0.23625	0.00002	106	0.51244	0.00004
		Shichironai_d-5	Darker	0.1924	0.0038	0.51260	0.00004	0.34842	0.00002	0.23624	0.00002	106	0.51246	0.00004
		Shichironai_d-6	Darker	0.1930	0.0038	0.51260	0.00004	0.34842	0.00002	0.23622	0.00001	106	0.51246	0.00004
10	From ilmenite-series pegmatite	Shiozawa_core-1	Brighter	0.1426	0.0022	0.51260	0.00002	0.34844	0.00001	0.23648	0.00002	106	0.51250	0.00002
		Shiozawa_core-2	Brighter	0.1415	0.0022	0.51261	0.00002	0.34842	0.00001	0.23648	0.00002	106	0.51251	0.00002
		Shiozawa_core-3	Brighter	0.1429	0.0029	0.51262	0.00003	0.34841	0.00002	0.23625	0.00002	106	0.51252	0.00003
		Shiozawa_core-4	Brighter	0.1425	0.0029	0.51261	0.00003	0.34842	0.00002	0.23626	0.00003	106	0.51251	0.00003
		Shiozawa_core-5	Brighter	0.1433	0.0029	0.51262	0.00003	0.34843	0.00002	0.23625	0.00002	106	0.51252	0.00003
		Shiozawa_core-6	Brighter	0.1433	0.0029	0.51260	0.00003	0.34842	0.00002	0.23627	0.00002	106	0.51251	0.00003
		Shiozawa_rim-1	Darker	0.1548	0.0024	0.51261	0.00002	0.34841	0.00001	0.23650	0.00002	106	0.51251	0.00002
		Shiozawa_rim-2	Darker	0.1556	0.0031	0.51263	0.00003	0.34842	0.00002	0.23627	0.00002	106	0.51252	0.00003
		Shiozawa_rim-3	Darker	0.1556	0.0032	0.51261	0.00003	0.34842	0.00002	0.23627	0.00002	106	0.51250	0.00003
		Shiozawa_rim-4	Darker	0.1558	0.0032	0.51260	0.00003	0.34843	0.00002	0.23630	0.00003	106	0.51249	0.00003
11	From ilmenite-series pegmatite	Shimo-ono-1		0.7277	0.0119	0.51295	0.00002	0.34841	0.00001	0.23648	0.00002	115	0.51240	0.00002
		Shimo-ono-2		0.7218	0.0113	0.51295	0.00001	0.34841	0.00001	0.23646	0.00002	115	0.51240	0.00002
		Shimo-ono-3		0.7660	0.0119	0.51298	0.00002	0.34841	0.00001	0.23645	0.00001	115	0.51240	0.00002
		Shimo-ono-4		0.7519	0.0117	0.51295	0.00002	0.34840	0.00001	0.23647	0.00001	115	0.51238	0.00002
		Shimo-ono-5		0.7546	0.0117	0.51297	0.00002	0.34843	0.00001	0.23646	0.00003	115	0.51240	0.00002
		Shimo-ono-6		0.7112	0.0176	0.51296	0.00003	0.34842	0.00002	0.23629	0.00003	115	0.51242	0.00004
12	From ilmenite-series pegmatite	Misugi_b-1	Brighter	0.2569	0.0040	0.51237	0.00002	0.34842	0.00001	0.23641	0.00002	75	0.51225	0.00002
		Misugi_b-2	Brighter	0.2470	0.0039	0.51237	0.00002	0.34841	0.00001	0.23642	0.00002	75	0.51225	0.00002
		Misugi_b-3	Brighter	0.2482	0.0021	0.51239	0.00002	0.34841	0.00002	0.23636	0.00002	75	0.51227	0.00002
		Misugi_b-4	Brighter	0.2465	0.0021	0.51239	0.00002	0.34840	0.00001	0.23636	0.00002	75	0.51227	0.00002
		Misugi_b-5	Brighter	0.2480	0.0021	0.51238	0.00002	0.34841	0.00001	0.23635	0.00002	75	0.51226	0.00002
		Misugi_d-1	Darker	0.2504	0.0039	0.51237	0.00001	0.34841	0.00001	0.23640	0.00002	75	0.51224	0.00001
		Misugi_d-2	Darker	0.2469	0.0039	0.51236	0.00002	0.34842	0.00001	0.23639	0.00002	75	0.51224	0.00002
		Misugi_d-3	Darker	0.2484	0.0021	0.51238	0.00002	0.34841	0.00002	0.23638	0.00002	75	0.51226	0.00002
		Misugi_d-4	Darker	0.2448	0.0021	0.51239	0.00002	0.34841	0.00001	0.23637	0.00002	75	0.51227	0.00002
		Misugi_d-5	Darker	0.2472	0.0021	0.51239	0.00002	0.34840	0.00001	0.23634	0.00001	75	0.51227	0.00002
13	From ilmenite-series pegmatite	Masaki_core-1	Darker	0.1776	0.0030	0.51258	0.00002	0.34841	0.00001	0.23641	0.00002	105	0.51246	0.00002
		Masaki_core-2	Darker	0.1725	0.0035	0.51259	0.00002	0.34843	0.00001	0.23641	0.00002	105	0.51247	0.00002
		Masaki_core-3	Darker	0.1725	0.0037	0.51257	0.00001	0.34843	0.00001	0.23643	0.00003	105	0.51245	0.00002
		Masaki_core-4	Darker	0.1786	0.0035	0.51259	0.00001	0.34842	0.00001	0.23630	0.00002	105	0.51246	0.00001
		Masaki_core-6	Darker	0.1766	0.0035	0.51258	0.00001	0.34843	0.00001	0.23628	0.00001	105	0.51246	0.00001
		Masaki_core-7	Darker	0.1777	0.0036	0.51259	0.00001	0.34841	0.00001	0.23627	0.00002	105	0.51247	0.00001
		Masaki_rim-1	Brighter	0.1592	0.0040	0.51260	0.00001	0.34841	0.00002	0.23639	0.00003	105	0.51249	0.00001
		Masaki_rim-2	Brighter	0.1679	0.0027	0.51257	0.00002	0.34841	0.00001	0.23643	0.00002	105	0.51245	0.00002
		Masaki_rim-3	Brighter	0.1789	0.0028	0.51257	0.00002	0.34843	0.00001	0.23643	0.00003	105	0.51245	0.00002
		Masaki_rim-4	Brighter	0.1811	0.0036	0.51259	0.00002	0.34842	0.00001	0.23632	0.00003	105	0.51246	0.00002
		Masaki_rim-5†	Brighter	0.1776	0.0035	0.51252	0.00003	0.34847	0.00002	0.23649	0.00003	105	0.51240	0.00003
		Masaki_rim-6†	Brighter	0.1803	0.0036	0.51259	0.00008	0.34848	0.00003	0.23646	0.00006	105	0.51247	0.00008

Appendix Figure 5-1

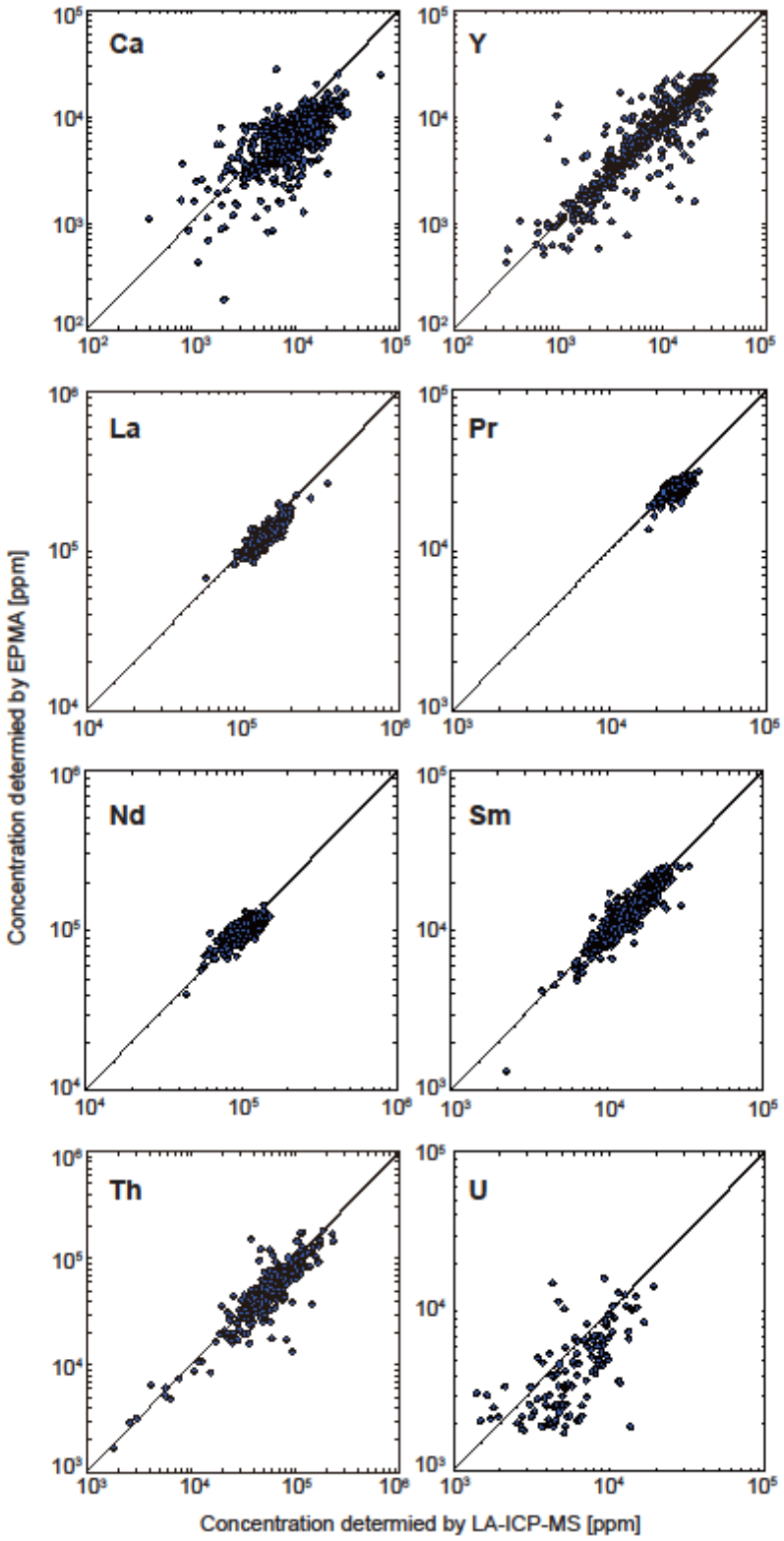

Appendix Table 5-1: Results from U-Pb dating of the secondary monazite standards

	$^{206}Pb/^{238}U$	2σ	$^{206}Pb/^{238}U$	2σ	$^{207}Pb^*/^{206}Pb^*$	2σ	$^{207}Pb^*/^{206}Pb^*$	2σ	Disc.†
	ratio		age (Ma)		ratio		age (Ma)		(%)
Manangotry									
Manangotry-1	0.090	0.002	557	9	0.060	0.001	618	36	10%
Manangotry-2	0.090	0.001	557	9	0.059	0.001	557	38	0%
Manangotry-3	0.089	0.002	552	12	0.059	0.001	566	34	2%
Manangotry-4	0.091	0.002	559	12	0.062	0.003	659	89	16%
Manangotry-5	0.091	0.002	561	13	0.060	0.001	619	46	10%
Manangotry-6	0.090	0.002	557	12	0.059	0.001	585	44	5%
Manangotry-7	0.091	0.002	563	10	0.058	0.001	535	45	-6%
Manangotry-8	0.090	0.002	558	9	0.060	0.001	592	40	6%
Manangotry-9	0.089	0.001	550	8	0.057	0.003	493	134	-12%
Manangotry-10	0.092	0.002	566	10	0.056	0.003	468	135	-22%
Manangotry-11	0.093	0.002	574	10	0.059	0.001	561	44	-3%
Manangotry-12	0.092	0.002	569	13	0.061	0.001	645	52	12%
Manangotry-13	0.089	0.003	549	17	0.059	0.003	574	119	5%
Manangotry-14	0.089	0.002	550	15	0.058	0.003	516	114	-7%
Manangotry-15	0.089	0.001	552	9	0.059	0.001	553	38	0%
Manangotry-16	0.089	0.001	551	7	0.057	0.001	502	39	-10%
Manangotry-17	0.088	0.002	545	12	0.059	0.002	585	57	7%
Manangotry-18	0.090	0.002	554	11	0.060	0.001	598	53	8%
16-F-6									
16-F-6-1	0.535	0.015	2761	62	0.204	0.004	2859	30	4%
16-F-6-2	0.545	0.011	2806	44	0.204	0.004	2859	33	2%
16-F-6-3	0.561	0.009	2871	39	0.199	0.002	2820	17	-2%
16-F-6-4	0.572	0.009	2915	37	0.203	0.002	2847	20	-3%
16-F-6-5	0.547	0.011	2814	45	0.205	0.002	2865	20	2%
16-F-6-6	0.560	0.012	2867	50	0.204	0.002	2862	17	0%
16-F-6-7	0.556	0.012	2850	49	0.202	0.002	2840	18	0%
16-F-6-8	0.557	0.011	2853	45	0.202	0.002	2846	18	0%
16-F-6-9	0.558	0.009	2857	36	0.204	0.002	2859	19	0%
16-F-6-10	0.543	0.022	2795	91	0.203	0.003	2852	20	3%
16-F-6-11	0.561	0.012	2870	49	0.202	0.003	2839	24	-1%
16-F-6-12	0.558	0.009	2858	39	0.203	0.003	2854	27	0%
16-F-6-13	0.521	0.019	2705	80	0.206	0.004	2873	34	7%
16-F-6-14	0.546	0.011	2810	46	0.203	0.003	2852	22	2%
16-F-6-15	0.533	0.018	2753	74	0.202	0.003	2845	26	4%
16-F-6-16	0.571	0.011	2914	45	0.199	0.003	2820	22	-4%
16-F-6-17	0.524	0.019	2718	81	0.206	0.006	2874	45	7%
16-F-6-18	0.552	0.013	2833	54	0.205	0.004	2863	35	1%
16-F-6-19	0.557	0.007	2856	30	0.199	0.002	2821	18	-2%
16-F-6-20	0.559	0.008	2862	33	0.199	0.002	2818	20	-2%
16-F-6-21	0.531	0.010	2747	44	0.204	0.003	2857	24	5%
16-F-6-22	0.550	0.011	2826	47	0.200	0.003	2823	25	0%
16-F-6-23	0.551	0.015	2829	61	0.206	0.004	2871	31	2%
16-F-6-24	0.532	0.026	2749	110	0.205	0.005	2862	42	5%
16-F-6-25	0.531	0.019	2748	78	0.210	0.007	2904	51	7%
16-F-6-26	0.512	0.015	2663	65	0.213	0.005	2930	37	11%
16-F-6-27	0.560	0.012	2865	49	0.204	0.004	2861	35	0%
16-F-6-28	0.550	0.011	2824	46	0.204	0.004	2860	33	2%
16-F-6-29	0.554	0.012	2843	48	0.200	0.002	2830	18	-1%
16-F-6-30	0.586	0.019	2973	77	0.205	0.003	2864	21	-5%
16-F-6-31	0.550	0.007	2826	31	0.204	0.003	2860	21	1%
16-F-6-32	0.543	0.008	2796	34	0.202	0.003	2842	20	2%
16-F-6-33	0.567	0.019	2897	78	0.200	0.012	2827	94	-3%
16-F-6-34	0.566	0.021	2891	88	0.200	0.011	2828	92	-3%
16-F-6-35	0.546	0.010	2807	40	0.201	0.002	2832	16	1%
16-F-6-36	0.542	0.008	2791	35	0.199	0.002	2816	21	1%
16-F-6-37	0.552	0.009	2832	38	0.201	0.003	2832	23	0%
16-F-6-38	0.560	0.010	2865	41	0.202	0.003	2841	24	-1%
16-F-6-39	0.540	0.009	2783	36	0.201	0.003	2835	24	2%
16-F-6-40	0.543	0.009	2795	38	0.201	0.003	2833	22	2%

†The % discordance was calculated as $\{1-[^{206}Pb/^{238}U]_{measured}/[^{206}Pb/^{238}U]_{^{207}Pb^*/^{206}Pb^*\ age}\}$

Table EA-2: U-Pb age data for detrital monazites from the African major rivers

	$^{238}U/^{206}Pb$	2σ	$^{207}Pb/^{206}Pb$	2σ	$^{206}Pb/^{204}Pb$	$^{238}U/^{206}Pb^*$	2σ	$^{207}Pb^*/^{206}Pb^*$	2σ	$^{206}Pb^*/^{238}U$	2σ	$^{207}Pb^*/^{206}Pb^*$	2σ	Disc.[†]	internal structure	Used da
	ratio		ratio		ratio	ratio		ratio		age (Ma)		age (Ma)		(%)		
Nile River																
NIL-mnz-1	10.00	0.244	0.0596	0.0012		10.00	0.244	0.0596	0.0012	614	14	590	45	-4%	patchy-brighter	✔
NIL-mnz-2	10.38	0.228	0.0599	0.0019		10.38	0.228	0.0599	0.0019	592	12	600	67	1%	unzoned	✔
NIL-mnz-3	10.26	0.217	0.0598	0.0013		10.26	0.217	0.0598	0.0013	599	12	596	46	-1%	unzoned	✔
NIL-mnz-4	9.67	0.201	0.0619	0.0016		9.67	0.201	0.0619	0.0016	633	13	671	54	6%	unzoned	✔
NIL-mnz-5	10.20	0.242	0.0606	0.0012		10.20	0.242	0.0606	0.0012	602	14	626	43	4%	unzoned	✔
NIL-mnz-6	10.51	0.227	0.0584	0.0013		10.51	0.227	0.0584	0.0013	586	12	543	50	-8%	unzoned	✔
NIL-mnz-7	10.35	0.228	0.0601	0.0016		10.35	0.228	0.0601	0.0016	593	12	607	56	2%	unzoned	✔
NIL-mnz-8	8.33	0.204	0.0633	0.0013		8.33	0.204	0.0633	0.0013	731	17	717	45	-2%	unzoned	✔
NIL-mnz-9	10.58	0.156	0.0587	0.0007		10.58	0.156	0.0587	0.0007	581	8	556	27	-5%	core	✔
NIL-mnz-10	2.58	0.140	0.4862	0.0252		2.58	0.140	0.4862	0.0252	2112	97	4200	77	58%	unzoned	
NIL-mnz-11	10.26	0.179	0.0585	0.0010		10.26	0.179	0.0585	0.0010	599	10	549	38	-10%	unzoned	
NIL-mnz-12	10.36	0.136	0.0599	0.0010		10.36	0.136	0.0599	0.0010	593	7	601	36	1%	patchy-darker	✔
NIL-mnz-13	9.84	0.160	0.0610	0.0014		9.84	0.160	0.0610	0.0014	623	10	638	50	2%	patchy-darker	✔
NIL-mnz-14	9.64	0.203	0.0600	0.0026		9.64	0.203	0.0600	0.0026	636	13	604	94	-6%	unzoned	✔
NIL-mnz-15	8.52	0.177	0.0765	0.0039		8.52	0.177	0.0765	0.0039	703	14	1109	102	38%	unzoned	
NIL-mnz-16	8.01	0.181	0.0645	0.0026		8.01	0.181	0.0645	0.0026	757	16	757	84	0%	unzoned	✔
NIL-mnz-17	10.35	0.154	0.0593	0.0011		10.35	0.154	0.0593	0.0011	594	8	578	40	-3%	unzoned	✔
NIL-mnz-18	8.21	0.163	0.0637	0.0011		8.21	0.163	0.0637	0.0011	740	14	732	38	-1%	mosaic	✔
NIL-mnz-19	8.97	0.221	0.0615	0.0014		8.97	0.221	0.0615	0.0014	681	16	655	48	-4%	unzoned	✔
NIL-mnz-20	10.08	0.202	0.0586	0.0014		10.08	0.202	0.0586	0.0014	610	12	554	53	-11%	unzoned	✔
NIL-mnz-21	9.62	0.167	0.0592	0.0015		9.62	0.167	0.0592	0.0015	638	11	574	56	-12%	unzoned	✔
NIL-mnz-22	9.94	0.238	0.0601	0.0015		9.94	0.238	0.0601	0.0015	618	14	608	55	-2%	core	✔
NIL-mnz-23	10.31	0.191	0.0603	0.0015		10.31	0.191	0.0603	0.0015	596	11	613	55	3%	unzoned	✔
NIL-mnz-24	10.02	0.225	0.0614	0.0017		10.02	0.225	0.0614	0.0017	612	13	653	58	6%	patchy-darker	✔
NIL-mnz-25	10.09	0.206	0.0595	0.0014		10.09	0.206	0.0595	0.0014	609	12	586	52	-4%	unzoned	✔
NIL-mnz-26	9.90	0.247	0.0595	0.0013		9.90	0.247	0.0595	0.0013	620	15	584	48	-6%	patchy-brighter	✔
NIL-mnz-27	9.91	0.191	0.0600	0.0021		9.91	0.191	0.0600	0.0021	620	11	604	75	-3%	mosaic	✔
NIL-mnz-28	8.56	0.250	0.1538	0.0226		8.56	0.250	0.1538	0.0226	636	18	2389	250	74%	unzoned	
NIL-mnz-29	10.77	0.313	0.0631	0.0016		10.77	0.313	0.0631	0.0016	570	16	713	52	21%	unzoned	
NIL-mnz-30	9.30	0.158	0.0672	0.0024		9.30	0.158	0.0672	0.0024	653	11	844	74	23%	patchy-darker	
NIL-mnz-31	10.33	0.162	0.0605	0.0012		10.33	0.162	0.0605	0.0012	595	9	623	42	5%	patchy-darker	✔
NIL-mnz-32	9.69	0.218	0.0617	0.0018		9.69	0.218	0.0617	0.0018	632	14	664	62	5%	unzoned	✔
NIL-mnz-33	10.02	0.191	0.0602	0.0011		10.02	0.191	0.0602	0.0011	613	11	612	39	0%	unzoned	✔
NIL-mnz-34	7.74	0.142	0.0651	0.0014		7.74	0.142	0.0651	0.0014	783	14	778	46	-1%	patchy-brighter	✔
NIL-mnz-35	9.97	0.217	0.0594	0.0011		9.97	0.217	0.0594	0.0011	616	13	581	40	-6%	unzoned	✔
NIL-mnz-36	8.77	0.196	0.0629	0.0011		8.77	0.196	0.0629	0.0011	695	15	703	37	1%	unzoned	✔
NIL-mnz-37	6.98	0.145	0.0910	0.0048		6.98	0.145	0.0910	0.0048	839	16	1446	101	43%	unzoned	
NIL-mnz-38	10.25	0.208	0.0607	0.0014		10.25	0.208	0.0607	0.0014	599	12	628	50	5%	unzoned	✔
NIL-mnz-39	10.26	0.245	0.0595	0.0009		10.26	0.245	0.0595	0.0009	599	14	586	32	-3%	unzoned	✔
NIL-mnz-40	9.90	0.196	0.0598	0.0013		9.90	0.196	0.0598	0.0013	620	12	595	47	-4%	unzoned	✔
NIL-mnz-41	10.04	0.225	0.0580	0.0011		10.04	0.225	0.0580	0.0011	612	13	531	41	-16%	core	
NIL-mnz-42	10.37	0.178	0.0600	0.0009		10.37	0.178	0.0600	0.0009	593	10	603	32	2%	patchy-darker	✔
NIL-mnz-43	5.90	0.086	0.0748	0.0011		5.90	0.086	0.0748	0.0011	1005	21	1064	31	6%	patchy-brighter	
NIL-mnz-44	11.43	0.360	0.0591	0.0014		11.43	0.360	0.0591	0.0014	540	12	571	51	5%	core	✔
NIL-mnz-45	9.87	0.226	0.0620	0.0009		9.87	0.226	0.0620	0.0009	620	14	675	32	8%	unzoned	
NIL-mnz-46	9.58	0.187	0.0625	0.0011		9.58	0.187	0.0625	0.0011	638	16	692	39	8%	core	✔
NIL-mnz-47	10.26	0.254	0.0590	0.0008		10.26	0.254	0.0590	0.0008	599	14	567	31	-6%	patchy-darker	✔
NIL-mnz-48	10.27	0.238	0.0611	0.0008		10.27	0.238	0.0611	0.0008	598	12	642	29	7%	unzoned	
NIL-mnz-49	9.22	0.195	0.0619	0.0021		9.22	0.195	0.0619	0.0021	663	14	672	74	1%	mosaic	✔
NIL-mnz-50	10.52	0.270	0.0599	0.0011		10.52	0.270	0.0599	0.0011	585	13	601	38	3%	unzoned	✔
NIL-mnz-51	10.16	0.210	0.0607	0.0014		10.16	0.210	0.0607	0.0014	604	13	628	48	4%	core	✔
NIL-mnz-52	9.53	0.199	0.0617	0.0009		9.53	0.199	0.0617	0.0009	642	14	664	31	3%	unzoned	✔
NIL-mnz-53	9.46	0.170	0.0628	0.0012		9.46	0.170	0.0628	0.0012	646	12	702	41	8%	unzoned	
NIL-mnz-54	10.48	0.246	0.0590	0.0041		10.48	0.246	0.0590	0.0041	587	13	566	152	-4%	unzoned	✔
NIL-mnz-55	11.54	0.254	0.0587	0.0013		11.54	0.254	0.0587	0.0013	534	11	557	48	4%	mosaic	✔
NIL-mnz-56	9.99	0.327	0.0668	0.0019		9.99	0.327	0.0668	0.0019	609	13	833	60	27%	mosaic	
NIL-mnz-57	10.24	0.215	0.0602	0.0010		10.24	0.215	0.0602	0.0010	599	11	612	37	2%	patchy-darker	✔
NIL-mnz-58*	10.23	0.343	0.0661	0.0019	2328	10.29	0.349	0.0598	0.0019	598	19	595	70	-1%	unzoned	✔
NIL-mnz-59	10.41	0.239	0.0605	0.0012		10.41	0.239	0.0605	0.0012	590	12	622	42	5%	unzoned	✔
NIL-mnz-60	10.24	0.214	0.0606	0.0019		10.24	0.214	0.0606	0.0019	599	15	626	67	4%	unzoned	✔
NIL-mnz-61	9.67	0.211	0.0611	0.0013		9.67	0.211	0.0611	0.0013	634	13	643	47	1%	patchy-darker	✔
NIL-mnz-62	10.04	0.220	0.0607	0.0014		10.04	0.220	0.0607	0.0014	611	13	630	49	3%	mosaic	✔
NIL-mnz-63	9.29	0.167	0.0636	0.0008		9.29	0.167	0.0636	0.0008	657	11	730	27	10%	unzoned	
NIL-mnz-64	9.21	0.199	0.0632	0.0014		9.21	0.199	0.0632	0.0014	663	14	714	48	7%	unzoned	✔
NIL-mnz-65	8.24	0.181	0.0635	0.0014		8.24	0.181	0.0635	0.0014	738	15	723	46	-2%	unzoned	✔
NIL-mnz-66	12.43	0.346	0.0575	0.0012		12.43	0.346	0.0575	0.0012	657	13	511	45	2%	patchy-brighter	✔
NIL-mnz-67	9.29	0.157	0.0628	0.0010		9.29	0.157	0.0628	0.0010	498	11	702	35	6%	unzoned	
NIL-mnz-68	10.34	0.181	0.0592	0.0009		10.34	0.181	0.0592	0.0009	595	10	576	34	-3%	unzoned	✔
NIL-mnz-69	10.03	0.274	0.0589	0.0017		10.03	0.274	0.0589	0.0017	613	16	563	61	-9%	unzoned	✔
NIL-mnz-70	9.95	0.172	0.0570	0.0010		9.95	0.172	0.0570	0.0010	618	10	490	41	-27%	mosaic	
NIL-mnz-71	8.84	0.238	0.0619	0.0013		8.84	0.238	0.0619	0.0013	691	18	671	44	-3%	patchy-darker	✔
NIL-mnz-72	10.10	0.323	0.0613	0.0013		10.10	0.323	0.0613	0.0013	609	19	649	44	7%	patchy-brighter	✔
NIL-mnz-73	9.06	0.269	0.0634	0.0016		9.06	0.269	0.0634	0.0016	675	19	722	54	7%	unzoned	✔
NIL-mnz-74	10.15	0.285	0.0609	0.0017		10.15	0.285	0.0609	0.0017	606	16	636	60	5%	patchy-darker	✔
NIL-mnz-75	10.31	0.280	0.0616	0.0025		10.31	0.280	0.0616	0.0025	597	15	660	88	10%	core	✔
NIL-mnz-76	9.02	0.243	0.0639	0.0014		9.02	0.243	0.0639	0.0014	678	17	737	46	8%	patchy-darker	✔
NIL-mnz-77	7.92	0.364	0.2125	0.0297		7.92	0.364	0.2125	0.0297	629	27	2925	226	78%	patchy-brighter	
NIL-mnz-78	8.80	0.167	0.0626	0.0013		8.80	0.167	0.0626	0.0013	694	12	694	45	0%	patchy-brighter	✔
NIL-mnz-79	10.07	0.226	0.0598	0.0009		10.07	0.226	0.0598	0.0009	611	13	598	32	-2%	core	✔
NIL-mnz-80	8.91	0.171	0.0628	0.0009		8.91	0.171	0.0628	0.0009	686	13	703	31	3%	mosaic	✔
NIL-mnz-81	9.85	0.198	0.0604	0.0012		9.85	0.198	0.0604	0.0012	623	12	619	42	-1%	unzoned	✔
NIL-mnz-82	10.26	0.232	0.0591	0.0013		10.26	0.232	0.0591	0.0013	600	13	572	48	-5%	mosaic	✔
NIL-mnz-83	10.35	0.162	0.0566	0.0034		10.35	0.162	0.0566	0.0034	595	9	475	131	-26%	unzoned	✔
NIL-mnz-84	10.49	0.170	0.0588	0.0036		10.49	0.170	0.0588	0.0036	587	9	560	132	-5%	unzoned	✔
NIL-mnz-85	10.56	0.172	0.0566	0.0033		10.56	0.172	0.0566	0.0033	583	9	475	129	-24%	patchy-darker	✔
NIL-mnz-86	8.71	0.172	0.0604	0.0037		8.71	0.172	0.0604	0.0037	701	13	618	131	-14%	patchy-darker	✔
NIL-mnz-87	9.29	0.187	0.0604	0.0036		9.29	0.187	0.0604	0.0036	659	13	619	128	-7%	rim	✔
NIL-mnz-88	9.78	0.185	0.0602	0.0044		9.78	0.185	0.0602	0.0044	627	11	610	157	-3%	unzoned	✔
NIL-mnz-89	10.66	0.172	0.0576	0.0034		10.66	0.172	0.0576	0.0034	578	9	516	131	-12%	rim	✔
NIL-mnz-90	10.29	0.192	0.0569	0.0034		10.29	0.192	0.0569	0.0034	598	11	489	130	-23%	patchy-darker	✔
NIL-mnz-91	8.23	0.145	0.0621	0.0029		8.23	0.145	0.0621	0.0029	739	12	676	99	-10%	patchy-darker	✔
NIL-mnz-92	10.21	0.174	0.0606	0.0027		10.21	0.174	0.0606	0.0027	602	10	624	96	4%	unzoned	✔
NIL-mnz-93	10.36	0.168	0.0585	0.0025		10.36	0.168	0.0585	0.0025	594	9	548	94	-9%	unzoned	✔
NIL-mnz-94	10.29	0.150	0.0573	0.0025		10.29	0.150	0.0573	0.0025	598	8	504	97	-20%	mosaic	✔
NIL-mnz-95	9.80	0.168	0.0609	0.0010		9.80	0.168	0.0609	0.0010	626	10	637	35	2%	mosaic	✔

$^{238}U/^{206}Pb$ ratio	2σ	$^{207}Pb/^{206}Pb$ ratio	2σ	$^{206}Pb/^{204}Pb$ ratio	$^{238}U/^{206}Pb^{*}$ ratio	2σ	$^{207}Pb^{*}/^{206}Pb^{*}$ ratio	2σ	$^{206}Pb^{*}/^{238}U$ age (Ma)	2σ	$^{207}Pb^{*}/^{206}Pb^{*}$ age (Ma)	2σ	Disc.† (%)	internal structure	Used data††	
Niger Rver																
NGR1-mnz-1*	10.87	0.239	0.0691	0.0022	1123	11.02	0.260	0.0560	0.0024	560	13	452	93	-25%	core	
NGR1-mnz-2	10.62	0.219	0.0586	0.0011		10.62	0.219	0.0586	0.0011	580	11	554	40	-5%	patchy-brig	✔
NGR1-mnz-3	10.27	0.221	0.0653	0.0037		10.27	0.221	0.0653	0.0037	599	12	784	119	25%	mosaic	
NGR1-mnz-4 (	10.22	0.277	0.0611	0.0018		10.22	0.277	0.0611	0.0018	600	16	644	62	7%	core	✔
NGR1-mnz-4 (	10.11	0.173	0.0605	0.0020		10.11	0.173	0.0605	0.0020	608	10	596	73	-2%	rim	
NGR1-mnz-5	10.01	0.242	0.0636	0.0029		10.01	0.242	0.0636	0.0029	611	14	728	96	16%	unzoned	
NGR1-mnz-6	10.37	0.259	0.0604	0.0019		10.37	0.259	0.0604	0.0019	592	14	617	67	4%	unzoned	✔
NGR1-mnz-7	11.22	0.225	0.0590	0.0010		11.22	0.225	0.0590	0.0010	549	11	568	37	3%	unzoned	✔
NGR1-mnz-8	10.52	0.253	0.0620	0.0013		10.52	0.253	0.0620	0.0013	583	13	673	46	14%	unzoned	
NGR1-mnz-9	38.02	0.732	0.0507	0.0018		38.02	0.732	0.0507	0.0018	167	3	227	83	27%	patchy-dar	✔
NGR1-mnz-10	10.76	0.241	0.0637	0.0018		10.76	0.241	0.0637	0.0018	569	12	732	61	23%	patchy-brighter	
NGR1-mnz-11	10.66	0.228	0.0609	0.0018		10.66	0.228	0.0609	0.0018	577	12	637	62	10%	unzoned	✔
NGR1-mnz-12	9.55	0.184	0.0725	0.0039		9.55	0.184	0.0725	0.0039	633	12	1000	108	38%	unzoned	
NGR1-mnz-13	10.35	0.179	0.0597	0.0015		10.35	0.179	0.0597	0.0015	608	10	593	54	0%	unzoned	✔
NGR1-mnz-14	11.10	0.224	0.0615	0.0017		11.10	0.224	0.0615	0.0017	554	11	658	58	16%	core	
NGR1-mnz-15	10.86	0.193	0.0605	0.0018		10.86	0.193	0.0605	0.0018	567	10	621	66	9%	core	✔
NGR1-mnz-16	10.52	0.204	0.0590	0.0014		10.52	0.204	0.0590	0.0014	585	11	569	51	-3%	patchy-brig	✔
NGR1-mnz-17	10.89	0.240	0.0596	0.0011		10.89	0.240	0.0596	0.0011	565	12	590	41	4%	mosaic	✔
NGR1-mnz-18	9.90	0.234	0.0599	0.0015		9.90	0.234	0.0599	0.0015	620	14	602	54	-3%	unzoned	✔
NGR1-mnz-19	11.17	0.222	0.0589	0.0010		11.17	0.222	0.0589	0.0010	552	10	565	38	2%	patchy-dar	✔
NGR1-mnz-20	10.91	0.197	0.0598	0.0016		10.91	0.197	0.0598	0.0016	564	10	596	58	5%	unzoned	
NGR1-mnz-21	10.07	0.165	0.0640	0.0021		10.07	0.165	0.0640	0.0021	607	9	741	71	18%	patchy-darker	
NGR1-mnz-22	10.58	0.231	0.0645	0.0018		10.58	0.231	0.0645	0.0018	578	12	759	58	24%	unzoned	
NGR1-mnz-23	10.38	0.157	0.0591	0.0009		10.38	0.157	0.0591	0.0009	592	9	570	34	-4%	patchy-brig	✔
NGR1-mnz-24	10.81	0.225	0.0597	0.0009		10.81	0.225	0.0597	0.0009	569	11	593	34	4%	patchy-dar	✔
NGR1-mnz-25	11.05	0.265	0.0587	0.0010		11.05	0.265	0.0587	0.0010	558	13	557	37	0%	patchy-brig	✔
NGR1-mnz-26	10.93	0.242	0.0607	0.0010		10.93	0.242	0.0607	0.0010	563	12	628	36	11%	unzoned	
NGR1-mnz-27	11.59	0.272	0.0592	0.0009		11.59	0.272	0.0592	0.0009	532	12	575	32	7%	unzoned	✔
NGR1-mnz-28	9.65	0.202	0.0607	0.0013		9.65	0.202	0.0607	0.0013	635	13	628	46	-1%	patchy-brig	✔
NGR1-mnz-29	11.19	0.272	0.0609	0.0010		11.19	0.272	0.0609	0.0010	550	13	636	36	14%	patchy-darker	
NGR1-mnz-30	9.84	0.214	0.0604	0.0010		9.84	0.214	0.0604	0.0010	623	13	619	35	-1%	patchy-dar	✔
NGR1-mnz-31	10.33	0.243	0.0620	0.0016		10.33	0.243	0.0620	0.0016	593	13	674	57	12%	core	
NGR1-mnz-32	10.70	0.235	0.0580	0.0010		10.70	0.235	0.0580	0.0010	576	12	528	37	-9%	core	✔
NGR1-mnz-33	10.45	0.203	0.0595	0.0008		10.45	0.203	0.0595	0.0008	588	11	584	31	-1%	mosaic	✔
NGR1-mnz-34	10.27	0.181	0.0650	0.0018		10.27	0.181	0.0650	0.0018	594	10	776	58	24%	unzoned	
NGR1-mnz-35	10.21	0.199	0.0585	0.0011		10.21	0.199	0.0585	0.0011	602	11	550	41	-10%	unzoned	
NGR1-mnz-36	11.07	0.198	0.0583	0.0009		11.07	0.198	0.0583	0.0009	557	10	540	35	-3%	core	✔
NGR1-mnz-37	10.37	0.205	0.0677	0.0029	2503	10.43	0.211	0.0618	0.0016	590	11	668	56	12%	unzoned	
NGR1-mnz-38	9.80	0.223	0.0624	0.0011		9.80	0.223	0.0624	0.0011	624	14	686	39	9%	unzoned	
NGR1-mnz-39	10.55	0.216	0.0574	0.0012		10.55	0.216	0.0574	0.0012	584	11	505	48	-16%	mosaic	
NGR1-mnz-40	11.14	0.242	0.0591	0.0008		11.14	0.242	0.0591	0.0008	553	11	569	31	3%	patchy-dar	✔
NGR1-mnz-41	10.48	0.237	0.0590	0.0010		10.48	0.237	0.0590	0.0010	587	13	566	37	-4%	patchy-brig	✔
NGR1-mnz-42	10.79	0.211	0.0584	0.0008		10.79	0.211	0.0584	0.0008	571	11	546	29	-5%	patchy-brig	✔
NGR1-mnz-43	9.70	0.210	0.0689	0.0040		9.70	0.210	0.0689	0.0040	625	13	897	120	31%	unzoned	
NGR1-mnz-44	10.79	0.246	0.0586	0.0014		10.79	0.246	0.0586	0.0014	571	12	550	53	-4%	unzoned	✔
NGR1-mnz-45	10.52	0.203	0.0594	0.0015		10.52	0.203	0.0594	0.0015	585	11	581	54	-1%	unzoned	✔
NGR1-mnz-46	10.57	0.311	0.0584	0.0012		10.57	0.311	0.0584	0.0012	583	16	544	45	-8%	patchy-dar	✔
NGR1-mnz-47	10.71	0.163	0.0582	0.0009		10.71	0.163	0.0582	0.0009	575	8	539	32	-7%	unzoned	✔
NGR1-mnz-48	10.27	0.204	0.0597	0.0010		10.27	0.204	0.0597	0.0010	598	11	593	38	-1%	unzoned	✔
NGR1-mnz-49	10.10	0.215	0.0599	0.0012		10.10	0.215	0.0599	0.0012	608	12	598	42	-2%	mosaic	✔
NGR1-mnz-50	10.67	0.212	0.0586	0.0010		10.67	0.212	0.0586	0.0010	577	11	551	37	-5%	patchy-dar	✔
NGR1-mnz-51	10.67	0.220	0.0593	0.0010		10.67	0.220	0.0593	0.0010	577	11	577	35	0%	mosaic	✔
NGR1-mnz-52	10.35	0.217	0.0597	0.0009		10.35	0.217	0.0597	0.0009	594	12	591	34	-1%	unzoned	✔
NGR1-mnz-53	9.49	0.216	0.0690	0.0036		9.49	0.216	0.0690	0.0036	639	14	898	108	29%	mosaic	
NGR1-mnz-54	10.68	0.246	0.0633	0.0021		10.68	0.246	0.0633	0.0021	573	13	717	71	20%	mosaic	
NGR1-mnz-55	10.54	0.208	0.0591	0.0011		10.54	0.208	0.0591	0.0011	584	11	570	39	-3%	unzoned	✔
NGR1-mnz-56	11.60	0.236	0.0588	0.0011		11.60	0.236	0.0588	0.0011	532	10	561	39	5%	patchy-dar	✔
NGR1-mnz-57	10.58	0.213	0.0597	0.0010		10.58	0.213	0.0597	0.0010	581	11	593	35	2%	core	✔
NGR1-mnz-58	10.84	0.229	0.0592	0.0010		10.84	0.229	0.0592	0.0010	568	11	575	35	1%	unzoned	✔
NGR1-mnz-59	10.62	0.238	0.0601	0.0011		10.62	0.238	0.0601	0.0011	579	12	609	41	5%	mosaic	✔
NGR1-mnz-60	10.61	0.194	0.0601	0.0011		10.61	0.194	0.0601	0.0011	579	10	608	40	5%	patchy-brig	✔
NGR1-mnz-61	10.80	0.211	0.0730	0.0041		10.80	0.211	0.0730	0.0041	561	10	1015	113	46%	unzoned	
NGR1-mnz-62	11.04	0.221	0.0593	0.0010		11.04	0.221	0.0593	0.0010	558	11	579	37	4%	unzoned	✔
NGR1-mnz-63	9.82	0.201	0.0626	0.0012		9.82	0.201	0.0626	0.0012	623	12	694	39	10%	unzoned	
NGR1-mnz-64	9.54	0.189	0.0613	0.0014		9.54	0.189	0.0613	0.0014	641	12	650	48	1%	mosaic	✔
NGR1-mnz-65	10.70	0.233	0.0588	0.0011		10.70	0.233	0.0588	0.0011	576	12	558	43	-3%	unzoned	✔
NGR1-mnz-66	10.41	0.195	0.0599	0.0009		10.41	0.195	0.0599	0.0009	591	11	602	32	2%	patchy-dar	✔
NGR1-mnz-67	10.60	0.205	0.0585	0.0010		10.60	0.205	0.0585	0.0010	581	11	550	38	-6%	patchy-brig	✔
NGR1-mnz-68	10.58	0.229	0.0616	0.0009		10.58	0.229	0.0616	0.0009	580	12	660	32	12%	core	
NGR1-mnz-69	10.17	0.221	0.0616	0.0016		10.17	0.221	0.0616	0.0016	603	12	659	54	9%	core	✔
NGR1-mnz-70	11.45	0.216	0.0590	0.0007		11.45	0.216	0.0590	0.0007	539	10	567	25	5%	unzoned	✔
NGR1-mnz-71	10.94	0.218	0.0588	0.0010		10.94	0.218	0.0588	0.0010	563	11	560	37	-1%	unzoned	✔
NGR1-mnz-72	10.35	0.207	0.0589	0.0011		10.35	0.207	0.0589	0.0011	594	11	565	42	-5%	core	✔
NGR1-mnz-73	10.76	0.207	0.0617	0.0026		10.76	0.207	0.0617	0.0026	571	11	664	91	14%	unzoned	✔
NGR1-mnz-74	10.37	0.204	0.0606	0.0009		10.37	0.204	0.0606	0.0009	592	11	626	32	5%	unzoned	✔
NGR1-mnz-75	9.95	0.239	0.0604	0.0020		9.95	0.239	0.0604	0.0020	617	14	619	70	0%	mosaic	✔
NGR1-mnz-76	11.09	0.224	0.0583	0.0012		11.09	0.224	0.0583	0.0012	556	11	540	46	-3%	rim	✔
NGR1-mnz-77	10.37	0.246	0.0598	0.0017		10.37	0.246	0.0598	0.0017	593	13	596	61	0%	mosaic	✔
NGR1-mnz-78	9.52	0.211	0.0645	0.0016		9.52	0.211	0.0645	0.0016	641	14	760	52	16%	mosaic	
NGR1-mnz-79	10.12	0.219	0.0580	0.0013		10.12	0.219	0.0580	0.0013	607	13	529	50	-16%	patchy-darker	
NGR1-mnz-80	10.55	0.227	0.0589	0.0013		10.55	0.227	0.0589	0.0013	583	12	562	47	-4%	patchy-brig	✔
NGR1-mnz-81	10.32	0.228	0.0595	0.0009		10.32	0.228	0.0595	0.0009	596	13	584	33	-2%	unzoned	✔
NGR1-mnz-82	10.49	0.234	0.0609	0.0010		10.49	0.234	0.0609	0.0010	585	12	635	36	8%	patchy-brighter	
NGR1-mnz-83	9.83	0.199	0.0612	0.0009		9.83	0.199	0.0612	0.0009	623	12	647	31	4%	unzoned	✔
NGR1-mnz-84	10.70	0.244	0.0629	0.0030		10.70	0.244	0.0629	0.0030	573	12	706	101	19%	unzoned	
NGR1-mnz-85	11.26	0.274	0.0578	0.0007		11.26	0.274	0.0578	0.0007	548	13	524	25	-5%	unzoned	✔
NGR1-mnz-86	10.46	0.229	0.0595	0.0025		10.46	0.229	0.0595	0.0025	588	12	587	89	0%	unzoned	✔
NGR1-mnz-87	10.81	0.252	0.0606	0.0009		10.81	0.252	0.0606	0.0009	568	13	624	34	9%	unzoned	
NGR1-mnz-88	11.31	0.228	0.0584	0.0011		11.31	0.228	0.0584	0.0011	546	11	543	42	-1%	patchy-dar	✔
NGR1-mnz-89	10.45	0.200	0.0596	0.0007		10.45	0.200	0.0596	0.0007	588	11	589	26	0%	mosaic	✔
NGR1-mnz-90	10.25	0.209	0.0652	0.0029		10.25	0.209	0.0652	0.0029	595	12	782	94	24%	unzoned	
NGR1-mnz-91	9.41	0.168	0.0618	0.0011		9.41	0.168	0.0618	0.0011	650	11	666	38	2%	mosaic	✔
NGR1-mnz-92	10.24	0.268	0.0603	0.0013		10.24	0.268	0.0603	0.0013	600	15	615	45	2%	unzoned	✔
NGR1-mnz-93	10.55	0.302	0.0708	0.0034	915	10.69	0.315	0.0574	0.0019	576	16	506	71	-15%	unzoned	✔
NGR1-mnz-94	10.57	0.286	0.0590	0.0036		10.57	0.286	0.0590	0.0036	583	15	567	132	-3%	unzoned	✔
NGR1-mnz-95	10.96	0.200	0.0616	0.0014		10.96	0.200	0.0616	0.0014	560	10	661	49	16%	patchy-brighter	
NGR1-mnz-96	10.51	0.230	0.0595	0.0009		10.51	0.230	0.0595	0.0009	585	12	587	33	0%	unzoned	✔
NGR1-mnz-97	10.93	0.249	0.0590	0.0008		10.93	0.249	0.0590	0.0008	564	12	567	30	0%	patchy-dar	✔
NGR1-mnz-98	10.89	0.256	0.0595	0.0007		10.89	0.256	0.0595	0.0007	565	13	584	25	3%	unzoned	✔
NGR1-mnz-99	10.58	0.242	0.0591	0.0008		10.58	0.242	0.0591	0.0008	582	13	570	30	-2%	unzoned	✔
NGR1-mnz-10(	10.66	0.241	0.0591	0.0014		10.66	0.241	0.0591	0.0014	577	12	572	53	-1%	unzoned	✔
NGR1-mnz-10	10.69	0.244	0.0594	0.0012		10.69	0.244	0.0594	0.0012	576	13	580	43	1%	unzoned	✔
NGR1-mnz-10	10.69	0.255	0.0596	0.0009		10.69	0.255	0.0596	0.0009	576	13	587	33	2%	mosaic	✔
NGR1-mnz-10	9.88	0.241	0.0616	0.0008		9.88	0.241	0.0616	0.0008	620	14	659	27	6%	unzoned	✔

$^{238}U/^{206}Pb$ ratio	2σ	$^{207}Pb/^{206}Pb$ ratio	2σ	$^{206}Pb/^{204}Pb$ ratio	$^{238}U/^{206}Pb^{*}$ ratio	2σ	$^{207}Pb^{*}/^{206}Pb^{*}$ ratio	2σ	$^{206}Pb^{*}/^{238}U$ age (Ma)	2σ	$^{207}Pb^{*}/^{206}Pb^{*}$ age (Ma)	2σ	Disc.† (%)	internal structure	Used data††	
Congo River																
CNG2-mnz-1	5.85	0.104	0.0743	0.0013		5.85	0.104	0.0743	0.0013	1014	17	1049	35	3%	unzoned	✔
CNG2-mnz-2	1.67	0.027	0.2289	0.0048		1.67	0.027	0.2289	0.0048	3015	39	3044	34	1%	patchy-dar	✔
CNG2-mnz-3	6.42	0.127	0.0725	0.0014		6.42	0.127	0.0725	0.0014	929	17	1001	38	7%	patchy-brighter	
CNG2-mnz-4	9.79	0.175	0.0608	0.0011		9.79	0.175	0.0608	0.0011	626	11	632	40	1%	patchy-bri	✔
CNG2-mnz-5	6.38	0.118	0.0718	0.0013		6.38	0.118	0.0718	0.0013	935	16	981	37	5%	mosaic	✔
CNG2-mnz-6	5.57	0.104	0.0748	0.0014		5.57	0.104	0.0748	0.0014	1064	18	1063	38	0%	patchy-bri	✔
CNG2-mnz-7	12.29	0.258	0.0581	0.0015		12.29	0.258	0.0581	0.0015	503	10	535	57	6%	unzoned	✔
CNG2-mnz-8	4.19	0.080	0.0873	0.0019		4.19	0.080	0.0873	0.0019	1379	24	1368	41	-1%	unzoned	✔
CNG2-mnz-9	9.61	0.190	0.0622	0.0014		9.61	0.190	0.0622	0.0014	637	12	679	49	6%	mosaic	✔
CNG2-mnz-10	9.67	0.212	0.0625	0.0013		9.67	0.212	0.0625	0.0013	633	13	693	43	9%	patchy-brighter	
CNG2-mnz-11	9.14	0.180	0.0635	0.0016		9.14	0.180	0.0635	0.0016	668	12	725	53	8%	unzoned	✔
CNG2-mnz-12	11.12	0.252	0.0600	0.0036		11.12	0.252	0.0600	0.0036	554	12	605	131	9%	unzoned	✔
CNG2-mnz-13	5.54	0.098	0.0758	0.0012		5.54	0.098	0.0758	0.0012	1068	17	1090	32	2%	patchy-dar	✔
CNG2-mnz-14	10.17	0.208	0.0599	0.0010		10.17	0.208	0.0599	0.0010	604	12	600	37	-1%	unzoned	✔
CNG2-mnz-15	11.37	0.211	0.0579	0.0010		11.37	0.211	0.0579	0.0010	543	10	526	40	-3%	mosaic	✔
CNG2-mnz-16	9.91	0.181	0.0604	0.0011		9.91	0.181	0.0604	0.0011	619	11	617	39	0%	mosaic	✔
CNG2-mnz-17	11.03	0.247	0.0596	0.0021		11.03	0.247	0.0596	0.0021	559	12	588	75	5%	unzoned	✔
CNG2-mnz-18	5.80	0.133	0.0735	0.0014		5.80	0.133	0.0735	0.0014	1024	22	1028	40	0%	patchy-dar	✔
CNG2-mnz-19	9.37	0.185	0.0657	0.0012		9.37	0.185	0.0657	0.0012	650	12	797	37	19%	unzoned	
CNG2-mnz-20	10.61	0.256	0.0608	0.0008		10.61	0.256	0.0608	0.0008	579	13	631	30	8%	patchy-darker	
CNG2-mnz-21	6.21	0.151	0.0712	0.0009		6.21	0.151	0.0712	0.0009	962	22	962	26	0%	mosaic	✔
CNG2-mnz-22	11.95	0.270	0.0570	0.0006		11.95	0.270	0.0570	0.0006	518	11	490	23	-6%	patchy-bri	✔
CNG2-mnz-23	5.52	0.134	0.0769	0.0009		5.52	0.134	0.0769	0.0009	1070	24	1119	24	4%	patchy-bri	✔
CNG2-mnz-24	11.08	0.260	0.0592	0.0008		11.08	0.260	0.0592	0.0008	556	13	574	29	3%	patchy-dar	✔
CNG2-mnz-25	7.04	0.438	0.0858	0.0067		7.04	0.438	0.0858	0.0067	838	49	1334	150	38%	mosaic	
CNG2-mnz-26	5.94	0.132	0.0733	0.0012		5.94	0.132	0.0733	0.0012	1001	21	1022	34	2%	mosaic	✔
CNG2-mnz-27	11.12	0.362	0.0624	0.0012		11.12	0.362	0.0624	0.0012	552	17	688	41	20%	unzoned	
CNG2-mnz-28	9.58	0.203	0.0619	0.0008		9.58	0.203	0.0619	0.0008	639	13	670	27	5%	patchy-dar	✔
CNG2-mnz-29	11.06	0.194	0.0583	0.0009		11.06	0.194	0.0583	0.0009	558	9	541	32	-3%	patchy-dar	✔
CNG2-mnz-30	10.94	0.216	0.0587	0.0007		10.94	0.216	0.0587	0.0007	563	11	555	26	-2%	patchy-dar	✔
CNG2-mnz-31	10.79	0.201	0.0591	0.0009		10.79	0.201	0.0591	0.0009	571	10	571	31	0%	unzoned	✔
CNG2-mnz-32	8.91	0.286	0.1031	0.0118		8.91	0.286	0.1031	0.0118	651	20	1681	211	62%	unzoned	
CNG2-mnz-33	8.88	0.207	0.0652	0.0017		8.88	0.207	0.0652	0.0017	685	15	780	55	12%	patchy-darker	
CNG2-mnz-34	10.96	0.171	0.0574	0.0007		10.96	0.171	0.0574	0.0007	563	8	505	26	-12%	core	
CNG2-mnz-35	9.72	0.154	0.0608	0.0008		9.72	0.154	0.0608	0.0008	630	10	632	28	0%	patchy-bri	✔
CNG2-mnz-36	6.21	0.165	0.0743	0.0019		6.21	0.165	0.0743	0.0019	958	24	1050	50	9%	unzoned	
CNG2-mnz-37	5.97	0.150	0.0752	0.0012		5.97	0.150	0.0752	0.0012	995	23	1074	31	8%	patchy-darker	
CNG2-mnz-38	11.43	0.195	0.0588	0.0011		11.43	0.195	0.0588	0.0011	540	9	561	42	4%	unzoned	✔
CNG2-mnz-39	2.78	0.045	0.1231	0.0016		2.78	0.045	0.1231	0.0016	1978	28	2001	23	1%	mosaic	✔
CNG2-mnz-40	2.83	0.044	0.1238	0.0018		2.83	0.044	0.1238	0.0018	1938	26	2012	25	4%	mosaic	✔
CNG2-mnz-41	10.76	0.181	0.0593	0.0010		10.76	0.181	0.0593	0.0010	572	9	580	37	1%	core	✔
CNG2-mnz-42	9.70	0.235	0.0643	0.0021		9.70	0.235	0.0643	0.0021	629	14	752	69	17%	patchy-brighter	
CNG2-mnz-43	8.51	0.785	0.1047	0.0095		8.51	0.785	0.1047	0.0095	681	59	1709	167	61%	unzoned	
CNG2-mnz-44	11.31	0.189	0.0577	0.0009		11.31	0.189	0.0577	0.0009	546	9	517	36	-6%	unzoned	✔
CNG2-mnz-45	6.35	0.142	0.0757	0.0014		6.35	0.142	0.0757	0.0014	936	19	1086	38	14%	unzoned	
CNG2-mnz-46	5.60	0.115	0.0762	0.0009	6916	5.61	0.115	0.0741	0.0011	1058	20	1044	31	-1%	unzoned	✔
CNG2-mnz-47	9.69	0.192	0.0611	0.0018		9.69	0.192	0.0611	0.0018	633	12	644	64	2%	unzoned	✔
CNG2-mnz-48	10.62	0.198	0.0584	0.0012		10.62	0.198	0.0584	0.0012	580	10	546	46	-6%	unzoned	✔
CNG2-mnz-49	11.09	0.185	0.0580	0.0009		11.09	0.185	0.0580	0.0009	557	9	531	33	-5%	unzoned	✔
CNG2-mnz-50	6.36	0.269	0.0817	0.0027		6.36	0.269	0.0817	0.0027	928	36	1238	66	26%	unzoned	
CNG2-mnz-51	10.11	0.185	0.0595	0.0010		10.11	0.185	0.0595	0.0010	608	11	586	36	-4%	unzoned	✔
CNG2-mnz-52	10.06	0.168	0.0597	0.0010		10.06	0.168	0.0597	0.0010	611	10	594	37	-3%	patchy-dar	✔
CNG2-mnz-53	5.72	0.106	0.0766	0.0010		5.72	0.106	0.0766	0.0010	1034	18	1112	27	7%	patchy-darker	
CNG2-mnz-54	5.64	0.165	0.0774	0.0016		5.64	0.165	0.0774	0.0016	1048	28	1132	42	8%	unzoned	
CNG2-mnz-55	10.18	0.181	0.0600	0.0006		10.18	0.181	0.0600	0.0006	603	10	604	20	0%	unzoned	✔
CNG2-mnz-56	12.73	0.320	0.0577	0.0007		12.73	0.320	0.0577	0.0007	487	12	517	27	6%	unzoned	✔
CNG2-mnz-57	4.50	0.095	0.0877	0.0011		4.50	0.095	0.0877	0.0011	1287	25	1376	25	7%	patchy-darker	
CNG2-mnz-58	11.54	0.254	0.0609	0.0012		11.54	0.254	0.0609	0.0012	533	11	634	43	16%	mosaic	
CNG2-mnz-59	5.35	0.115	0.0783	0.0008		5.35	0.115	0.0783	0.0008	1101	22	1156	20	5%	unzoned	✔
CNG2-mnz-60	10.03	0.232	0.0594	0.0011		10.03	0.232	0.0594	0.0011	613	14	580	39	-6%	unzoned	✔
CNG2-mnz-61	6.39	0.107	0.0706	0.0008		6.39	0.107	0.0706	0.0008	936	15	946	22	1%	unzoned	✔
CNG2-mnz-62	11.10	0.217	0.0582	0.0009		11.10	0.217	0.0582	0.0009	556	10	536	33	-4%	unzoned	✔
CNG2-mnz-63	6.30	0.229	0.0776	0.0025		6.30	0.229	0.0776	0.0025	941	32	1137	64	18%	unzoned	
CNG2-mnz-64	11.18	0.256	0.0588	0.0008		11.18	0.256	0.0588	0.0008	552	12	560	29	1%	patchy-bri	✔
CNG2-mnz-65	13.11	0.492	0.0616	0.0019	4278	13.16	0.496	0.0582	0.0014	472	17	536	54	12%	core	✔
CNG2-mnz-66	6.22	0.124	0.0733	0.0010		6.22	0.124	0.0733	0.0010	957	18	1022	26	7%	patchy-darker	
CNG2-mnz-67	12.13	0.228	0.0590	0.0008		12.13	0.228	0.0590	0.0008	509	9	568	28	11%	mosaic	
CNG2-mnz-68	10.00	0.310	0.0609	0.0011		10.00	0.310	0.0609	0.0011	613	18	637	37	4%	unzoned	✔
CNG2-mnz-69	6.57	0.136	0.0695	0.0009		6.57	0.136	0.0695	0.0009	912	18	914	26	0%	unzoned	✔
CNG2-mnz-70															unzoned	
CNG2-mnz-71	11.19	0.208	0.0578	0.0012		11.19	0.208	0.0578	0.0012	552	10	521	45	-6%	patchy-dar	✔
CNG2-mnz-72	5.32	0.099	0.0782	0.0009		5.32	0.099	0.0782	0.0009	1108	19	1151	23	4%	unzoned	✔
CNG2-mnz-73	9.85	0.217	0.0601	0.0014		9.85	0.217	0.0601	0.0014	623	13	609	49	-2%	unzoned	✔
CNG2-mnz-74	6.21	0.143	0.0730	0.0012		6.21	0.143	0.0730	0.0012	960	21	1015	33	5%	unzoned	
CNG2-mnz-75	11.99	0.300	0.0584	0.0016		11.99	0.300	0.0584	0.0016	516	12	545	61	6%	mosaic	✔
CNG2-mnz-76	11.54	0.300	0.0590	0.0010		11.54	0.300	0.0590	0.0010	535	13	569	35	6%	mosaic	✔
CNG2-mnz-77	5.44	0.118	0.0739	0.0011		5.44	0.118	0.0739	0.0011	1088	22	1039	31	-5%	mosaic	✔
CNG2-mnz-78	12.11	0.309	0.0572	0.0009		12.11	0.309	0.0572	0.0009	511	13	499	33	-3%	unzoned	✔
CNG2-mnz-79	9.69	0.221	0.0608	0.0008		9.69	0.221	0.0608	0.0008	633	14	633	29	0%	patchy-dar	✔
CNG2-mnz-80	11.55	0.358	0.0585	0.0007		11.55	0.358	0.0585	0.0007	535	16	548	26	2%	unzoned	✔
CNG2-mnz-81	8.40	0.678	0.1074	0.0107	7656	8.42	0.679	0.1052	0.0007	723	55	1717	12	61%	patchy-darker	
CNG2-mnz-82	5.59	0.116	0.0758	0.0007		5.59	0.116	0.0758	0.0007	1059	20	1091	19	3%	unzoned	✔
CNG2-mnz-83	6.34	0.136	0.0732	0.0010		6.34	0.136	0.0732	0.0010	941	19	1020	27	8%	patchy-darker	
CNG2-mnz-84	6.07	0.150	0.0738	0.0012		6.07	0.150	0.0738	0.0012	980	22	1037	33	6%	unzoned	
CNG2-mnz-85	12.48	0.227	0.0585	0.0007		12.48	0.227	0.0585	0.0007	496	9	550	27	10%	patchy-brighter	
CNG2-mnz-86	8.67	0.337	0.1963	0.0185	111	9.99	0.844	0.0647	0.0123	615	49	765	401	21%	mosaic	✔
CNG2-mnz-87	10.99	0.226	0.0596	0.0008		10.99	0.226	0.0596	0.0008	560	11	588	29	5%	mosaic	✔
CNG2-mnz-88	10.90	0.190	0.0590	0.0007		10.90	0.190	0.0590	0.0007	565	9	568	25	0%	patchy-dar	✔
CNG2-mnz-89	10.12	0.206	0.0606	0.0008		10.12	0.206	0.0606	0.0008	607	12	624	28	3%	unzoned	✔
CNG2-mnz-90	11.51	0.286	0.0608	0.0011		11.51	0.286	0.0608	0.0011	535	13	633	39	16%	unzoned	
CNG2-mnz-91	3.00	0.064	0.1155	0.0014		3.00	0.064	0.1155	0.0014	1848	34	1888	22	2%	unzoned	✔
CNG2-mnz-92	10.86	0.205	0.0599	0.0007		10.86	0.205	0.0599	0.0007	567	10	599	26	5%	unzoned	✔
CNG2-mnz-93	11.30	0.182	0.0586	0.0008		11.30	0.182	0.0586	0.0008	546	8	554	31	1%	unzoned	✔
CNG2-mnz-94	6.31	0.207	0.0754	0.0013		6.31	0.207	0.0754	0.0013	942	29	1079	36	13%	patchy-darker	
CNG2-mnz-95	11.17	0.216	0.0594	0.0008		11.17	0.216	0.0594	0.0008	552	10	581	30	5%	patchy-dar	✔
CNG2-mnz-96	11.05	0.199	0.0585	0.0009		11.05	0.199	0.0585	0.0009	558	10	550	33	-2%	mosaic	✔
CNG2-mnz-97	11.81	0.228	0.0577	0.0016		11.81	0.228	0.0577	0.0016	523	10	520	60	-1%	core	✔
CNG2-mnz-98	5.78	0.102	0.0741	0.0010		5.78	0.102	0.0741	0.0010	1026	17	1045	27	2%	unzoned	✔
CNG2-mnz-99	12.24	0.233	0.0624	0.0017		12.24	0.233	0.0624	0.0017	503	9	687	57	27%	mosaic	
CNG2-mnz-10	11.41	0.200	0.0591	0.0008		11.41	0.200	0.0591	0.0008	541	9	570	29	5%	unzoned	✔
CNG2-mnz-10	5.90	0.135	0.0748	0.0015		5.90	0.135	0.0748	0.0015	1005	21	1064	41	6%	unzoned	✔
CNG2-mnz-10	11.43	0.262	0.0591	0.0008		11.43	0.262	0.0591	0.0008	540	12	571	28	5%	unzoned	✔

$^{238}U/^{206}Pb$	2σ	$^{207}Pb/^{206}Pb$	2σ	$^{206}Pb/^{204}Pb$	$^{238}U/^{206}Pb^{*}$	2σ	$^{207}Pb^{*}/^{206}Pb^{*}$	2σ	$^{206}Pb^{*}/^{238}U$	2σ	$^{207}Pb^{*}/^{206}Pb^{*}$	2σ	Disc.†	internal structure	Used data††	
ratio		ratio		ratio	ratio		ratio		age (Ma)		age (Ma)		(%)			
Zambezi River																
ZMB2-mnz-1	2.96	0.057	0.1175	0.0023		2.96	0.057	0.1175	0.0023	1866	31	1919	34	3%	patchy-dar	✔
ZMB2-mnz-2	5.48	0.101	0.0753	0.0013		5.48	0.101	0.0753	0.0013	1078	18	1076	35	0%	patchy-bri	✔
ZMB2-mnz-3	12.71	0.248	0.0570	0.0010		12.71	0.248	0.0570	0.0010	487	9	493	39	1%	unzoned	✔
ZMB2-mnz-4	12.42	0.252	0.0577	0.0012		12.42	0.252	0.0577	0.0012	498	10	519	46	4%	patchy-bri	✔
ZMB2-mnz-5	6.44	0.159	0.0776	0.0022		6.44	0.159	0.0776	0.0022	920	21	1136	56	19%	unzoned	
ZMB2-mnz-6	12.53	0.243	0.0574	0.0012		12.53	0.243	0.0574	0.0012	494	9	508	45	3%	unzoned	✔
ZMB2-mnz-7	11.90	0.198	0.0631	0.0016		11.90	0.198	0.0631	0.0016	516	8	711	54	28%	patchy-darker	
ZMB2-mnz-8	4.93	0.084	0.0814	0.0016		4.93	0.084	0.0814	0.0016	1185	18	1231	39	4%	mosaic	✔
ZMB2-mnz-9	12.36	0.283	0.0658	0.0042		12.36	0.283	0.0658	0.0042	501	11	800	135	39%	core	
ZMB2-mnz-10	12.01	0.200	0.0578	0.0013		12.01	0.200	0.0578	0.0013	515	8	521	50	1%	unzoned	✔
ZMB2-mnz-11	12.52	0.219	0.0583	0.0012		12.52	0.219	0.0583	0.0012	494	8	540	47	9%	unzoned	✔
ZMB2-mnz-12	12.50	0.238	0.0580	0.0012		12.50	0.238	0.0580	0.0012	495	9	528	46	6%	patchy-dar	✔
ZMB2-mnz-13	11.37	0.289	0.0655	0.0037		11.37	0.289	0.0655	0.0037	538	13	791	119	33%	unzoned	
ZMB2-mnz-14	12.60	0.228	0.0574	0.0013		12.60	0.228	0.0574	0.0013	491	9	507	50	3%	patchy-dar	✔
ZMB2-mnz-15	2.86	0.045	0.1192	0.0025		2.86	0.045	0.1192	0.0025	1926	26	1944	37	1%	core	✔
ZMB2-mnz-16	12.02	0.287	0.0672	0.0021	1868	12.12	0.303	0.0593	0.0025	511	12	580	91	12%	patchy-dar	✔
ZMB2-mnz-17	5.61	0.114	0.0754	0.0012		5.61	0.114	0.0754	0.0012	1055	20	1081	33	2%	mosaic	✔
ZMB2-mnz-18	12.51	0.301	0.0584	0.0013		12.51	0.301	0.0584	0.0013	495	11	546	47	10%	unzoned	✔
ZMB2-mnz-19	12.89	0.269	0.0563	0.0009		12.89	0.269	0.0563	0.0009	481	10	462	35	-4%	rim	✔
ZMB2-mnz-20	12.41	0.215	0.0585	0.0014		12.41	0.215	0.0585	0.0014	498	8	548	52	9%	unzoned	✔
ZMB2-mnz-21	12.63	0.281	0.0585	0.0014		12.63	0.281	0.0585	0.0014	490	10	549	54	11%	unzoned	✔
ZMB2-mnz-22	10.99	0.199	0.0631	0.0017		10.99	0.199	0.0631	0.0017	558	10	712	57	22%	unzoned	
ZMB2-mnz-23	12.47	0.236	0.0573	0.0010		12.47	0.236	0.0573	0.0010	497	9	503	38	1%	patchy-dar	✔
ZMB2-mnz-24	11.94	0.247	0.0579	0.0009		11.94	0.247	0.0579	0.0009	518	10	525	36	1%	unzoned	✔
ZMB2-mnz-25	11.51	0.196	0.0596	0.0019		11.51	0.196	0.0596	0.0019	535	9	590	70	9%	core	✔
ZMB2-mnz-26	12.39	0.198	0.0567	0.0010		12.39	0.198	0.0567	0.0010	500	8	480	41	-4%	unzoned	✔
ZMB2-mnz-27	12.47	0.219	0.0579	0.0009		12.47	0.219	0.0579	0.0009	496	8	526	35	6%	mosaic	✔
ZMB2-mnz-28	12.26	0.224	0.0577	0.0008		12.26	0.224	0.0577	0.0008	504	9	517	32	2%	unzoned	✔
ZMB2-mnz-29	11.31	0.228	0.0585	0.0009		11.31	0.228	0.0585	0.0009	545	11	549	34	1%	unzoned	✔
ZMB2-mnz-30	12.48	0.216	0.0572	0.0008		12.48	0.216	0.0572	0.0008	496	8	498	30	0%	core	✔
ZMB2-mnz-31	12.87	0.233	0.0571	0.0009		12.87	0.233	0.0571	0.0009	482	8	497	35	3%	mosaic	✔
ZMB2-mnz-32	12.44	0.224	0.0586	0.0009		12.44	0.224	0.0586	0.0009	497	9	552	32	10%	mosaic	
ZMB2-mnz-33	12.23	0.226	0.0587	0.0009		12.23	0.226	0.0587	0.0009	505	9	555	34	9%	mosaic	
ZMB2-mnz-34	12.36	0.222	0.0579	0.0012		12.36	0.222	0.0579	0.0012	501	9	528	45	5%	patchy-bri	✔
ZMB2-mnz-35	12.13	0.209	0.0586	0.0008		12.13	0.209	0.0586	0.0008	510	8	554	31	8%	unzoned	
ZMB2-mnz-36	5.71	0.117	0.0749	0.0012		5.71	0.117	0.0749	0.0012	1038	20	1067	32	3%	patchy-dar	✔
ZMB2-mnz-37	11.88	0.165	0.0590	0.0010		11.88	0.165	0.0590	0.0010	520	7	569	36	9%	patchy-brighter	
ZMB2-mnz-38	12.50	0.248	0.0571	0.0010		12.50	0.248	0.0571	0.0010	496	9	496	39	0%	unzoned	✔
ZMB2-mnz-39	12.69	0.215	0.0583	0.0013		12.69	0.215	0.0583	0.0013	488	8	540	47	10%	unzoned	✔
ZMB2-mnz-40	12.56	0.228	0.0582	0.0015		12.56	0.228	0.0582	0.0015	493	9	539	56	9%	unzoned	✔
ZMB2-mnz-41	11.91	0.267	0.0582	0.0014		11.91	0.267	0.0582	0.0014	519	11	536	52	3%	patchy-dar	✔
ZMB2-mnz-42	12.47	0.249	0.0573	0.0014		12.47	0.249	0.0573	0.0014	497	10	504	54	1%	unzoned	✔
ZMB2-mnz-43	5.84	0.125	0.0748	0.0012		5.84	0.125	0.0748	0.0012	1016	20	1064	33	5%	unzoned	✔
ZMB2-mnz-44	10.17	0.341	0.0670	0.0024		10.17	0.341	0.0670	0.0024	599	19	839	74	29%	unzoned	
ZMB2-mnz-45	10.03	0.199	0.0596	0.0011		10.03	0.199	0.0596	0.0011	613	12	588	40	-5%	unzoned	✔
ZMB2-mnz-46	12.26	0.198	0.0584	0.0008		12.26	0.198	0.0584	0.0008	505	8	545	31	8%	patchy-darker	
ZMB2-mnz-47	12.52	0.180	0.0585	0.0008		12.52	0.180	0.0585	0.0008	494	7	548	31	10%	patchy-brighter	
ZMB2-mnz-48	12.46	0.276	0.0597	0.0017		12.46	0.276	0.0597	0.0017	496	11	591	61	16%	patchy-darker	
ZMB2-mnz-49	12.68	0.334	0.0610	0.0017		12.68	0.334	0.0610	0.0017	487	12	639	59	24%	core	
ZMB2-mnz-50	6.09	0.221	0.0759	0.0010		6.09	0.221	0.0759	0.0010	976	33	1091	26	11%	patchy-brighter	
ZMB2-mnz-51	12.44	0.227	0.0599	0.0014		12.44	0.227	0.0599	0.0014	497	9	598	51	17%	patchy-brighter	
ZMB2-mnz-52	3.01	0.052	0.1202	0.0013		3.01	0.052	0.1202	0.0013	1836	28	1960	20	6%	core	
ZMB2-mnz-53	11.38	0.220	0.0593	0.0017		11.38	0.220	0.0593	0.0017	542	10	580	62	7%	unzoned	✔
ZMB2-mnz-54	12.33	0.238	0.0579	0.0011		12.33	0.238	0.0579	0.0011	502	9	527	43	5%	mosaic	✔
ZMB2-mnz-55	13.02	0.270	0.0581	0.0008		13.02	0.270	0.0581	0.0008	476	9	535	29	11%	patchy-brighter	
ZMB2-mnz-56	12.21	0.297	0.0602	0.0012		12.21	0.297	0.0602	0.0012	505	12	610	42	18%	patchy-brighter	
ZMB2-mnz-57	12.14	0.215	0.0578	0.0009		12.14	0.215	0.0578	0.0009	510	9	522	33	2%	patchy-dar	✔
ZMB2-mnz-58	5.84	0.104	0.0780	0.0025		5.84	0.104	0.0780	0.0025	1013	17	1146	64	12%	core	
ZMB2-mnz-59	12.45	0.255	0.0631	0.0018		12.45	0.255	0.0631	0.0018	494	10	712	61	31%	core	
ZMB2-mnz-60	12.58	0.212	0.0582	0.0010		12.58	0.212	0.0582	0.0010	492	8	539	38	9%	patchy-darker	
ZMB2-mnz-61	13.15	0.193	0.0576	0.0008		13.15	0.193	0.0576	0.0008	472	7	514	32	8%	unzoned	
ZMB2-mnz-62	12.50	0.229	0.0586	0.0009		12.50	0.229	0.0586	0.0009	495	9	553	35	11%	patchy-brighter	
ZMB2-mnz-63	9.73	0.243	0.0612	0.0010		9.73	0.243	0.0612	0.0010	630	15	646	35	2%	mosaic	✔
ZMB2-mnz-64	12.39	0.290	0.0681	0.0020		12.39	0.290	0.0681	0.0020	493	11	871	61	44%	patchy-darker	
ZMB2-mnz-65	12.15	0.278	0.0570	0.0013		12.15	0.278	0.0570	0.0013	509	11	493	52	-3%	core	✔
ZMB2-mnz-66	12.12	0.300	0.0581	0.0011		12.12	0.300	0.0581	0.0011	510	12	534	41	5%	unzoned	✔
ZMB2-mnz-67	6.93	0.159	0.0709	0.0013		6.93	0.159	0.0709	0.0013	865	19	955	38	10%	unzoned	
ZMB2-mnz-68	8.99	0.447	0.0671	0.0020		8.99	0.447	0.0671	0.0020	675	32	841	61	20%	patchy-darker	
ZMB2-mnz-69	12.43	0.269	0.0571	0.0011		12.43	0.269	0.0571	0.0011	498	10	496	41	-1%	core	✔
ZMB2-mnz-70	12.45	0.301	0.0589	0.0015		12.45	0.301	0.0589	0.0015	496	12	564	55	12%	unzoned	
ZMB2-mnz-71	10.95	0.151	0.0589	0.0010		10.95	0.151	0.0589	0.0010	562	7	563	36	0%	mosaic	✔
ZMB2-mnz-72	12.78	0.266	0.0580	0.0008		12.78	0.266	0.0580	0.0008	484	10	528	29	8%	unzoned	
ZMB2-mnz-73	2.83	0.051	0.1192	0.0017		2.83	0.051	0.1192	0.0017	1944	30	1945	25	0%	patchy-dar	✔
ZMB2-mnz-74	12.39	0.215	0.0569	0.0014		12.39	0.215	0.0569	0.0014	500	8	489	55	-2%	patchy-bri	✔
ZMB2-mnz-75	11.87	0.209	0.0563	0.0008		11.87	0.209	0.0563	0.0008	521	9	466	31	-12%	unzoned	
ZMB2-mnz-76	7.59	0.320	0.0702	0.0015		7.59	0.320	0.0702	0.0015	793	31	934	45	15%	mosaic	
ZMB2-mnz-77	5.76	0.099	0.0722	0.0013		5.76	0.099	0.0722	0.0013	1031	16	992	38	-4%	unzoned	✔
ZMB2-mnz-78	11.45	0.218	0.0605	0.0017		11.45	0.218	0.0605	0.0017	538	10	622	61	14%	unzoned	
ZMB2-mnz-79	11.65	0.302	0.0580	0.0046		11.65	0.302	0.0580	0.0046	530	13	528	175	0%	unzoned	✔
ZMB2-mnz-80	12.08	0.289	0.0576	0.0018		12.08	0.289	0.0576	0.0018	512	12	516	68	1%	mosaic	✔
ZMB2-mnz-81	12.08	0.222	0.0634	0.0018		12.08	0.222	0.0634	0.0018	509	9	721	59	30%	mosaic	
ZMB2-mnz-82	11.70	0.215	0.0571	0.0011		11.70	0.215	0.0571	0.0011	529	9	496	43	-7%	unzoned	✔
ZMB2-mnz-83	12.78	0.306	0.0575	0.0012		12.78	0.306	0.0575	0.0012	485	11	511	47	5%	patchy-bri	✔
ZMB2-mnz-84	5.43	0.125	0.0742	0.0016		5.43	0.125	0.0742	0.0016	1090	23	1046	43	-5%	core	✔
ZMB2-mnz-85	11.69	0.314	0.0665	0.0016		11.69	0.314	0.0665	0.0016	523	13	823	49	37%	unzoned	
ZMB2-mnz-86	7.49	0.310	0.0707	0.0015		7.49	0.310	0.0707	0.0015	803	31	948	43	16%	mosaic	
ZMB2-mnz-87	5.76	0.092	0.0725	0.0012		5.76	0.092	0.0725	0.0012	1032	15	999	34	-4%	unzoned	✔
ZMB2-mnz-88	11.42	0.210	0.0610	0.0017		11.42	0.210	0.0610	0.0017	539	9	638	59	16%	unzoned	
ZMB2-mnz-89	11.65	0.292	0.0582	0.0046		11.65	0.292	0.0582	0.0046	530	13	536	174	1%	unzoned	✔
ZMB2-mnz-90	12.08	0.279	0.0578	0.0017		12.08	0.279	0.0578	0.0017	512	11	523	65	2%	unzoned	✔
ZMB2-mnz-91	12.08	0.207	0.0636	0.0017		12.08	0.207	0.0636	0.0017	509	8	728	56	31%	unzoned	
ZMB2-mnz-92	11.69	0.201	0.0573	0.0010		11.69	0.201	0.0573	0.0010	529	9	503	39	-5%	mosaic	✔
ZMB2-mnz-93	12.66	0.287	0.0579	0.0011		12.66	0.287	0.0579	0.0011	489	11	524	43	7%	unzoned	✔
ZMB2-mnz-94	5.43	0.120	0.0744	0.0015		5.43	0.120	0.0744	0.0015	1090	22	1053	40	-4%	patchy-bri	✔
ZMB2-mnz-95	11.68	0.305	0.0668	0.0015	1158	11.84	0.343	0.0540	0.0035	523	15	370	146	-43%	patchy-bri	✔
ZMB2-mnz-96	2.82	0.072	0.1208	0.0021		2.82	0.072	0.1208	0.0021	1955	43	1968	31	1%	unzoned	✔
ZMB2-mnz-97	6.19	0.154	0.0753	0.0015		6.19	0.154	0.0753	0.0015	961	22	1075	40	11%	unzoned	
ZMB2-mnz-98	9.35	0.239	0.0631	0.0015		9.35	0.239	0.0631	0.0015	653	16	711	49	8%	unzoned	✔
ZMB2-mnz-99	11.72	0.359	0.0599	0.0020		11.72	0.359	0.0599	0.0020	526	15	600	73	12%	mosaic	✔
ZMB2-mnz-10	12.69	0.321	0.0589	0.0013		12.69	0.321	0.0589	0.0013	488	12	564	49	14%	unzoned	
ZMB2-mnz-10	12.45	0.278	0.0577	0.0013		12.45	0.278	0.0577	0.0013	498	11	520	48	4%	unzoned	✔
ZMB2-mnz-10	12.56	0.282	0.0567	0.0012		12.56	0.282	0.0567	0.0012	494	11	481	46	-3%	unzoned	✔
ZMB2-mnz-10	12.37	0.332	0.0578	0.0011		12.37	0.332	0.0578	0.0011	501	13	524	43	4%	unzoned	✔
ZMB2-mnz-10	12.18	0.273	0.0584	0.0012		12.18	0.273	0.0584	0.0012	508	11	543	45	7%	unzoned	✔
ZMB2-mnz-10	2.87	0.076	0.1273	0.0029	7189	2.87	0.076	0.1254	0.0011	1925	44	2034	15	6%	unzoned	
ZMB2-mnz-10	5.73	0.134	0.0755	0.0017		5.73	0.134	0.0755	0.0017	1034	22	1083	44	5%	unzoned	✔
ZMB2-mnz-10	12.63	0.217	0.0576	0.0012		12.63	0.217	0.0576	0.0012	490	8	513	45	4%	unzoned	✔
ZMB2-mnz-10	8.19	0.449	0.0834	0.0040		8.19	0.449	0.0834	0.0040	725	38	1279	92	44%	unzoned	
ZMB2-mnz-10	12.31	0.290	0.0583	0.0016		12.31	0.290	0.0583	0.0016	502	11	541	59	7%	unzoned	✔

$^{238}U/^{206}Pb$	2σ	$^{207}Pb/^{206}Pb$	2σ	$^{206}Pb/^{204}Pb$	$^{238}U/^{206}Pb$*	2σ	$^{207}Pb*/^{206}Pb*$	2σ	$^{206}Pb*/^{238}U$	2σ	$^{207}Pb*/^{206}Pb*$	2σ	Disc.†	internal structure	Used data††	
ratio		ratio		ratio	ratio		ratio		age (Ma)		age (Ma)		(%)			
Orange River																
ORG2-mnz-1	5.39	0.096	0.0758	0.0013		5.39	0.096	0.0758	0.0013	1095	18	1089	34	-1% patchy-dar	✔	
ORG2-mnz-2	5.39	0.105	0.0768	0.0014		5.39	0.105	0.0768	0.0014	1094	20	1117	35	2% unzoned	✔	
ORG2-mnz-3	5.72	0.091	0.0736	0.0012		5.72	0.091	0.0736	0.0012	1038	15	1029	33	-1% mosaic	✔	
ORG2-mnz-4	5.29	0.147	0.0730	0.0037		5.29	0.147	0.0730	0.0037	1116	28	1013	102	-11% mosaic	✔	
ORG2-mnz-5	5.29	0.136	0.0752	0.0038		5.29	0.136	0.0752	0.0038	1116	26	1075	102	-4% patchy-bri	✔	
ORG2-mnz-6	6.27	0.159	0.0732	0.0037		6.27	0.159	0.0732	0.0037	949	22	1018	102	7% patchy-bri	✔	
ORG2-mnz-7	5.94	0.186	0.0729	0.0041		5.94	0.186	0.0729	0.0041	1001	29	1011	115	1% patchy-dar	✔	
ORG2-mnz-8	5.37	0.152	0.0761	0.0043		5.37	0.152	0.0761	0.0043	1098	28	1098	114	0% patchy-bri	✔	
ORG2-mnz-9*	5.28	0.162	0.0779	0.0045	4173	5.30	0.163	0.0744	0.0013	1114	31	1053	34	-6% patchy-bri	✔	
ORG2-mnz-10	5.68	0.168	0.0716	0.0041		5.68	0.168	0.0716	0.0041	1045	28	973	117	-8% mosaic	✔	
ORG2-mnz-11	5.58	0.186	0.0748	0.0035		5.58	0.186	0.0748	0.0035	1062	33	1064	94	0% unzoned	✔	
ORG2-mnz-12	22.09	4.039	0.3113	0.0571		22.09	4.039	0.3113	0.0571	285	51	3527	283	94% core		
ORG2-mnz-13	6.02	0.145	0.0728	0.0033		6.02	0.145	0.0728	0.0033	991	22	1009	92	2% mosaic	✔	
ORG2-mnz-14	5.48	0.110	0.0747	0.0033		5.48	0.110	0.0747	0.0033	1080	20	1059	88	-2% mosaic	✔	
ORG2-mnz-15	6.09	0.114	0.0730	0.0013		6.09	0.114	0.0730	0.0013	980	17	1015	36	4% mosaic	✔	
ORG2-mnz-16	5.02	0.083	0.0801	0.0016		5.02	0.083	0.0801	0.0016	1172	18	1199	39	3% core	✔	
ORG2-mnz-17	4.90	0.085	0.0793	0.0016		4.90	0.085	0.0793	0.0016	1197	19	1178	40	-2% unzoned	✔	
ORG2-mnz-18	6.56	0.221	0.0787	0.0025		6.56	0.221	0.0787	0.0025	915	29	1165	63	23% mosaic		
ORG2-mnz-19	5.22	0.141	0.0760	0.0014		5.22	0.141	0.0760	0.0014	1129	28	1095	37	-3% patchy-dar	✔	
ORG2-mnz-20	5.45	0.187	0.0898	0.0020	1083	5.52	0.191	0.0765	0.0013	1073	34	1108	35	3% core	✔	
ORG2-mnz-21	5.79	0.091	0.0732	0.0015		5.79	0.091	0.0732	0.0015	1027	15	1020	42	-1% patchy-dar	✔	
ORG2-mnz-22	4.93	0.098	0.0790	0.0014		4.93	0.098	0.0790	0.0014	1190	22	1173	35	-2% patchy-bri	✔	
ORG2-mnz-23	6.41	0.190	0.0722	0.0014		6.41	0.190	0.0722	0.0014	935	26	992	40	6% patchy-dar	✔	
ORG2-mnz-24	5.96	0.143	0.0732	0.0015		5.96	0.143	0.0732	0.0015	999	22	1019	42	2% unzoned	✔	
ORG2-mnz-25	5.07	0.140	0.0807	0.0015		5.07	0.140	0.0807	0.0015	1162	29	1215	36	5% unzoned	✔	
ORG2-mnz-26	5.21	0.142	0.0779	0.0015		5.21	0.142	0.0779	0.0015	1131	28	1144	39	1% patchy-dar	✔	
ORG2-mnz-27	6.70	0.353	0.0831	0.0033		6.70	0.353	0.0831	0.0033	897	44	1272	78	32% patchy-darker		
ORG2-mnz-28	5.07	0.125	0.0794	0.0015		5.07	0.125	0.0794	0.0015	1159	26	1183	36	2% unzoned	✔	
ORG2-mnz-29	5.20	0.134	0.0802	0.0016		5.20	0.134	0.0802	0.0016	1135	27	1203	40	6% core		
ORG2-mnz-30	6.53	0.207	0.0731	0.0009		6.53	0.207	0.0731	0.0009	918	27	1017	25	10% patchy-brighter		
ORG2-mnz-31	5.61	0.119	0.0778	0.0015		5.61	0.119	0.0778	0.0015	1058	21	1143	38	8% rim		
ORG2-mnz-32	5.13	0.129	0.0768	0.0015		5.13	0.129	0.0768	0.0015	1148	26	1116	38	-3% patchy-bri	✔	
ORG2-mnz-33	4.94	0.131	0.0795	0.0012		4.94	0.131	0.0795	0.0012	1188	29	1183	30	0% mosaic	✔	
ORG2-mnz-34	12.52	0.224	0.0604	0.0016		12.52	0.224	0.0604	0.0016	495	9	616	58	20% patchy-brighter		
ORG2-mnz-35	5.73	0.124	0.0779	0.0014		5.73	0.124	0.0779	0.0014	1037	21	1144	35	10% unzoned		
ORG2-mnz-36	5.10	0.091	0.0793	0.0012		5.10	0.091	0.0793	0.0012	1153	19	1180	31	2% patchy-dar	✔	
ORG2-mnz-37	5.52	0.094	0.0751	0.0013		5.52	0.094	0.0751	0.0013	1073	17	1071	35	0% patchy-bri	✔	
ORG2-mnz-38	5.00	0.071	0.0794	0.0014		5.00	0.071	0.0794	0.0014	1174	15	1182	36	1% patchy-bri	✔	
ORG2-mnz-39	5.58	0.175	0.0739	0.0012		5.58	0.175	0.0739	0.0012	1063	31	1038	34	-3% patchy-dar	✔	
ORG2-mnz-40	5.11	0.104	0.0754	0.0014		5.11	0.104	0.0754	0.0014	1153	22	1080	37	-7% unzoned		
ORG2-mnz-41	12.24	0.289	0.0577	0.0011		12.24	0.289	0.0577	0.0011	506	11	517	40	2% core	✔	
ORG2-mnz-42	6.00	0.079	0.0725	0.0010		6.00	0.079	0.0725	0.0010	994	12	1001	29	1% patchy-bri	✔	
ORG2-mnz-43	5.37	0.109	0.0753	0.0013		5.37	0.109	0.0753	0.0013	1101	21	1078	33	-2% unzoned	✔	
ORG2-mnz-44	6.11	0.175	0.0837	0.0025		6.11	0.175	0.0837	0.0025	977	26	1286	58	26% patchy-darker		
ORG2-mnz-45	5.53	0.085	0.0768	0.0009	4552	5.55	0.087	0.0736	0.0016	1068	15	1030	43	-4% unzoned	✔	
ORG2-mnz-46	5.05	0.114	0.0821	0.0016	10158	5.06	0.114	0.0807	0.0009	1163	24	1214	21	5% mosaic	✔	
ORG2-mnz-47	4.57	0.091	0.0810	0.0016		4.57	0.091	0.0810	0.0016	1277	23	1220	38	-5% mosaic	✔	
ORG2-mnz-48	5.14	0.130	0.0763	0.0015		5.14	0.130	0.0763	0.0015	1146	26	1103	39	-4% patchy-bri	✔	
ORG2-mnz-49	5.48	0.180	0.0806	0.0023		5.48	0.180	0.0806	0.0023	1081	33	1212	56	12% patchy-brighter		
ORG2-mnz-50	6.42	0.414	0.0945	0.0056		6.42	0.414	0.0945	0.0056	933	56	1518	112	41% mosaic		
ORG2-mnz-51	5.07	0.106	0.0806	0.0014		5.07	0.106	0.0806	0.0014	1161	22	1211	33	5% patchy-bri	✔	
ORG2-mnz-52	4.86	0.116	0.0799	0.0013		4.86	0.116	0.0799	0.0013	1207	26	1195	33	-1% unzoned	✔	
ORG2-mnz-53	5.57	0.107	0.0776	0.0014		5.57	0.107	0.0776	0.0014	1065	19	1137	35	7% unzoned		
ORG2-mnz-54	4.40	0.069	0.0864	0.0016		4.40	0.069	0.0864	0.0016	1320	19	1346	36	2% unzoned	✔	
ORG2-mnz-55	5.21	0.124	0.0786	0.0014		5.21	0.124	0.0786	0.0014	1132	25	1161	36	3% patchy-bri	✔	
ORG2-mnz-56	4.87	0.110	0.0797	0.0015		4.87	0.110	0.0797	0.0015	1204	25	1189	38	-1% patchy-bri	✔	
ORG2-mnz-57	12.14	0.188	0.0600	0.0013		12.14	0.188	0.0600	0.0013	510	8	604	45	16% unzoned		
ORG2-mnz-58	4.95	0.098	0.0794	0.0014		4.95	0.098	0.0794	0.0014	1187	21	1183	34	0% unzoned	✔	
ORG2-mnz-59	5.05	0.111	0.0795	0.0017		5.05	0.111	0.0795	0.0017	1165	23	1185	42	2% unzoned	✔	
ORG2-mnz-60	5.20	0.113	0.0780	0.0014		5.20	0.113	0.0780	0.0014	1133	23	1146	36	1% mosaic	✔	
ORG2-mnz-61	6.16	0.244	0.0883	0.0037	11244	6.17	0.244	0.0871	0.0006	968	35	1362	14	31% patchy-darker		
ORG2-mnz-62	5.37	0.078	0.0778	0.0008		5.37	0.078	0.0778	0.0008	1102	15	1142	20	4% patchy-dar	✔	
ORG2-mnz-63	5.78	0.128	0.0817	0.0019		5.78	0.128	0.0817	0.0019	1029	21	1238	45	18% patchy-brighter		
ORG2-mnz-64	6.13	0.215	0.0919	0.0034		6.13	0.215	0.0919	0.0034	974	32	1464	71	36% unzoned		
ORG2-mnz-65	12.34	0.210	0.0582	0.0010		12.34	0.210	0.0582	0.0010	502	8	537	38	7% patchy-bri	✔	
ORG2-mnz-66	4.79	0.056	0.0810	0.0010		4.79	0.056	0.0810	0.0010	1222	13	1221	24	0% patchy-bri	✔	
ORG2-mnz-67	4.92	0.068	0.0803	0.0012		4.92	0.068	0.0803	0.0012	1192	15	1205	29	1% patchy-dar	✔	
ORG2-mnz-68	10.12	0.176	0.0598	0.0007		10.12	0.176	0.0598	0.0007	607	10	597	25	-2% unzoned	✔	
ORG2-mnz-69	5.50	0.077	0.0767	0.0011		5.50	0.077	0.0767	0.0011	1076	14	1114	29	4% rim	✔	
ORG2-mnz-70	6.17	0.155	0.0733	0.0014		6.17	0.155	0.0733	0.0014	969	23	1021	39	6% patchy-bri	✔	
ORG2-mnz-71	5.02	0.089	0.0800	0.0008		5.02	0.089	0.0800	0.0008	1172	19	1197	20	2% mosaic	✔	
ORG2-mnz-72	3.41	0.056	0.1092	0.0013		3.41	0.056	0.1092	0.0013	1656	24	1786	22	8% rim		
ORG2-mnz-73	6.07	0.141	0.0740	0.0010		6.07	0.141	0.0740	0.0010	983	21	1042	27	6% patchy-darker		
ORG2-mnz-74	5.77	0.112	0.0723	0.0012		5.77	0.112	0.0723	0.0012	1031	18	994	33	-4% patchy-dar	✔	
ORG2-mnz-75	4.63	0.153	0.0851	0.0019		4.63	0.153	0.0851	0.0019	1261	38	1317	42	5% unzoned	✔	
ORG2-mnz-76	6.09	0.113	0.0743	0.0013		6.09	0.113	0.0743	0.0013	980	17	1048	34	7% patchy-darker		
ORG2-mnz-77	4.98	0.095	0.0815	0.0012		4.98	0.095	0.0815	0.0012	1179	20	1234	28	5% core	✔	
ORG2-mnz-78	5.95	0.121	0.0741	0.0011		5.95	0.121	0.0741	0.0011	1001	19	1045	29	5% patchy-bri	✔	
ORG2-mnz-79	5.78	0.150	0.0726	0.0014		5.78	0.150	0.0726	0.0014	1029	25	1003	40	-3% patchy-bri	✔	
ORG2-mnz-80	5.15	0.155	0.0817	0.0018		5.15	0.155	0.0817	0.0018	1145	31	1238	42	8% patchy-brighter		
ORG2-mnz-81	4.53	0.101	0.0799	0.0012		4.53	0.101	0.0799	0.0012	1287	26	1194	30	-9% mosaic		
ORG2-mnz-82	5.98	0.139	0.0720	0.0008		5.98	0.139	0.0720	0.0008	997	21	985	23	-1% unzoned	✔	
ORG2-mnz-83	5.89	0.145	0.0723	0.0009		5.89	0.145	0.0723	0.0009	1010	23	995	25	-2% unzoned	✔	
ORG2-mnz-84	5.54	0.164	0.0733	0.0011		5.54	0.164	0.0733	0.0011	1070	29	1022	29	-5% unzoned	✔	
ORG2-mnz-85	5.26	0.124	0.0764	0.0012		5.26	0.124	0.0764	0.0012	1122	24	1106	31	-2% mosaic	✔	
ORG2-mnz-86	5.36	0.106	0.0775	0.0014		5.36	0.106	0.0775	0.0014	1103	20	1134	35	3% unzoned	✔	
ORG2-mnz-87	6.11	0.169	0.0731	0.0020		6.11	0.169	0.0731	0.0020	977	25	1017	54	4% mosaic	✔	
ORG2-mnz-88	6.01	0.110	0.0720	0.0011		6.01	0.110	0.0720	0.0011	992	17	986	30	-1% unzoned	✔	
ORG2-mnz-89	5.60	0.118	0.0778	0.0012		5.60	0.118	0.0778	0.0012	1059	21	1142	30	8% patchy-darker		
ORG2-mnz-90	5.32	0.098	0.0756	0.0013		5.32	0.098	0.0756	0.0013	1110	19	1086	35	-2% patchy-bri	✔	
ORG2-mnz-91	6.07	0.126	0.0715	0.0013		6.07	0.126	0.0715	0.0013	983	19	970	38	-1% unzoned	✔	
ORG2-mnz-92	5.72	0.132	0.0741	0.0014		5.72	0.132	0.0741	0.0014	1039	22	1043	39	0% patchy-dar	✔	
ORG2-mnz-93	6.03	0.169	0.0729	0.0012		6.03	0.169	0.0729	0.0012	989	26	1011	33	2% mosaic	✔	
ORG2-mnz-94	7.00	0.475	0.1115	0.0080		7.00	0.475	0.1115	0.0080	861	54	1823	131	56% unzoned		
ORG2-mnz-95	6.07	0.148	0.0742	0.0016	14032	6.08	0.148	0.0732	0.0007	982	22	1019	20	4% mosaic	✔	
ORG2-mnz-96	4.34	0.386	0.0857	0.0025	898	4.41	0.392	0.0703	0.0012	1318	105	938	35	-45% mosaic		
ORG2-mnz-97	6.19	0.147	0.0718	0.0013		6.19	0.147	0.0718	0.0013	966	21	979	36	1% core	✔	
ORG2-mnz-98	5.73	0.124	0.0718	0.0014		5.73	0.124	0.0718	0.0014	1037	21	980	39	-6% unzoned	✔	
ORG2-mnz-99	4.93	0.108	0.0797	0.0013		4.93	0.108	0.0797	0.0013	1191	24	1189	32	0% mosaic	✔	
ORG2-mnz-100	5.91	0.114	0.0722	0.0011		5.91	0.114	0.0722	0.0011	1008	18	991	31	-2% unzoned	✔	
ORG2-mnz-101	12.47	0.297	0.0585	0.0013		12.47	0.297	0.0585	0.0013	497	11	548	48	10% mosaic	✔	
ORG2-mnz-102	10.86	0.261	0.0588	0.0029		10.86	0.261	0.0588	0.0029	568	13	559	109	-2% unzoned	✔	
ORG2-mnz-103	5.47	0.088	0.0761	0.0008		5.47	0.088	0.0761	0.0008	1083	16	1098	21	2% patchy-bri	✔	
ORG2-mnz-104	6.00	0.089	0.0726	0.0009		6.00	0.089	0.0726	0.0009	994	14	1002	24	1% patchy-bri	✔	
ORG2-mnz-105	5.63	0.116	0.0730	0.0009		5.63	0.116	0.0730	0.0009	1054	20	1015	24	-4% patchy-dar	✔	
ORG2-mnz-106	5.31	0.103	0.0756	0.0010		5.31	0.103	0.0756	0.0010	1112	20	1086	27	-3% patchy-bri	✔	
ORG2-mnz-107	5.34	0.085	0.0761	0.0012		5.34	0.085	0.0761	0.0012	1106	16	1099	31	-1% unzoned	✔	
ORG2-mnz-108	6.41	0.317	0.0910	0.0037		6.41	0.317	0.0910	0.0037	934	43	1446	78	38% rim		
ORG2-mnz-109	5.27	0.079	0.0766	0.0012		5.27	0.079	0.0766	0.0012	1121	15	1111	32	-1% core	✔	
ORG2-mnz-110	5.93	0.109	0.0726	0.0011		5.93	0.109	0.0726	0.0011	1004	17	1004	31	0% unzoned	✔	
ORG2-mnz-111	5.37	0.113	0.0769	0.0011		5.37	0.113	0.0769	0.0011	1101	21	1118	29	2% core	✔	
ORG2-mnz-112	12.74	0.236	0.0568	0.0009		12.74	0.236	0.0568	0.0009	487	9	483	34	-1% patchy-dar	✔	
ORG2-mnz-113	5.05	0.085	0.0779	0.0014		5.05	0.085	0.0779	0.0014	1165	18	1145	35	-2% rim	✔	
ORG2-mnz-114	5.80	0.092	0.0731	0.0013		5.80	0.092	0.0731	0.0013	1025	15	1017	37	-1% unzoned	✔	

* ^{204}Pb were detedted and $^{206}Pb/^{204}Pb$ were used for ^{204}Pb common Pb correction.

† The % discordance was calculated as $\{1-[^{206}Pb/^{238}U]_{measured}/[^{206}Pb/^{238}U]_{^{207}Pb*/^{206}Pb*\ age}\}$

†† Either concordant U–Pb ages within analytical uncertainty or those with <5% discordance

Appendix Table 5-3. Geochemical data for detrital monazites from the African major rivers

LA-ICP-MS DATA	ppm	ppm	ppm	ppm	ppm	ppm	ppm	ppm	ppm	ppm	ppm	ppm	ppm	ppm	ppm	ppm	ppm	ppm	ppm	ppm
Nile River	**Ca**	**Sr**	**Y**	**La**	**Ce**	**Pr**	**Nd**	**Sm**	**Eu**	**Gd**	**Tb**	**Dy**	**Ho**	**Er**	**Tm**	**Yb†**	**Lu††**	**Th**	**U**
NIL-mnz-1	14224	80	6511	154583	246665	25446	101558	11410	743	7559	614	2189	249	395	30	102	6	61481	1738
NIL-mnz-2	5892	46	7399	154876	247698	26264	104348	11185	544	6675	609	2376	275	500	35	91	9	81836	837
NIL-mnz-3	4374	50	5043	166795	269434	29550	107377	13054	208	6907	571	1973	230	302	32	72	6	49202	2232
NIL-mnz-4	4727	136	2137	143494	247203	34183	134967	18522	249	8989	478	1113	99	126	5	4	0.5	78878	707
NIL-mnz-5	6939	31	1440	171955	273003	25860	88027	7823	216	3441	198	567	67	89	7	11	3	97377	539
NIL-mnz-6	17157	79	7304	161133	253068	30078	107404	14139	162	8623	699	2640	309	490	44	105	13	98632	1595
NIL-mnz-7	1773	92	5279	189050	284460	33715	128349	11230	822	5353	413	1524	195	302	32	102	11	12693	2560
NIL-mnz-8	6868	21	5410	199039	281139	28674	99690	11473	39	6236	476	1717	208	339	26	62	6	44897	2684
NIL-mnz-9	9759	15	26712	102046	208374	28278	139316	33365	208	24274	2430	9274	1076	1792	163	655	44	157480	4602
NIL-mnz-10	5387	548	645	201654	308049	30581	104317	8055	196	4014	204	423	35	46	3	6	0.5	10543	60
NIL-mnz-11	7623	14	8441	195808	292033	33186	125302	12267	234	6857	673	2999	358	484	36	67	2	94492	1637
NIL-mnz-12	22618	194	16950	159608	234875	23276	85917	9781	336	6946	780	3326	560	963	99	401	29	97277	9424
NIL-mnz-13	9284	89	11743	159362	252325	29350	123212	14810	1107	9022	922	3295	492	670	68	346	27	66408	2221
NIL-mnz-14	5347	6	2098	204863	291333	25156	99151	6820	89	2996	176	778	84	76	7	25	1.2	22552	242
NIL-mnz-15	14972	62	2979	165955	268213	30589	139258	16816	158	7676	448	1333	125	137	9	25	0.4	60749	848
NIL-mnz-16	4623	13	4003	169953	281472	29145	108159	10042	105	5319	394	1301	175	233	19	79	6	31015	522
NIL-mnz-17†	21946	39	5828	118967	233235	28461	121322	20595	250	17409	1383	3581	256	154	10	<8	<0.8	82863	4677
NIL-mnz-18	7528	52	15961	137539	250327	30331	152977	21340	411	16744	1422	5044	582	776	71	249	27	39587	1496
NIL-mnz-19†	12611	62	2451	152136	254041	30664	140102	20601	179	12831	770	1775	115	69	4	<5	<0.4	79854	1890
NIL-mnz-20	6858	23	7139	127040	248885	25005	101254	14251	110	8163	681	2653	300	467	36	131	11	53846	3819
NIL-mnz-21	1428	12	7841	142697	268777	25333	86014	10362	390	4961	476	1764	240	434	38	174	13	46946	1572
NIL-mnz-22	12174	61	4134	122378	249328	26710	104801	14102	147	7023	582	1751	186	218	14	33	1	109998	2749
NIL-mnz-23	22366	31	9491	87788	234977	30684	131693	21507	313	13408	1210	4227	459	453	22	25	3	70988	1642
NIL-mnz-24	5725	47	24268	141374	258745	29020	114534	16248	519	9494	1070	5083	823	1775	196	926	88	59795	4982
NIL-mnz-25	7840	30	5997	165327	267983	25494	85593	8807	137	4504	349	1469	257	576	57	262	24	80699	2202
NIL-mnz-26	11417	40	9635	131666	244206	27714	111578	20390	249	15019	1416	4279	373	346	21	25	2	64895	3525
NIL-mnz-27	3097	126	3124	177651	283000	26706	96024	7831	551	3340	293	990	126	220	20	81	6	22300	744
NIL-mnz-28	7764	76	1724	174821	283000	25066	85884	7095	502	2744	179	619	77	144	10	31	5	41373	150
NIL-mnz-29	12316	65	10177	139945	253563	27757	107645	15425	279	9357	934	3114	390	526	43	117	10	49814	7159
NIL-mnz-30	9368	52	5533	161630	265763	27356	98842	11931	504	6995	589	1965	251	315	27	76	5	49357	429
NIL-mnz-31	8390	65	3228	148350	211994	19416	76635	6433	133	3962	339	916	133	224	18	67	4	224755	10036
NIL-mnz-32	7531	48	3873	164042	266933	27686	107269	13304	442	6697	485	1377	165	210	19	55	6	68263	399
NIL-mnz-33	3792	17	10077	145003	265276	29457	111298	14119	147	7304	737	2947	385	625	53	213	20	61221	1854
NIL-mnz-34	6281	41	7177	127765	243241	25593	90371	12976	146	7525	702	2530	315	479	34	100	8	88195	1403
NIL-mnz-35	6342	30	17196	128998	257140	25889	116187	19402	512	11210	1292	4899	645	1071	105	449	42	48442	1557
NIL-mnz-36	11734	88	13310	135108	253913	26808	105873	17620	456	9488	1007	4490	601	917	66	205	12	50003	2578
NIL-mnz-37	3593	37	2229	189462	275325	22220	78740	7469	251	4038	316	921	96	142	9	19	1	49615	172
NIL-mnz-38	13501	71	7433	176123	261247	27231	99313	11838	125	6493	703	2343	308	518	35	174	15	70988	1335
NIL-mnz-39	9467	7	20756	111222	207239	29108	109604	29700	227	17551	2053	7204	803	1381	125	376	36	143750	4131
NIL-mnz-40	6796	60	1911	175433	262331	26021	90790	8030	165	3637	273	853	84	142	8	17	2	73177	697
NIL-mnz-41	3135	4	23399	149096	258429	26094	88452	14248	157	8781	1214	6088	845	1566	162	597	49	74553	2492
NIL-mnz-42	16601	59	19250	138598	234832	27118	105510	20688	693	11787	1614	6175	730	1121	104	406	39	74113	3744
NIL-mnz-43	13501	71	7433	176123	259975	27231	99313	11838	125	6493	703	2343	308	518	35	174	15	70988	1335
NIL-mnz-44	9467	7	20756	111222	269178	29108	109604	29700	227	17551	2053	7204	803	1381	125	376	36	143750	4131
NIL-mnz-45	6796	60	1911	175433	250515	26021	90790	8030	165	3637	273	853	84	142	8	17	2	73177	697
NIL-mnz-46	3135	4	23399	149096	271056	26094	88452	14248	157	8781	1214	6088	845	1566	162	597	49	74553	2492
NIL-mnz-47	16601	59	19250	138598	245990	27118	105510	20688	693	11787	1614	6175	730	1121	104	406	39	74113	3744
NIL-mnz-48	3575	92	5075	163995	274642	27147	99309	10784	307	5272	461	1815	200	288	30	91	7	37073	3869
NIL-mnz-49	2450	41	3480	175378	262092	27202	88243	9240	215	4297	369	1154	139	176	17	34	3	71892	268
NIL-mnz-50	7164	65	29590	152396	253973	27631	96297	16891	239	11857	1812	9005	995	1538	115	317	24	40039	7626
NIL-mnz-51	12374	76	4766	145557	258464	26698	93907	13961	885	7313	538	1702	175	269	18	53	7	49220	966
NIL-mnz-52	11690	149	6560	130364	231272	25481	98490	13576	61	8221	966	3231	245	311	20	45	3	103118	5419
NIL-mnz-53	13810	27	2905	165919	266438	29997	103241	11486	59	5134	373	1245	119	161	9	31	2	88973	1565
NIL-mnz-54	10843	51	2375	181237	258233	24209	89341	7503	241	4450	287	919	103	155	12	35	3	117665	99
NIL-mnz-55	11755	28	17835	149343	245640	26494	95701	14307	276	9028	1056	4483	606	1192	93	324	26	128975	1171
NIL-mnz-56	5792	65	7562	141425	255578	28960	109457	17843	1657	9278	749	2529	275	476	32	98	6	57577	1172
NIL-mnz-57	10234	137	3306	165445	259027	31364	129832	20405	1483	11700	748	1829	152	256	18	54	4	60426	8958
NIL-mnz-58	8783	35	23029	149765	236941	30224	115774	17602	463	11079	1331	5203	756	1461	109	464	41	29365	8889
NIL-mnz-59	13370	50	12028	144516	256500	31880	140829	20860	591	15637	1526	5247	509	645	42	101	8	42619	6659
NIL-mnz-60	18766	70	3890	164178	254511	30279	97353	11227	375	5599	383	1439	161	282	17	74	7	92987	661
NIL-mnz-61	5792	68	3106	172949	276580	30492	102661	12073	369	5268	371	1098	134	151	10	55	4	19206	861
NIL-mnz-62	17565	50	6013	114829	236112	24135	103837	13768	125	8877	695	2241	235	294	20	69	6	105592	1428
NIL-mnz-63	8727	57	30591	142443	244061	27289	111566	15312	677	14122	1783	7409	1051	1506	100	260	15	41449	9001
NIL-mnz-64†	3954	27	2078	137411	264184	30426	113586	15197	356	7363	475	1093	81	96	5	<5	<0.3	54615	597
NIL-mnz-65	7571	62	6898	161052	262459	26259	98602	9804	195	6181	510	2000	274	456	28	134	8	56234	895
NIL-mnz-66	9954	107	3933	134772	243984	26444	108776	15776	162	8220	713	1865	162	152	14	14	2	79738	2591
NIL-mnz-67	13099	59	3080	152060	250003	28907	97749	10920	277	6337	508	1251	115	148	9	9	0.9	83071	3624
NIL-mnz-68	3806	37	16222	146729	284861	30342	102826	12200	675	8314	957	4017	634	1076	77	324	23	58742	3520
NIL-mnz-69	6007	13	2863	130281	285920	37173	140401	15861	257	9186	564	1403	123	136	7	<5	2	1790	682
NIL-mnz-70	12082	43	40601	93783	204063	25461	110476	17881	164	15793	2197	8954	1351	2680	244	944	93	69718	5562
NIL-mnz-71	3982	13	16689	138535	248116	26953	98236	14058	134	9153	1109	4660	656	1383	92	345	28	47266	2690
NIL-mnz-72	18618	60	22253	138129	227046	23105	101419	13251	583	9611	1420	5647	728	1390	109	430	35	103049	4205
NIL-mnz-73	10736	36	4935	141696	254255	23595	101255	12487	238	6478	541	1794	195	332	26	111	7	50176	998
NIL-mnz-74	25038	1156	24387	129803	221274	25711	106442	16682	3554	11829	1482	5525	881	1762	152	690	60	58782	1346
NIL-mnz-75	6937	117	1737	165279	291265	30108	102489	9458	917	4424	268	751	78	133	10	36	5	20635	451
NIL-mnz-76†	11914	31	3255	112586	243771	24779	106150	19544	167	11666	949	2044	148	158	10	<10	<0.8	49674	2054
NIL-mnz-77	9803	73	2509	156569	262280	26782	101776	12005	400	5959	381	1230	126	194	11	24	4	64609	357
NIL-mnz-78†	19924	37	4930	90375	238588	26338	109956	21363	146	12443	1077	2529	222	248	14	14	<0.98	84434	2704
NIL-mnz-79	8304	6	10997	129646	259667	27020	103413	13412	86	9717	968	3679	438	587	31	72	4	29101	2477
NIL-mnz-80	16105	20	21309	110536	243352	26349	96796	17116	423	14408	1570	6110	797	1461	108	499	41	50463	4397
NIL-mnz-81†	19024	27	6977	115921	229590	26949	106036	18210	217	14696	1567	4020	340	352	16	25	<1.1	68698	2682
NIL-mnz-82	2246	22	4332	166257	266941	28787	97410	9658	79	5492	429	1375	213	322	21	78	7	72103	960
NIL-mnz-83	10626	9	9340	147485	297130	27126	91337	10047	111	6233	646	2358	423	801	58	250	19	18763	1816
NIL-mnz-84	19317	90	4506	137649	252248	24772	102522	10908	201	6213	512	1847	234	374	23	110	7	70313	1181
NIL-mnz-85	8153	204	10225	187096	273199	29936	86571	8191	1355	3996	444	2142	373	1002	122	870	101	41047	3312
NIL-mnz-86	20329	82	4485	154520	265174	27235	85726	11814	296	7195	628	1952	241	310	26	100	8	25731	896
NIL-mnz-87	12077	110	2543	143270	263279	31365	93883	14880	259	7735	595	1515	121	155	8	23	4	81324	1752
NIL-mnz-88	17738	142	1111	190613	278014	26260	76646	6477	413	3144	206	433	56	81	5	17	3	60586	137
NIL-mnz-89	5352	20	5714	166728	264448	24061	86477	8426	345	3974	374	1591	261	509	62	351	27	58171	2108
NIL-mnz-90	9493	191	5451	127969	257405	25165	94319	14902	60	7938	828	2553	263	311	11	19	2	56240	910
NIL-mnz-91	7092	37	4310	161251	259556	26249	80041	8540	234	4610	371	1508	190	326	27	62	7	56759	624
NIL-mnz-92	10623	1094	6599	144336	286279	31526	95482	11400	1943	6836	695	2320	305	456	36	181	12	21345	1065
NIL-mnz-93	22434	75	5544	130684	239476	28220	97440	17528	175	10996	924	2476	241	284	22	46	7	93053	3013
NIL-mnz-94	3683	65	7341	141203	248048	28355	109576	18085	456	13042	1270	3450	358	394	20	34	2	61817	3596
NIL-mnz-95	14908	59	3833	192326	262058	29783	81175	8394	328	4689	401	1449	169	192	13	42	5	76990	4579

LA-ICP-MS DATA	ppm	ppm	ppm	ppm	ppm	ppm	ppm	ppm	ppm	ppm	ppm	ppm	ppm	ppm	ppm	ppm	ppm	ppm	ppm
	Ca	Sr	Y	La	Ce	Pr	Nd	Sm	Eu	Gd	Tb	Dy	Ho	Er	Tm	Yb†	Lu††	Th	U
Niger Rver																			
NGR1-mnz-1	2727	7	13297	170636	277750	30358	107324	15290	144	8976	919	3822	505	878	73	301	22	45321	3814
NGR1-mnz-2	3107	8	17648	128030	241064	28910	101174	18446	354	10130	1099	4961	639	1188	103	451	40	101447	2678
NGR1-mnz-3	1449	1	12864	112893	252163	32298	95733	15775	11	4482	336	918	75	144	20	123	11	113725	371
NGR1-mnz-4	2105	4	11924	159724	271867	28461	104198	14721	292	8746	944	4164	529	884	68	217	15	37155	1292
NGR1-mnz-5	8736	68	3652	183607	281745	29735	105947	13678	523	6239	436	1456	153	232	15	41	4	53042	222
NGR1-mnz-6	5222	25	3495	155891	273626	30156	107565	16056	156	7543	518	1505	142	196	13	27	3	61615	963
NGR1-mnz-7	13788	27	23273	151072	264209	29496	105642	17107	260	11344	1335	6658	881	1608	137	555	42	65654	8192
NGR1-mnz-8	8172	27	11590	140457	259633	31393	116228	24762	593	19148	1907	5184	447	511	30	51	3	32070	3932
NGR1-mnz-9	2080	1	26039	127896	257781	33113	122909	23828	33	15150	1652	8062	973	1893	189	796	68	166668	4835
NGR1-mnz-10	6449	15	11764	150600	263108	29081	104867	16229	344	8089	899	3446	380	590	51	169	11	73656	1608
NGR1-mnz-11	4205	6	17235	152342	273891	28224	108378	16341	337	9668	1116	4259	611	1204	146	622	57	32296	990
NGR1-mnz-12	6373	83	3391	174340	258096	24124	77450	6331	266	2997	234	912	129	214	20	107	8	121781	183
NGR1-mnz-13	7917	24	16939	121285	239613	24653	110045	22473	237	18482	1983	6757	563	694	50	107	6	56011	2503
NGR1-mnz-14	3114	39	7800	155995	259411	29225	114631	17008	92	8443	737	2372	306	525	46	150	16	66994	1751
NGR1-mnz-15	4505	34	14139	168192	277494	27474	108755	14985	940	8007	858	3628	521	942	97	457	35	37992	1319
NGR1-mnz-16	4697	57	26711	129950	230017	26854	103191	20377	757	14538	1644	8589	1199	1607	128	448	44	38957	2039
NGR1-mnz-17†	7054	72	9095	135137	238938	27234	115527	21891	220	14003	1505	4449	398	270	18	22	<1.2	61971	2652
NGR1-mnz-18†	8061	9	635	158083	262220	29911	112805	14627	509	6010	269	485	34	29	2	<5	<0.2	37591	585
NGR1-mnz-19	6245	2	11375	158939	272661	28870	114460	15902	132	8054	924	3706	448	595	39	111	10	32745	4238
NGR1-mnz-20	6451	19	14106	156668	269409	29454	117738	18576	1148	12139	1369	4786	578	839	63	230	18	55084	948
NGR1-mnz-21	6673	30	12885	181136	290769	31397	112257	14020	696	8186	783	3549	532	962	88	360	27	57529	1498
NGR1-mnz-22	13540	88	4619	180142	266181	25193	99147	10603	659	5055	392	1477	201	307	22	74	10	47406	220
NGR1-mnz-23	13516	15	4846	158390	259838	26106	95283	14112	207	8441	776	2327	199	218	13	20	0.9	80455	2089
NGR1-mnz-24	26220	130	27099	134061	236198	29593	122264	18919	1211	11891	1355	6541	1009	1885	165	741	66	59534	5584
NGR1-mnz-25	5890	23	6888	162491	266181	32228	117943	14057	98	8817	776	2488	298	473	35	84	8	59200	5224
NGR1-mnz-26	9858	261	5420	173359	256534	30232	114213	14213	1709	6482	701	2104	208	282	22	56	3	48671	5202
NGR1-mnz-27	14262	26	26243	145050	252641	31688	129356	22457	690	15901	1872	8120	969	1653	141	566	43	24483	11301
NGR1-mnz-28	3275	55	7279	159138	278006	30411	117805	14979	458	7920	696	2459	311	469	32	108	7	26965	401
NGR1-mnz-29	12335	78	25464	137084	226269	27198	118202	19371	952	14880	1779	7820	902	1287	91	237	17	52358	8333
NGR1-mnz-30	11719	41	14563	147511	252274	32367	105769	19169	722	16124	1669	5362	602	652	35	89	6	49716	2068
NGR1-mnz-31	4812	81	1811	196853	262698	24773	75535	6420	265	2588	174	623	73	123	9	28	4	101363	397
NGR1-mnz-32	3642	9	8111	183279	275914	31095	104277	13494	414	8553	788	3121	383	655	52	161	10	33640	1256
NGR1-mnz-33	7217	22	20284	115827	221078	27281	100747	27905	178	20730	2082	7430	771	1100	79	273	23	107562	2498
NGR1-mnz-34	8076	273	5252	164732	266344	28315	102323	11969	531	6746	569	1881	215	361	23	75	9	36496	986
NGR1-mnz-35	10647	101	8678	130069	240023	29177	110830	18947	436	13019	1051	3511	424	681	50	120	12	67839	1434
NGR1-mnz-36	2666	63	5985	171380	270083	31277	123279	16108	283	7519	617	2138	250	505	44	157	17	55247	2934
NGR1-mnz-37	10447	92	13370	129564	253341	28012	117026	19528	762	14811	1404	5095	561	657	36	67	4	40341	2996
NGR1-mnz-38†	9781	126	793	137682	271731	30055	107111	18279	2154	9936	439	632	34	42	2	<5	<0.7	51109	4757
NGR1-mnz-39	3253	12	12486	185205	284486	31910	117721	13691	488	8113	825	3574	518	917	87	362	31	36673	1164
NGR1-mnz-40	1917	140	16717	131137	247826	27372	106256	18737	538	13863	1670	5997	737	1215	92	324	21	35170	9289
NGR1-mnz-41	11111	47	15037	155542	256133	29724	105510	17848	679	14131	1186	4079	575	821	56	144	10	77605	2355
NGR1-mnz-42	5340	73	7013	153069	260034	28121	105607	13876	288	8564	683	2319	305	519	41	130	12	65825	3450
NGR1-mnz-43	4309	30	4616	185223	279466	28690	100522	10118	194	5269	414	1581	228	313	23	70	12	59278	310
NGR1-mnz-44	11536	26	3916	194954	281907	26618	79496	9768	323	4546	357	1309	182	324	31	127	10	46333	974
NGR1-mnz-45	10400	16	5941	152304	258336	26824	87514	14381	214	8412	672	2418	282	414	32	90	5	97257	1154
NGR1-mnz-46	4456	8	34828	128170	245777	29089	110545	18494	336	14161	1696	8647	1394	2820	267	952	85	33519	1212
NGR1-mnz-47	12033	23	23540	124260	239732	26905	98054	18378	267	14169	1781	6884	969	1677	145	492	37	75993	3358
NGR1-mnz-48	11723	77	26564	148503	246972	27400	102679	19495	1614	15032	1829	7913	1118	1757	139	497	36	36295	2520
NGR1-mnz-49	12842	112	8348	132360	253640	28381	108845	18920	584	11990	974	3447	362	479	38	64	7	56488	1221
NGR1-mnz-50	9851	31	18827	149718	261904	30822	107417	22608	509	14589	1655	6015	699	1107	99	322	24	104241	2623
NGR1-mnz-51	20102	92	18130	126036	241218	29617	108980	19827	260	13287	1693	6057	716	1246	91	297	30	67507	10613
NGR1-mnz-52†	18839	119	5411	164704	243967	26526	111189	20139	745	12632	1169	2973	257	302	13	16	<0.6	62296	7707
NGR1-mnz-53	11564	42	6440	159191	272269	29449	95979	14332	363	7096	735	2714	325	420	27	67	5	46606	1719
NGR1-mnz-54	4378	43	10721	153955	247322	28044	101744	15365	117	9508	948	3525	450	685	48	176	13	112379	4073
NGR1-mnz-55	20016	104	2340	132754	254938	27071	101603	16928	845	8067	609	1379	108	101	5	<4	0.8	65267	3657
NGR1-mnz-56	8693	52	6819	173848	275189	27467	98229	11137	499	5649	520	2035	271	526	44	191	19	44579	1849
NGR1-mnz-57	13304	41	8040	161739	253128	26995	103458	12892	650	7424	667	2717	355	593	57	199	21	108629	4609
NGR1-mnz-58	6702	44	19732	131933	236078	25579	100165	17784	186	12487	1247	4900	655	1042	122	517	59	79435	3731
NGR1-mnz-59	3270	62	6388	171103	281728	23863	94082	9614	325	4946	493	1912	244	428	34	141	10	39203	2487
NGR1-mnz-60	11411	50	11225	172791	271782	28590	112175	16693	396	11806	1036	4029	476	702	53	139	8	34824	1809
NGR1-mnz-61	11717	44	12294	158985	247339	29004	110521	14783	739	9741	941	3969	483	669	47	150	11	111647	1476
NGR1-mnz-62	10965	56	6762	146699	243933	26482	105173	12015	156	8085	638	2535	307	477	32	105	10	83549	1478
NGR1-mnz-63	17076	296	12975	126325	238093	28119	119559	25760	1115	22520	1978	6644	626	561	37	54	3	57008	4049
NGR1-mnz-64	11582	25	812	134218	255066	26679	119354	15870	287	7575	297	498	42	40	4	<4	0.3	61263	666
NGR1-mnz-65	3798	25	13712	162609	254767	24821	94376	15076	515	10019	949	4511	602	952	108	443	35	37305	4775
NGR1-mnz-66	9354	74	9843	155256	255860	28617	113245	20002	854	10794	821	3292	426	596	59	232	23	60972	2850
NGR1-mnz-67	5482	54	13888	136345	261785	30251	125152	26220	969	19447	1620	5575	607	795	64	176	14	28910	3089
NGR1-mnz-68	8408	41	21952	175114	251728	25707	93201	10922	492	8091	950	4387	739	1482	145	495	46	61581	4848
NGR1-mnz-69	6340	47	5206	148959	255510	28441	109129	13213	575	7408	568	1911	211	292	20	75	9	61808	801
NGR1-mnz-70	13685	152	26093	146398	240603	26979	112044	16546	424	11341	1334	6182	897	1674	154	527	45	44627	12745
NGR1-mnz-71	5176	63	17982	148509	259855	28913	125890	19000	942	13701	1525	5708	704	1069	76	324	20	21748	1889
NGR1-mnz-72	7062	12	3603	147806	268563	27291	113684	14324	241	6533	487	1417	154	244	14	49	4	64818	1084
NGR1-mnz-73	11326	170	3286	177139	277972	32568	125283	16240	1317	6896	456	1237	134	255	19	72	7	36503	1370
NGR1-mnz-74†	3761	118	1753	167670	279201	31081	136884	18936	1463	9592	507	1040	75	71	2	<6	<0.4	50048	3436
NGR1-mnz-75	15147	25	4527	191539	283282	29324	93469	9505	181	4919	424	1265	192	326	23	104	8	52737	487
NGR1-mnz-76	9138	42	20291	155314	249209	32132	126893	20078	256	14883	1828	6770	850	1103	83	239	20	67486	2768
NGR1-mnz-77	10749	113	5238	153932	271680	30332	118745	14608	326	6960	582	1695	237	391	23	86	6	32955	231
NGR1-mnz-78	6254	78	6627	177704	262570	27187	99894	12847	942	5614	521	1623	249	412	39	126	14	46598	1900
NGR1-mnz-79	12690	44	4078	163074	263876	27638	105232	10721	511	5148	393	1392	164	243	23	122	12	66589	507
NGR1-mnz-80	11697	86	5622	145099	261418	35264	129052	20094	295	9994	771	2207	210	330	19	50	4	55886	2258
NGR1-mnz-81	6627	51	10940	148640	247416	29923	107225	17977	341	12260	1413	4276	468	487	23	69	2	39786	3488
NGR1-mnz-82	14906	279	28016	144683	239937	25376	104962	16411	2285	11662	1432	5878	1061	1822	173	935	81	43620	13282
NGR1-mnz-83†	15641	93	11247	148462	243993	28591	126909	18465	932	16332	1698	5010	518	496	32	55	<0.8	50891	14721
NGR1-mnz-84	3186	17	2275	163888	289753	31941	106560	10169	198	3960	289	851	96	139	8	15	2	53765	183
NGR1-mnz-85	17957	26	14459	131619	244095	26825	98331	16356	293	11157	1306	4448	604	841	53	180	14	72841	8137
NGR1-mnz-86	7589	23	5332	174656	267325	29717	110801	13002	277	6490	531	1813	243	355	23	116	8	68918	225
NGR1-mnz-87	11817	15	21817	139768	243011	25592	101065	17789	247	13702	1593	5980	798	1271	138	693	47	58591	6245
NGR1-mnz-88	1103	140	8514	159707	260914	32797	134978	20740	604	14523	1329	4064	458	475	28	49	4	52217	599
NGR1-mnz-89	4989	43	4163	166225	258037	30390	113104	14690	289	8543	791	1974	203	186	14	33	3	54920	5998
NGR1-mnz-90	5229	3	23832	149786	251839	31191	119621	20697	96	14636	1710	7227	1175	1663	144	428	33	46354	1118
NGR1-mnz-91	28698	53	19650	135940	235694	28697	132277	18333	1844	12846	1502	5351	804	1119	102	339	22	55480	3921
NGR1-mnz-92	3951	132	730	172517	287926	32064	119286	12380	307	4150	182	374	45	39	3	10	1	35896	981
NGR1-mnz-93	18010	130	22675	137744	229393	26725	106025	16979	295	14632	1582	6482	954	1397	105	419	28	74199	9459
NGR1-mnz-94†	4574	725	319	343717	258592	17818	44484	2250	357	715	51	118	14	14	1	12	<0.13	41157	111
NGR1-mnz-95	13886	146	9161	153065	215085	28783	121175	16922	223	11492	1027	3378	436	458	40	128	10	172040	4530
NGR1-mnz-96	6069	232	4095	173846	274335	29456	131854	15301	595	8398	637	1738	175	171	14	<5	2	48791	1951
NGR1-mnz-97	6212	43	31942	144376	220438	23948	93615	12017	505	10003	1215	6216	1058	2134	242	1119	95	81709	7767
NGR1-mnz-98	8324	54	19001	147143	254075	25212	81011	11487	574	8282	979	4960	735	1371	133	571	40	44077	10801
NGR1-mnz-99	9557	81	29615	140785	246767	29416	98261	19250	484	16177	1942	8125	1064	1731	122	404	31	34968	2802
NGR1-mnz-100	11856	66	1591	169033	260666	26991	82116	10196	185	4232	284	756	69	113	9	8	2	78735	1167
NGR1-mnz-101	790	15	2426	178516	295960	28865	88609	10245	339	4218	306	875	109	126	9	14	2	25249	975
NGR1-mnz-102	3345	57	8277	173141	274173	32281	104867	15115	633	8071	767	2878	368	621	41	169	14	39752	1274
NGR1-mnz-103†	17667	174	885	165063	259240	28422	99971	14996	908	6685	367	615	33	32	1	<7	<0.5	74558	5787

LA-ICP-MS DATA	ppm	ppm	ppm	ppm	ppm	ppm	ppm	ppm	ppm	ppm	ppm	ppm	ppm	ppm	ppm	ppm	ppm	ppm	ppm
	Ca	Sr	Y	La	Ce	Pr	Nd	Sm	Eu	Gd	Tb	Dy	Ho	Er	Tm	Yb†	Lu††	Th	U
Congo River																			
CNG2-mnz-1	18473	24	12065	141498	225278	24276	80064	15584	143	9336	1034	4135	454	645	47	138	11	66545	8777
CNG2-mnz-2	5500	22	7197	145104	260854	23649	89518	12054	171	7526	759	2968	341	508	36	141	10	60799	659
CNG2-mnz-3	21064	12	22839	88103	199606	21755	85504	21872	72	16829	2113	8219	878	1339	117	417	31	103516	7518
CNG2-mnz-4	14961	39	9046	121526	246998	25301	111132	21133	299	16229	1549	5008	389	467	21	44	2	56650	4432
CNG2-mnz-5	6864	27	4571	129462	266446	24221	87713	11572	178	5694	529	1913	199	313	21	59	5	84301	2578
CNG2-mnz-6	3988	40	6495	136975	257106	25707	114602	14206	692	8187	684	2886	372	657	59	260	22	43450	711
CNG2-mnz-7	5532	25	4805	140241	256688	22522	82701	9097	188	4859	461	1725	207	318	33	102	8	72346	1067
CNG2-mnz-8	7639	34	21874	128371	244163	25787	110156	16976	143	11518	1373	6510	803	1588	123	533	43	52684	1777
CNG2-mnz-9†	6185	20	1397	140753	272269	29076	117491	14523	94	5921	385	1066	57	57	3	<4	<0.3	42214	665
CNG2-mnz-10†	6437	46	4823	127644	253367	22278	101620	14411	624	9169	759	2543	233	238	11	<7	<0.6	37521	2419
CNG2-mnz-11†	5183	23	435	137088	269682	24459	98100	8432	83	2768	117	286	18	27	1	<2	<0.1	49819	327
CNG2-mnz-12	2498	16	5753	149305	273268	26895	104695	18319	1711	13193	1047	3722	328	395	24	40	1	4019	98
CNG2-mnz-13	8991	25	19165	121517	240390	24333	99266	18207	299	14514	1543	6414	755	1120	90	256	19	53944	5198
CNG2-mnz-14	9241	34	7502	132485	254067	27241	105814	14017	322	10810	996	3474	314	368	21	44	3	57158	4461
CNG2-mnz-15	7298	20	9053	131902	237248	21353	69033	10542	191	6201	658	2918	353	646	57	187	18	46178	2995
CNG2-mnz-16	16885	39	21693	132978	235942	24240	88538	14884	182	11761	1183	6192	793	1447	130	480	36	75727	3675
CNG2-mnz-17	2191	42	1584	219868	291205	21722	67607	5053	737	2849	184	620	68	94	7	18	1	2965	217
CNG2-mnz-18	13173	93	20889	141587	233893	25951	105098	17700	1622	13097	1387	6132	762	1486	120	414	35	41218	2368
CNG2-mnz-19	15456	77	12698	147836	245444	22226	76222	11818	1275	9220	785	3469	447	891	88	483	44	66918	734
CNG2-mnz-20	12278	85	17789	123269	234917	25482	95285	16936	1833	12979	1390	5357	752	1231	100	369	35	49800	12526
CNG2-mnz-21	7489	26	19258	119568	232057	28264	110129	22114	392	22315	2369	7547	810	956	50	93	7	43565	3980
CNG2-mnz-22	16595	15	31123	113065	231886	27816	92129	16226	172	14635	1682	7707	1195	2361	190	694	64	104456	3041
CNG2-mnz-23†	6283	123	3032	128030	254186	27853	105092	18084	1369	11383	631	1692	144	172	6	<6	<0.5	41293	4372
CNG2-mnz-24	12622	85	2841	161225	263296	24221	75141	8136	168	5230	355	1283	156	231	16	37	4	54753	2262
CNG2-mnz-25	18199	243	10887	111390	242806	27303	99898	16780	2003	14868	1501	5530	610	754	55	192	14	78403	3744
CNG2-mnz-26	5008	39	3032	146965	267104	27192	85741	10034	400	5104	376	1115	152	235	22	52	5	52404	713
CNG2-mnz-27†	5384	102	1800	135289	280123	29816	112778	17902	1490	14189	977	1965	111	53	2	<7	<0.6	28002	5156
CNG2-mnz-28†	7862	86	5990	123360	254349	29893	110791	14385	271	11407	937	3095	283	262	13	<7	<0.9	55234	2070
CNG2-mnz-29	10434	20	18273	125620	244701	28620	99286	17842	66	13965	1328	5538	674	1047	78	249	18	69158	3424
CNG2-mnz-30	13925	94	17249	147363	253478	26418	76827	11531	204	9415	1014	4700	607	965	80	245	22	65372	5927
CNG2-mnz-31	14892	21	6844	132781	259599	24507	93295	11123	113	7012	671	2754	296	452	42	120	10	58998	2009
CNG2-mnz-32	19472	127	20716	133977	237692	28166	91444	15212	2694	12656	1215	5839	817	1466	140	477	45	47945	362
CNG2-mnz-33†	12034	14	5917	118273	242217	27321	100710	18601	232	15231	1190	3381	253	212	12	<9	<0.9	64296	2430
CNG2-mnz-34	19940	28	20968	119018	237035	24471	88158	13383	189	10963	1141	5589	768	1237	138	506	40	68370	11629
CNG2-mnz-35	13877	286	249	137416	261520	27026	103755	16444	2171	9296	351	459	13	9	1	<6	0.6	72920	3886
CNG2-mnz-36†	7997	42	1410	140277	265387	31064	111648	17980	326	10221	586	1246	75	69	6	<5	<0.4	45908	2841
CNG2-mnz-37	11197	184	6443	122882	242396	26865	105216	13351	1688	10468	987	3503	286	319	21	61	3	41043	5140
CNG2-mnz-38	17220	20	10667	140662	254400	29081	97555	13376	114	9466	869	3664	449	708	58	175	16	69446	2617
CNG2-mnz-39	9474	74	23330	119843	250805	28230	106769	13743	2379	11603	1380	6813	1002	1471	127	493	36	40699	2563
CNG2-mnz-40	9431	9	5051	133807	240373	30772	112166	17756	842	11238	850	2522	180	182	11	<7	3	53774	2135
CNG2-mnz-41	14284	42	1107	122804	248022	32994	111098	14864	164	7117	325	678	38	56	2	<4	0.4	79577	3259
CNG2-mnz-42	4635	12	5657	157359	274915	27719	95372	10016	262	5771	452	1666	207	338	32	118	11	42730	703
CNG2-mnz-43	19575	41	20498	114778	217364	28237	98234	21182	386	16462	1795	6763	714	1141	119	435	35	53411	21942
CNG2-mnz-44	6884	10	6176	151374	275334	27217	91563	11095	136	6183	543	2343	256	423	46	145	12	35572	2591
CNG2-mnz-45	10901	62	1987	134635	270373	33029	111918	19592	1048	14292	930	1801	73	54	4	<5	0.8	36371	13556
CNG2-mnz-46	12475	60	16124	140336	241807	30213	107609	16097	2114	14332	1488	6168	570	680	42	101	6	65595	4187
CNG2-mnz-47	8099	16	8309	161848	272875	30729	104426	11639	106	7373	703	2725	347	450	33	93	6	35217	490
CNG2-mnz-48	8286	61	6105	164858	263842	28919	95646	11244	153	6364	493	1860	237	411	32	92	7	66304	2014
CNG2-mnz-49	9508	24	1499	119195	258267	29970	109940	15921	100	5806	309	801	61	85	5	5	0.5	64534	3509
CNG2-mnz-50	23916	55	13645	116276	234892	23923	82986	14155	394	9203	822	3834	420	913	81	344	21	77352	7798
CNG2-mnz-51	7260	151	2563	175477	283239	29825	107043	8974	1559	4587	278	928	93	187	10	37	4	27131	555
CNG2-mnz-52	14282	141	26156	137385	252095	29057	110694	17320	2423	13074	1343	6943	972	1895	142	652	51	17165	863
CNG2-mnz-53	15717	76	19405	141460	242951	25777	112481	14344	1235	11946	1341	6303	716	884	64	182	13	48671	11504
CNG2-mnz-54	4170	9	9332	148705	289412	30080	103101	14075	1146	8020	724	2762	389	749	60	268	23	15275	1680
CNG2-mnz-55	10000	28	31568	134419	223989	24072	86693	14586	1685	11215	1379	6828	1107	2329	204	884	76	57345	4630
CNG2-mnz-56	21127	65	2384	145145	246836	25572	85076	15321	465	9628	669	1468	87	92	2	<7	1	93353	3138
CNG2-mnz-57	15567	34	19980	122061	242405	26568	100998	19021	365	13366	1287	5387	654	1329	136	528	39	47434	6236
CNG2-mnz-58	6814	24	20935	130155	228207	21326	72597	11641	112	10228	1212	6225	890	1534	125	435	25	66767	4720
CNG2-mnz-59	8403	25	22185	126780	243967	24865	92001	15335	384	12329	1270	5942	800	1324	118	528	46	40828	4980
CNG2-mnz-60	9693	45	33126	116553	232749	26443	100291	16723	2203	14682	1717	8292	1109	1849	118	310	24	44883	2050
CNG2-mnz-61	9742	14	5965	129346	257789	24971	86004	14155	181	9155	774	2757	266	292	12	6	1	48696	3717
CNG2-mnz-62	8297	102	2366	178705	270237	23540	76832	7738	249	4472	301	899	108	187	12	30	5	53231	2176
CNG2-mnz-63	20699	32	12671	113498	226294	22462	83110	15938	127	11235	948	3699	475	918	76	211	24	89345	3867
CNG2-mnz-64	6096	12	5105	140015	266779	26339	89034	11075	122	6900	592	2208	260	387	31	78	4	87784	3615
CNG2-mnz-65	5452	44	3437	137418	269631	28762	101043	15845	614	10107	641	1771	159	180	9	<6	0.9	42465	5818
CNG2-mnz-66	17267	28	7546	111217	220105	22220	74158	12615	394	8633	764	2758	357	605	47	185	14	92441	4234
CNG2-mnz-67	16569	172	21155	129526	243403	26070	98232	17121	2289	15197	1458	6384	886	1626	121	457	32	56786	2923
CNG2-mnz-68†	4958	130	627	122127	254733	26635	100350	18141	2556	13454	687	989	24	5	<1	<5	<0.6	36772	2664
CNG2-mnz-69	13323	24	9792	115182	231528	25256	90263	17181	101	12650	1062	4027	448	539	44	120	8	96821	2764
CNG2-mnz-70	1170	22	146	167955	290795	25533	79391	6268	761	2393	71	122	9	23	0	3	1.0	2536	<7
CNG2-mnz-71	1055	8	4179	150219	288037	25167	77217	10307	122	5301	363	1512	192	355	23	92	8	34297	520
CNG2-mnz-72†	8910	42	2887	138388	267121	29740	114825	20286	658	14414	831	2180	136	85	3	<7	<0.6	29162	5228
CNG2-mnz-73	2644	19	6163	130577	284639	25656	90865	19795	995	10566	867	2919	236	320	25	37	3	11524	517
CNG2-mnz-74	11846	110	14649	109879	233380	23856	90129	24808	1087	19024	1800	6218	597	711	46	102	8	49226	4471
CNG2-mnz-75	9530	86	3442	141019	264687	22278	76514	7805	438	4752	346	1214	155	219	22	77	7	61854	357
CNG2-mnz-76	7517	11	22667	130360	236292	26347	81872	16820	107	10794	1273	6240	862	1443	138	610	49	76540	4978
CNG2-mnz-77	8750	10	2014	142156	274864	34221	138310	19552	166	10258	538	1211	93	113	5	<6	0.5	23012	2076
CNG2-mnz-78	8005	52	8445	139962	253051	29701	113142	17898	1251	13883	1344	4298	325	257	16	20	2	41694	6385
CNG2-mnz-79	20401	41	36275	121134	222922	25759	94738	19720	192	16390	2398	8979	1348	2115	156	491	35	52410	3903
CNG2-mnz-80	18333	10	26521	111956	224134	23746	82318	16623	66	12672	1887	7683	1051	1429	98	315	26	81542	9380
CNG2-mnz-81	18673	47	29078	103999	217467	27156	98081	18026	460	15504	2317	9470	1019	1104	75	137	6	48746	27237
CNG2-mnz-82	14474	41	8597	122683	241303	26381	95959	19341	269	11756	1135	3376	386	542	38	116	9	68551	4974
CNG2-mnz-83	8953	9	25072	97251	208451	24294	104853	23650	52	23965	2809	9153	790	924	52	111	1	69665	7087
CNG2-mnz-84	1918	9	22045	115687	243873	26077	104275	19942	593	16475	2069	8390	864	988	70	162	17	22362	3010
CNG2-mnz-85†	13780	45	6445	127552	235037	23543	82343	13272	121	8578	897	2677	256	216	13	12	<0.6	75324	6442
CNG2-mnz-86	939	54	2814	178176	283931	27201	85726	8754	359	4418	393	1079	125	128	11	20	1	63102	171
CNG2-mnz-87	16281	32	9228	141329	252547	27134	90544	12237	225	6978	759	3017	390	654	53	217	23	73531	4619
CNG2-mnz-88	10671	76	3640	162865	243728	21905	75377	9782	195	5083	433	1488	165	258	16	56	2	108734	3856
CNG2-mnz-89	14961	32	18903	137188	248637	25942	109580	17059	1793	11984	1446	6066	744	1080	79	318	21	49137	4363
CNG2-mnz-90	19998	200	24761	120737	227037	23218	75102	13617	215	9729	1382	6043	872	1657	154	487	39	74919	10378
CNG2-mnz-91	10813	64	7963	121695	225594	23758	101442	12986	652	7552	710	2897	377	601	52	188	19	90757	2291
CNG2-mnz-92	7099	70	2667	141041	259983	29796	117307	18710	1422	10497	631	1796	121	112	5	<6	1	44302	6991
CNG2-mnz-93	14404	46	5935	155764	269699	24892	91669	9652	226	4505	450	1888	276	474	32	111	9	42187	4466
CNG2-mnz-94	13599	58	18989	123517	238605	25202	117687	17680	2242	11432	1451	5920	812	1327	90	372	32	45347	6902
CNG2-mnz-95	14748	147	4326	174354	267257	27333	87404	10710	354	5843	474	1627	203	315	31	133	11	59222	5342
CNG2-mnz-96	12913	20	13043	133255	248628	26311	92291	13837	126	8825	993	4014	515	710	41	143	12	63646	3172
CNG2-mnz-97	1422	23	2938	173601	300237	28561	90694	11518	2123	6518	484	1382	120	137	6	15	2	3025	731
CNG2-mnz-98	16985	52	20472	119847	228164	22588	90844	16254	283	12329	1283	5587	812	1611	111	441	37	76605	4576
CNG2-mnz-99	10553	125	5647	164618	257234	28100	96951	9994	672	5598	460	1852	241	420	29	86	7	88894	662
CNG2-mnz-100	24089	30	26078	117681	234994	21693	81897	11853	201	7880	1238	5929	877	1763	129	501	41	72086	15034
CNG2-mnz-101	15493	82	11839	143872	262416	28146	108820	16926	1445	13432	1418	5452	530	763	55	212	15	45917	3159
CNG2-mnz-102	16111	24	24831	148827	240595	27276	89322	12345	431	8312	1131	5547	887	1780	158	539	43	64890	8735

LA-ICP-MS DATA	ppm	ppm	ppm	ppm	ppm	ppm	ppm	ppm	ppm	ppm	ppm	ppm	ppm	ppm	ppm	ppm	ppm	ppm	ppm
	Ca	Sr	Y	La	Ce	Pr	Nd	Sm	Eu	Gd	Tb	Dy	Ho	Er	Tm	Yb†	Lu††	Th	U
Zambezi River																			
ZMB2-mnz-1	27304	62	4078	123036	240373	25291	96143	11736	62	7582	517	1831	178	219	10	18	1	95314	762
ZMB2-mnz-2	10677	22	14781	120262	241414	25365	102525	15086	931	10434	1284	5576	585	813	41	118	8	57616	7120
ZMB2-mnz-3	8842	58	4890	158542	277494	25929	103913	10547	233	4850	447	1632	229	393	36	142	11	50055	5557
ZMB2-mnz-4†	20685	87	1029	153038	271714	27024	93650	10441	97	5403	307	703	43	50	4	<3	<0.2	82423	1411
ZMB2-mnz-5	26687	60	3986	120257	234943	24720	93972	11471	60	7410	505	1790	174	214	10	18	1	93161	745
ZMB2-mnz-6	10472	22	14498	117957	236787	24879	100560	14796	913	10234	1260	5469	573	798	40	116	8	56511	6984
ZMB2-mnz-7	6534	43	3614	117155	205053	19160	76786	7794	172	3584	331	1206	170	291	26	105	8	36988	4106
ZMB2-mnz-8†	20539	86	1022	151957	269793	26833	92988	10367	97	5365	304	698	43	50	4	<3	<0.2	81841	1401
ZMB2-mnz-9	15708	83	12003	145862	266045	28536	110325	17160	1465	13618	1437	5527	537	774	56	215	15	46552	3203
ZMB2-mnz-10	8141	99	8668	181930	277664	28572	97907	13308	2243	7153	682	2466	347	537	38	113	9	24293	2068
ZMB2-mnz-11†	17146	48	980	122590	250208	24558	96211	11865	196	4956	263	523	27	39	2	<3	<0.2	82603	2428
ZMB2-mnz-12	7298	54	7998	120299	254630	25840	92093	9490	293	4959	478	2101	306	635	57	255	21	64127	3163
ZMB2-mnz-13	2922	16	1718	181378	280883	20124	58021	4595	512	2898	173	562	78	114	10	43	2	39856	406
ZMB2-mnz-14	8265	60	7101	176130	272772	24160	79452	7594	1096	4873	420	1704	249	613	54	254	20	32435	2876
ZMB2-mnz-15	27437	46	3539	98163	191948	17912	68269	9267	79	6228	527	1599	136	132	6	18	0.4	183706	2759
ZMB2-mnz-16	5624	53	1100	123761	278151	26245	103696	9783	256	4184	256	652	54	60	3	<3	1	60896	1222
ZMB2-mnz-17	9362	81	18752	119387	252129	25221	97458	16119	1116	12518	1376	6200	717	1331	97	363	32	64646	5454
ZMB2-mnz-18†	16948	67	792	111515	241730	25659	112063	17532	223	7594	299	526	27	42	1	<5	<0.2	85755	2531
ZMB2-mnz-19	810	6	4608	102872	244616	23576	91657	9442	112	5786	445	1606	198	302	22	95	10	59333	1787
ZMB2-mnz-20†	8722	18	506	144968	274164	26483	90093	9371	59	3621	152	315	19	31	2	3	<1	71836	382
ZMB2-mnz-21	10573	43	13185	139058	255621	22859	83309	10742	1245	7700	772	3486	472	947	68	249	22	66804	952
ZMB2-mnz-22	3303	217	799	172050	279611	21703	61275	3834	386	2227	109	312	35	53	4	18	3	29000	213
ZMB2-mnz-23	3807	13	9377	115562	240962	23830	101480	16058	285	11944	1174	4117	398	481	27	30	2	41192	2124
ZMB2-mnz-24	4119	47	21181	115464	242490	23286	95273	16568	2501	13511	1619	6515	740	1101	77	303	19	32269	4108
ZMB2-mnz-25	5062	34	10987	144082	285596	27333	101054	14236	2263	8470	793	3768	397	842	54	255	22	7572	506
ZMB2-mnz-26†	9488	86	177	176184	291179	24626	75511	6295	203	1888	82	167	9	18	0	<2	<0.6	30350	1342
ZMB2-mnz-27	12972	9	3573	112847	250020	22786	75006	10661	36	5309	401	1690	120	206	12	30	2	109346	1086
ZMB2-mnz-28†	11073	84	3551	125670	259377	22577	85546	13469	1533	11125	880	2254	114	152	3	<2	<0.1	68960	4198
ZMB2-mnz-29†	1933	6	1648	135829	288456	29870	109541	14952	263	7330	357	1101	65	97	5	<4	<0.6	5537	5972
ZMB2-mnz-30†	13521	55	1364	133413	262186	27084	93859	14470	278	7362	421	896	42	57	2	<5	<0.4	64413	4291
ZMB2-mnz-31	3551	29	2224	156883	267112	22559	79984	9173	98	5654	391	1280	80	88	4	<3	0.4	78476	2296
ZMB2-mnz-32	5699	19	5582	124906	265285	23526	80936	10653	203	6307	487	1954	212	438	29	119	10	80731	894
ZMB2-mnz-33	5372	48	12513	127308	238648	20455	74502	9124	362	5918	600	3145	408	1113	86	359	41	89712	2506
ZMB2-mnz-34†	10146	40	977	121922	252914	25321	94291	11131	119	5050	282	670	41	58	3	5	<1.4	101729	953
ZMB2-mnz-35	7374	40	10286	147872	264679	25515	87613	11587	1259	6232	652	2737	321	579	51	245	23	29860	6265
ZMB2-mnz-36	12614	37	2185	127682	254758	26865	99497	15239	189	8390	704	1502	87	78	2	<5	0.5	66301	3610
ZMB2-mnz-37	18034	102	7099	141587	229137	19574	74955	8001	252	5439	551	2272	288	565	42	171	14	121073	2271
ZMB2-mnz-38†	8454	54	647	114816	256065	24309	96965	14982	350	6586	337	565	28	34	1	6	<2	56608	2084
ZMB2-mnz-39	15337	60	6860	131670	246938	24635	92372	11087	332	6228	582	1997	268	546	53	196	17	83459	1919
ZMB2-mnz-40	3801	40	605	152580	278603	25234	86465	9270	82	3209	168	386	23	39	2	<3	0.8	55455	795
ZMB2-mnz-41†	6579	69	926	157733	276742	24568	91652	10183	269	4570	276	650	33	25	0	<3	<0.2	39806	1641
ZMB2-mnz-42†	5469	31	805	148623	266002	28916	109358	13760	121	5885	311	731	30	57	3	<4	<0.3	73912	1050
ZMB2-mnz-43	22670	57	3325	127973	256082	26888	101368	14646	199	8262	627	1737	141	188	10	42	3	62873	1466
ZMB2-mnz-44	11994	18	3327	169615	294517	29084	106081	13142	157	5044	355	1070	129	191	15	43	4	5598	967
ZMB2-mnz-45	1242	45	4839	184842	278954	26751	89502	9252	465	3837	351	1211	192	349	29	121	8	40963	1592
ZMB2-mnz-46	18794	51	3231	127548	258822	30386	110326	14519	360	5944	486	1192	129	155	8	17	1	88082	3392
ZMB2-mnz-47	15376	50	3840	128220	217919	24359	84176	14155	405	6165	547	1518	158	213	10	29	0.8	227932	1920
ZMB2-mnz-48	13936	17	1158	163507	259855	27898	87429	8340	161	3330	219	534	62	52	4	9	2	88761	303
ZMB2-mnz-49†	10680	33	434	145385	268350	30807	113296	13691	142	4641	245	350	25	25	2	3	<1.7	75641	433
ZMB2-mnz-50†	19621	51	999	112663	227635	22175	85180	11078	119	4589	286	520	46	44	3	13	<1.7	103591	2179
ZMB2-mnz-51	7030	51	1242	137787	253452	29008	97069	11811	65	3634	212	582	45	54	5	10	2	96576	759
ZMB2-mnz-52	14635	33	1286	129056	252171	29492	113096	20100	293	9730	593	942	57	42	1	<6	0.6	56365	2501
ZMB2-mnz-53	2806	181	2186	177835	296233	27245	98542	7994	1166	2704	202	650	86	160	10	52	6	328	511
ZMB2-mnz-54	5667	104	2192	161937	270587	26005	86067	9284	226	4178	291	887	105	126	8	6	1	46913	2431
ZMB2-mnz-55†	14463	42	10521	142273	259838	29388	97330	16455	1141	9882	1254	4157	444	408	17	18	<0.7	40480	4735
ZMB2-mnz-56	7502	131	9366	133744	245461	28168	95852	16979	2640	9843	1083	3244	359	533	39	131	10	39300	10298
ZMB2-mnz-57	12473	66	714	148723	264303	30242	100581	12485	260	4154	229	405	29	22	1	<3	2	69786	2711
ZMB2-mnz-58†	8772	50	1321	122847	260000	31073	113517	11265	384	3386	228	540	59	83	6	12	<2.9	89706	263
ZMB2-mnz-59†	14761	29	450	103823	222973	29386	104520	9779	95	3193	142	249	21	29	2	8	<1.1	169408	656
ZMB2-mnz-60†	5847	23	843	142484	262877	28574	95707	13502	166	6052	379	624	34	22	2	<3	<0.2	117651	2034
ZMB2-mnz-61	4266	7	1005	118683	260538	28077	91933	11137	92	3692	243	589	42	34	2	<3	0.6	112083	3744
ZMB2-mnz-62†	12469	59	9528	136932	232868	24858	88464	13140	593	9107	926	3241	401	479	28	49	<0.5	91049	2839
ZMB2-mnz-63	12236	33	5838	132934	233748	24971	78163	11433	87	4464	469	1483	229	413	32	136	12	138399	4568
ZMB2-mnz-64†	4430	32	908	143365	259480	27423	90298	10633	58	4526	316	583	41	46	3	8	<1.2	44834	321
ZMB2-mnz-65	6999	27	635	133085	258856	32619	113192	13351	80	4710	208	423	25	42	4	<3	1	95101	1633
ZMB2-mnz-66†	10900	83	780	147636	268299	32727	122811	17411	333	7408	434	708	35	22	1	<5	<0.2	51368	2602
ZMB2-mnz-67	4658	79	1984	154423	265268	32250	123886	13648	373	6205	439	922	80	83	7	17	2	68036	1341
ZMB2-mnz-68	8585	446	10036	133752	276597	31638	116570	15731	1589	8583	1021	3646	480	724	57	141	16	45867	1844
ZMB2-mnz-69†	16948	30	1332	155440	264833	28189	108929	12957	161	5054	337	735	53	66	3	<4	<0.3	84971	2492
ZMB2-mnz-70	1761	28	4533	140269	258455	26634	100534	10629	169	4833	500	1691	193	273	20	48	3	68221	605
ZMB2-mnz-71	21635	94	6704	128203	248833	28830	125167	18403	2043	10551	1152	3310	340	360	16	53	7	50781	3336
ZMB2-mnz-72†	12426	18	5009	122043	234559	26732	97568	17032	324	8649	1070	2705	194	159	7	<4	<0.5	95853	19301
ZMB2-mnz-73	9126	41	10249	138398	245879	27203	96559	14261	67	8051	1020	3897	416	423	20	15	1	82921	2920
ZMB2-mnz-74	6826	33	3185	145944	258788	28056	96131	11015	49	5179	451	1364	125	152	10	23	1	75010	656
ZMB2-mnz-75	17147	18	30290	117363	211977	26206	112256	18480	1963	14748	1932	8713	1123	1894	121	417	28	70899	8541
ZMB2-mnz-76	10810	20	9431	147110	273891	29036	108980	14656	152	8410	906	3312	426	607	43	124	8	43916	1062
ZMB2-mnz-77	<4800	83	30319	113226	215426	24353	109843	17859	2124	10790	1457	6698	979	1770	140	585	50	95294	4641
ZMB2-mnz-78†	15476	31	641	152787	263595	26976	104542	9448	132	3092	164	369	26	33	2	<2	<0.2	90457	1067
ZMB2-mnz-79	14463	101	19008	130906	241995	25087	98787	14072	1162	8545	1009	4961	679	1272	98	432	41	46273	10532
ZMB2-mnz-80	7166	66	20663	133664	245239	26382	109897	18072	2547	13209	1653	7398	854	1324	84	307	25	44003	8958
ZMB2-mnz-81†	23982	41	1629	114989	253059	28101	112445	14487	143	6733	452	1000	72	70	6	<4	<0.3	138405	9924
ZMB2-mnz-82†	7166	28	2269	142189	256261	27153	111237	14343	174	6264	533	1445	86	90	3	<3	<0.3	76275	2285
ZMB2-mnz-83	23321	41	14295	123695	220250	21704	88792	12069	515	8352	917	3493	500	742	56	172	18	109533	6062
ZMB2-mnz-84†	15118	74	741	115769	207674	21894	83670	12831	235	6379	295	559	26	19	2	<3	<0.2	116552	2436
ZMB2-mnz-85†	16520	67	334	146446	255014	26861	87762	9711	356	3962	172	234	17	20	1	2	<0.7	94779	892
ZMB2-mnz-86	15348	19	14264	124246	242524	26161	114134	19289	361	15115	1414	5509	564	779	55	156	16	56674	3500
ZMB2-mnz-87	3790	7	1063	124565	245154	27369	82522	10506	26	5085	301	725	50	37	3	2	1	141240	1017
ZMB2-mnz-88	3001	16	23614	154320	260564	28922	111990	14808	782	8305	1023	5187	909	1839	165	696	61	38463	967
ZMB2-mnz-89	1937	150	3076	200948	297710	26884	99765	9027	1106	4827	379	1226	150	184	16	75	4	6317	101
ZMB2-mnz-90	11496	10	24317	118854	227584	23730	86952	16526	268	8978	1136	4394	553	943	74	326	21	109109	1782
ZMB2-mnz-91	9423	29	184	174873	265635	22430	84580	6393	112	2172	65	182	6	11	0	<2	0.3	95802	626
ZMB2-mnz-92	16184	37	19267	139769	244394	25353	100687	15506	1480	9328	1121	4928	700	1237	108	454	29	50973	2948
ZMB2-mnz-93†	14663	20	2271	132449	271577	30779	117058	19713	517	7461	554	1432	84	102	8	<6	<0.6	45357	2286
ZMB2-mnz-94	11280	47	1751	157190	260163	32147	134520	18775	242	8870	590	1274	72	54	2	7	1	62866	1042
ZMB2-mnz-95	6052	482	10912	149563	255544	27096	130027	16503	2332	9212	811	3417	440	649	62	201	16	50885	1432
ZMB2-mnz-96	5054	23	6537	126354	252052	25503	102432	16009	73	10092	822	2470	258	369	30	78	9	68701	1690
ZMB2-mnz-97†	8946	282	14773	131730	294816	21488	87618	11943	2163	8358	1015	4721	450	481	25	48	<0.8	24426	4779
ZMB2-mnz-98	6690	183	2116	124005	233645	21827	89718	7209	342	2682	192	737	89	142	11	46	4	112428	1874
ZMB2-mnz-99†	9590	24	391	177882	282454	29732	106434	10918	224	4852	278	412	21	27	1	<3	<0.2	48673	3611
ZMB2-mnz-100	5131	109	948	156550	276307	23916	112827	11165	912	4236	231	420	36	44	2	5	1	36291	2613
ZMB2-mnz-101	16570	45	1259	137194	251898	26486	115294	15725	243	7568	442	803	42	44	2	<4	0.6	62881	4056
ZMB2-mnz-102†	4024	26	1713	148125	278894	26336	105505	12112	108	5219	328	968	71	88	4	<3	<0.6	44261	2089
ZMB2-mnz-103	7194	128	16897	116773	229615	26401	126840	20749	3532	20723	2314	8204	689	813	31	64	5	37238	9810
ZMB2-mnz-104†	9554	58	2128	134517	250532	26205	99079	11214	350	5999	415	1027	71	68	5	<4	<0.3	80901	1894
ZMB2-mnz-105	17867	39	10995	119739	233560	25633	98642	20336	210	13850	1319	4952	467	677	41	122	11	67464	4066
ZMB2-mnz-106	20095	229	16344	165637	237829	27155	100414	15437	1699	12904	1559	6183	584	780	47	166	9	82707	9190
ZMB2-mnz-107	19069	170	21342	146404	209715	21238	81591	8571	907	6909	791	3725	666	1408	148	604	52	166207	3470
ZMB2-mnz-108	8514	94	22866	129004	244283	24637	103717	15081	1114	10837	1415	6511	840	1023	58	155	11	41193	4632
ZMB2-mnz-109	18130	59	1032	157688	263945	22260	69846	7337	139	3941	219	497	50	62	3	16	2	50114	812

LA-ICP-MS DATA	ppm	ppm	ppm	ppm	ppm	ppm	ppm	ppm	ppm	ppm	ppm	ppm	ppm	ppm	ppm	ppm	ppm	ppm	ppm
	Ca	Sr	Y	La	Ce	Pr	Nd	Sm	Eu	Gd	Tb	Dy	Ho	Er	Tm	Yb†	Lu††	Th	U
Orange River																			
ORG2-muz-1	5294	14	20423	106181	230478	24596	103977	21211	360	15558	1924	8664	848	1412	92	281	17	50361	4169
ORG2-muz-2	15530	19	30015	137180	238964	28617	118066	22576	729	17889	2172	9662	1173	1809	108	309	21	59374	7523
ORG2-muz-3†	4140	11	3423	127973	270254	28027	94371	12652	306	7292	703	2070	166	139	5	2	<0.3	57659	1279
ORG2-muz-4	11308	15	6437	128870	265883	30819	115024	21445	933	11639	982	2595	297	438	39	243	24	31655	2509
ORG2-muz-5†	14822	29	2466	123978	251796	31382	120467	19004	379	12624	935	1793	107	89	4	<5	<0.6	64603	3075
ORG2-muz-6	8514	14	21911	114710	249883	27070	110781	15422	294	10894	1139	5356	780	1790	144	609	59	57800	2777
ORG2-muz-7	1918	42	15041	132247	225031	20415	82386	10170	336	7813	954	4071	585	1058	82	332	23	78722	3189
ORG2-muz-8†	19866	12	3449	108925	244966	25612	113180	21277	156	12558	978	2301	146	136	5	<5	<1.2	57725	4526
ORG2-muz-9	10616	67	9670	138229	232407	24006	81732	12370	302	8418	970	3535	452	641	42	163	10	120939	5109
ORG2-muz-10	9036	25	15201	156582	269861	25804	104962	15052	540	8844	1019	4356	619	1253	113	425	38	47807	3158
ORG2-muz-11	14660	33	24220	122219	214316	26354	98618	16886	337	14125	1607	7219	843	1370	116	379	39	61946	9547
ORG2-muz-12	25271	105	23544	114905	222043	28123	99487	20298	244	17129	1856	7556	953	1505	137	543	47	65067	25852
ORG2-muz-13	13516	17	18932	125816	237274	28797	96946	11691	202	9733	1025	5874	690	1357	130	535	57	55610	5328
ORG2-muz-14	13824	18	12148	133162	239877	31977	118171	20583	308	17856	1598	5155	548	532	26	48	1	58667	9566
ORG2-muz-15	5892	6	12774	123626	239988	33361	107164	17369	241	10544	946	3987	552	909	74	304	23	80739	3930
ORG2-muz-16	11097	32	4219	133510	259377	32856	119208	20100	215	13341	777	2028	193	233	18	47	7	48365	1005
ORG2-muz-17	11579	26	4660	119209	252411	29509	112815	21853	112	16692	1090	2593	158	157	8	24	2	65803	1770
ORG2-muz-18	19325	28	25604	106357	218201	25876	97132	16078	139	14613	1839	7528	822	1185	87	323	21	101439	12999
ORG2-muz-19	12074	13	2156	165227	231921	26461	89316	12425	121	7310	495	1181	90	124	4	<4	0.4	148003	4459
ORG2-muz-20	6385	11	16741	115176	232638	24272	83608	14295	192	10047	1004	4845	623	1388	112	311	32	86528	4184
ORG2-muz-21	18610	102	13147	150009	251736	25264	92498	12083	1243	7284	804	3138	457	922	69	266	27	38370	1047
ORG2-muz-22	14868	32	12077	123099	250404	29993	115930	17334	659	14892	1442	5072	436	742	38	132	13	46993	3243
ORG2-muz-23	7504	16	19187	129760	245359	28896	90888	13756	337	10312	1232	5363	677	1069	96	315	31	71969	2275
ORG2-muz-24	2098	10	7648	146117	268965	31054	92355	11478	429	6879	663	2672	372	578	41	153	17	28919	586
ORG2-muz-25	6324	44	18504	123284	243941	27970	107191	18773	752	13947	1468	5891	838	1396	97	427	38	30427	8323
ORG2-muz-26	13691	21	18865	112627	228779	29335	98270	18220	201	15424	1594	5971	704	1217	83	233	22	60985	4554
ORG2-muz-27	25707	11	32171	57795	169947	25353	93388	23010	61	16961	2304	10661	1281	2181	183	750	63	109452	19989
ORG2-muz-28†	4168	15	4977	120890	253939	29131	112076	18744	134	15038	1210	3356	209	294	13	<10	<1	30257	5368
ORG2-muz-29	20091	19	14244	111774	247980	25678	107062	19809	285	12727	1607	5087	527	705	63	202	9	45766	7608
ORG2-muz-30	15207	43	14428	117708	236650	26106	91804	13811	247	8556	929	3995	493	829	70	252	21	90226	5376
ORG2-muz-31	19191	25	25652	104506	220668	22852	83840	16673	657	11634	1522	7618	1013	1522	119	452	40	49890	7942
ORG2-muz-32	12155	28	6442	138422	233141	21325	73379	9951	414	6293	613	2309	246	372	23	72	7	85344	1302
ORG2-muz-33	14224	23	10058	109420	238161	29144	102757	17133	99	11726	1055	3687	420	532	37	110	12	48506	1483
ORG2-muz-34	11243	141	13097	147241	248842	26746	89975	11351	727	6951	828	3539	500	782	69	272	23	81995	1257
ORG2-muz-35	9939	96	14410	135877	244351	25305	96887	12788	252	8796	1104	4561	562	796	71	215	20	65121	13236
ORG2-muz-36	15025	24	16439	126820	244411	29387	115275	23224	326	18166	1628	6663	580	738	46	81	4	51024	4115
ORG2-muz-37	7931	23	11944	118794	241483	25602	113576	15577	61	10437	974	3932	519	820	63	247	23	57920	488
ORG2-muz-38	7166	22	14964	123665	245717	31517	122887	24859	194	17818	1705	6244	610	807	40	126	5	56588	4438
ORG2-muz-39	13988	29	24969	138534	234021	29182	112335	18491	331	14904	1691	7867	1001	1553	109	403	31	70435	13641
ORG2-muz-40	6135	6	3498	134796	261879	27645	99231	13337	96	8098	623	1872	133	133	5	<5	1	69438	2264
ORG2-muz-41†	11169	20	2062	146245	259087	28651	103708	13438	166	7735	601	1562	96	92	4	<4	<0.4	86313	2841
ORG2-muz-42	9038	41	10975	158153	272124	30237	111032	14574	1224	7871	731	3207	438	765	73	351	34	39455	1729
ORG2-muz-43	7554	13	9075	146455	261674	29383	106662	13368	279	7890	779	3505	404	576	50	167	16	47482	824
ORG2-muz-44	25235	31	22650	104206	211465	21011	79337	13892	153	10768	1342	7248	777	1146	88	271	20	99821	16742
ORG2-muz-45†	14419	26	2614	126118	254767	33015	115074	19829	235	9974	659	1732	110	124	5	<6	<0.5	60324	2472
ORG2-muz-46	7067	29	20800	130137	231280	26778	123447	22323	294	17590	1802	6969	773	1336	86	378	25	59066	3384
ORG2-muz-47	16631	20	20656	109646	234960	25961	100077	16237	269	10614	1018	5736	777	1383	127	599	49	63980	2673
ORG2-muz-48	14654	36	4194	129908	254681	30373	105707	16881	364	9584	794	2076	167	216	9	17	1	57442	732
ORG2-muz-49	9464	27	13041	127884	244641	27285	106408	19869	408	18217	2014	6234	405	450	30	36	3	38319	6173
ORG2-muz-50	21059	30	22943	115759	221001	25476	103901	24034	181	19205	2277	8149	950	1201	80	327	22	64781	4308
ORG2-muz-51†	31419	20	5310	119407	233833	30094	116735	23189	148	14903	1209	3064	195	213	9	<9	<0.9	78497	3759
ORG2-muz-52†	12311	30	2955	131989	243993	29411	107350	19170	243	11616	853	1913	102	109	5	<6	<0.5	57342	3072
ORG2-muz-53	16550	22	13992	121452	235250	28839	102039	18054	244	13093	1355	5495	538	637	33	79	5	73857	6647
ORG2-muz-54	17831	33	14982	128384	239929	26924	97811	13648	232	8939	935	4671	526	852	43	138	12	81311	667
ORG2-muz-55	15127	47	7136	127632	235293	26439	90969	16463	408	11267	999	3569	349	447	23	41	2	78561	5114
ORG2-muz-56†	15095	25	4994	146378	250165	25992	91139	12712	363	8402	805	2481	196	112	3	<6	<0.7	63791	2852
ORG2-muz-57	16404	22	1538	128264	259078	29396	103108	12467	332	4469	241	612	69	103	8	28	2	74780	471
ORG2-muz-58	6397	10	25308	120152	237675	29117	110994	20840	1553	13994	2009	7694	1027	1612	149	617	46	49845	2688
ORG2-muz-59	22721	149	18698	156194	257260	29277	90953	13340	1525	7810	978	4630	620	1259	109	474	39	52469	1964
ORG2-muz-60†	4868	15	10876	106665	221701	26618	103132	19678	209	14092	1429	5020	433	463	38	52	<3	90018	2525
ORG2-muz-61	20313	27	19405	103301	203696	24907	75660	14287	220	10582	1409	5988	731	972	78	211	25	120738	7134
ORG2-muz-62	10317	21	20020	127681	240151	29987	128815	20674	803	15248	1882	7263	803	691	32	69	4	51189	5000
ORG2-muz-63	21550	32	26597	113529	221983	31372	107567	22822	646	15639	1905	8583	980	1623	150	630	53	68022	9028
ORG2-muz-64	14505	73	24271	117935	227029	27065	96495	18689	978	13419	1756	7524	842	1523	118	541	41	47055	9555
ORG2-muz-65	9869	78	4264	151732	273344	28325	91534	9185	400	4398	423	1480	186	332	28	109	8	46442	1193
ORG2-muz-66	9638	22	1393	102562	250566	35210	139620	23205	44	7797	392	863	55	68	3	<5	0.2	65411	1123
ORG2-muz-67	18570	34	16962	151921	243310	24511	85239	14367	921	10174	1274	4877	675	1089	98	356	29	59844	2075
ORG2-muz-68	9168	32	13812	109878	249866	27091	119651	17631	230	9658	846	3221	509	1109	141	823	77	43228	1792
ORG2-muz-69	16806	14	9973	91945	229282	29307	126295	22020	138	14615	1442	4200	390	489	27	61	4	62828	4265
ORG2-muz-70	16393	8	26607	147720	238255	21446	57289	7928	114	5231	847	4387	753	1937	216	1264	144	118124	4368
ORG2-muz-71	10801	21	17057	128174	239459	29560	112376	19752	252	11979	1402	4918	627	832	67	156	11	55495	2867
ORG2-muz-72	22086	20	3357	125192	247851	28529	110779	15577	92	9312	643	1529	153	184	9	37	3	85081	1350
ORG2-muz-73	17154	40	25445	103401	223545	26051	110140	20660	404	14767	2278	7848	843	1185	84	350	21	67153	9798
ORG2-muz-74	30319	36	26710	161820	217970	19291	55346	8276	1433	5964	844	4574	845	2035	269	1189	131	129987	918
ORG2-muz-75	8828	23	11876	154817	272627	28831	101490	13499	470	8961	896	3457	438	701	54	214	18	44757	295
ORG2-muz-76†	13791	26	6728	136327	252112	27363	96161	12346	256	7607	838	2905	240	211	8	<5	<0.6	77911	4904
ORG2-muz-77	7505	21	26432	118883	234909	30627	129830	22425	601	15992	1909	7211	862	1478	137	417	39	51708	8398
ORG2-muz-78	14750	45	15755	125080	221693	24749	100754	15689	515	11973	1476	5024	555	678	29	77	9	63852	4677
ORG2-muz-79	14005	13	22733	127523	239630	24059	91036	14694	252	11994	1471	6592	871	1451	107	342	29	85529	4236
ORG2-muz-80†	19504	38	4426	127469	242097	27716	113169	20806	158	14070	1196	2741	146	138	4	<8	<0.8	68154	2757
ORG2-muz-81	8126	22	11170	125557	249448	28520	121651	21723	156	14944	1661	5139	455	439	23	24	1	47500	2842
ORG2-muz-82	13060	32	28077	126444	246596	29155	109865	18564	506	13982	1650	7371	906	1949	181	591	66	63634	8260
ORG2-muz-83	9151	41	10492	138419	241594	28475	132792	20966	613	15332	1503	4419	361	500	20	8	0.8	47575	5271
ORG2-muz-84	22370	26	12008	113939	229957	31443	128579	20406	270	9805	980	3402	445	767	69	317	26	80372	4044
ORG2-muz-85	5273	15	12403	125081	245973	26776	108939	16270	360	9867	935	3509	457	712	47	161	13	57313	3600
ORG2-muz-86	13315	18	1851	123424	251207	32913	138621	20720	352	9994	581	994	70	63	4	15	1	70903	711
ORG2-muz-87	4162	34	9810	127311	246357	26843	112243	16590	3044	11393	1027	3370	413	536	31	82	4	78401	569
ORG2-muz-88	15978	84	27257	123098	199965	21524	80617	13378	1218	9327	1143	5485	855	1875	178	801	71	129607	6219
ORG2-muz-89	13219	33	18157	138815	236693	24826	79810	12049	960	7728	918	4063	647	1154	95	329	34	75174	5995
ORG2-muz-90†	5279	27	1179	127099	250703	32512	132101	22215	52	9198	392	742	46	36	5	<5	<0.2	71300	1216
ORG2-muz-91	2413	28	22151	170515	277041	27963	110196	15577	1125	10127	1261	5267	769	1434	114	386	36	34219	2285
ORG2-muz-92	8987	50	20916	153221	245401	24896	96362	15406	697	8326	950	4250	698	1585	128	621	55	57703	1262
ORG2-muz-93	25378	48	21017	149732	229829	24851	95984	15170	270	8800	1159	5147	716	1357	103	333	30	80480	13935
ORG2-muz-94	14790	57	21431	120788	223895	24773	98224	24531	332	16034	2119	6943	761	1227	90	390	22	53366	26541
ORG2-muz-95	65202	165	28312	110373	185203	19327	63578	11783	2248	8572	1142	5520	944	1918	187	843	80	166807	5329
ORG2-muz-96	16866	26	7169	131741	245094	25511	101777	17450	105	11011	967	2813	284	400	21	34	2	104488	6097
ORG2-muz-97	11830	30	23016	125033	224203	25288	90052	16951	246	12167	1335	5335	806	1495	105	391	35	94393	2894
ORG2-muz-98	7354	17	12456	164540	266796	28426	88581	12030	719	7578	862	3445	477	862	70	192	13	30017	692
ORG2-muz-99	19196	55	7986	152361	235677	23228	86707	12712	698	7108	749	3015	352	556	45	160	13	93269	2434
ORG2-muz-100	11651	82	16692	160373	258233	29189	100901	14231	1283	8760	949	3880	618	1162	123	480	52	40310	3108
ORG2-muz-101	8293	60	5118	181565	254306	26820	89806	10643	337	5135	454	1600	211	383	24	97	7	100697	839
ORG2-muz-102†	391	558	1756	269663	291154	25627	81458	6921	1453	3763	259	759	64	96	5	15	<2	1293	92
ORG2-muz-103	12154	17	8628	120778	239459	27454	110637	22477	300	14654	1376	4337	322	358	22	31	4	52813	4214
ORG2-muz-104	16093	30	22991	156641	237146	26337	85657	14559	907	10177	1298	5775	865	1582	155	655	62	50497	2778
ORG2-muz-105	14190	77	18929	142306	234670	22162	63488	10081	1341	8826	1087	4568	624	1116	86	347	33	64091	4730
ORG2-muz-106	17208	25	9391	132106	220455	27665	102626	17108	463	10958	1153	4164	443	557	33	70	6	66410	2254
ORG2-muz-107	5797	15	5968	145728	268102	27053	103956	15138	144	7544	618	2384	256	412	32	108	9	40184	795
ORG2-muz-108†	11367	8	4595	107450	229171	27835	95040	17050	221	11759	1135	3464	232	188	8	<9	<1	78144	9907
ORG2-muz-109	8863	63	1836	141880	250259	26429	76121	12202	249	6251	429	1108	87	124	4	16	0.9	62480	671
ORG2-muz-110	9441	4	4955	121776	257354	31570	94456	15362	166	6992	718	2117	215	302	16	69	8	41808	3018
ORG2-muz-111	5943	19	7644	120205	241645	30195	100382	22158	111	12702	1160	4421	285	542	22	75	5	47364	2769
ORG2-muz-112	13625	27	4344	105305	226175	25427	63595	14893	147	11214	986	2499	170	169	12	28	1	96780	4500
ORG2-muz-113	10572	23	3432	129796	245154	32135	115129	21820	92	12714	876	1888	136	162	4	24	3	59792	1273
ORG2-muz-114	21415	54	14571	131457	219584	24984	81382	14273	2082	9300	1171	5610	643	1250	121	411	39	31137	806

†: the detection limits were estimated 3 SD of background measurements by taking into account the oxide interferences of $^{157}Gd^{16}O$ onto ^{173}Yb

††: the detection limits were estimated 3 SD of background measurements by taking into account the oxide interferences of $^{159}Tb^{16}O$ onto ^{175}Lu

***: calculated with the following equations**

$X_{monazite} = A_i/D$ Ai = La, Ce, Pr, Nd, Sm

$X_{xenotime} = 2Ca/D$

$X_{britholite} = (Th+U-Ca)/D$

$D = (La+Ce+Pr+Nd+Sm)+2Ca+(Th+U-Ca)$